



University of
Nottingham
UK | CHINA | MALAYSIA

Faculty of Science and Engineering

Department of Electrical and Electronic Engineering

**Improved Maximum Torque Per Ampere and
Anti-disturbance Control for a Permanent
Magnet Assisted Synchronous Reluctance
Machine**

by

Dong yang Li, M.Sc.

20272924

A thesis submitted to the University of Nottingham for the degree of
Doctor of Philosophy, 2024.

Under the supervision of

Prof. He Zhang

A/Prof. Chunyang Gu

Dr. Shuo Wang

Sep 2024

Abstract

The increasing demand for rare earth materials in the electric vehicle and power electronics industries has led to dwindling reserves and rising costs, particularly for Permanent Magnet Synchronous Machines (PMSMs). To address these challenges, rare-earth-free motors such as Permanent Magnet assisted Synchronous Reluctance Machines (PMA-SynRMs) have emerged as promising alternatives. The PMA-SynRM motor design aims to balance cost and performance. However, compared to Interior Permanent Magnet Synchronous Machines (IPMSMs), PMA-SynRMs exhibit more severe flux linkage nonlinearity, along with significant variations in inductance, flux saturation, and cross-saturation phenomena, all of which must be considered for high-performance control.

This thesis focuses on enhancing both the steady-state performance and dynamic response of PMA-SynRMs. To achieve this, an improved Maximum Torque per Ampere (MTPA) control strategy and an enhanced Extended State Observer (ESO) were proposed.

In Chapter 3, a comprehensive PMA-SynRM model was developed, incorporating inductance variation, flux saturation, and cross-saturation to accurately capture the machine's flux characteristics.

In Chapter 4, three improved MTPA control methods were introduced to optimize steady-state response:

- 1) A novel Pseudorandom Frequency Signal Injection (PRFSI) method that achieves continuous harmonic distribution, reduced MTPA angle detection

errors, and better dynamic response compared to traditional Constant Frequency Signal Injection (CFSI).

2) An online MTPA control strategy based on High Frequency Signal Injection (HSI), which leverages only the permanent magnet flux linkage data. Error analysis and a supplementary control loop were proposed to compensate for MTPA detection discrepancies.

3) An online tracking detection MTPA strategy, robust against resistance variations and parameter uncertainties, featuring an improved convergence function for faster response and a Self-learning Control (SLC) mechanism to adapt to flux characteristics.

In Chapter 5, an enhanced anti-disturbance ESO-based control strategy was proposed to improve dynamic response. A second-order Anti-Disturbance Extended State Observer (A-DESO) was designed to minimize observation errors at low frequencies and enhance noise suppression at high frequencies, particularly for analog position signals and current sensor noise. Additionally, a third-order Improved Extended State Observer (IESO) was introduced to further reduce sensorless control noise, minimize observed position errors, and shorten convergence time.

The proposed methodologies were validated through both simulations and experiments, demonstrating significant improvements in machine modeling, steady-state performance, and dynamic response.

Research Achievements

- [1] D. Li, S. Wang, C. Gu, Y. Bao, X. Zhang, C. Gerada, and H. Zhang. 2024. "High Precision Online MTPA Algorithm Considering Magnet Flux Parameter Mismatch for a PMa-SynRM" IEEE Transactions on Energy Conversion. (Accepted)
- [2] D. Li, S. Wang, C. Gu, Y. Bao, X. Zhang, C. Gerada, and H. Zhang. 2024. "An Anti-Disturbance Extended State Observer-Based Control of a PMa-SynRM for Fast Dynamic Response", *Energies*, 17, no. 17: 4260. <https://doi.org/10.3390/en17174260>.
- [3] D. Li, C. Gu, S. Wang and H. Zhang, "An Improved Control Strategy of PM-Assisted Synchronous Reluctance Machines Based on an Extended State Observer," 2022 IEEE Transportation Electrification Conference and Expo, Asia-Pacific (ITEC Asia-Pacific), Haining, China, 2022, pp. 1-6, doi: 10.1109/ITECAsia-Pacific56316.2022.9941931.
- [4] D. Li, C. Gu, S. Wang and H. Zhang, "Maximum torque per ampere control of a PMa-SynRM based on a signal injection method considering the flux characteristics," 3rd International Symposium on Electrical, Electronics and Information Engineering (ISEEIE 2023), Hangzhou, China, 2023, pp. 88-91, doi: 10.1049/icp.2023.1877.

Acknowledgement

First, I would like to sincerely thank my supervisors, Professor He Zhang, Dr. Chunyang Gu, and Dr. Shuo Wang. They not only gave me unlimited guidance in academics but also gave me care and support in life. The profound insights of the three supervisors and professors on research methods and thesis conception pointed out the direction for my research work.

Thanks to the friends from PEMC research group, whose cooperation made the heavy experimental work go smoothly. We have experienced many challenges and unforgettable moments together, and this experience will remain a treasured memory for me. Furthermore, I would like to thank PEMC for providing financial support that allows me to focus on my research.

Thanks to my parents, whose understanding and support were an important force for me to persevere until the end. They have been my strongest support throughout my doctoral career. Finally, I am full of expectations for the future and hope that I can continue to explore the unknown and contribute my strength on the future academic road.

Table of Contents

Abstract.....	I
Research Achievements	III
Acknowledgement	IV
Table of Contents.....	V
List of Figures.....	X
List of Tables	XVI
List of Abbreviations	XVII
List of Symbols.....	XIX
Chapter 1 Introduction.....	1
1.1 Background and Motivations.....	1
1.2 Comparison between IPMSM, SynRM, and PMA-SynRM.....	1
1.2.1. Comparison of Technical Principles	1
1.2.2. Comparison of Performance and Application Areas	2
1.2.3. Cost Benefit Analysis	3
1.3 Aims and Scope	4
1.4 Methodologies of PMA-SynRM.....	5
1.4.1. Structure and Working Principle.....	5
1.4.2. Mathematical Model.....	7
1.4.3. Nonlinear Characteristics of Parameters	9
1.4.4. MTPA Considering Flux Characteristics	11
1.5 Contributions	13
1.6 Thesis Structure	15

Chapter 2 Literature Review.....	18
2.1 PMA-SynRM Modelling Method.....	18
2.1.1. Machine Analysis on Flux Characteristics	18
2.1.2. Machine Analysis on Iron loss and Copper Loss.....	22
2.1.3. Machine Parameter Identification Method	27
2.1.4. Combination of Machine Modelling and Parameter Identification.....	31
2.2 MTPA Control for Steady State Improvements.....	33
2.2.1. MTPA Control Based on Signal Injection Method.....	34
2.2.2. MTPA Control Based on Non-invasive Online Detection.....	36
2.3 Dynamic Response Improvements Control.....	39
2.3.1. High-Performance Control	39
2.3.2. Extended State Observer-Based Control	41
2.3.3. Dynamic Response Improvements for High-Speed Sensor-less Control.....	43
Chapter 3 An Improved PMA-SynRM Modelling Method.....	47
3.1 Flux Modelling Considering Inductance Variation and Saturation	47
3.2 Flux Data Observation Considering Self and Cross Saturation Through Online Identification.....	49
3.2.1. Identification for Magnetic Saturation Flux	50
3.2.2 Identification for Cross-Saturation Flux.....	52
3.3 Model Parameters Identification.....	54
3.3.1. Permanent Magnet Model Parameter	54

3.3.2. Magnetic saturation Model Parameter	54
3.3.3. Cross Saturation Model Parameter	56
3.4 Model Validation with FEA Data	56
3.5 Experimental Verification	58
3.5.1. Experimental Platform.....	58
3.5.2. Machine Parameters.....	58
3.5.3. Model Parameter Calculation and Error Analysis	59
3.6 Chapter Summary	60
Chapter 4 Advanced MTPA Control Methods for Steady-State Performance Improvement.....	62
4.1 Online MTPA Angle Detection Based Pseudorandom Signal Injection for Improved Dynamic Response	62
4.1.1. Description of Injection Method.....	62
4.1.2. Evaluation of $\partial T_e / \partial \theta$	64
4.1.3. MTPA Tracking Based Fixed Frequency.....	66
4.1.4. Utilization of PRFSI Control	68
4.1.5. Analysis on PRFSI.....	72
4.1.6. Analysis and Effect of Filters	78
4.1.7. Simulation Verification	79
4.1.8. Experiments Verification	86
4.2 Improved Precision Online MTPA Considering Magnet Flux Mismatch for Reduced Control Error	89
4.2.1. Error Analysis on the traditional method.....	89

4.2.2. Error Compensation Method	91
4.2.3. Magnet Flux Modelling and Overall Control	93
4.2.4. Experiments Verification	95
4.3 SLC Based MTPA Online Control for Better Dynamic Performance	103
4.3.1. Methodology of Proposed Online Detection	103
4.3.2. Analysis of the Proposed Method	106
4.3.3. Improved Gradient Descent	109
4.3.4. Self-Learning-Based Control	111
4.3.5. Improved Current Angle Estimation Method for SLC	113
4.3.6. Simulation Verification	115
4.3.7. Experiments Verification	116
4.4 Chapter Summary	119
Chapter 5 High Dynamic Performance Control of PMa-SynRM.....	121
5.1 A-DESO Based Control for Noise Suppression and Fast Dynamic Response	121
5.1.1. Problem Statement and Parameter Calculation of ESO	121
5.1.2. Research Aims and Content Arrangements	123
5.1.3. Design of the Extended State Observer	123
5.1.4. Performance Analysis of the Conventional ESO.....	124
5.1.5. Design and Analysis of A-DESO.....	126
5.1.6. Stability of A-DESO and Parameter Design	132
5.1.7. Parameter Mismatch Analysis	134

5.1.8. Overall Control Diagram	135
5.1.9. Simulation Results	137
5.1.10. Experiments Results	141
5.2 IESO for Reduced Position Noise and Phase-lag and Better Dynamic Response in Sensor-less Control	146
5.2.1 Proposed Control Structure.....	146
5.2.2 Speed Controller Design.....	149
5.2.3 Design of the IESO	150
5.2.4 Overall control scheme design.....	153
5.2.5 Analysis on Load Disturbance Observation Performance	155
5.2.6 Analysis on Position Observation Performance	158
5.2.7 Analysis on System Stability	160
5.2.8 Analysis on Parameter Selection	161
5.2.9 Experiments Verification	163
5.3 Chapter Summary	168
Chapter 6 Conclusions and Further Work.....	171
6.1 Summary of this Thesis	171
6.2 Further Work.....	172

List of Figures

Fig. 1.2-1 Comparison of IPMSM and PMA-SynRM.....	2
Fig. 1.2-2 Comparison of SynRM and PMA-SynRM.....	2
Fig. 1.4-1 Structure of PMA-SynRM	7
Fig.1.4-2 Equivalent circuit of the PMA-SynRM	8
Fig.1.4-3 Flux characteristics of the PMA-SynRM.....	10
Fig. 1.4-4 Relationship between the current and MTPA of the PMA-SynRM..	11
Fig. 1.6-1 Overall structure of the thesis	17
Fig. 2.1-1 Research summary on the flux characteristics.....	19
Fig. 2.1-2 Research summary on the modelling of power loss	22
Fig. 2.1-3 Research summary on the parameter identification.....	28
Fig. 2.2-1 Research summary on the MTPA control	33
Fig. 2.3-1 Research comparison summary on ESO	42
Fig. 2.3-2 Research summary on sensor-less control	45
Fig. 3.2-1 Flux estimation diagram	49
Fig. 3.2-2 Magnetic saturation model identification for d -axis flux;	51
Fig. 3.2-3 Magnetic saturation model identification for q -axis flux.....	52
Fig. 3.2-4 Cross-saturation model identification for d - and q -axis flux	53
Fig. 3.4-1 d - axis flux with the proposed modelling method.....	57
Fig. 3.4-2 q - axis flux with the proposed modelling method.....	57
Fig. 3.4-3 Permanent magnet flux with the proposed modelling method.	57
Fig. 3.5-1 Hardware platform for the PMA-SynRM	58
Fig. 3.5-2 d - axis flux with the proposed modelling method.....	60

Fig. 3.5-3 q - axis flux with the proposed modelling method.....	60
Fig. 3.5-4 Permanent magnet flux with the proposed modelling method	60
Fig. 4.1-1 Signal processing to get the MTPA criterion	66
Fig. 4.1-2 PRFSI method signal generation diagram	69
Fig. 4.1-3 Overall control diagram of PRFSI	69
Fig. 4.1-4 Configuration of high-frequency current loop and adaptive bandpass filter.....	70
Fig. 4.1-5 PSD Analysis of PRFSI	77
Fig. 4.1-6 P_o output with CFSI and PRFSI.....	78
Fig. 4.1-7 Phase current and its harmonic distribution without signal injection.	79
Fig. 4.1-8 Phase current and its harmonic distribution with CFSI	80
Fig. 4.1-9 Phase current and its harmonic distribution with PRFSI.....	82
Fig. 4.1-10 PSD of different pair of frequencies selection	83
Fig. 4.1-11 Possibility selection of frequency for PRFSI.....	84
Fig. 4.1-12 Output of the LPF under the rated load.....	85
Fig. 4.1-13 High frequency current loop and tracking error of CFSI and PRFSI	87
Fig. 4.1-14 Speed response of CFSI and PRFSI.....	88
Fig. 4.1-15 Rated load current angle detection with CFSI and PRFSI.....	88
Fig. 4.1-16 Stator current with CFSI and PRFSI.....	88
Fig. 4.2-2 Error analysis of the proposed polynomial function.....	94
Fig. 4.2-3 Performance of the proposed supplementation control strategy	96

Fig. 4.2-4 Phase current with the proposed MTPA detection method.	97
Fig. 4.2-5 Proposed MTPA method in cold machine condition.....	98
Fig. 4.2-6 Proposed MTPA method in hot machine condition	98
Fig. 4.2-7 d - and q -axis current under the whole working condition.	99
Fig. 4.2-8 Step load from 0 Nm– 1.9 Nm.....	100
Fig. 4.2-9 Step speed reference variation from 1350 rpm to 2700 rpm.....	101
Fig. 4.3-1 Overall control diagram of Online Tracking method.....	106
Fig. 4.3-2 Principal diagram of gradient descent algorithm	106
Fig. 4.3-3 Principal diagram of improved descent algorithm.....	111
Fig. 4.3-4 Diagram of current angle reference calculation scheme for SLC reference generation and data recording module.....	112
Fig. 4.3-5 Schematic of the proposed SLC scheme.....	113
Fig. 4.3-6 Simulation results under different resistance setting	115
Fig. 4.3-7 MTPA detection in different convergence function	116
Fig. 4.3-8 MTPA detection performance at different speed.....	117
Fig. 4.3-9 MTPA detection with original SLC and improved SLC estimation function.....	118
Fig. 5.1-1 Relationship between maximum error and frequency	122
Fig. 5.1-2 Error dynamics diagram of the ESO	124
Fig. 5.1-3 Frequency responses of disturbance estimation for the ESO.....	125
Fig. 5.1-4 Frequency responses of noise suppression for the ESO	125
Fig. 5.1-5 Error dynamics diagram of A-DESO.....	126
Fig. 5.1-6 Frequency responses of disturbance estimation error for the A-DESO	

and ESO	128
Fig. 5.1-7 Frequency responses of noise suppression for the A-DESO and ESO	129
Fig. 5.1-8 Error dynamic response for speed of ESO and A-DESO	130
Fig. 5.1-9 Error suppression response for position observation of ESO and A- DESO	131
Fig. 5.1-10 Frequency responses of load torque estimation with different k and τ	132
Fig. 5.1-11 Frequency responses of noise suppression with different k and τ .	133
Fig. 5.1-12 Parameter calculation process of A-DESO based on the PMA- SynRM.....	133
Fig. 5.1-13 Observation error with d - and q -axis inductance mismatch. (a) observation error in rated load condition;(b) observation error in half load condition	135
Fig. 5.1-14 Overall control diagram of dynamic improvements based on A- DESO.....	136
Fig. 5.1-15 Overall control diagram of i_d and i_q generation.	137
Fig. 5.1-16 Simulation results on step load response in MTPA region	138
Fig. 5.1-17 Simulation results on step load response in FW region.	140
Fig. 5.1-18 Experiments results in MTPA region: Speed fluctuation with A- DESO and without ESO; Current fluctuation with A-DESO and without ESO; Load torque and observed disturbance	142
Fig. 5.1-19 Experiments results in FW region: Speed fluctuation with A-DESO	

and without ESO; Current fluctuation with A-DESO and without ESO; Load torque and observed disturbance	143
Fig. 5.1-20 Experiments results in repeating step-load response in MTPA working condition: Speed fluctuation with A-DESO and without ESO; Load torque and observed disturbance	144
Fig. 5.1-21 Experiments results in repeating step-load response in FW working condition: Speed fluctuation with A-DESO and without ESO; Load torque and observed disturbance	144
Fig. 5.1-22 Experiments results in ramp load response in the whole working condition: Speed fluctuation with ESO and without ESO; Load torque and observed disturbance	145
Fig. 5.2-1 Structure of speed controller	150
Fig. 5.2-2 Error dynamics of conventional ESO	151
Fig. 5.2-3 Error dynamic of the IESO	152
Fig. 5.2-4 Overall control diagram of sensor-less scheme	154
Fig. 5.2-5 Error dynamic response for torque disturbance of ESO and IESO	156
Fig. 5.2-6 Error suppression response of ESO and IESO.....	157
Fig. 5.2-7 Error dynamic response for position of ESO and IESO	159
Fig. 5.2-8 Error suppression response for position observation of ESO and IESO	160
Fig. 5.2-9 Error dynamics with different k and τ	161
Fig. 5.2-10 Noise suppression with different k and τ	162
Fig. 5.2-11 Error dynamics for position with different k and τ	162

Fig. 5.2-12 Noise suppression for position with different k and τ	163
Fig. 5.2-13 Parameter selection procedure	163
Fig. 5.2-14 Speed and current response for the step load.....	164
Fig. 5.2-15 Sensor-less performance of a step load.....	166
Fig. 5.2-16 Response of ESO and IESO under current noise.....	167
Fig. 5.2-17 Position error under injected noise.....	167

List of Tables

Table 1.2-1 Comparison Table of IPMSM, SynRM, and PMA-SynRM	2
Table 2.1-1 Comparative for different loss modeling methods	26
Table 2.1-2 Comparison of Parameter Identification Methods for Motor Control.....	31
Table 2.2-1 Comparison of different MTPA Control Methods.....	38
Table 3.2-1 Working Condition for estimation.....	50
Table 3.5-1 PMA-SynRM Parameters	59
Table 4.2-1 PMA-SynRM Signal Injection Parameters.....	95
Table 4.2-2 Comparison between original signal injection method and the proposed compensation method	96
Table 4.3-1 PMA-SynRM test angles in different working conditions ...	116

List of Abbreviations

- ABS: Adaptive Backstepping
- A-DESO: Anti-Disturbance Extended State Observer
- BPF: Band-pass Filter
- CFSI: Constant Frequency Signal Injection
- DFO: Direct Flux Observer
- EEMF: Extended Electromotive Force
- EKF: Extended Kalman Filter
- EMF: Electromotive Force
- ESO: Extended State Observer
- FEM: Finite Element Method
- FEA: Finite Element Analysis
- FFT: Fast Fourier Transform
- FW: Flux Weakening
- HSI: High Frequency Signal Injection
- IESO: Improved Extended State Observer
- IPMSM: Interior Permanent Magnet Synchronous Machine
- LFSR: Linear Feedback Shift Register
- LPF: Low-pass Filter
- LSM: Least Squares Method
- LUT: Look-Up Table
- MTPA: Maximum Torque per Ampere
- MPC: Model Predictive Control

MRAS: Model Reference Adaptive System

PMSM: Permanent Magnet Synchronous Machine

PMa-SynRM: Permanent Magnet assisted Synchronous Reluctance Machine

PLL: Phase-locked Loop

PRFSI: Pseudorandom Frequency Signal Injection

PSD: Power Spectral Density

PSO: Particle Swarm Optimization

PWM: Pulse Width Modulation

RFSFNN: Recurrent Feature Selection Fuzzy Neural Network

RLS: Recursive Least Squares

SLC: Self-learning Control

SNR: Signal Noise Ratio

SynRM: Synchronous Reluctance Machine

THD: Total Harmonic Distortion

List of Symbols

u_d : voltage of d -axis

u_q : voltage of q -axis

R_s : stator resistance

i_d : d -axis current

i_q : q -axis current

ψ_d : d -axis flux linkage

ψ_q : q -axis flux linkage

ω_e : electrical speed of the PMA-SynRM

L_d : d -axis inductances

L_q : q -axis inductances

ψ_{pm} : permanent magnet flux

T_e : electrical torque

p : pole pairs of the machine

J : moment of inertia,

ω_m : the mechanical speed,

T_L : load torque,

B : viscous friction coefficient.

i_s : stator current

θ : angle between i_s and the d -axis direction

K_d : model parameter represents cross saturation according to d - axis current magnitudes

K_q : model parameter represents cross saturation according to q - axis current

magnitudes

D_{dq} : model parameter represents the overall cross-saturation

A_d, B_d, C_d : d -axis related model parameters

A_q, B_q, C_q : q -axis related model parameters

L_{dyn} : inductance dynamic matrix

$\hat{\psi}_{pm}$: estimated permanent magnet flux

$p_0, p_1, p_2, p_3, \text{ and } p_4$: polynomial coefficients of permanent flux

u_{inj} : magnitude of the voltage that creates the stator flux

I_{max} : current limit

u_{ref} : voltage reference

V_{dc} : DC-link voltage

$I_{dmax@cross}, I_{qmax@cross}$: d - and q - axis current limits of the identification process

for cross saturation

ΔR_s : resistance variation caused by temperature changes

L_{qd}, L_{dq} : cross saturation inductance for q - and d -axis

θ_{avg} : current angle in fundamental frequency

θ_h : injected current angle

A_{mag} : magnitude of the injected signal

f_h : frequency of the injected signal

t : time unit

$i_{db}, i_{di}, i_{qb}, i_{qi}$: d -axis high frequency current; d -axis base frequency current; q -

axis high frequency current; q -axis base frequency current

ω_h : high frequency electrical velocity

P_e : electrical power

P_{copper} : copper loss

P_{reactive} : reactive power

P_{mech} : mechanical power

P_o : calculated output power from filters

$f_{1d}, f_{1q}, f_{2d}, f_{2q}$: generated d - and q -axis current in high frequency

P : possibilities of signal occurrence

$\delta ()$: unit impulse function

K_f : coefficient of signal analysis part

f_0 : injected signal

$E[]$: the expectation operator

$I(f)$: the FFT applied to a single cycle of the given signal.

$I^*(f)$: represent the complex conjugate of $I(f)$

T : the period of $i_0 (t-t_k)$

T_s : sampling cycle

f_s : sampling frequency

r_- : improvement ratio

$\Delta L_d, \Delta L_q$: inductance variation caused by the d - and q -axis flux saturation

U_d^* and U_q^* : reference d - and q -axis voltages from the PI controllers

V_d and V_q : voltages imposed on d - and q -axis due to deadtime

V_{dead} : distorted voltage term that is dependent on the deadtime

\dot{e}, \ddot{e} : first differential of error and second differential error of ω_m , respectively.

T_F : the viscous friction of the system

$d(t)$: observed load torque

$x_f(t)$, τ : state and the time constant of the filter

β : ESO cut-off frequency related parameters

k : parameter to adjust ESO

Chapter 1 Introduction

1.1 Background and Motivations

PMA-SynRMs have attracted considerable attention in both academia and industry due to their low cost and elimination of rare-earth material dependency compared to PMSMs [1]. However, the high nonlinear characteristic, and parameter uncertainty including parameter variation, flux variation, flux saturation, and cross saturation make it harder to achieve high control performance [2]. PMA-SynRM is a compromise choice to balance performance and cost.

The PMA-SynRM is a new type of high-efficiency motor developed in recent years. It combines the advantages of IPMSM (Interior Permanent Machine) and SynRM, aiming to provide higher efficiency and performance. To better understand the unique value and application potential of PMA-SynRM, a comprehensive comparison was carried out compared to IPMSM and SynRM.

1.2 Comparison between IPMSM, SynRM, and PMA-SynRM

1.2.1. Comparison of Technical Principles

IPMSM: A permanent magnet is built into the rotor of an IPMSM, which allows it to generate torque without rotor current. Despite their high efficiency, permanent magnets cost is high and are more susceptible to temperature changes.

SynRM: SynRM generates reluctance torque using the geometry of the rotor without expensive permanent magnet materials. In comparison with permanent magnet motors, this type is usually less expensive but does not offer the same efficiency or power density.

PMa-SynRM: The PMa-SynRM combines SynRM's reluctance torque with the IPMSM's permanent magnet torque. The efficiency and power density of the machine are improved while its cost and material use are controlled by adding a small amount of ferrite material to the rotor.

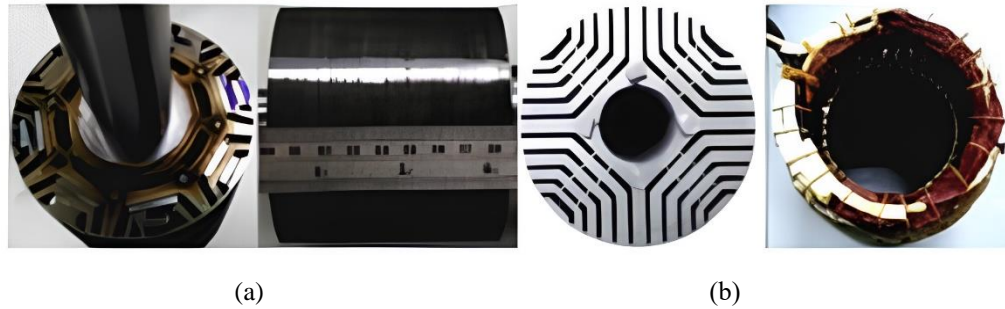


Fig. 1.2-1 Comparison of IPMSM and PMa-SynRM; (a) IPMSM (b) PMa-SynRM [3]

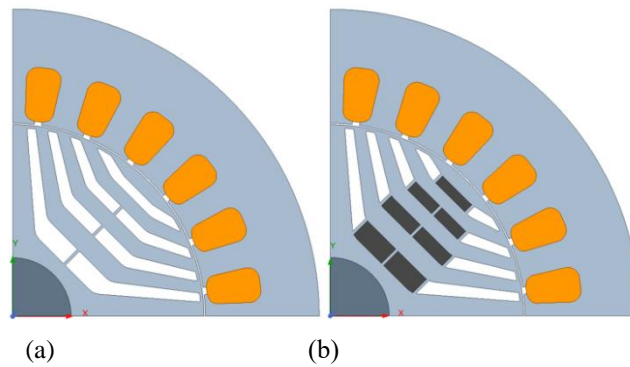


Fig. 1.2-2 Comparison of SynRM and PMa-SynRM; (a) SynRM (b) PMa-SynRM [4]

1.2.2. Comparison of Performance and Application Areas

Table 1.2-1 Comparison Table of IPMSM, SynRM, and PMa-SynRM

Feature	IPMSM	SynRM	PMa-SynRM
Rotor Structure	Permanent magnets are embedded in the rotor.	No permanent magnets; utilizes rotor geometry to generate reluctance torque.	Combines reluctance torque of SynRM with additional torque from a small amount of ferrite magnets.
Torque Generation	Generates torque without the need for rotor current, purely magnetic.	Generates reluctance torque through magnetic reluctance variations.	Generates both reluctance torque and magnetic torque, enhancing overall torque production.
Material Cost	High, due to the use of rare-earth permanent magnets.	Low, as it does not require rare-earth materials.	Medium, uses a small amount of ferrite which is less costly than rare-earth magnets.

Feature	IPMSM	SynRM	PMa-SynRM
Efficiency	High efficiency, but sensitive to temperature changes.	Moderate efficiency, generally lower than IPMSM.	Higher efficiency than SynRM, slightly less than IPMSM, with better cost-effectiveness.
Power Density	High power density due to strong magnetic fields from permanent magnets.	Lower power density compared to IPMSM.	Improved power density compared to SynRM by adding ferrite magnets.
Thermal Sensitivity	More sensitive to temperature variations due to permanent magnets.	Less sensitive as there are no permanent magnets.	Less sensitive than IPMSM, improved with ferrite usage.
Application Areas	Electric vehicles, industrial drives, robotics.	Low-cost applications, pumps, and fans where efficiency is less critical.	Hybrid electric vehicles, cost-effective industrial motors.

IPMSM: Due to its high efficiency and good high-speed performance, it is often used in applications requiring high performance and efficiency, such as electric vehicles and high-end industrial applications.

SynRM: Because of its cost-effectiveness and good environmental adaptability, it is mostly used in industrial and commercial applications that do not require extremely high efficiency and high-speed operation.

PMa-SynRM: it combines the advantages of IPMSM and SynRM and is suitable for application scenarios that require high efficiency and high reliability but have certain cost considerations, such as new energy vehicles and industrial drive systems with high performance requirements.

1.2.3. Cost Benefit Analysis

IPMSM: Although it provides the best performance, the high permanent magnet material and complex manufacturing process make the cost higher.

SynRM: Lower material costs make it more attractive in cost-sensitive

markets.

PMa-SynRM: By optimizing the use of permanent magnet materials, costs are reduced while maintaining high performance, providing an intermediate cost-effective solution.

Through the comparison, the PMa-SynRM features the advantages of high-power factor, high efficiency and low cost. Furthermore, the use of ferrite material makes it less dependent on rare earth materials. In this way, the PMa-SynRM is a compromising choice for both the power factor, efficiency and cost consideration. However, the specially designed structure and use of ferrite materials make the flux characteristic more complicated, which increases the difficulty of machine control and hinders the application scenarios of machines.

The main characteristics considering the control stage are as follows:

- a. The inductance variation is more severe compared to IPMSM.
- b. The phenomenon of magnetic saturation invalidates the current loop and observers that rely on flux information being considered as a fixed value.
- c. The cross-saturation caused by the materials of PMa-SynRM makes the flux influenced by both d - and q -axis current.
- d. The high temperature and high current demagnetization of IPMSM makes the PMa-SynRM more suitable for high-speed situations with deep flux weakening control.

1.3 Aims and Scope

Although PMa-SynRM motors offer significant benefits such as reduced reliance on rare-earth materials and cost-effectiveness, current control strategies

often inadequately address the machine's complex flux characteristics, including inductance variation, magnetic saturation, and cross saturation. Conventional MTPA control methods frequently rely on preset machine parameters, leading to inaccuracies and suboptimal performance under changing operating conditions. To bridge this research gap, this study aims to perform an in-depth analysis and evaluation of PMA-SynRM characteristics to develop an accurate control model accounting for these flux complexities. Specifically, steady-state performance is enhanced by proposing a novel MTPA control strategy without the need for preset machine parameters, aiming to decrease average MTPA angle error and root mean square error, thereby improving current accuracy and system efficiency. The response time of the MTPA control angle is also optimized. Furthermore, dynamic response is improved through advanced observer-based feedback control strategies to enhance the system's anti-disturbance capability, reduce convergence time during large torque disturbances, and mitigate disturbances from analog position sensors, current sensors, and sensor-less control techniques.

1.4 Methodologies of PMA-SynRM

1.4.1. Structure and Working Principle

Unlike IPMSM, there is no permanent magnet in the rotor of PMA-SynRM. The rotor structure of PMA-SynRM mostly adopts a multi-layer magnetic barrier form. The insertion of ferrite material is used to suppress the q-axis flux linkage to obtain greater torque. As shown in Fig. 1.4-1, there are two axes of symmetry in the PMA-SynRM rotor structure, corresponding to the direction of smaller

magnetic resistance (i.e. larger magnetic permeance) and the direction of larger magnetic resistance (i.e. smaller magnetic permeance). In this thesis, the direction with smaller magnetic resistance is selected as the d-axis, and the direction with larger magnetic resistance is selected as the q-axis. The d-axis leads the q-axis by an electrical angle of 90° .

To further clarify, the dq-axis reference frame is defined as a rotating reference frame that aligns with the rotor's magnetic flux direction. In this configuration:

The d-axis (direct axis) corresponds to the path of minimal magnetic reluctance, where the magnetic flux primarily flows. This axis is aligned with the magnetic barrier structure that optimally conducts flux.

The q-axis (quadrature axis) is oriented 90° electrically from the d-axis and represents the direction of higher magnetic reluctance. The flux linkage in this axis is typically suppressed through the insertion of ferrite materials to enhance torque production.

This dq reference frame is crucial for analyzing the magnetic flux distribution and optimizing the control strategies for PMA-SynRM. It allows for decoupled control of torque and flux, enabling more efficient operation under various load conditions. Throughout this thesis, all control methods and analysis are based on this rotating reference frame, which simplifies the expressions of voltage and current in synchronous machines.

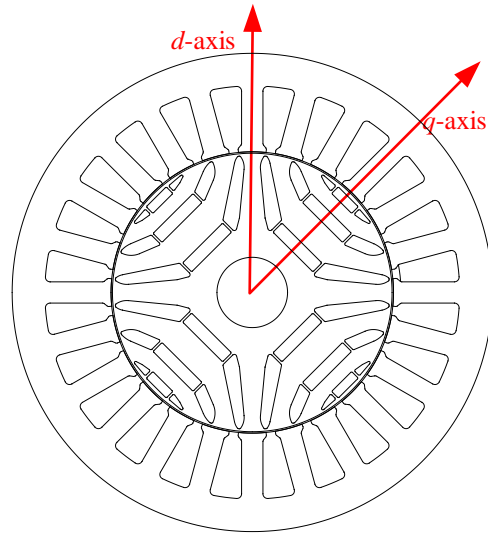


Fig. 1.4-1 Structure of PMa-SynRM

1.4.2. Mathematical Model

To facilitate theoretical and simulation research, the controlled motor is considered an ideal one, and the following assumptions are set:

(1) Assume that the three-phase windings of the motor are symmetrically distributed and differ from each other in space by 120° electrical angles. The magnetomotive force generated by the motor is sinusoidally distributed along the air gap, and space harmonics are ignored.

(2) Ignore the saturation effect of the motor's magnetic circuit and assume that the self-inductance and mutual inductance parameters of each winding of the motor are constant.

(3) Ignore core loss.

(4) Ignore changes in winding resistance due to frequency changes (such as skin effect), temperature changes, etc.

Based on the assumptions, d - and q -axis equivalent circuit could be obtained as shown in Fig.1.4-2.

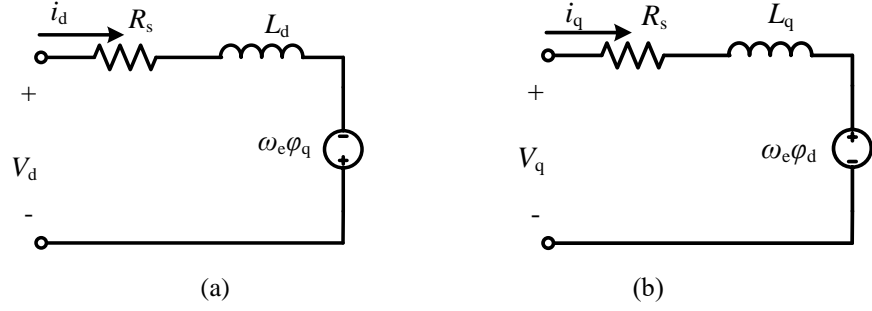


Fig.1.4-2 Equivalent circuit of the PMA-SynRM (a) d - axis equivalent circuit; (b) q -axis equivalent circuit

As shown in Fig.1.4-2, the voltage equation in d - and q -axis is adopted in Eq.n 1.4-1.

$$\begin{cases} u_d = R_s i_d + \frac{d\psi_d}{dt} - \omega_e \psi_q \\ u_q = R_s i_q + \frac{d\psi_q}{dt} + \omega_e \psi_d \end{cases} \quad \text{Eq.n 1.4-1}$$

where, u_d and u_q is the voltage of d - and q -axis, respectively; R_s is the stator resistance; i_d and i_q is the d - and q -axis current, respectively; ψ_d and ψ_q is the d - and q -axis flux linkage, respectively; ω_e is the electrical speed of the PMA-SynRM.

The flux linkage equation is:

$$\begin{cases} \psi_d = L_d i_d \\ \psi_q = L_q i_q - \psi_{pm} \end{cases} \quad \text{Eq.n 1.4-2}$$

where, L_d and L_q are the d - and q -axis inductances. ψ_{pm} is the permanent magnet flux.

The torque equation is:

$$T_e = \frac{3}{2} p [\psi_{pm} i_q + (L_d - L_q) i_d i_q] \quad \text{Eq.n 1.4-3}$$

where p is the pole pairs of the machine.

The Eq.n 1.4-3 plus the mechanical motion equation as Eq.n 1.4-4 are the dynamic mathematical model of the PMA-SynRM in the d - and q -axis two-phase rotating coordinate system.

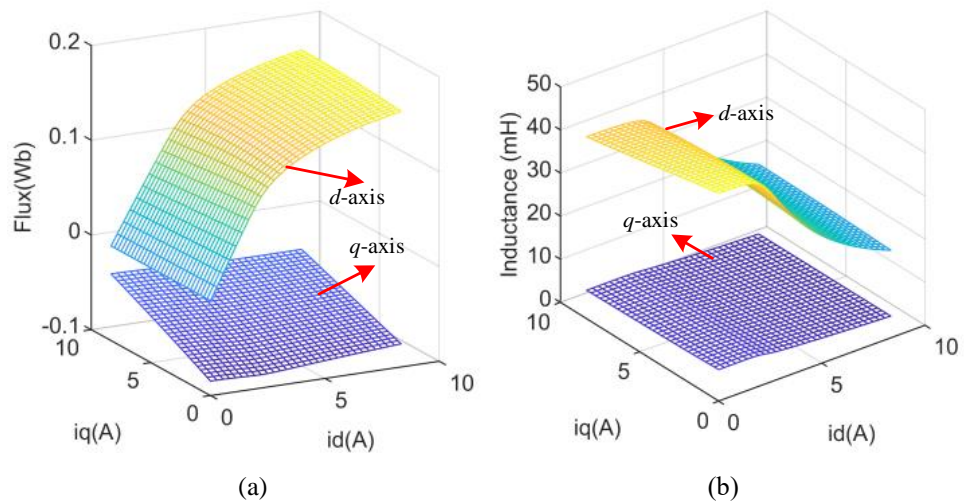
$$J \frac{d\omega_m}{dt} = T_e - T_L - B\omega_m \quad \text{Eq.n 1.4-4}$$

where J is moment of inertia, ω_m is the mechanical speed, T_e is the electrical torque, T_L is the load torque, B is the viscous friction coefficient.

1.4.3. Nonlinear Characteristics of Parameters

In the model discussed in Chapter 1.4.2, the d - and q -axis inductance parameters L_d and L_q are regarded as a fixed value. However, in actual applications, affected by factors such as the saturation effect of the magnetic circuit for the PMA-SynRM and temperature variations, the L_d and L_q feature nonlinear characteristics, specifically.

PMA-SynRM currents affect the magnetic circuit characteristics of the machine, resulting in significant nonlinearities. A nonlinear saturation of the core magnetic circuit is caused by the stator current during the operation of PMA-SynRM. In addition, there is cross coupling between the d - and q -axis inductances, which causes significant nonlinear changes in the motor's d - and q -axis inductances. In this thesis, a FEM (Finite Element Method) was applied to the controlled PMA-SynRM.



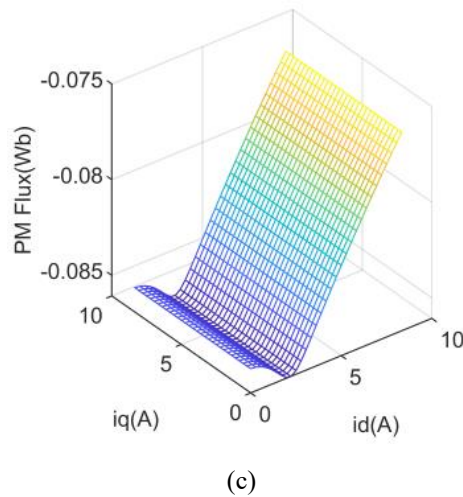


Fig. 1.4-3 Flux characteristics of the PMA-SynRM (a) d - and q -axis flux with different d - and q -axis current; (b) d - and q -axis inductance with different d - and q -axis current; (c) permanent magnet flux with different d - and q -axis current.

In this thesis, cross-saturation, magnet saturation, and inductance variations of the machine were considered in the machine modeling. Fig. 1.4-3 shows the inductance and flux of the PMA-SynRM obtained from the FEA (Finite Element Analysis) data. According to the d - and q -axis inductance of the machine in Fig. 1.4-3(b), d - and q -axis inductance is largely influenced by d - and q -axis current. It should be noted that the d -axis inductance is affected by both the d -axis current and the q -axis current.

The flux along the d - and q -axis could also be used for further verification. In Fig. 1.4-3(a), as the current increases, the flux linkage gradually tends to remain unchanged, which means that the magnetic saturation phenomenon greatly influences the flux and inductance. The change in q -axis flux has the same trend as the change in d -axis flux.

The calculation of the MTPA method of Eq.n 1.4-8 is based on a fixed value of d - and q -axis current. However, inductance variation, magnetic saturation, and cross-saturation need to be considered for this machine for the calculation of the

MTPA working trajectory.

It is possible to calculate the torque of the machine for different currents based on the inductance and flux linkage of the machine as shown in Fig. 1.4-3 in which the maximum torque could be obtained from a finite current value as depicted. From the calculated maximum torque with the limited current, the MTPA curve with different d - and q -axis currents could be obtained.

1.4.4. MTPA Considering Flux Characteristics

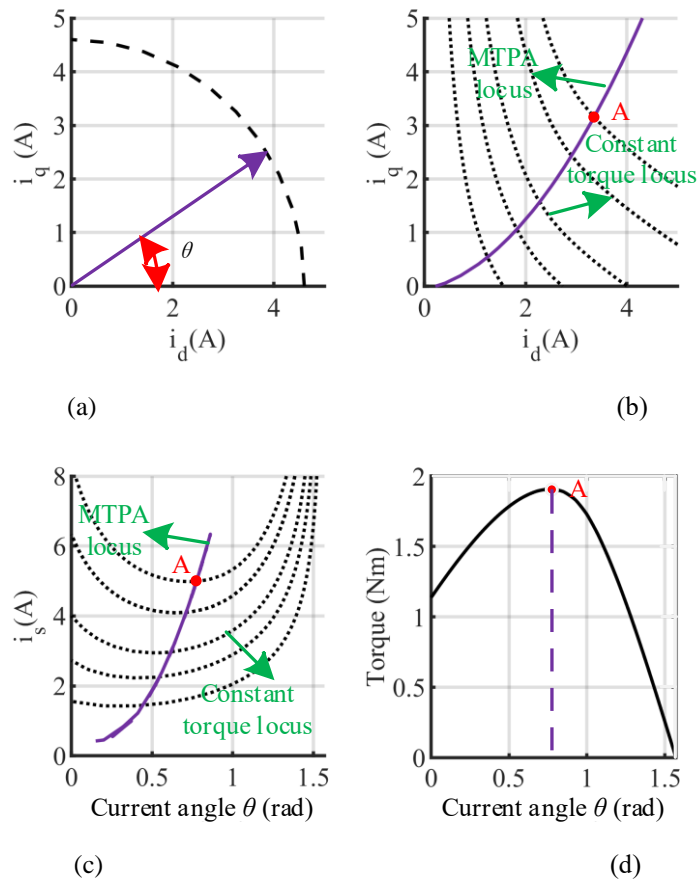


Fig. 1.4-4 Relationship between the current and MTPA of the PMA-SynRM (a) d - and q -axis current with stator current limit; (b) torque locus with different d - and q -axis current; (c) torque locus with different stator current and current angle; (d) output torque with different current angle.

Fig. 1.4-4 shows the machine's current limit, and output electrical torque at different current angles. The OA curve represents the MTPA working trajectory in which maximum efficiency could be achieved. As indicated in Fig. 1.4-4(d),

the output torque differs under different working conditions such as those depicted at working condition A, B, and C with the same magnitude of stator current. In working condition A, the maximum torque could be obtained. In the case of moving from working condition C to A, the output torque T_e increases with a decrease in the current angle θ . So, $\partial T_e / \partial \theta < 0$ could be obtained in the left half of the current limit path. Meanwhile, the output torque increases with an increase in current angle θ , which means $\partial T_e / \partial \theta > 0$. In working condition A, $\partial T_e / \partial \theta = 0$ is satisfied, which means that the MTPA problem could be simplified into finding the $\partial T_e / \partial \theta = 0$ working point.

With the working point discussed, $\partial T_e / \partial \theta = 0$ working point is necessary for the MTPA control. In general, the MTPA working point could be calculated with the computational method. A minimum current magnitude is obtained because of this solution (i_d, i_q pair). By using MTPA i_d and i_q , the following constrained optimization problem could be obtained as shown in Eq.n 1.4-5.

$$\begin{cases} \text{minimize } |i_s| = \sqrt{i_d^2 + i_q^2} \\ \text{subject to } \frac{3}{2} p [\psi_d i_q - \psi_q i_d] = T_e \end{cases} \quad \text{Eq.n 1.4-5}$$

Let the Eq.n 1.4-6 hold:

$$\begin{cases} i_d = |i_s| \times \cos \theta \\ i_q = |i_s| \times \sin \theta \end{cases} \quad \text{Eq.n 1.4-6}$$

where $|i_s|$ is the current vector magnitude, θ is the angle between i_s and the d -axis direction, that is, the current angle. Eq.n 1.4-7 could be obtained based on Eq.n 1.4-5 and Eq.n 1.4-6.

$$T_e = p \left[\psi_{pm} i_s \cos \theta + \frac{1}{2} (L_d - L_q) i_s^2 \sin 2\theta \right] \quad \text{Eq.n 1.4-7}$$

As a result of Eq.n 1.4-5, the d - and q -axis currents should comply with Eq.n 1.4-8 under the MTPA condition.

$$\theta = \arcsin \left[\frac{-\psi_{pm} + \sqrt{\psi_{pm}^2 + 8(L_d - L_q)^2 i_s^2}}{4(L_d - L_q) i_s} \right] \quad \text{Eq.n 1.4-8}$$

From Eq.n 1.4-8, the MTPA angle could be obtained from a LUT (Looking-up Table), which is used to act as the theoretical value to check the MTPA detection performance in the later simulations and experiments. However, it should be noted that the derivation of inductance to current angle is ignored in the calculation.

Based on the machine model, the MTPA control of PMA-SynRM needs to be solved. Permanent magnets are contained in the IPMSM, which generate a bias magnetic field that causes the magnetic circuit to approach saturation. Consequently, the influence of the motor current on inductance, flux linkage, and other parameters is small, and the dynamic changes in the motor parameters are not readily apparent. By treating the motor parameters as constants in the model, MTPA control is still capable of providing good control effects on PMSMs; however, the PMA-SynRM motor current directly affects the motor's inductance. Due to the saturation of the magnetic circuit, the inductance changes significantly nonlinearly under different working conditions. As a result, it is particularly crucial to consider the nonlinear changes in the parameters of the inductance in the process of realizing MTPA control of PMA-SynRM. When motor parameters are treated as constants, certain errors will occur, which will be discussed in Chapter 4.

1.5 Contributions

This thesis focusses on improving performance by adopting the advanced

modelling for the PMa-SynRM and control strategies. The main contributions are listed as follows:

1. By employing the proposed modeling strategy for the PMa-SynRM, which accounts for inductance variation, magnetic saturation, and cross-saturation, the flux characteristics can be effectively described using only a limited set of parameters. Both magnetic saturation and cross-saturation effects are incorporated within the model.

2. MTPA control was proposed for a better steady-state response and reduced MTPA steady-state convergence time using three different methods. The innovations are as follows:

- a) A new PRFSI method for the MTPA detection was proposed to improve the injected signal harmonic distribution, which features continuous harmonic distribution compared to CFSI method, and smaller MTPA angle detection error, Therefore, better dynamic response compared to CFSI could be achieved.

- b) An online MTPA control strategy was proposed based on HSI which only relies on the permanent magnet flux of the machine; Error analysis was carried out to analyze between the practical control angle and theoretical value through mathematical differential equations analysis; Then, an error supplementary loop was added to compensate for the MTPA detection error, in which only the information of magnet flux in polynomial form is needed.

- c) An online tracking detection MTPA control strategy was proposed without the need of parameter information and signal injection, which is robust to resistance variation. Meanwhile, an improved MTPA convergence function

and SLC is designed considering the flux characteristics for better MTPA angle dynamic response.

3. An improved anti-disturbance ESO based control was proposed to improve the dynamic response of the control system by introducing a feed-forward path. The innovations are as follows:

a) A second order anti-disturbance ESO was proposed, which features a smaller observation error in low frequencies with the nonlinear characteristic of flux inductance, and better noise suppression ability in high frequencies to weaken the noise brought by the analog position signal for the speed calculation and the current sensor noise for the torque observation.

b) A third order anti-disturbance was proposed to eliminate the noise brought by the sensor-less control, and improve the dynamic response of the control system, including reducing the observed position error and reducing the response time.

1.6 Thesis Structure

This thesis was divided into 6 chapters, in which Chapter 1 introduces the background and motivations of the research, methodologies of the PMA-SynRM, and contributions of the whole thesis.

Chapter 2 did the literature of the cutting-edge control method for three parts: modelling of the SynRM and PMA-SynRM; MTPA control for IPMSM and other machines; dynamic response improvements control. Research found that most of the research focuses on the IPMSM and SynRM, in which the characteristics of the PMA-SynRMs are not fully considered.

Chapter 3 proposes the modelling of the PMA-SynRM, in which the cross-saturation, magnetic saturation, and inductance variation were fully considered with several parameters to describe the trend.

Chapter 4 proposes three control methods, namely PRFSI based control, MTPA error compensation control, and online MTPA tracking control, to improve the steady-state performance of the MTPA control, in which the ripple of the MTPA angle was reduced by adopting the PRFSI method. In the next stage, the error of the MTPA by using the proposed method was analyzed, and an error compensation link was designed to reduce the steady-state error. In addition, an online MTPA tracking method was proposed without the need to inject any current signal in the control loop and machine parameters. Besides, an SLC module was introduced considering the flux characteristics of the machine. In this way, a better dynamic response of MTPA angle with smaller error could be obtained.

Chapter 5 proposes an improved ESO to balance the low frequency observation ability and anti-disturbance ability in high frequency, in which the observation ability and anti-disturbance performance could be guaranteed sanctimoniously. Based on the proposed topology, a second order ESO was designed to reduce the high frequency noise brought by the analog position error, current sensor, and improve the dynamic response of the system. A third order ESO was proposed to improve the dynamic response and reduce the error in the observation position signal.

Chapter 6 summarizes the whole thesis and points out the possible ways to

do further research and improvements.

The overall structure of the theses is attached as Fig. 1.6-1.

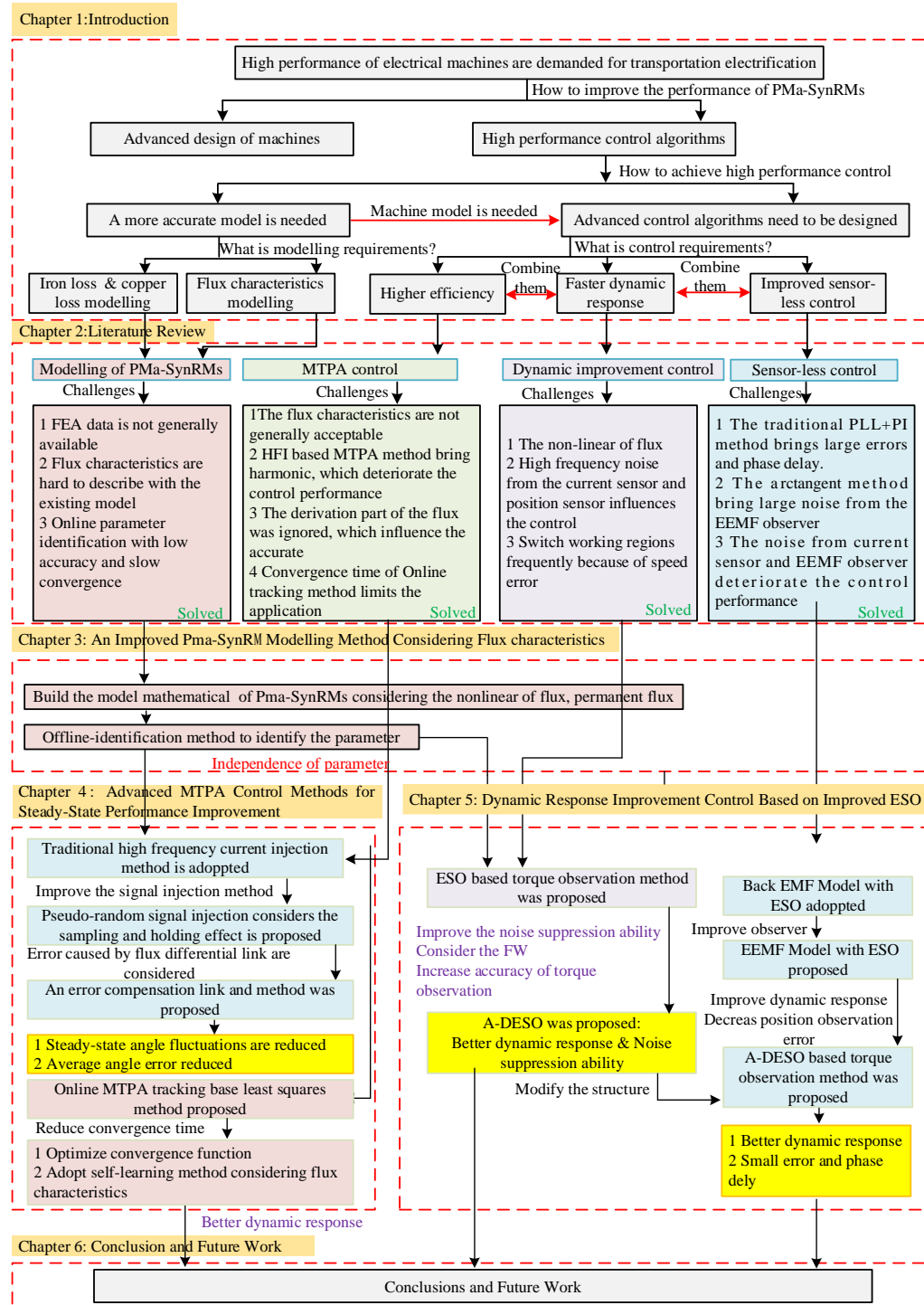


Fig. 1.6-1 Overall structure of the thesis

Chapter 2 Literature Review

2.1 PMA-SynRM Modelling Method

This chapter focuses on the modeling methods for PMA-SynRM. The analysis includes various aspects such as flux characteristics, iron and copper losses, machine parameter identification, and the integration of modeling with parameter identification, which are essential for optimizing the performance and efficiency of PMA-SynRM systems.

2.1.1. Machine Analysis on Flux Characteristics

The references studies span a wide range of research focused on the modeling and optimization of magnetic flux characteristics in various rotating machines, including IPMSM, SynRMs, and PMSMs. In the first part, as seen in [5-8], centered on optimizing magnetic flux characteristics to enhance machine performance and efficiency, often utilizing FEA and experimental data. For other research, such as those in [9], [10], [12], [15], [16], [18], and [22], introduced more sophisticated modeling techniques that account for complex factors like cross-coupling, magnetic saturation, and hysteresis effects, significantly improving the accuracy and reliability of machine models. The research in [13], [14], [17], [18], [20], [21], [23], [24] further advanced the understanding of magnetic saturation and cross-coupling, particularly in SynRMs and PMSMs, offering refined models and identification methods essential for precise control and performance prediction. Despite these advancements, the modeling of cross-saturation effects in PMA-SynRM, especially with ferrite materials, remains underexplored, indicating a promising area for future research to build on the

methodologies developed for other machine types.

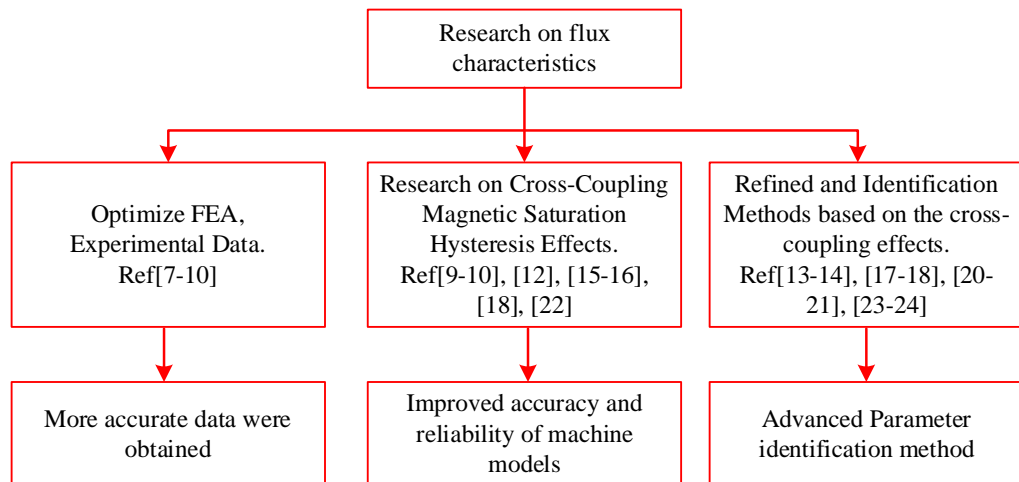


Fig. 2.1-1 Research summary on the flux characteristics

Ref [5] solves the problem of optimizing the magnetic flux characteristics of the IPMSM to improve performance and efficiency. This study evaluates the designed machine performance through FEA, with special emphasis on variable flux characteristics and their advantages in reducing losses. Similarly, [6] addresses the analysis on flux linkage characteristics, with particular focus on hysteresis loop characteristics derived from experimental data. Through experimental data analysis, the magnetic flux linkage characteristics are accurately evaluated, improving the accuracy of the analysis. Ref [7] studies the electromagnetic flux characteristics of double-sided switched reluctance linear machines and provides a flux link prediction method based on magnetic circuit analysis. Furthermore, [8] analyzes the dynamic characteristics of transverse flux linear machines with solid cores, especially considering core losses. Based on the characteristics of the flux mentioned, more research built the model for the flux and then did the experiments for the control[9-24].

Ref [9,15] research the modelling method for the SynRM, in which [9] proposes an accurate analytical model of a multi-channel flux barrier for a

SynRM. This work optimizes motor design and performance evaluation by improving model accuracy. A flux saturation model of a SynRM including cross saturation and its identification method at rest are developed in [15]. This model provides more accurate data for motor control and performance prediction.

Ref [10,19] focus on the modelling of PMSM, in which [10] proposed an improved IPMSM side-band current harmonic model that takes into account magnetic saturation and cross-coupling effects for more accurate prediction of the dynamic behavior of the machine. In addition, [19] improves the d - and q -axis inductance model of PMSM, taking into account the air gap flux harmonics and saturation effects, improving the accuracy and reliability of the motor model.

Ref [12,16,22] focus on the modelling of the IPMSM, where [12] designed and analyzed a new equivalent magnetic network model of IPMSM machines, which enhances the predictive ability of the model. Ref [16] proposed a high-fidelity nonlinear IPMSM model was developed based on the measured stator winding flux linkage. Saturation, cross-coupling, spatial harmonics, and temperature effects are considered in the model, providing a more comprehensive understanding and analysis framework for IPMSMs in [22].

Comprehensive study of magnetic saturation and cross-coupling were researched in [13,14,20,21]. Ref [13,14] identifies the flux saturation model of the SynRMs, compensates for the dead zone effect, and selects a more appropriate injection voltage, thereby providing better input conditions for motor control. Ref [20] proposes an improved small-signal injection-based online multi-parameter identification method that considers cross-coupled magnetic

saturation, providing a technical means for online monitoring and optimization of IPMSM performance. Ref [21] proposed methods to reduce rotor motion when estimating magnetic saturation models of SynRMs and IPMSMs, which helps to evaluate machine characteristics under stationary conditions more accurately.

Ref [17,18] respectively studies the impact of cross saturation on the accuracy of the saturated induction motor model and the impact of dynamic cross saturation on the accuracy of the saturated synchronous machine model. These studies provided theoretical foundations and experimental validation for the development of subsequent models. Methods for modeling magnetization dynamics using saturation wavefronts have been investigated in [23], providing new avenues for understanding and predicting the magnetic behavior of materials. Ref [24] proposed a dynamic SynRM model based on space vector state, considering magnetic saturation, cross-saturation and iron loss, and its related identification technology.

To sum up, the cross-coupling phenomenon was researched from an early age. However, the modelling method was not provided until recent years. Most of the methods come from the machine design process. For the machine control considering these parts, only a few papers made progress. From the aspects of machine modelling to improving the control stage, most of the papers are focused on the PMSM and IPMSMs. Although the basic methodology could be provided for the PMa-SynRM modelling, the cross saturation is more severe for the PMa-SynRM. For the modelling of SynRM, the ideas could be provided from

the modelling process. However, the cross saturation of the ferrite was not modelled and considered, in which the modelling of it is different from the rare earth materials one.

2.1.2. Machine Analysis on Iron loss and Copper Loss

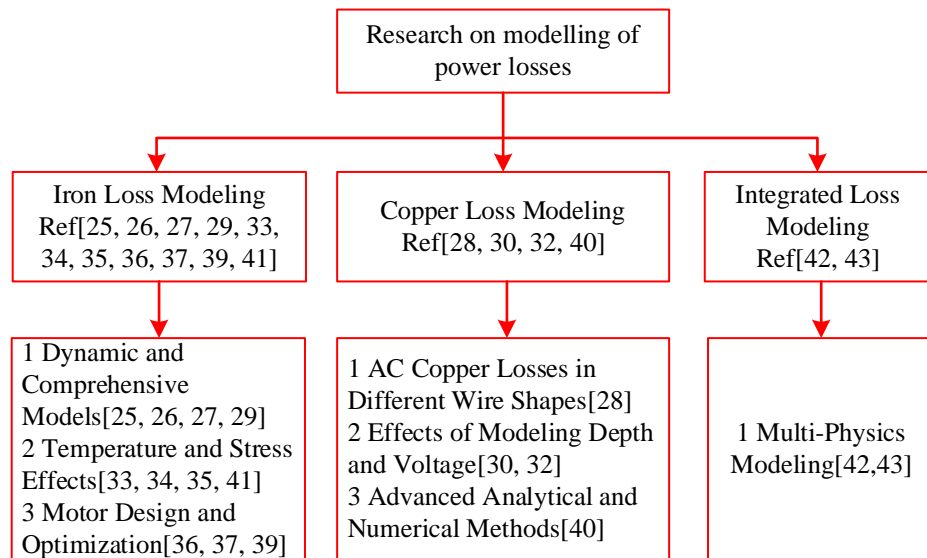


Fig. 2.1-2 Research summary on the modelling of power loss

The reviewed literature on machine loss modeling can be categorized into three primary research areas: iron loss modeling, copper loss modeling, and integrated loss modeling. Iron loss studies predominantly focus on developing dynamic, multi-dimensional models that consider various operational factors, such as magnetic field rotation, temperature, and high-frequency harmonics, leading to improved motor efficiency and performance. Copper loss research emphasizes optimizing motor design through accurate modeling of losses under different conditions, particularly in relation to wire shape and AC losses. Integrated loss modeling combines iron and copper loss considerations into comprehensive models, often utilizing advanced numerical methods, thereby enhancing the precision and efficiency of motor design processes. The summary

of the research could be summarized as Fig. 2.1-2.

Ref [25-43] researched the modelling and control of the iron loss and copper loss, which provides the theory basis of the control stage. Ref [25-27,29,31,33-39,41,42] focus on the iron loss modelling. Based on the vector playback model, [25] proposes a dynamic hysteresis model to consider the impact of rotating magnetic fields on iron loss estimation. This method predicts iron losses under complex magnetic field conditions more accurately and has practical application value in improving and optimizing motor efficiency. A general three-phase induction motor core loss model under an arbitrary reference frame was developed in the [26]. Ref [27] proposes a universal accurate iron loss calculation method considering harmonics based on the loss surface hysteresis model and the FEM. This method can accurately predict iron loss in complex electromagnetic environments containing high-frequency harmonics, providing theoretical support for efficient operation of motors. Ref [29] uses a dynamic finite element hysteresis model to calculate iron loss in PWM excitation under non-oriented grain iron sheets. This research considers the nonlinear properties of materials, improving the accuracy and reliability of the model in real industrial applications. Ref [33] evaluates iron losses in reactor cores with air gaps under high-frequency excitation through magnetic field analysis. This research provides an effective analytical tool for loss assessment of core materials in high-frequency power applications, helping to optimize the design of electromagnetic equipment. Ref [34,35] proposes an iron loss model for motors powered by low switching frequency inverters and DC bias density, considering temperature

effects. Ref [36] considers the iron loss model of induction motor considering the influence of rotating iron loss. This model provides a more comprehensive loss calculation by integrating rotating iron loss factors. Ref [37] proposes a motor Fe simulation iron loss model considering the secondary loop. This model can simulate secondary effects in motor operation, providing deeper understanding and data support for motor design and testing. Ref [39] describes a PMSM loss optimization method based on an accurate stator iron loss model. This method optimizes motor design and improves the overall performance and efficiency of the motor by accurately controlling and predicting iron losses. Ref [41] uses the Jiles-Atherton model to predict iron losses under frequency and compressive stress conditions. This study expands the application scope of the model, allowing it to make accurate predictions under different mechanical and electromagnetic stresses. Ref [42] uses an improved temperature-dependent iron loss model to perform thermal loss coupling analysis of the motor. This analysis method takes into account the dynamic changes of the effect of temperature on iron loss and provides important guidance for the design and operation of motors at high temperatures.

Ref [28,30,32,40,42] did the research on the copper loss modeling and minimum it uses the current control method. Specially, [28] conducts a comparative analysis of AC copper losses in high-speed stator PM flux switches using round copper wires and flat copper wires. This study compares the performance of two different shapes of copper wires under the same operating conditions through experiments and simulations, provides a scientific basis for

the selection of wire shapes in motor design, and can help engineers optimize the thermal efficiency and cost-effectiveness of the motor. Ref [30] discusses the effects of modeling depth and voltage level on AC losses in parallel conductors of PMSMs. The study provides in-depth understanding of efficient design and operating modes of motors through detailed simulation of loss differences under different modeling accuracy and voltage conditions, emphasizing the importance of accurate modeling in reducing unnecessary losses. Ref [32] uses the Bessel function to conduct analytical modeling of rotor eddy current losses in PM machine rotors with copper shielding. This research accurately describes the distribution and influence of eddy currents in copper shielding by applying mathematical methods, improves the accuracy of eddy current loss calculations, and is of great significance for improving the efficiency and reliability of motors. Ref [40] uses the perturbation finite element method to efficiently calculate the copper losses of switched reluctance machines. This method optimizes the calculation process by introducing perturbation technology, improves simulation speed and accuracy, and is particularly suitable for quickly evaluating the performance of different design solutions in complex motor designs. Ref [43] proposed kriging surrogate model design of ultra-high-speed surface-mounted PMSM considering stator iron loss and rotor eddy current loss. This design method uses advanced statistical models to optimize the motor design process, reduces the need for experiments and prototyping, and significantly improves design efficiency and motor performance. It especially shows its advantages when dealing with complex multi-physics problems. Table 2.1-1 shows the

comparative for different loss modeling method.

Table 2.1-1 Comparative for different loss modeling methods

Category	Subcategory	Benefits	Disadvantages	Comparison
Iron Loss Model	Dynamic and Comprehensive Models. [25, 26, 27, 29]	Predicts losses under complex conditions (magnetic fields, harmonics).	Some models lack robustness in nonlinear applications.	Ref [25] focuses on magnetic field rotation. Ref [27] integrates harmonics, while Ref [29] adds material nonlinearity, offering more specific applications.
	Temperature and Stress Effects [33, 34, 35, 41]	Considers the impact of operational conditions on losses (e.g., stress, temperature)	Computationally intensive for real-time operations.	Ref [33] analyzes high-frequency effects in air gaps; Ref [34] and [35] focus on switching frequency and DC bias effects; Ref [41] adds mechanical stress predictions.
	Motor Design and Optimization [36, 37, 39]	Optimizes motor performance by accurately predicting iron losses.	Limited applicability to varying motor designs without extensive parameter tuning.	Ref [36] and [37] focus on rotating iron losses and secondary loop effects, while Ref [39] is more specialized in PMSM optimization for performance improvements.
Copper Loss Model	AC Copper Losses in Different Wire Shapes [28]	Provides clear guidelines for wire shape selection to optimize performance.	Limited to specific wire configurations, less generalizable.	Comparative analysis between round and flat copper wires offers detailed insights into their performance under similar conditions, but results are wire shape specific.
	Effects of Modeling Depth and Voltage [30,32]	Helps optimize motor design by understanding depth and voltage impact on AC losses.	Requires fine-tuning of parameters, which may not be generalized easily.	Ref [30] focuses on the effects of modeling accuracy, while Ref [32] uses Bessel functions to model eddy currents, offering more advanced mathematical insight.

	Advanced Analytical and Numerical Methods [40]	Improves speed and accuracy of loss calculations through advanced methods.	Methodology may not extend well to other motor types.	Ref [40] introduces perturbation methods to streamline analysis, but is primarily focused on switched reluctance machines, limiting broader applicability.
Integrated Loss Modeling	Multi-Physics Modeling 42, 43	Provides a holistic view of iron and copper losses through advanced multi-physics methods.	Computational cost is high, and models can be complex to implement.	Ref [42] emphasizes thermal coupling in multi-physics models, while Ref. 43 integrates surrogate modeling for higher efficiency in high-speed applications.

To sum up, these references focus on iron loss and copper loss issues in motor design and propose a variety of innovative calculation models and analysis methods. The literature covers the establishment of dynamic models, loss optimization techniques, accuracy improvements in loss predictions, and models that consider multiple physical and operating conditions. These studies are of great significance for improving the energy efficiency of motors, reducing energy consumption, and optimizing the motor design process, and provide theoretical basis and guidance for the modeling and optimal control of PMA-SynRM.

2.1.3. Machine Parameter Identification Method

Ref [44-63] focus on the parameter identification to solve the problem of flux variation and to get a satisfactory control performance, in which it could be further divided into three categories: online parameter identification [44,45,48,50-52,54-58], off-line parameter identification [46,47,49,53,61], and

other method [60,62,63].

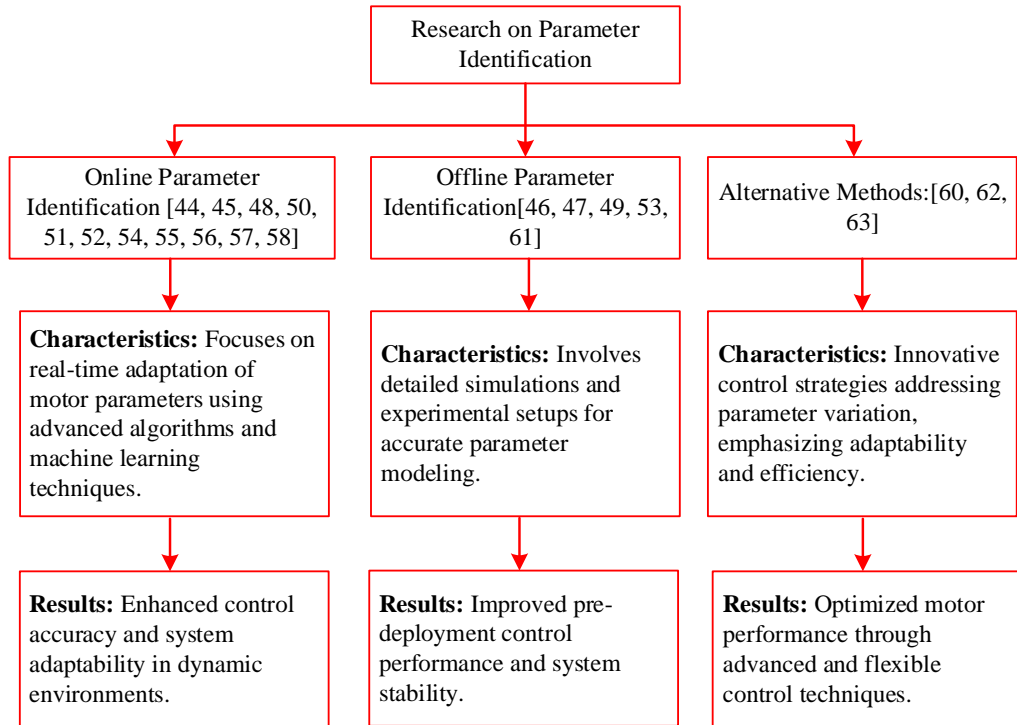


Fig. 2.1-3 Research summary on the parameter identification

For the online parameter identification, [44] proposed a parameter identification method based on current prediction error for PMSM with dead-band predictive current control. This approach optimizes the performance of the control system by improving parameter identification accuracy. Ref [45] studied a dynamic parameter identification method assisted by deep learning for a six-degree-of-freedom robot manipulator. This method uses deep learning algorithms to automatically learn and update the dynamic parameters of the robot, improving control accuracy and response speed. Ref [48] proposed a fast and comprehensive online parameter identification method for switched reluctance motors. This method updates motor parameters in real time to adapt to changing operating conditions and ensure control effects. Ref [50] explores the global identification of PMSM drive electrical and mechanical parameters based on the

dynamic self-learning PSO (particle swarm optimization) algorithm. Ref [51] proposed an improved online temperature prediction method based on global parameter identification for PMSMs. This method effectively predicts and controls motor temperature to prevent overheating through more accurate parameter identification. Ref [52] studied an improved online multi-parameter identification method based on small signal injection, considering the influence of cross-coupling magnetic saturation. This method improves control accuracy and stability in complex working environments. Ref [54] analyzes the problem of online identification of PMSM parameters and compares the performance of different estimators. Ref [55] proposed a parameter estimation method for poly-phase motors, which is suitable for variable phase pole motors. Ref [56] reviews the technical status of parameter identification and self-tuning technology in AC motor drives. The article summarizes the advantages and disadvantages of existing technologies and points out the direction of future research. Ref [57] studied the performance of the RLS (recursive least squares) algorithm configuration for online identification of induction motor parameters in an automotive environment. This approach is suitable for dynamic and rapidly changing application scenarios. Ref [58] proposed an improved dead zone predictive thrust control method for linear induction motors, combined with online parameter identification. This method improves the operating efficiency and accuracy of the motor by precisely controlling thrust.

For the off-line parameter identification, [46] discusses the discrete-time parameter identification of PMSMs. The article improves the effect of the control

algorithm and the operating efficiency of the motor by accurately simulating the dynamic behavior of the motor. Ref [47] evaluates a PMSM parameter identification method and verifies it through parameter sensitivity analysis. This method helps to accurately predict the impact of motor parameter changes on the control system and enhances the stability and reliability of the system. Ref [49] studies the full parameter identification of SynRM based on field and armature current short circuits. Ref [53] explores a method for offline identification of induction motor parameters, including core loss estimation, using stator current traces. This approach helps to evaluate motor performance and losses more accurately. Ref [61] compares two test methods to measure the d -axis and q -axis inductance of a built-in PMSM. This comparison allows the selection of a measurement technology that is better suited to the needs of a specific application.

As for other methods to solve the parameter variation problem in the control system. Ref [60] reviews the offline synchronous inductance measurement method of PMSM. This approach provides fundamental data for motor design and control, supporting more efficient motor applications. Ref [62] proposes an adaptive MTPA control method using a radial basis function network for SynRM. This method automatically adjusts control parameters to adapt to different operating conditions, improving motor performance. Ref [63] studies an online MTPA control method for SynRM driving, based on an emotion controller. This novel control strategy optimizes motor control by simulating human emotional responses, improving control flexibility and efficiency. Table 2.1-2 shows the

comparison of different methods for machine parameter identification.

Table 2.1-2 Comparison of Parameter Identification Methods for Motor Control

Category	Subcategory	Benefits	Disadvantages	Comparison
Online Parameter Identification	Online Parameter Identification [44, 45, 48, 50, 51, 52, 54, 55, 56, 57, 58]	Provides real-time adaptation for varying conditions, improving control accuracy and response speed.	Higher computational demands, may not be suitable for every motor type in fast-changing environments.	Ref [44] uses current prediction, Ref [50] applies PSO for parameter updates, while Ref [45] integrates deep learning.
Offline Parameter Identification	Pre-deployment modeling [46, 47, 49, 53, 61]	Ensures accurate parameter determination before deployment, leading to more stable systems during operation.	Lacks adaptability during real-time operations, results may become outdated quickly in dynamic environments.	Ref. 47 focuses on sensitivity analysis, while Ref. 61 emphasizes inductance measurements, providing diverse approaches.
Other Methods		Innovative strategies improve motor performance by adjusting parameters dynamically under varying conditions.	Can be complex to implement and may require specialized hardware or software.	Ref [62] proposes an adaptive MTPA control method, while Ref [63] utilizes an emotion-based controller for flexibility.

2.1.4. Combination of Machine Modelling and Parameter Identification

Ref [64-71,13] build the model to describe the variation of the flux, cross-saturation phenomenon, and then the control performance was improved by using the proposed model. Ref [64] proposes a predictive torque control method for SynRM considering magnetic cross saturation. This method improves the accuracy and efficiency of motor control by accurately simulating magnetic saturation. Ref [63] conducts an experimental identification of the magnetic model of a SynRM, which helps to understand the magnetic characteristics of

the motor more accurately under different working conditions. Ref [64] developed an adaptive magnetic flux observer for online inductive reactance estimation, considering the influence of magnetic saturation to improve the control performance of the built-in PMSM. Ref [67] improves the method of considering magnetic saturation in the SynRM. This method provides a more accurate prediction of the dynamic performance of the motor. Ref [68] fits the magnetic saturation and hysteresis curves through arctangent functions, which is an improvement on the traditional magnetic material modeling method. Ref [69] uses a genetic algorithm to identify the saturation model of a SynRM. This method applies modern optimization algorithms in parameter optimization to improve the accuracy of the model. Ref [70] considers the magnetic saturation effect in the dynamic model of the SynRM, which enhances the practicability and accuracy of the model. Ref [71] uses a nonlinear mathematical model to provide a drive system for a PMSM. This model can better handle the nonlinear behavior of the motor.

In summary, significant research efforts have been dedicated to modeling flux characteristics, magnetic saturation, and cross-saturation in synchronous reluctance machines (SynRMs) and permanent magnet-assisted synchronous reluctance machines (PMA-SynRMs). Various approaches have been employed, including predictive torque control [64], adaptive magnetic flux observers [64], experimental identification [63], and optimization-based parameter identification using genetic algorithms [69]. Advanced modeling techniques, such as nonlinear mathematical models [71] and arctangent function fitting [68],

have been applied to improve the accuracy of magnetic saturation representation. While substantial progress has been made in capturing magnetic saturation effects, the modeling of cross-saturation remains challenging due to its complex nonlinear behavior, and only a limited number of studies address this issue effectively. For PMA-SynRMs, an accurate representation of magnetic saturation, cross-saturation, and magnet flux saturation is crucial for enhancing control precision and achieving optimal performance. Thus, further improvements in modeling methods are required to bridge the gap in cross-saturation analysis and enhance machine parameter identification for high-performance control strategies.

2.2 MTPA Control for Steady State Improvements

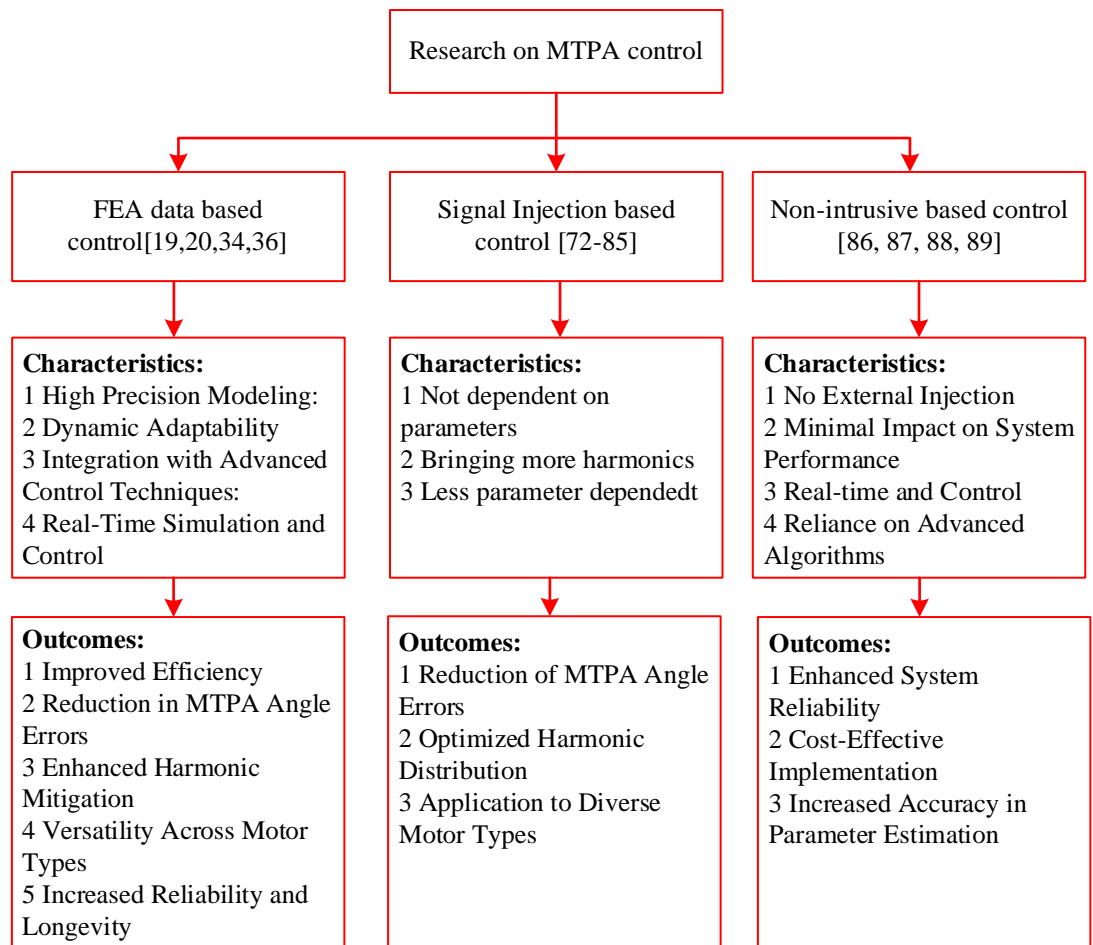


Fig. 2.2-1 Research summary on the MTPA control

The discussion on MTPA control methods for IPMSMSM and SynRM highlights the advancements in both signal injection and online detection techniques. Signal injection methods, including CFSI and PRFSI, have been extensively explored to achieve precise MTPA angle tracking and error compensation, though harmonic distortion might be introduced. On the other hand, online detection techniques provide a non-invasive alternative, focusing on real-time monitoring and control of motor parameters such as flux linkage and inductance without additional signal injection, thereby avoiding extra harmonic distortions. These developments are crucial for enhancing the reliability, efficiency, and accuracy of motor control systems in various applications. The overall classification and the outcomes could be described as Fig. 2.2-1.

2.2.1. MTPA Control Based on Signal Injection Method

Ref [72] introduced a novel MTPA tracking method for IPMSMs, utilizing a CFSI technique. This approach allowed the determination of the MTPA control angle independent of flux variations and flux saturation. The validity of this method was demonstrated in an 11-kW machine, where the current magnitude showed a tracking MTPA angle error of less than 0.5%. Subsequently, several other studies on MTPA control based on signal injection emerged, as discussed in [73-78].

In [73], a control method was presented that only required the measurement of the DC bus current, suggesting potential applications for cost-sensitive scenarios through a single resistor sampling method. Ref [74] proposed a flux-

weakening control strategy that integrates signal injection methods, effectively combining the constant torque region with the flux-weakening region, thus enabling a smooth transition even in deep flux-weakening conditions. Additionally, references [75], [76], [77], and [78] focus on error analysis and strategies to reduce MTPA angle errors. For instance, Ref [74] introduced a novel vector space signal method, which eliminates the necessity for specific bandwidths in both the speed and current loops. This literature demonstrates that MTPA angle error can be analyzed and compensated for in various ways, making it feasible for most control applications. However, MTPA control error can be exacerbated by harmonics from the injected current, indicating the need for further research to enhance harmonic distribution and mitigate harmonic amplitude.

Ref [78] presented an extended signal injection control that incorporates the derivative term of the flux. This method allows for the estimation and compensation of the derivative part, thereby reducing the MTPA angle error. Meanwhile, Ref [76] introduced an error compensation loop control that requires no additional information, and Ref [77] proposed an error compensation strategy that only necessitates the q -axis flux linkage. Despite this, the constancy of the magnet flux remains a challenge, as it can vary with different materials and working conditions in PMA-SynRM.

The signal injection techniques can be categorized into CFSI and PRFSI. Ref [79] provided the theoretical basis for PRFSI, showing that it translates the current harmonics into a continuous frequency distribution, thereby altering the

harmonic distribution. However, this study did not theoretically analyze the selection of the injected frequency or the feasibility of the signal. Furthermore, the study did not discuss the selection of current sampling frequency or switching frequency. Although PRFSI is not widely used in MTPA detection control, it has been successfully applied in sensor-less control applications. For example, Ref [80] proposed a sensor-less control strategy employing PRFSI to reduce position observation errors. Ref [81] advanced a sensor-less control strategy with PRFSI that accounts for system delay, thereby improving reliability. Additionally, Finally, [82-85] proposed improvements to the CFSI method aimed at modifying the harmonic distribution to decrease harmonic content.

2.2.2. MTPA Control Based on Non-invasive Online Detection

Refer [86-89] focus on the MTPA angle detection without injecting any signals, which no extra harmonic distortion is brought. Ref [86] proposes a new scheme to identify the entire flux linkage diagram of a PMSM, by which the diagram of the d -axis and q -axis flux linkage can be identified under different load or saturation conditions. The conventional three-phase inverter basic vector control system is employed, and immune cloning is utilized to perform a global search for the minimum point using a quantum genetic algorithm. This approach overcomes the challenges posed by flux linkage under conditions of uncertain circuit resistance and inverter nonlinearity. Ref [87] proposes a method for online measurement of stator inductance of PMSMs using PWM excitation relationships. Accurate knowledge of motor parameters, such as inductance, is crucial for efficient and optimal control of motors. The innovation of this study

is to propose an online measurement technology that can update inductance parameters in real time to cope with dynamic changes without interrupting motor operation. Ref [88] proposes a novel particle filter-based flux linkage estimation method that exploits harmonics of the machine speed. In the proposed method, a particle filter is applied to estimate the flux linkage from the velocity harmonics. It provides a high-precision magnetic linkage monitoring method for PMSM, which is especially suitable for complex operating environments. Ref [89] proposes a magnetic linkage estimation method based on particle filters. This method utilizes the harmonics of the machine speed. Table 2.2.1 shows the comparison of different MTPA control methods.

The literature presents a comprehensive study of MTPA control methods, primarily classified into two major categories: Signal Injection Methods and Non-invasive Online Detection Techniques. Signal injection methods, including Constant Frequency Signal Injection (CFSI) and Pseudorandom Frequency Signal Injection (PRFSI), are widely employed to enhance MTPA tracking accuracy by introducing controlled disturbances into the motor drive. These methods, as demonstrated in [72-85], allow for precise estimation of the MTPA angle, even under magnetic saturation and cross-saturation conditions. However, the injected signals may introduce additional harmonic distortion, which necessitates compensation techniques to maintain optimal control performance. PRFSI, as discussed in [79], further extends this approach by continuously distributing harmonic frequencies, improving detection accuracy for sensor-less control. Despite these advancements, the dependency on signal injection can

complicate the control design and increase the need for harmonic mitigation.

In contrast, Non-invasive Online Detection Techniques eliminate the need for injected signals, thereby avoiding the issue of harmonic distortion. Studies such as [86-89] focus on real-time parameter estimation of flux linkage and inductance using advanced algorithms like quantum genetic algorithms, PWM excitation analysis, and particle filter-based estimation. These methods demonstrate the capability to track MTPA paths accurately without interrupting motor operation, offering a more seamless control experience. However, certain methods may experience limitations in precision under highly dynamic conditions compared to signal injection-based approaches.

In summary, signal injection methods prioritize high tracking accuracy at the expense of potential harmonics, while non-invasive online detection focuses on real-time estimation without disturbing the system, albeit with some trade-offs in dynamic precision. Both strategies provide valuable contributions to the enhancement of MTPA control, depending on the application requirements and system constraints.

Table 2.2-1 Comparison of different MTPA Control Methods

Category	Benefits	Disadvantages	Comparison
FEA Data-Based Control [19 20 34 36]	Uses FEA data to achieve high precision in MTPA control and optimization.	Dependent on detailed motor model data, may be computationally expensive for real-time applications.	Ref [19,20] focus on a LUT based method and [34 36] try to simplify the data using fitted method
Offline Parameter Identification [72-85]	Signal injection allows error compensation and control angle tracking under dynamic conditions.	May introduce harmonic distortions that need mitigation, higher complexity in implementation.	Ref [72] focuses on tracking errors, while Ref [74] integrates flux-weakening control for high flexibility. Ref [79] emphasizes frequency selection, while Ref. 81 focuses on reducing

			sensor-less control system delays.
Other Methods [86-89]	Non-invasive methods avoid harmonic distortions and work in real-time without interrupting operation.	Some methods may not achieve the same level of precision in dynamic environments as signal injection.	Ref [86] introduces a flux linkage diagram method, while Ref [88] focuses on high-precision magnetic linkage estimation.

2.3 Dynamic Response Improvements Control

2.3.1. High-Performance Control

FEA is essential for deriving motor parameters during design. Ref [90] presents a current angle-based ABS (adaptive backstepping) speed control system to address unmodeled dynamics and magnetic saturation in SynRM. An intelligent speed transient control system with a recurrent Hermite fuzzy neural network improves SynRM's transient response under MTPA conditions by generating compensated current angle commands. Ref [91] offers an alternative control strategy without the FEA-based LUT, focusing on online training parameter identification but with similar drawbacks. This study introduces the RFSFNN (recurrent feature selection fuzzy neural network) to approximate an ideal ABS control, along with an improved adaptive compensator, increasing algorithm complexity.

Ref [92] introduces neural network-based algorithms for modeling synchronous motors, including saturation and cross-coupling effects. Compared to [90] and [91], this strategy directly models the SynRM rather than compensating for the control system, with a simplified neural network to meet controller demands. This approach suits precise flux linkage estimation and

online tracking from motor current and voltage measurements. However, it requires current and voltage signals, which might not be available in low-cost situations, and its calculation time can cause delays in real-time control systems.

Ref [93] proposes a control strategy to identify the MTPA working point, enhancing control performance, and reducing copper loss using an emotional controller with an online flux searching observer. This method, specific to SynRM, saves calculation time but involves complex adaptive laws that need further stability verification under load fluctuations. High computational demands contradict the design's efficiency goal, requiring powerful controllers, thus increasing power consumption.

Ref [94] discusses MPC (Model Predictive Control) for SynRM, showing good performance in simulations. However, MPC needs simplification for real-time use, and further experiments are necessary. Ref [95] presents an enhanced MPC strategy that reduces THD (Total Harmonic Distortion) and ripple by employing multiple cost functions to select optimal vectors. However, its high computational complexity poses challenges for practical implementation.

Ref [96] introduces a finite-state Direct Predictive Control for SynRM, which is less computationally demanding than conventional MPC and suitable for real-time control. However, it requires an additional comparator for selecting the switching status, increasing costs. A backstepping decoupling control strategy, also presented in [96], simplifies the design and reduces coupling effects with minimal system resources, making it appropriate for industrial and low-cost applications, though further experimentation is required for validation.

Ref [97] utilizes a neural network inverse system method to decouple the bearing-less SynRM, achieving improved control performance, but the high computational demands limit its industrial feasibility. In contrast, Ref [98] proposes a deviation-based torque control for SynRM, which operates independently of motor parameters, simplifying the control system but restricting its applicability to SynRM systems.

Ref [99] compares various SynRM control strategies including MTPA and MPC, in which merits and demerits for different control strategies were compared. Ref [100] introduces a fuzzy inference system for automatic PI parameter adjustment to enhance control performance despite inductance changes and torque fluctuations, showing good simulation results but lacking experimental validation.

2.3.2. Extended State Observer-Based Control

According to the improved structure of the ESO (Extended State Observer), it could be divided into mixed and enhanced ESO, sliding mode control based ESO, nonlinear control, adaptive ESO, and others.

For the mix and enhance ESO, A hybrid ESO control technology is proposed in [101], especially for integral chain structure systems with both matching and mismatching disturbances. The innovation of this research lies in the integration of different disturbance processing technologies [101]. Ref [102] focuses on an enhanced ESO strategy for non-integral chain systems with mismatch uncertainties, which improves the disturbance attenuation capability. Its innovation lies in the introduction of an improved observer design to better

manage uncertainty.

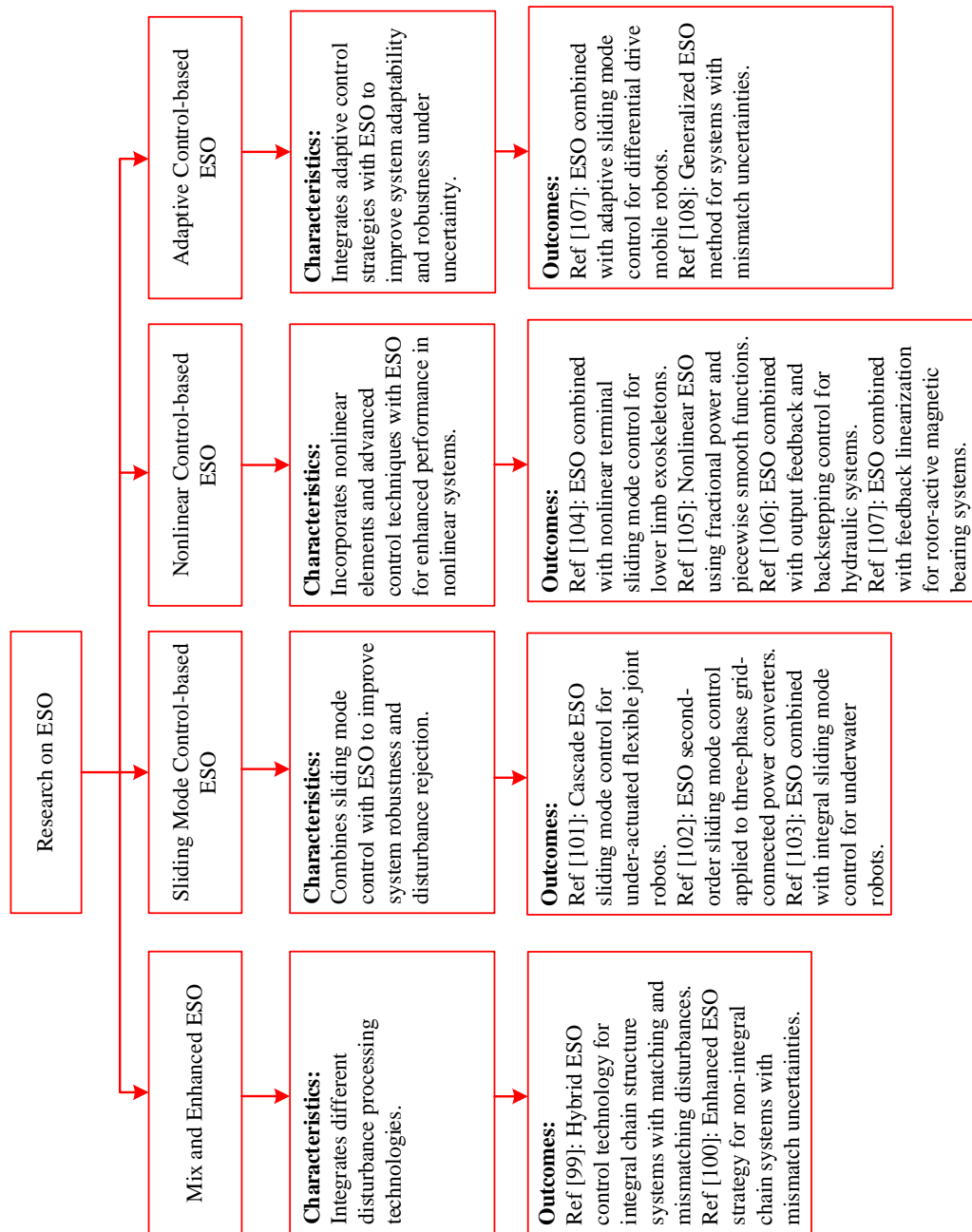


Fig. 2.3-1 Research comparison summary on ESO

For the sliding mode control based ESO, A cascade ESO sliding mode control for under-actuated flexible joint robots is developed to solve the control problem of flexible joints. The cascade observer design improves the accuracy and robustness of the under-actuated system in [103]. Ref [104] applies ESO second order sliding mode control to three-phase grid-connected power

converter. Ref [105] combines ESO with integral sliding mode control, applied to underwater robots with unknown disturbances and uncertain nonlinearities.

For the nonlinear control, Ref [106] introduces a control strategy that combines ESO with nonlinear terminal sliding mode control and is applied to lower limb exoskeletons. The integration of advanced control technologies contributes to the enhancement of robotic performance. Ref [107] proposes a nonlinear ESO based on fractional power functions is studied, and nonlinear ESO constructed by piecewise smooth functions is introduced.

Ref [108] combines ESO with output feedback and backstepping control for robust control of hydraulic systems. To further improve the structure, [109] combines feedback linearization with ESO for controlling rotor-active magnetic bearing systems under uncertainty conditions, which improves the effectiveness of ESO in complex electromechanical systems.

For the adaptive Control based ESO. Ref [109] combines ESO with adaptive sliding mode control for differential drive mobile robots under uncertainty conditions. Its innovation lies in the adaptive control method, which enhances the robustness and performance of mobile robots in uncertain environments. Ref [110] proposed a generalized ESO method is proposed to deal with systems with mismatch uncertainties, which enhances robustness and adaptability. Fig. 2.3-1 shows the comparison summary of the ESO

2.3.3. Dynamic Response Improvements for High-Speed Sensor-less Control

For the high speed sensor-less control, it could be divided into three

categories: EMF based model, Flux observer based model and other observers.

For the EMF model, [111] compares MRAS (Model Reference Adaptive System), EEMF(Extended Electromotive Force), and Flux-based sensor-less control methods for SynRM, finding MRAS suitable for low speeds due to its use of current error to design adaptive laws, while EEMF is recommended for medium and high speeds.

Ref [112] improves control strategy using an EMF (Electromotive Force) and EKF (Extended Kalman Filter) to reduce observation noise. The reduced-order EKF, based on an inverse electrical model of the motor, shows better performance in experiments, but motor characteristics and changing inductance parameters are not fully considered. Ref [113] enhances Ref [112] by integrating a neural magnetic model with EEMF and EKF, improving accuracy despite increased computational burden. Ref [114] proposes a speed-adaptive full-order observer with parameter adaptation laws for SynRM drives. It adapts inductances using a back-EMF method, with the d -axis inductance adaptation enabled only at medium and high speeds.

For the Flux Observer Model based model, the rotor position can be computed by the inverse tangent of the flux linkage in the stationary reference frame. The accuracy of the DFO (Direct Flux Observer) method is less precise than EEMF, but the PLL (Phase-locked Loop) offers high precision, reliability, and low computational burden. Ref [115] introduces a novel flux observer with a fictitious flux variable, achieving global stability and stable estimation under various conditions through simulation, though not yet experimentally verified.

Ref [116] proposes a hybrid observer considering magnetic nonlinearity. It identifies regions of instability for various schemes and suggests six improved flux observers.

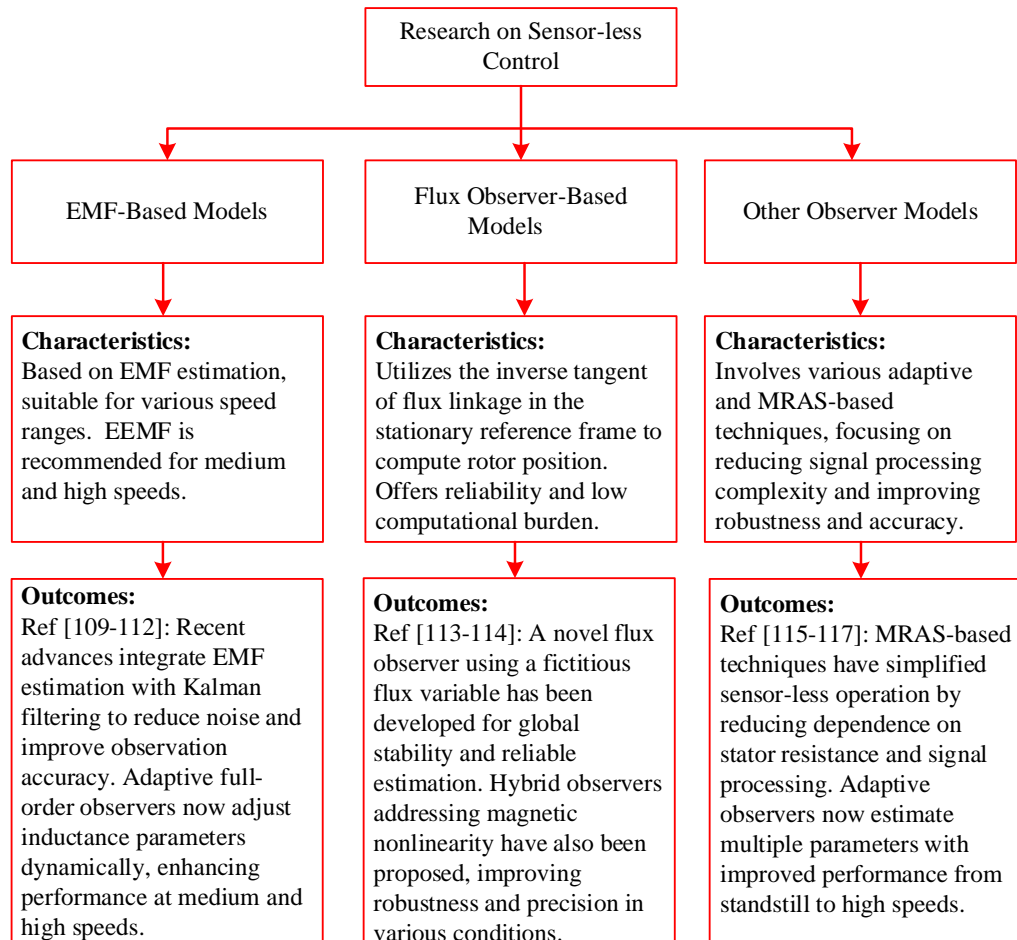


Fig. 2.3-2 Research summary on sensor-less control

For other observer models, [117] presents a MRAS-based speed estimation technique for vector-controlled SynRM, demonstrating successful sensor-less operation independent of stator resistance with less signal processing and hardware intensity compared to EEMF and flux observer models. Ref [118] details an adaptive observer designed to estimate rotor position, speed, core loss, and inductance parameters. This observer integrates a modified PWM switching scheme, current derivative measurement, and EKF design. This approach, specifically tailored for SynRM, demonstrates robust performance from

standstill to high speeds; however, additional reliability validation is required. Ref [119] proposes an adaptive sensor-less position control system for SynRM using a dual current slope estimating technique. The method is suitable for low-cost situations and improves transient response and load disturbance rejection. However, the differential links used to calculate the current slope introduce noise, potentially causing system instability and torque ripples. Fig. 2.3-2 shows the Research summary on sensor-less control.

The literature on dynamic response improvement for SynRM and PMSynRM includes high-performance control techniques such as ABS, MPC, and RFSFNN, which enhance transient response and reduce magnetic saturation effects. While these methods improve control precision, they often introduce complexity and computational challenges. In parallel, Extended State Observer (ESO)-based strategies are explored for disturbance rejection, categorized into mixed ESO, sliding mode ESO, and nonlinear ESO, effectively enhancing robustness and system stability. Together, these approaches contribute to improved dynamic response and reliable control in varying load conditions.

Chapter 3 An Improved PMA-SynRM Modelling Method

To achieve high-performance control for Permanent Magnet assisted Synchronous Reluctance Machines (PMA-SynRM), it is crucial to develop an accurate and robust model that captures the machine's complex flux characteristics, including inductance variation, magnetic saturation, and cross-saturation. This chapter presents the modeling approach for PMA-SynRM, focusing on establishing a comprehensive mathematical representation that reflects these flux behaviors under varying operating conditions. Furthermore, a novel control strategy based on Maximum Torque per Ampere (MTPA) optimization is proposed to enhance steady-state efficiency and torque output. The modeling framework and control strategy presented in this chapter serve as the foundation for achieving precise current regulation and improved anti-disturbance capability in PMA-SynRM applications.

3.1 Flux Modelling Considering Inductance Variation and Saturation

The modelling of the SynRM could be obtained as Eq.n 3.1-1 and Eq.n 3.1-2 [120].

$$\psi_d(i_d, i_q) = A_d \tan^{-1}(B_d i_d) + C_d i_d + \frac{D_{dq} i_d}{i_d^2 + K_d} \ln \left(1 + \frac{i_q^2}{K_q} \right) \quad \text{Eq.n 3.1-1}$$

$$\psi_q(i_d, i_q) = A_q \tan^{-1}(B_q i_q) + C_q i_q + \frac{D_{dq} i_q}{i_q^2 + K_q} \ln \left(1 + \frac{i_d^2}{K_d} \right) \quad \text{Eq.n 3.1-2}$$

where K_d and K_q are positive coefficients and D_{dq} is negative. K_d and K_q represent the cross saturation according to the d - and q -axis current magnitudes, and D_{dq} represents the cross-saturation. It is possible to calculate the dynamic inductance corresponding to the current operating point using the proposed flux saturation model. The dynamic inductance matrix is expressed as Eq.n 3.1-3.

$$\begin{aligned}
L_{\text{dyn}}(i_d, i_q) &= \begin{bmatrix} L_{d, \text{dyn}}(i_d, i_q) & L_{dq, \text{dyn}}(i_d, i_q) \\ L_{dq, \text{dyn}}(i_d, i_q) & L_{q, \text{dyn}}(i_d, i_q) \end{bmatrix} \\
&= \begin{bmatrix} \partial\psi_d(i_d, i_q)/\partial i_d & \partial\psi_d(i_d, i_q)/\partial i_q \\ \partial\psi_q(i_d, i_q)/\partial i_d & \partial\psi_q(i_d, i_q)/\partial i_q \end{bmatrix}
\end{aligned} \tag{Eq.n 3.1-3}$$

For Eq.n 3.1-2, the elements of Eq.n 3.1-3 are expressed as Eq.n 3.1-4 and

Eq.n 3.1-5:

$$\begin{aligned}
&\frac{\partial\psi_d(i_d, i_q)}{\partial i_d} \\
&= \frac{A_d B_d}{1 + (B_d i_d)^2} + C_d - D_{dq} \frac{i_d^2 - K_d}{(i_q^2 + K_d)^2} \ln \left(1 + \frac{i_q^2}{K_q} \right)
\end{aligned} \tag{Eq.n 3.1-4}$$

$$\begin{aligned}
&\frac{\partial\psi_q(i_d, i_q)}{\partial i_q} \\
&= \frac{A_q B_q}{1 + (B_q i_q)^2} + C_q - D_{dq} \frac{i_q^2 - K_q}{(i_d^2 + K_d)^2} \ln \left(1 + \frac{i_d^2}{K_d} \right)
\end{aligned} \tag{Eq.n 3.1-5}$$

According to Eq.n 3.1-4 and Eq.n 3.1-5, Eq.n 3.1-6 could be obtained.

$$\frac{\partial\psi_d(i_d, i_q)}{\partial i_q} = \frac{\partial\psi_q(i_d, i_q)}{\partial i_d} = 2D_{dq} \frac{i_d}{i_d^2 + K_d} \frac{i_q}{i_q^2 + K_q} \tag{Eq.n 3.1-6}$$

Equation 3.1-6 demonstrates that Equation 3.1-1 and Equation 3.1-2 satisfy the reciprocity condition, resulting in Equation 3.1-3 being a symmetric matrix.

Therefore, the model proposed in Equation 3.1-1 and Equation 3.1-2 is adopted.

According to the proposed modelling method, the FEA data are shown in Fig. 1.3-3. In model Eq.n 3.1-1 to Eq.n 3.1-6, the permanent magnet part is not considered. To solve the problem, a supplementary model for permanent considering the cross inductance are designed as follows.

Three sets of 31×31 flux linkage data are obtained from the FEA software as Fig. 1.3-3(c). To solve the mentioned problem, the permanent magnet flux needs to be further learned and modelled.

As shown in Fig. 1.3-3(c), the permanent magnet flux will be influenced by

the d -axis current because of the cross saturation. Meanwhile, the q -axis current has little influence on the magnet flux. So, the magnet flux linkage could be fitted as a polynomial and the accuracy will be more accurate with the increasing of the order. However, the calculation will be more complicated. The Taylor series expansion is often used to approximate smooth, continuous functions. To balance the calculation time and accuracy, the magnet flux could be expressed as Eq.n 3.1-7.

$$\hat{\psi}_{pm} = p_0 + p_1 i_d + p_2 i_d^2 + p_3 i_d^3 + p_4 i_d^4 \quad \text{Eq.n 3.1-7}$$

where, $\hat{\psi}_{pm}$ is the estimated permanent magnet flux, $p_0, p_1, p_2, p_3,$ and p_4 are the polynomial coefficients.

3.2 Flux Data Observation Considering Self and Cross Saturation Through Online Identification

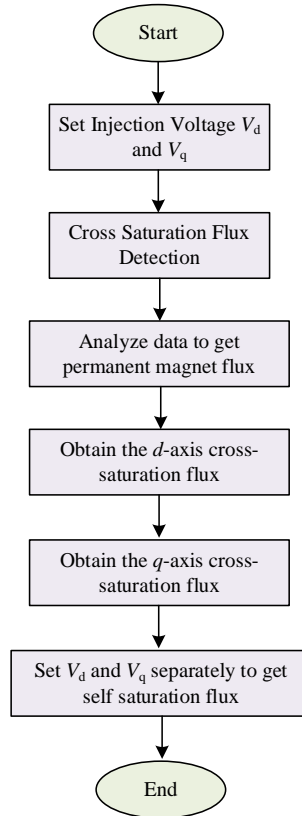


Fig. 3.2-1 Flux estimation diagram

This part aims to provide a method to estimate the flux data in different conditions to further estimate the parameters of the model, in which the magnetic saturation flux and cross saturation flux could be obtained. Then diagram of the estimated method is shown in Fig. 3.2-1.

3.2.1. Identification for Magnetic Saturation Flux

In real applications, 31×31 flux linkage data is not always acceptable. To address this issue, an online flux linkage estimation method is proposed to get the permanent magnet flux linkage.

The hysteresis voltage injection technique is used to estimate parameters at standstill. The hysteresis voltage injection method determines the voltage reference according to the current to pulsate the current within the set current range. The current and flux obtained during the hysteresis voltage injection process are used to estimate the parameters of the proposed magnetic saturation model. Voltage is injected considering the voltage drop of the stator resistance.

Therefore, the voltage reference is expressed as Eq.n 3.1-8:

$$u_{\text{ref}}(k) = \begin{cases} u_{\text{inj}} + R_s i(k) & \text{if } i(k) < -I_{\text{max}} \\ -u_{\text{inj}} + R_s i(k) & \text{if } i(k) > I_{\text{max}} \\ u_{\text{ref}}(k-1) & \text{otherwise} \end{cases} \quad \text{Eq.n 3.1-8}$$

where u_{inj} is the magnitude of the voltage that creates the stator flux, I_{max} is the current limit, and k is the discrete-time index.

Table 3.2-1 Working Condition for estimation

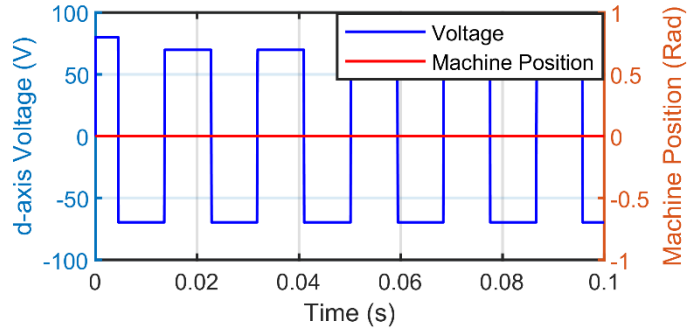
Parameter	Value (Unit)
Injected Voltage	30-150 V
Maximum Current	10 A

The d - and q - axis fluxes are calculated as Eq.n 3.1-9 if the rotor is stationary:

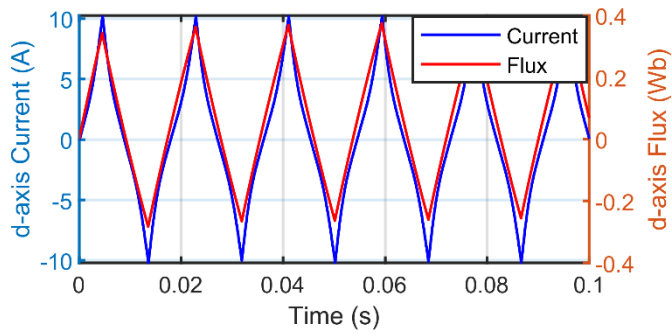
$$\psi_d = \int (u_{d, \text{ref}} - R_s i_d) dt$$

$$\psi_q = \int (u_{q, \text{ref}} - R_s i_q) dt$$
Eq.n 3.1-9

Fig. 3.2-2 shows the self-commissioning identification process for the d -axis flux and Fig. 3.2-3 for the q -axis flux.

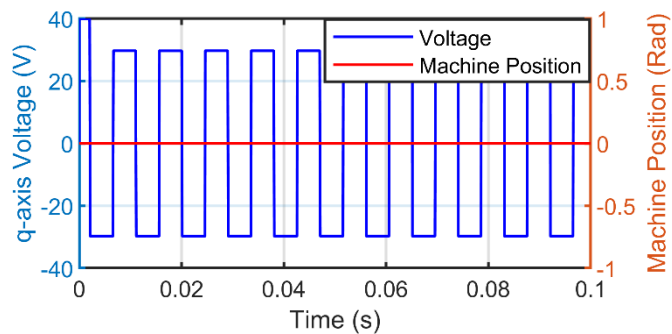


(a)

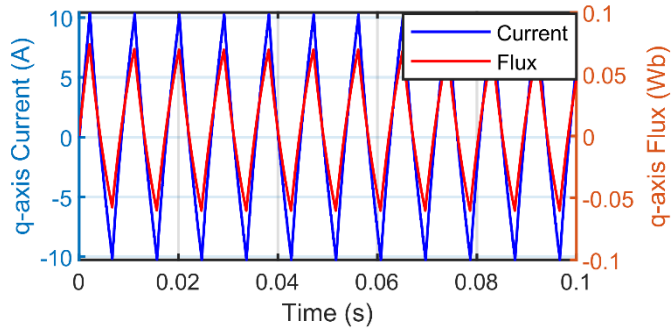


(b)

Fig. 3.2-2 Magnetic saturation model identification for d -axis flux; (a) volage reference and machine position; (b) current and calculated flux.



(a)

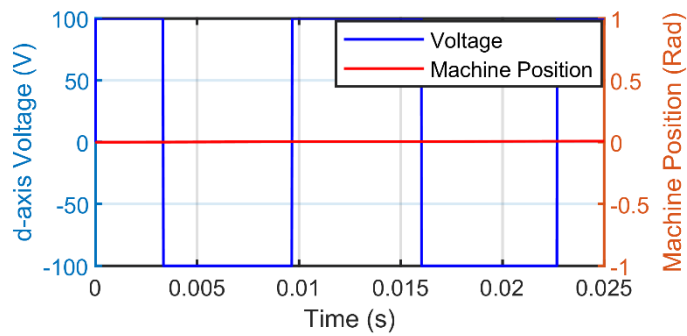


(b)

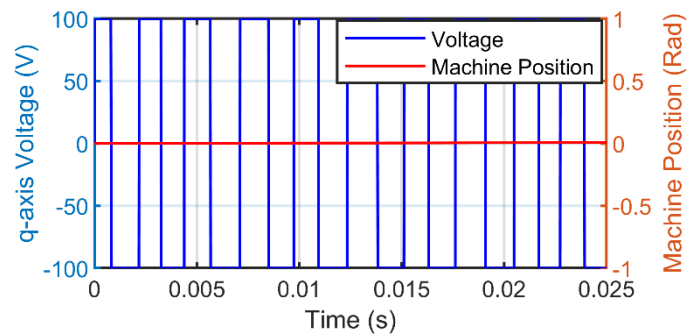
Fig. 3.2-3 Magnetic saturation model identification for q -axis flux; (a) voltage reference and machine position; (b) current and calculated flux.

3.2.2 Identification for Cross-Saturation Flux

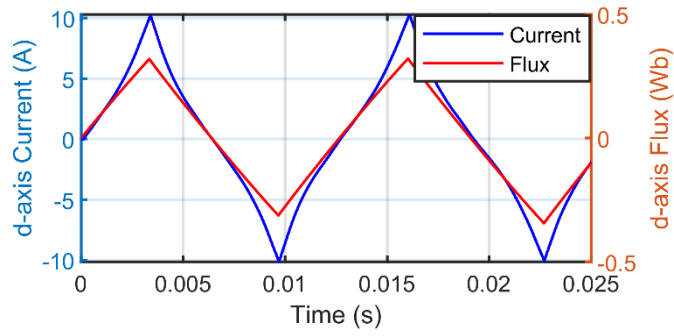
In this stage, the parameters for magnetic saturation and cross-saturation are estimated to ensure that the flux exhibits a linear increase or decrease. The sampled currents and calculated flux are used to estimate the parameters of the proposed saturation model.



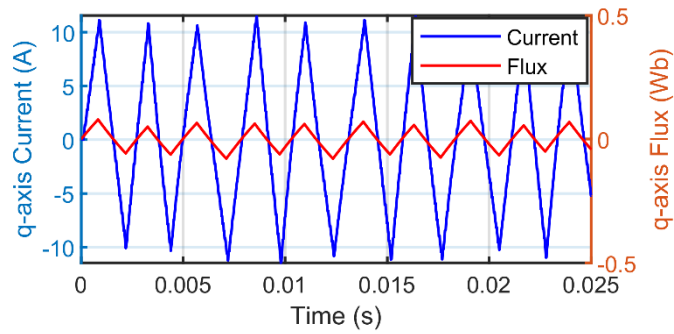
(a)



(b)



(c)



(d)

Fig. 3.2-4 Cross-saturation model identification for d - and q -axis flux; (a) Machine position and d -axis voltage reference; (b) Machine position and q -axis voltage reference; (c) d -axis current and flux; (d) q -axis current and flux.

The estimated cross-saturation model includes the flux resulting from the cross-saturation phenomenon, which is influenced by the d - and q -axis inductance, as well as the permanent magnet flux in the q -axis caused by the d -axis current.

To begin, the q -axis current was set to zero, and the q -axis flux was estimated to determine the permanent magnet flux.

Subsequently, both the d - and q -axis currents were applied simultaneously to estimate the cross-saturation model.

The d -axis and q -axis voltage should be selected carefully to mitigate rotor movements. The magnitude of the injection voltage is limited by the DC-link voltage as Eq.n 3.1-10:

$$\left(u_{d,\text{inj}} + R_s I_{d\text{max@cross}}\right)^2 + \left(u_{q,\text{inj}} + R_s I_{q\text{max@cross}}\right)^2 < \frac{V_{\text{dc}}^2}{3} \quad \text{Eq.n 3.1-10}$$

where V_{dc} is the DC-link voltage. $I_{d\text{max@cross}}$, and $I_{q\text{max@cross}}$, are the d - and q -axis current limits of the identification process for cross saturation.

Fig. 3.2-4 shows the cross-saturation model identification for d - and q -axis flux, in which the d - and q -axis voltage are injected simultaneously.

3.3 Model Parameters Identification

3.3.1. Permanent Magnet Model Parameter

From Chapter 1.4.2, the permanent flux is a fixed value when cross saturation is not considered.

From the magnetic saturation model, the permanent magnet flux could be obtained when the q -axis current is set to 0. However, the cross-saturation flux needs to be further analyzed to obtain the permanent magnet flux model considering cross saturation.

The data could be obtained when q -axis current is set to 0 in different d -axis current. According to the detected data from the method in Chapter 3.2.2, a complete magnet flux data could be obtained. Then, the LSM (Least Squares Method) was used to determine the parameters of the permanent magnet flux model [120].

3.3.2. Magnetic saturation Model Parameter

As discussed in Chapter 3.1, the LSM cannot be used to determine the parameters of the flux saturation model because it contains non-linear functions. So, the model needs to be transformed to a linear one first.

Multiplying both sides of Eq.n 3.1-1 by the d -axis current, the integral of both sides with respect to the d -axis current is expressed as Eq.n 3.1-11.

$$\int_{i_d}^{i_{d,k}} \psi_d i_d di_d = \int_{i_d}^{i_{d,k}} [A_d i_d \tan^{-1}(B_d i_d) + C_d i_d^2] di_d. \quad \text{Eq.n 3.1-11}$$

Using the trapezoidal approximation, the left side of Eq.n 3.1-11 is expressed as Eq.n 3.1-12:

$$\begin{cases} S_1 = 0 \\ S_k = S_{k-1} + \frac{1}{2}(\psi_{d,k} i_{d,k} + \psi_{d,k-1} i_{d,k-1})(i_{d,k} - i_{d,k-1}) \end{cases} \quad \text{Eq.n 3.1-12}$$

where $\psi_{d,k}$ and $i_{d,k}$ are the k th sampled d -axis flux and current, respectively, and k is the index of the sampled data.

Using the integral equation $\int x \tan^{-1}(x) dx = \{(x^2 + 1) \tan^{-1} x - x\}/2$, the right side of Eq.n 3.1-11 is expressed as Eq.n 3.1-13:

$$\begin{aligned} & \int_{i_{d,1}}^{i_{d,k}} [A_d i_d \tan^{-1}(B_d i_d) + C_d i_d^2] di_d \\ &= \frac{1}{2} \left[A_d \left(i_d^2 + \frac{1}{B_d^2} \right) \tan^{-1}(B_d i_d) - \frac{1}{B_d} i_d \right]_{i_{d,1}}^{i_{d,k}} \end{aligned} \quad \text{Eq.n 3.1-13}$$

Therefore, Eq.n 3.1-12 is expressed as a polynomial as Eq.n 3.1-14:

$$\begin{aligned} S_k &= \frac{1}{2} \{ (i_{d,k}^2 \psi_{d,k} - C_d i_{d,k}^3) - (i_{d,1}^2 \psi_{d,1} - C_d i_{d,1}^3) \} \\ &\quad + \frac{1}{2B_d^2} \{ (\psi_{d,k} - C_d i_{d,k}) - (\psi_{d,1} - C_d i_{d,1}) \} \\ &\quad - \frac{1}{2B_d} (i_{d,k} - i_{d,1}) + \frac{C_d}{3} (i_{d,k}^3 - i_{d,1}^3). \end{aligned} \quad \text{Eq.n 3.1-14}$$

And Eq.n 3.1-14 is expressed as Eq.n 3.1-15:

$$\begin{aligned} S_k &= \frac{1}{2} (i_{d,k}^2 \psi_{d,k} - i_{d,1}^2 \psi_{d,1}) \\ &\quad + \alpha (i_{d,k}^3 - i_{d,1}^3) + \gamma (i_{d,k} - i_{d,1}) + \beta (\psi_{d,k} - \psi_{d,1}) \end{aligned} \quad \text{Eq.n 3.1-15}$$

where $\alpha = -\frac{C_d}{6}$, $\beta = \frac{1}{2B_d^2}$, $\gamma = -\frac{C_d}{2B_d^2} - \frac{1}{2B_d}$. By applying LSM to Eq.n

3.1-15, α , β , and γ are estimated [120], In the observation process, γ was transformed to the expression of α and β to get a better precise. After

obtaining the parameters of B_d and C_d . $A_d \tan^{-1}(B_d i_d) = \psi_d(i_d) - C_d i_d$ was used to get the parameters of A_d using LSM through the same process as before. In the same way, the q -axis model could be obtained.

3.3.3. Cross Saturation Model Parameter

K_d and K_q can adequately represent cross saturation for d - and q - axis current. Because the cross saturation of the test motor appears similarly depending on the current of the orthogonal axis, K_d and K_q were set using the current range set in the self-identification process for cross saturation. K_d and K_q were selected as Eq.n 3.1-16:

$$K_d = (i_{d,\max@\text{cross}})^2, K_q = (i_{q,\max@\text{cross}})^2 \quad \text{Eq.n 3.1-16}$$

After selecting K_d and K_q , D_{dq} is estimated using LSM. Eq.n 3.1-11 is rearranged as Eq.n 3.1-17:

$$\begin{aligned} \psi_d(i_d, i_q) - A_d \tan^{-1}(B_d i_d) - C_d i_d \\ = D_{dq} \frac{i_d}{i_d^2 + K_d} \ln \left(1 + \frac{i_q^2}{K_q} \right) \end{aligned} \quad \text{Eq.n 3.1-17}$$

$$\begin{aligned} \psi_q(i_d, i_q) - A_q \tan^{-1}(B_q i_q) - C_q i_q - \hat{\psi}_{\text{pm}} \\ = D_{dq} \frac{i_d}{i_d^2 + K_d} \ln \left(1 + \frac{i_q^2}{K_q} \right) \end{aligned} \quad \text{Eq.n 3.1-18}$$

Applying the LSM, the parameters could be obtained.

3.4 Model Validation with FEA Data

Through the analysis in Chapter 3.3, the parameters of the proposed model could be obtained.

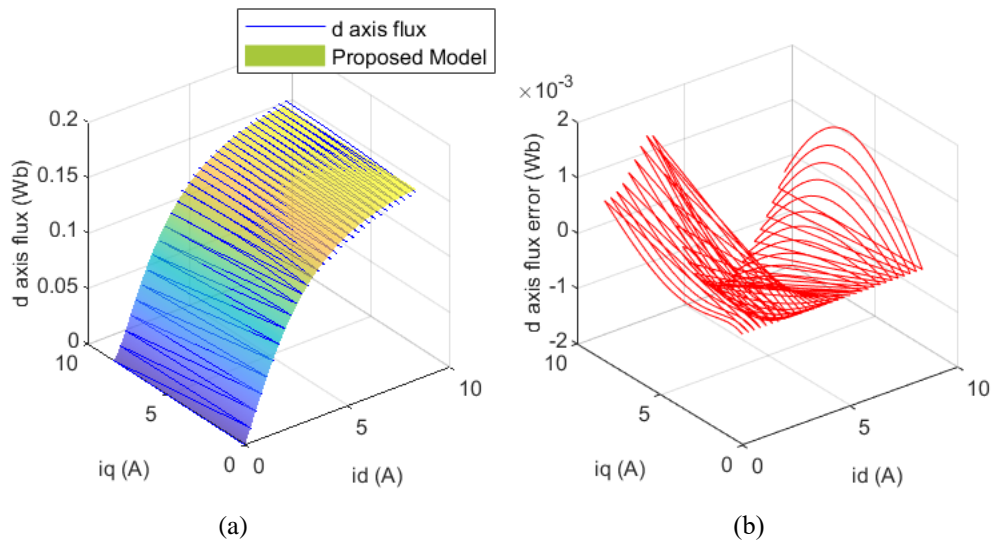


Fig. 3.4-1 *d*- axis flux with the proposed modelling method; (a) FEA data and proposed model; (b) error of the proposed modelling method and FEA data.

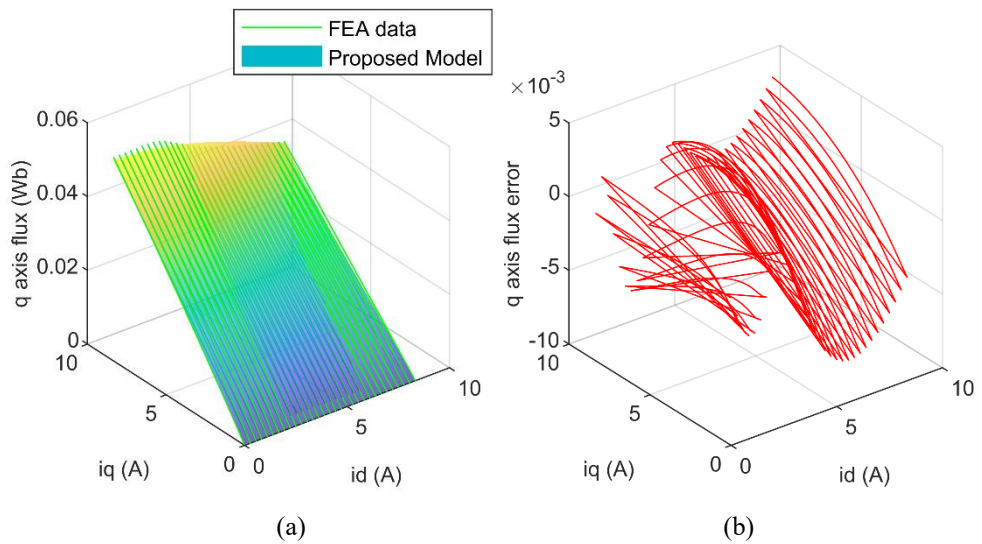


Fig. 3.4-2 *q*- axis flux with the proposed modelling method; (a) FEA data and proposed model; (b) error of the proposed modelling method and FEA data.

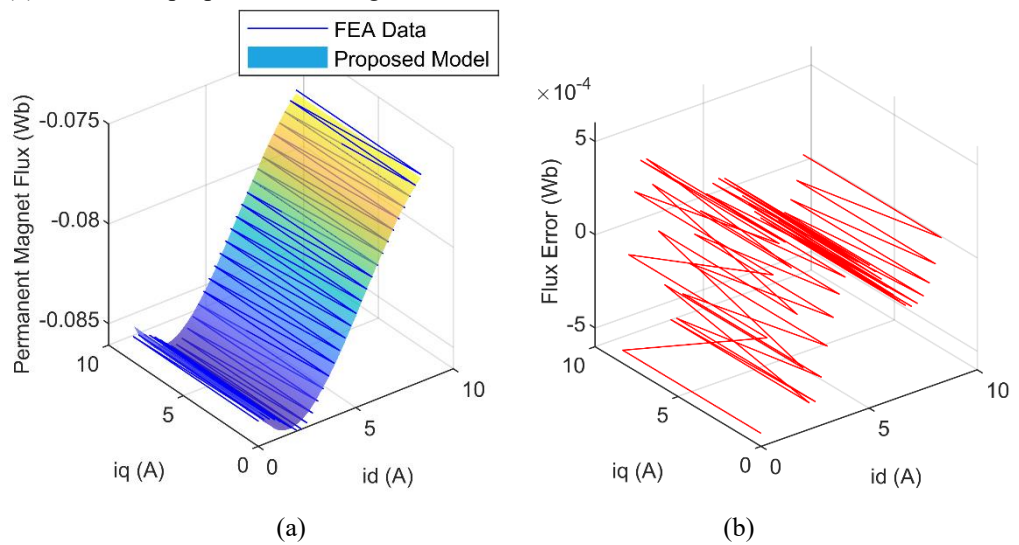


Fig. 3.4-3 Permanent magnet flux with the proposed modelling method; (a) FEA data and proposed model; (b) error of the proposed modelling method and FEA data.

From Fig. 3.4-3, the average errors are 1.2% for the magnate flux which is smaller than the variation of the magnate flux and is satisfied to describe the variation of magnate flux in the changing of working condition.

3.5 Experimental Verification

3.5.1. Experimental Platform

Throughout the entire system, the control part and the drive part were integrated onto a single circuit board based on the STM32-F303 platform.

Experimental tests were carried out in this thesis to verify the feasibility of the algorithm. Fig. 3.5-1 illustrates the main experimental platform, which mainly consists of the Sugawara test bench for loading and unloading, and the YAKOGAWA power analyzer is used for the three-phase voltage and current data acquisition. Simultaneously, oscilloscopes were used to real time measure voltages and currents. For the converter part of the board, AC power was used. STM32F303 micro-controller was used to achieve the proposed algorithm, and the power module using IGBT with 15A as peak current.

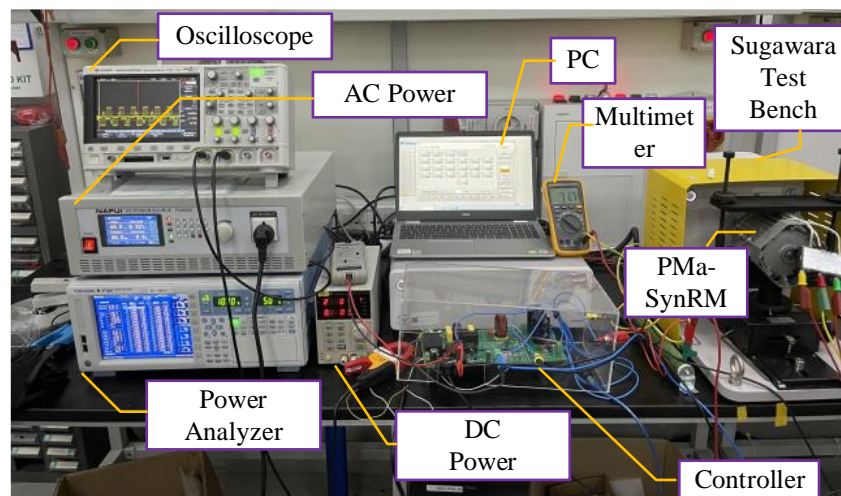


Fig. 3.5-1 Hardware platform for the PMA-SynRM

3.5.2. Machine Parameters

In the experiments, a two poles PMa-SynRM was selected to verify the effectiveness of the proposed modelling method. The main parameters are shown in Table 3.5-1

Table 3.5-1 PMa-SynRM Parameters

Symbol	Definition	Values with unit
n	rated speed	2,700 rpm
T_e	rated torque	1.9 Nm
i_{ab}, i_{bc}, i_{ca}	rated current (RMS)	3.265 A
u_a, u_b, u_c	rated voltage (RMS)	110.0 V
p	pole pairs	2
R	winding resistance	1.028,4 Ohm
φ	rotor flux linkage	0.084,83 Wb
E_{coef}	electromotive force coefficient (RMS)	0.02176 V/rpm
J	rotation inertia	3.296×10^{-4} kg.m ²

3.5.3. Model Parameter Calculation and Error Analysis

As discussed in Chapter 3.2, the magnetic saturation flux model and the cross-saturation model need to be identified separately. Firstly, the flux data could be obtained using the platform discussed in Chapter 3.5.1 and the flux detection process is shown in Fig. 3.1-1. Therefore, the flux data of the machine could be obtained. Once the flux data is obtained, the parameter of the model could be decided using the proposed LSM.

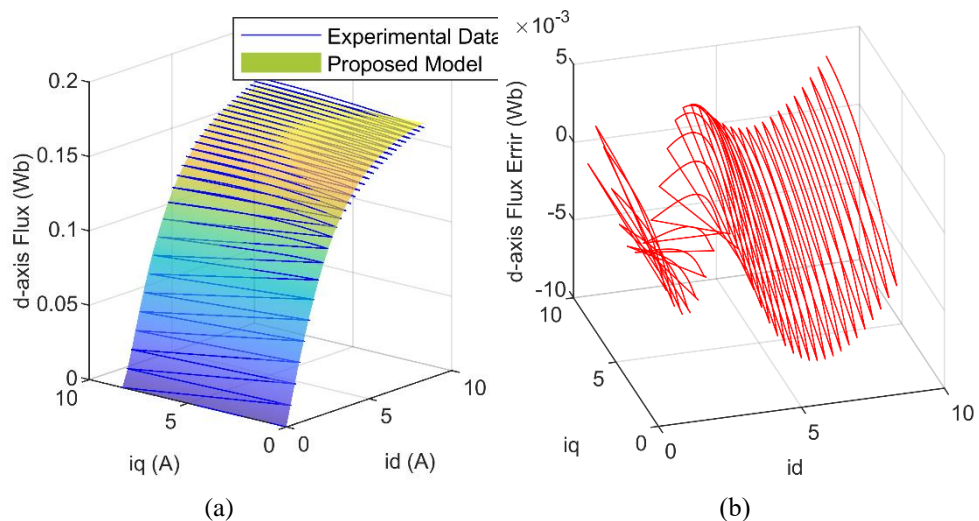


Fig. 3.5-2 d - axis flux with the proposed modelling method; (a) Experiments data and proposed model; (b) error of the proposed modelling method and experiments data.

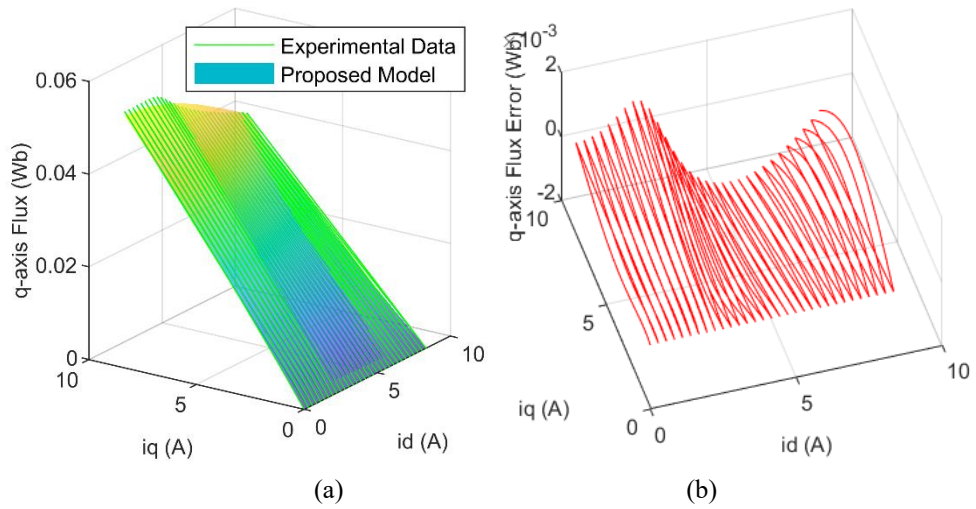


Fig. 3.5-3 q - axis flux with the proposed modelling method; (a) Experiments data and proposed model; (b) error of the proposed modelling method and experiments data.

From Chapter 3.2 and Chapter 3.3, the flux in d - and q -axis flux could be identified without considering the cross-saturation effects and the magnetic saturation model could be identified. Fig. 3.5-2, Fig. 3.5-3 and Fig. 3.5-4 shows the d -axis, q -axis and permanent flux model and errors compared to the tested data. According to the comparison analysis between the tested data and proposed model, the average error is within 5%, which is acceptable for machine control.

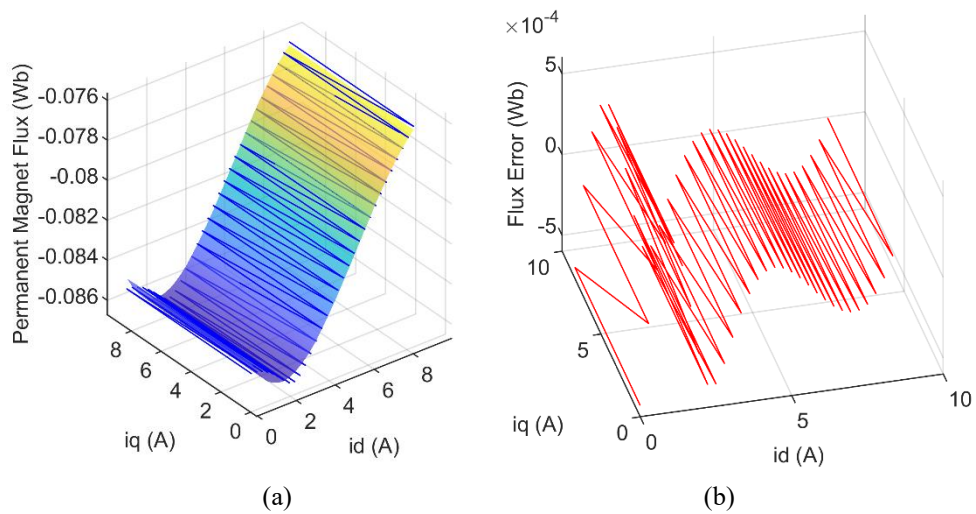


Fig. 3.5-4 Permanent magnet flux with the proposed modelling method; (a) Experiments data and proposed model; (b) error of the proposed modelling method and experiments data.

3.6 Chapter Summary

In this chapter, the modeling of the PMA-SynRM is discussed with a focus on flux characteristics considering inductance variation and saturation. The chapter introduces equations for flux modeling, accounting for variations in inductance and the effects of saturation. Specifically, flux linkage in the d - and q -axes is modeled using nonlinear expressions that incorporate parameters such as K_d , K_q , and D_{dq} . These parameters represent cross-saturation effects between the d - and q -axis currents.

Dynamic inductance matrices are derived from the proposed flux saturation models, resulting in a symmetric matrix satisfying the reciprocity condition. The proposed flux saturation model's accuracy is compared with FEA data and Experiments, showing acceptable error margins.

The cross-saturation model parameters are identified by considering the flux changes due to the d - and q -axis currents. The chapter describes the process of estimating the permanent magnet flux and magnetic saturation model parameters using LSM and transforming nonlinear models into linear ones for easier estimation.

The accuracy of the proposed model is validated against FEA data, showing that the average error for magnet flux is within an acceptable range. The chapter also outlines an experimental verification process, detailing the setup and parameters of the experimental platform, including a two-pole PMA-SynRM and various equipment used for data acquisition and analysis.

Chapter 4 Advanced MTPA Control Methods for Steady-State Performance

Improvement

To achieve optimal performance and improved efficiency in PMA-SynRM, advanced control strategies are essential. Chapter 4 focuses on the development and implementation of high-performance control techniques designed to address the inherent nonlinearities and flux characteristics of PMA-SynRM. This chapter introduces an enhanced MTPA control strategy that reduces parameter dependency and improves current tracking accuracy. Additionally, observer-based feedback mechanisms are proposed to enhance the anti-disturbance capabilities and dynamic response of the system. The methods presented in this chapter aim to achieve precise current regulation, minimize MTPA angle error, and effectively handle external disturbances during operation, thus contributing to the overall efficiency and stability of PMA-SynRM drive systems.

4.1 Online MTPA Angle Detection Based Pseudorandom Signal Injection for Improved Dynamic Response

4.1.1. Description of Injection Method

In the realm of MTPA control for electric machines, accurately determining the MTPA angle is crucial for optimizing performance. One innovative approach to achieve this is through online MTPA angle detection using pseudorandom signal injection. This method offers significant improvements in dynamic response and operational efficiency. The core idea behind this technique is to inject a pseudorandom signal into the current or voltage of the electric machine. Pseudorandom signals, characterized by their noise-like appearance but

deterministic nature, are used to perturb the system slightly. These perturbations are small enough to avoid disrupting normal operation but sufficient to elicit measurable responses from the machine.

The process begins with the generation of a pseudorandom sequence, typically using a LFSR (linear feedback shift register) or similar algorithm, which ensures a well-defined and repeatable sequence. This sequence is then injected into the machine's control loop. The resulting response of the machine—changes in current, voltage, or other relevant parameters—is monitored and analyzed.

By applying advanced signal processing techniques, such as correlation analysis, the injected pseudorandom signal can be distinguished from other noise and disturbances. This analysis helps in accurately identifying the machine's response to the injected signal. The key advantage here is the ability to continuously monitor and adjust the MTPA angle in real-time, leading to an optimized torque production per unit of current.

One of the significant benefits of this method is its improved dynamic response. Traditional MTPA angle detection methods often rely on steady-state conditions or extensive lookup tables, which can be slow to adapt to changing operating conditions. In contrast, the pseudo-random signal injection method can quickly respond to dynamic changes, ensuring that the MTPA angle is always optimal without pre-set of any machine parameters.

Additionally, this method enhances the robustness of the control system. The pseudo-random nature of the injected signal makes it less susceptible to

regular disturbances and noise, improving the reliability of the angle detection process.

4.1.2. Evaluation of $\partial T_e/\partial \theta$

The variation of resistance caused by temperature changes and cross saturation was also considered and used to model the PMA-SynRM [121-123].

$$\begin{cases} u_d = (R_s + \Delta R_s)i_d + \frac{d(L_d i_d + L_{dq} i_q)}{dt} \\ \quad - \omega_e(L_q i_q + L_{qd} i_d + \psi_{pm}) \\ u_q = (R_s + \Delta R_s)i_q + \frac{d(L_q i_q + L_{qd} i_d + \psi_{pm})}{dt} \\ \quad + \omega_e(L_d i_d + L_{dq} i_q) \end{cases} \quad \text{Eq.n 4.1-1}$$

where, u_d and u_q is the voltage of d - and q -axis, respectively; R_s is the stator resistance in 25 °C; ΔR_s is the resistance variation caused by temperature changes; i_d and i_q is the d - and q -axis current, respectively; L_d and L_q is the d - and q -axis inductance, respectively; ω_e is the electrical speed of the PMA-SynRM, $L_{qd}=L_{dq}$ is cross saturation inductance for q - and d -axis, ψ_{pm} is the permanent magnet flux.

Due to the inherent challenges in calculating or measuring torque accurately in industrial applications, the MTPA tracking method presented in this thesis employs a novel approach based on signal injection to evaluate $\partial T_e/\partial \theta$, the proposed method involves injecting a high-frequency, small signal into the system to facilitate the estimation process. So, the current angle θ with the injected signal could be obtained as Eq.n 4.1-2.

$$\theta = \theta_{avg} + \theta_h = \theta_{avg} + A_{mag} \sin(f_h \times 2\pi t) \quad \text{Eq.n 4.1-2}$$

where θ is the calculated current angle in the control process, θ_{avg} is the current angle in fundamental frequency, and θ_h is the injected current angle; A_{mag} is

the magnitude of the injected signal; f_h is the frequency of the injected signal; t represents time unit. Eq.n 4.1-3 and Eq.n 4.1-4 could be obtained according to Eq.n 1.3-5.

$$\begin{aligned} i_d &= i_s \cos(\theta_{avg} + A_{mag} \sin \omega_h t) & \text{Eq.n 4.1-3} \\ &\approx i_s \cos \theta_{avg} - i_s A_{mag} \sin \theta_{avg} \sin \omega_h t \\ &= i_{db} + i_{di} \end{aligned}$$

$$\begin{aligned} i_q &= i_s \sin(\theta_{avg} + A_{mag} \sin \omega_h t) & \text{Eq.n 4.1-4} \\ &\approx i_s \sin \theta_{avg} + i_s A_{mag} \cos \theta_{avg} \sin \omega_h t \\ &= i_{qb} + i_{qi} \end{aligned}$$

In control systems, the injected current angle will influence the d - and q -axis current, which may further cause speed loop oscillation and torque fluctuation. To minimize the further impact on the speed control loop, or to reduce any additional influence on the speed control loop, the injected current angle frequency as shown in Eq.n 4.1-3 and Eq.n 4.1-4 is selected as 400 Hz which means the d - and q -axis contains a 400 Hz harmonic. As for the torque fluctuation, the variation could be neglected using the Taylor series expansion [72]. Since the torque features a linear relationship with the output mechanical power at a fixed speed. The torque concerning the current angle could be analyzed through the calculated copper loss power, reactive power, and mechanical power as shown in Eq.n 4.1-5 - Eq.n 4.1-8.

$$\begin{aligned} P_e &= P_{copper} + P_{reactive} + P_{mech} \\ &= \frac{3}{2} [R_s (i_d^2 + i_q^2) + \Delta R_s (i_d^2 + i_q^2) + L_d \frac{di_d}{dt} i_d \\ &+ L_q \frac{di_q}{dt} i_q + L_{qd} \frac{di_q}{dt} i_d + L_{dq} \frac{di_d}{dt} i_q + \frac{d\psi_{pm}}{dt} i_q \\ &+ \omega_m \psi_{pm} i_d + \omega_m (L_d - L_q) i_d i_q + L_{dq} i_q^2 - L_{qd} i_d^2] \end{aligned} \quad \text{Eq.n 4.1-5}$$

$$P_{copper} = (R_s + \Delta R_s) i_s^2 = R_s i_s^2 + \Delta R_s i_s^2 \quad \text{Eq.n 4.1-6}$$

$$\begin{aligned}
P_{\text{reactive}} = & \frac{3}{2} ((L_{qd} \cos^2 \theta_{\text{avg}} - L_{dq} \sin^2 \theta_{\text{avg}}) \\
& - \frac{1}{2} (L_d - L_q) \sin 2\theta_{\text{avg}}) i_s^2 A_{\text{mag}} \omega_h \cos \omega_h t \\
& + \frac{3}{4} (L_d \sin^2 \theta_{\text{avg}} + L_q \cos^2 \theta_{\text{avg}} + \frac{1}{2} (L_{dq} - L_{qd}) \sin 2\theta_{\text{avg}}) \\
& \times i_s^2 A_{\text{mag}}^2 \omega_h \sin 2\omega_h t
\end{aligned} \tag{Eq.n 4.1-7}$$

$$\begin{aligned}
P_{\text{mech}} \approx & \frac{3}{2} \omega_m \left[\frac{1}{2} (L_d - L_q) i_s^2 \sin 2\theta_{\text{avg}} - \right. \\
& \left. \psi_{pm} i_s \cos \theta_{\text{avg}} + L_{dq} i_s^2 \sin^2 \theta_{\text{avg}} \right] \\
& - L_{qd} i_s^2 \cos^2 \theta_{\text{avg}} + \frac{3}{2} [\psi_{pm} \sin \theta_{\text{avg}} + (L_d - L_q)] \\
& i_s \cos 2\theta_{\text{avg}} \times i_s \omega_m A_{\text{mag}} \sin \omega_h t \\
& + \frac{3}{8} \omega_m (L_d - L_q) i_s^2 A_{\text{mag}}^2 \sin 2\theta_{\text{avg}} \cos 2\omega_h t \\
& + \frac{3}{4} (L_{dq} \cos^2 \theta_{\text{avg}} - L_{qd} \sin^2 \theta_{\text{avg}}) \omega_m i_s^2 A_{\text{mag}}^2 \\
& - \frac{3}{4} (L_{dq} \cos^2 \theta_{\text{avg}} - L_{qd} \sin^2 \theta_{\text{avg}}) \omega_m i_s^2 A_{\text{mag}}^2 \cos 2\omega_h t \\
& + \frac{3}{2} (L_{dq} + L_{qd}) \omega_m i_s^2 \sin 2\theta_{\text{avg}} A_{\text{mag}} \sin \omega_h t
\end{aligned} \tag{Eq.n 4.1-8}$$

4.1.3. MTPA Tracking Based Fixed Frequency

To further evaluate and extract the mechanical power, to get the MTPA working point, the following filters described in Fig. 4.1-1 were used to get the calculated output power P_o which used to do the MTPA control from the calculated input power P_e .

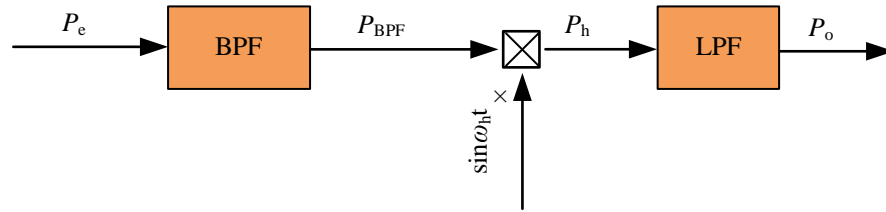


Fig. 4.1-1 Signal processing to get the MTPA criterion

From the proposed control structure in Fig. 4.1-1, the calculated output power P_o , which proved to have a linear relationship with the derivation of the output torque to the current angle θ , could be extracted.

From the first bandpass filter, the copper loss part could be eliminated because no high-frequency signal is contained in this part which is denoted as P_{BPF} .

Although the resistance varies with the temperature, it could be regarded as a constant value in the electrical power sampling process because it is a slowly varying component.

After the bandpass filter, the signal was then plus $\sin(\omega_h t)$ to eliminate the orthogonal component which is denoted as P_h . After that, a low-pass filter was used to extract the low-frequency part and the calculated output P_o , which could be expressed in Eq.n 4.1-9.

$$P_o = \frac{1}{2} A_{\text{mag}} \omega_m i_s [-\psi_{\text{pm}} \sin \theta + (L_d - L_q) i_s \cos 2\theta + (L_{\text{dq}} + L_{\text{qd}}) i_s \sin 2\theta] \quad \text{Eq.n 4.1-9}$$

According to Eq.n 4.1-9, Eq.n 4.1-10 could be obtained.

$$\frac{\partial T_e}{\partial \theta} = \frac{3}{2} p i_s [-\psi_{\text{pm}} \sin \theta + (L_d - L_q) i_s \cos 2\theta + (L_{\text{dq}} + L_{\text{qd}}) i_s \sin 2\theta] \quad \text{Eq.n 4.1-10}$$

In Eq.n 4.1-10, the derivation term respect to magnet flux, d - and q -axis flux were not considered. The P_o could be expressed as Eq.n 4.1-11 if this part were considered.

$$\begin{aligned} \frac{\partial T_e}{\partial \theta} = & \frac{3p}{2} i_s [-\psi_{\text{pm}} \sin \theta + (L_d - L_q) i_s \cos 2\theta \\ & + (L_{\text{dq}} + L_{\text{qd}}) i_s \sin 2\theta \\ & + \left(\frac{\partial L_d}{\partial \theta} - \frac{\partial L_q}{\partial \theta} \right) i_s \frac{1}{2} \sin 2\theta - \frac{\partial \psi_{\text{pm}}(\theta_{\text{avg}})}{\partial \theta} \cos \theta \\ & - \frac{\partial L_{\text{dq}}}{2 \partial \theta} i_s \cos 2\theta - \frac{\partial L_{\text{qd}}}{2 \partial \theta} i_s \cos 2\theta] \end{aligned} \quad \text{Eq.n 4.1-11}$$

The extracted P_o features a linear relationship with the derivation to torque,

which means the MTPA question could be simplified to control P_o and makes it equal to 0 to satisfy the MTPA working point requirements.

During the signal processing to identify the MTPA trajectory, potential current sampling errors, such as DC offset and random noise, are considered. The DC offset, which represents a constant deviation in the current measurement, is effectively eliminated through high-pass or band-pass filtering during the signal processing stage. Since the offset is a constant component, it does not affect the dynamic response of the MTPA detection mechanism. Moreover, random noise introduced during current sampling is suppressed by the integration process within the control loop. The integral operation naturally attenuates high-frequency noise, smoothing the current signal and preventing fluctuations from affecting the MTPA path tracking. Consequently, even if current sampling errors exist, the overall stability and accuracy of the MTPA control are not compromised.

To weaken the influence of the injected current, a high frequency supplementary current loop is needed to have a better performance [72]. According to the analysis of the CFSI (Constant Frequency Signal Injection) method, it solves the MTPA detection problem. However, it will bring more harmoniousness to the current, which needs to be further improved. In Chapter 4.1.4, the PRFSI method was proposed to improve the situation.

4.1.4. Utilization of PRFSI Control

As discussed in Chapter 2.2.1, the CFSI control strategy will bring a harmonic spike in the current, which leads to more harmonic distortion and

further deteriorates the control performance. In this part, an improved PRFSI method will be introduced and discussed.

A. Utilization of PRFSI Control

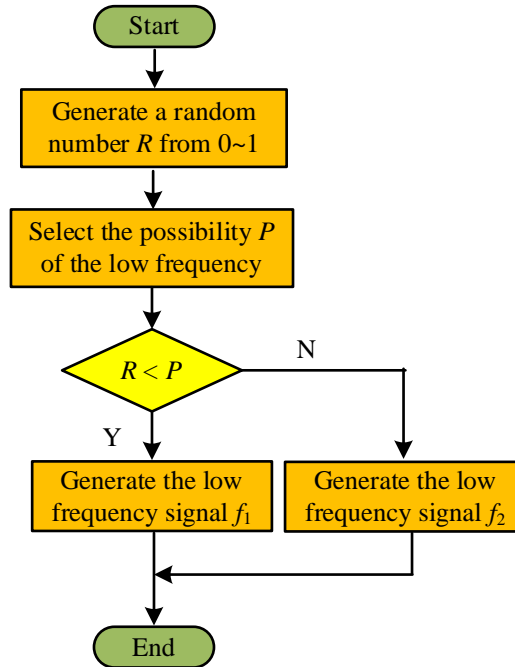


Fig. 4.1-2 PRFSI method signal generation diagram

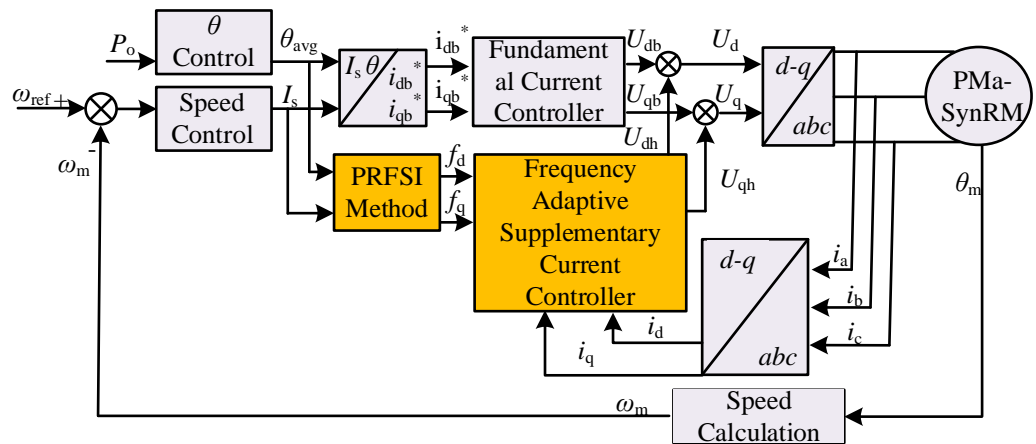


Fig. 4.1-3 Overall control diagram of PRFSI

Fig. 4.1-3. shows the improved control structure of the PMA-SynRM. In the control system, the CFSI was improved and replaced by the PRFSI. Meanwhile, the band-pass filter was updated to adjust according to the injected angle signal. In the control diagram, P_o was obtained from diagram shown in Fig. 4.1-4. However, the bandpass filter needs to be redesigned and improved with the

PRFSI control because the frequency of the injected current is no longer a constant value, which means the band-pass filter needs to be improved accordingly. The design of the band-pass filter is the same as the part of the frequency adaptive supplementary current controller, which will be discussed in a detail way in the next part.

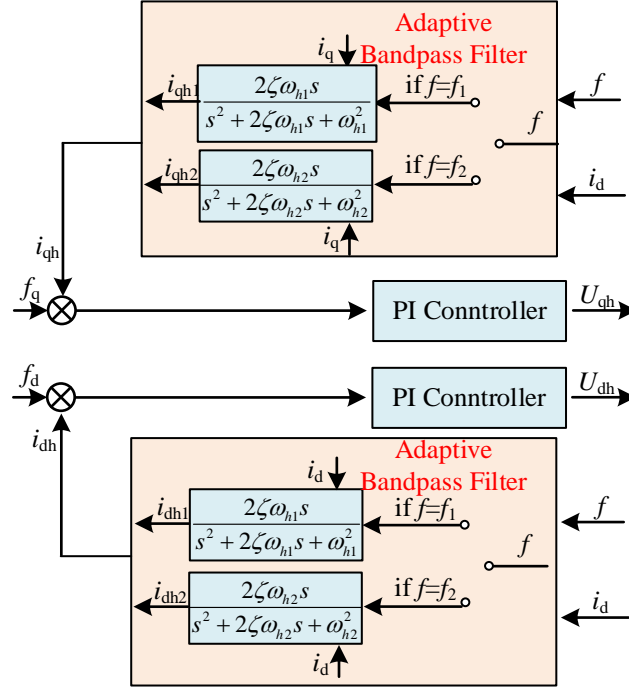


Fig. 4.1-4 Configuration of high-frequency current loop and adaptive bandpass filter

Fig. 4.1-2 shows the generation of the PRFSI, in which two frequency signals will be generated randomly. In the signal generation process, two kinds of signals were generated randomly while the generation possibility was set initially. The generated signal was shown in Eq.n 4.1-12 and Eq.n 4.1-13.

$$f_{1d} = -i_s A_{mag1} \sin\theta_{avg} \sin\omega_{h1} t \quad \text{Eq.n 4.1-12}$$

$$f_{1q} = i_s A_{mag1} \cos\theta_{avg} \sin\omega_{h1} t$$

$$f_{2d} = -i_s A_{mag2} \sin\theta_{avg} \sin\omega_{h2} t \quad \text{Eq.n 4.1-13}$$

$$f_{2q} = i_s A_{mag2} \cos\theta_{avg} \sin\omega_{h2} t$$

where f_{1d}, f_{1q}, f_{2d} and f_{2q} are generated d - and q -axis current in high frequency; ω_{h1} and ω_{h2} are injected signal angular frequency and $\omega_{h1} < \omega_{h2}$; A_{mag1} and A_{mag2} are the amplification factor of the injected signal. In the CFSI, A_{mag} is generally

a constant value selected as 0.02~0.04 to get a satisfactory control performance. However, in the PRFSI, to guarantee a constant SNR (Signal Noise Ratio), the magnitude of different frequency needs to be adjusted according Eq.n 4.1-14.

$$\omega_{h1}/\omega_{h2} = A_{mag1}/A_{mag2} = N \quad \text{Eq.n 4.1-14}$$

It is important to make sense that P does not represent the possibility of occurrence time for f_1 , due to the distinct duration of f_1 and f_2 . The actual probability of f_1 is described in Eq.n 4.1-15.

$$P_{\omega_{h2}} = P_{\omega_{h1}} \omega_{h1}/(\omega_{h1} + \omega_{h2}) \quad \text{Eq.n 4.1-15}$$

In Eq.n 4.1-15, the injected signal frequency was obtained according to the selected possibility. However, the cut-off frequency of the band-pass filter needs to be adjusted accordingly. To meet the frequency varying under PRFSI that the required signal could be extracted, an adaptive bandpass filter is designed, and a high-frequency PI controller is supplemented, which is shown in Fig. 4.1-4. Meanwhile, the cutoff frequency of the bandpass filter needs to be adjusted accordingly, because the injected frequency is never a constant value under PRFSI working condition. To filter out the high frequency noise, the injected signal was extracted and compared to the given signal, the injected voltage could be obtained through the PI controller. The adaptive filter will judge the injected signal and switch the cut-off frequency to filter out the current frequency of the signal.

B. Principle of Signal Frequency Selection

The following signal frequency selection method need to be satisfied considering the real control system:

a) Considering the digital controller and the overall calculation burden, the switching frequency of the power elements are selected as 20 kHz. However, the frequency of current sampling and current loop are selected as 4 kHz for the calculation burden consideration. In this way, the selection of the injected current frequency should be an integer multiple of 4 kHz.

b) The maximum injected frequency should be smaller than 2 kHz based on the assumption of a) to satisfy Shannon's law. The injected signal should be small enough to get a sine wave that is not distorted for the MCU calculation burden consideration. A higher sine wave means more points are needed to construct the wave in a limited time, which may cause calculation burden for the MCU.

c) The frequency of the injected signal should be higher than the speed loop. Otherwise, the performance of the whole system would deteriorate. On the other hand, the lower frequency means that the low-pass filter needs a lower cut-off frequency, which will influence the dynamic response of the whole control system.

d) The injected frequency is selected as 400 Hz for the CFSI control, and the selection of pseudorandom frequency is based on the discussion in Chapter 4.1.5, which is selected as 280 Hz and 350 Hz. The low frequency of the pseudorandom method is due to the complexity of the calculation, which means more calculation is needed. Meanwhile, the same SNR should be satisfied, which Eq.n 4.1-14 should be satisfied.

4.1.5. Analysis on PRFSI

The FFT (Fast Fourier Transform) is not suitable for stationary random

signals because FFT assumes that the signal is deterministic and periodic. In other words, FFT assumes that the signal repeats indefinitely, which is not the case for random signals. However, it could be used to analyze the THD. For analyzing stationary random signals, other methods such as the PSD (Power Spectral Density) estimation using techniques like the Welch method or the periodontal are more appropriate [124]. In this thesis, PSD was used to analyze the distribution of the harmonica. In the following, the PRFSI considering current loop frequency will be analyzed.

The system response with respect to PSD can be expressed as Eq.n 4.1-16 with the injected signal.

$$S_{CF}(f) = K_f[\delta(f - f_0) + \delta(f + f_0)] \quad \text{Eq.n 4.1-16}$$

where $\delta ()$ is the unit impulse function, accompanied by a coefficient denoted as K_f . The frequency of the injected signal is symbolized by f_0 . In this study, attention is exclusively given to the positive frequency aspect. From Eq.n 4.1-16, it is obvious that a peak would emerge around the injection frequency. The PRFSI was put forward to improve the distribution of the harmonica. The PSD of the injected signal can be expressed as Eq.n 4.1-17[125,126].

$$S(f) = \begin{cases} \frac{1}{E[T]} \left\{ \frac{2\text{Re} \left(\frac{E[I(f)e^{j2\pi fT}] - E[I^*(f)]}{1 - E[e^{j2\pi fT}]} \right)}{+E[|I(f)|^2]} \right\} & E[e^{j2\pi fT}] \neq 1 \\ \frac{1}{\{E[T]\}^2} \{E[|I(f)|]\}^2 & E[e^{j2\pi fT}] = 1 \end{cases} \quad \text{Eq.n 4.1-17}$$

In this context, the symbol $E[]$ is the expectation operator. The term $I(f)$ refers to the FFT applied to a single cycle of the given signal. Furthermore, $I^*(f)$

is used to represent the complex conjugate of $I(f)$, and T signifies the period of $i_0(t-t_k)$.

As evident from Eq.n 4.1-17, the components of the harmonica can be divided into two parts. To reduce the harmonica, it is essential to eliminate the discrete spectrum. From Eq.n 4.1-17, when Eq.n 4.1-18 and Eq.n 4.1-19 hold, the discrete part could be eliminated.

$$E[e^{j2\pi fT}] = 1 \quad \text{Eq.n 4.1-18}$$

$$E[|I(f)|] = 0 \quad \text{Eq.n 4.1-19}$$

Within the PRFSI scheme, the fundamental signals possess frequencies f_1 and f_2 , with corresponding periods T_1 and T_2 , and probabilities P_1 and P_2 , respectively. Consequently, Eq.n 4.1-18 can be rewritten in the form of Eq.n 4.1-20 and Eq.n 4.1-19 could be rewritten in Eq.n 4.1-21.

$$E[e^{j2\pi f_p T}] = [P_1, P_2] \cdot [e^{j2\pi f_p T_1}, e^{j2\pi f_p T_2}]^T = 1 \quad \text{Eq.n 4.1-20}$$

$$E[|I(f_p)|] = [P_1, P_2] \cdot [|I_1(f_p)|, |I_2(f_p)|]^T = 0 \quad \text{Eq.n 4.1-21}$$

According to $P_1+P_2=1$, and Eq.n 4.1-20, Eq.n 4.1-22 should be satisfied to get Eq.n 4.1-20.

$$e^{j2\pi f_p T_1} = e^{j2\pi f_p T_2} = 1 \quad \text{Eq.n 4.1-22}$$

To satisfy Eq.n 4.1-22, $f_p T_1$ and $f_p T_2$ should be integers. Considering the current sampling frequency f_s , Eq.n 4.1-23 should be further satisfied.

$$f_s = km_2 f_1 = m_1 f_2 \quad \text{Eq.n 4.1-23}$$

where m_1 , m_2 , and k are positive integers.

To conclude, when Eq.n 4.1-24 was satisfied, the discrete part of the harmonica could be eliminated.

$$I_1(kf_s) = I_2(kf_s) = 0 \quad \text{Eq.n 4.1-24}$$

Eq.n 4.1-25 could be obtained using FFT theory:

$$\begin{aligned} I_1(\omega) &= F[i_1(t)] = \int_{-\infty}^{+\infty} i_1(t)e^{-j\omega t} dt \\ &= \int_0^{\frac{2\pi}{\omega_1}} K_i K_v \cos(\omega_1 t) e^{-j\omega t} dt \\ &= jK_i K_v \omega \frac{1 - e^{-j2\pi\omega/\omega_1}}{\omega^2 - \omega_1^2} \end{aligned} \quad \text{Eq.n 4.1-25}$$

$$I_1(f) = \frac{jK_i K_v f}{2\pi} \frac{1 - e^{-j2\pi f/f_1}}{f_2^2 - f_1^2} \quad \text{Eq.n 4.1-26}$$

Similarly, the following can be obtained:

$$I_2(f) = \frac{jK_i K_v f}{2\pi} \frac{1 - e^{-j2\pi f/f_2}}{f_1^2 - f_2^2} \quad \text{Eq.n 4.1-27}$$

Since $m_1 > m_2$, two cases are discussed under the condition of $kf_s > 0$.

Case 1: $m_2=1$, this means that f_2 is an integer multiple of f_1 . From the same way as case 1, the harmonica content will not be reduced, and the spikes depends on f_1 .

Case 2: $m_2>1$, this means that f_2 is not an integer multiple of f_1 . In this case, $1 - e^{-\frac{j2\pi f_p}{f_1}} = 1 - e^{-j2\pi k m_2} = 0$. Therefore, Eq.n 4.1-24 was satisfied. And the harmonica spikes will be reduced.

In the selection of the pairs of frequency, case 2 should be satisfied to eliminate the harmonic spikes to get a continuous harmonic distribution.

C. PSD Analysis of Non-ideal PRFSI Considering Sampling Influence

In the actual system, the sampling frequency of the current loop should be considered. Eq.n 4.1-28 could be obtained for the injected signal.

$$f_{1d} = -i_s A_{\text{mag}1} \sin\theta_{\text{avg}} \sin\{\omega_{h1}[t - \text{mod}(t, T_s)]\} \quad \text{Eq.n 4.1-28}$$

Eq.n 4.1-29 could be obtained for the PRFSI method.

$$f_{1d}(t) = \sum_{k=1}^{\infty} f_0(t - t_k) \quad \text{Eq.n 4.1-29}$$

where,

$$f_{0d}(t) = \Re[f_{1d}(t), f_{2d}(t)] \quad \text{Eq.n 4.1-30}$$

$$f_{1d}(t) = \begin{cases} -i_s A_{\text{mag}1} \sin\theta_{\text{avg}} \sin\{\omega_{h1}[t - \text{mod}(t, T_s)]\}, & 0 < t < T_1 \\ 0, & \text{others} \end{cases} \quad \text{Eq.n 4.1-31}$$

$$f_{2d}(t) = \begin{cases} -i_s A_{\text{mag}1} \sin\theta_{\text{avg}} \sin\{\omega_{h2}[t - \text{mod}(t, T_s)]\}, & 0 < t < T_1 \\ 0, & \text{others} \end{cases} \quad \text{Eq.n 4.1-32}$$

According to Eq.n 4.1-23, the following could be get:

$$I_2(f) = \frac{jK_i K_v f}{2\pi} \frac{1 - e^{-j2\pi f/f_2}}{f_1^2 - f_2^2} \quad \text{Eq.n 4.1-33}$$

$$T_1 = n_1 T_s \text{ and } T_2 = n_2 T_s \quad \text{Eq.n 4.1-34}$$

Then

$$\begin{aligned} F_0(\omega) &= \sum_{n=1}^{n_1} \int_{(n-1)T_s}^{nT_s} -i_s A_{\text{mag}1} \sin\theta_{\text{avg}} \\ &\quad \times \sin\left[2\pi \frac{(n-1)T_s}{n_1 T_s}\right] e^{-j\omega t} dt \\ &= -i_s A_{\text{mag}1} \sin\theta_{\text{avg}} e^{-j(n_1+1)T_s\omega} \left(e^{\frac{4j\pi}{n_1}} - 1 \right) \\ &\quad \frac{(e^{jT_s\omega} - 1)(e^{jn_1 T_s\omega} - 1)}{2[e^{j(-T_s\omega+2\pi/n_1)} - 1][e^{j(T_s\omega+2\pi/n_1)} - 1]\omega} \end{aligned} \quad \text{Eq.n 4.1-35}$$

Supposing

$$\omega_s = k\omega_1 = 2\pi k/(n_1 T_s) \quad \text{Eq.n 4.1-36}$$

where k is a positive integer, Eq.n 4.1-37 could be obtained.

$$\begin{aligned} F_0(\omega_k) &= -i_s A_{\text{mag}1} \sin\theta_{\text{avg}}(\omega_s) \times \\ &\quad \frac{(e^{j2\pi k_0/n_1} - 1)(e^{j2\pi k_0} - 1)}{[e^{j2\pi(1-k)/n_1} - 1][e^{j2\pi(1+k_0)/n_1} - 1]} \end{aligned} \quad \text{Eq.n 4.1-37}$$

$$-i_s A_{\text{mag}1} \sin \theta_{\text{avg}}(\omega_s) = e^{-\frac{j2\pi k_0(n_1+1)}{n_1}} \left(e^{\frac{4j\pi}{n_1}} - 1 \right) \times \frac{-i_s A_{\text{mag}1} \sin \theta_{\text{avg}}}{2k} \quad \text{Eq.n 4.1-38}$$

Because $e^{j2\pi k} - 1 = 0$, furthermore, Eq.n 4.1-39 could be satisfied for the three sub multiples $e^{j2\pi k/n_1} - 1$, $e^{j2\pi(1-k)/n_1} - 1$ and $e^{j2\pi(1+k)/n_1} - 1$.

$$F_0(\omega_k) \neq 0 \quad \text{Eq.n 4.1-39}$$

Eq.n 4.1-39 is equivalent to

$$e^{j2\pi(1-k)/n_1} - 1 = 0 \text{ or } e^{j2\pi(1+k)/n_1} - 1 = 0 \quad \text{Eq.n 4.1-40}$$

that is:

$$k = n_1 k_n \pm 1 \quad \text{Eq.n 4.1-41}$$

Then, the following two cases can be expressed all the situations:

Case 1: $m_2 = 1$ and k exists:

$$k = n_1 k_n \pm 1 \quad \text{Eq.n 4.1-42}$$

$$f_p = k_n f_s \pm f_1 \quad \text{Eq.n 4.1-43}$$

Case 2: $m_2 > 1$ and k cannot be an integer:

$$I_1(k_p f_{12}) = I_2(k_p f_{12}) \equiv 0 \quad \text{Eq.n 4.1-44}$$

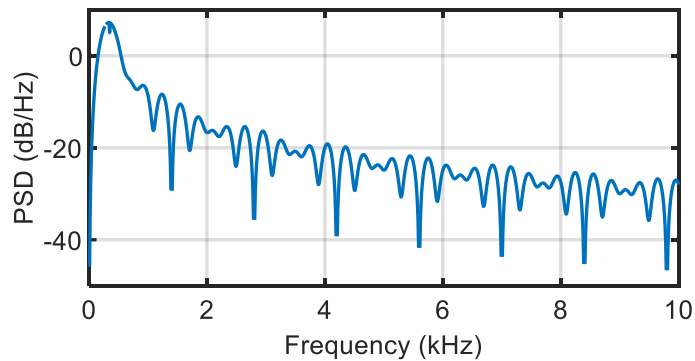


Fig. 4.1-5 PSD Analysis of PRFSI

Therefore, in the real control systems, the sampling frequency needs to be considered and case 2 should be satisfied to eliminate the harmonic spike. In this

way, the harmonica in the discrete part could be reduced.

4.1.6. Analysis and Effect of Filters

According to Eq.n 4.1-17, Eq.n 4.1-26 and Eq.n 4.1-27, the PSD of the injected signal could be expressed as Eq.n 4.1-45.

$$S(f) = \left(\frac{K_i K_v f}{2\pi}\right)^2 \left(\frac{2(1 - \cos(2\pi f/f_1))}{(f^2 - f_1^2)^2} + \frac{2(1 - \cos(2\pi f/f_2))}{(f^2 - f_2^2)^2} \right) \quad \text{Eq.n 4.1-45}$$

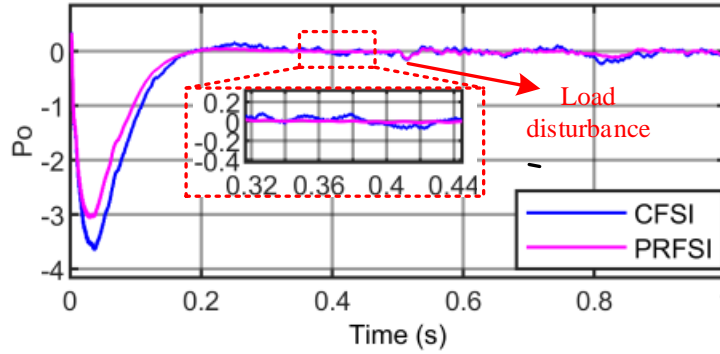


Fig. 4.1-6 P_o output with CFSI and PRFSI

It could be obtained from Fig. 4.1-5 that the discrete spike of signals disappears, which verifies the effectiveness of the proposed PRFSI method.

As shown in Fig. 4.1-6, the injected signal was further processed to get the P_o , which is used to do the MTPA control. In this way, the harmonic content directly determines the fluctuation of the MTPA angle. Therefore, the harmonic contents will be researched after the filters.

In Fig. 4.1-6, the P_o output signal of PRFSI features a smaller fluctuation compared to the CFSI, which means that a smaller MTPA control angle will be detected with the proposed PRFSI method.

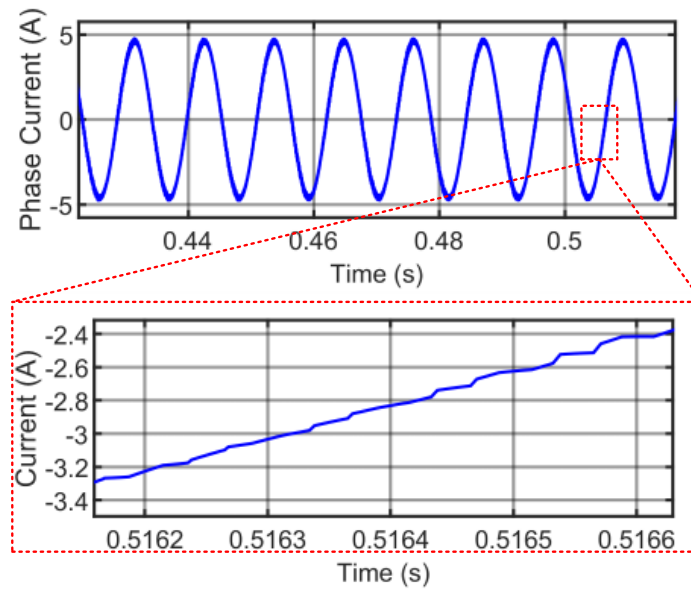
In the next part, simulations and experiments will be conducted to verify

the feasibility of the proposed PRFSI method.

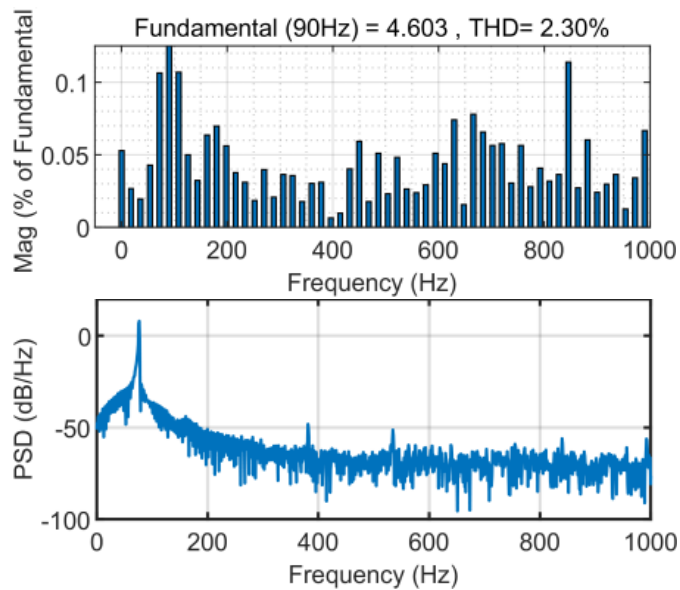
4.1.7. Simulation Verification

Throughout the entire system, the control part and the drive part were integrated onto a single circuit board based on the STM32-F303 platform. The parameters of the PMA-SynRM are shown in Chapter 5.3.2.

A. Harmonic Distribution Simulations



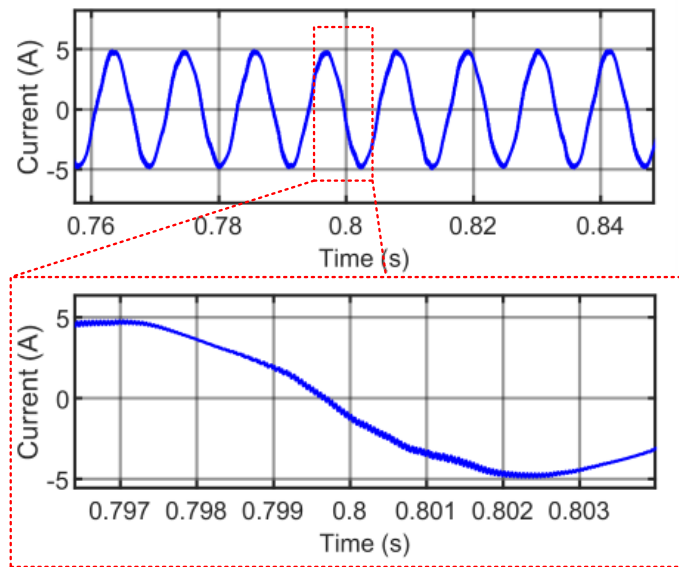
(a)



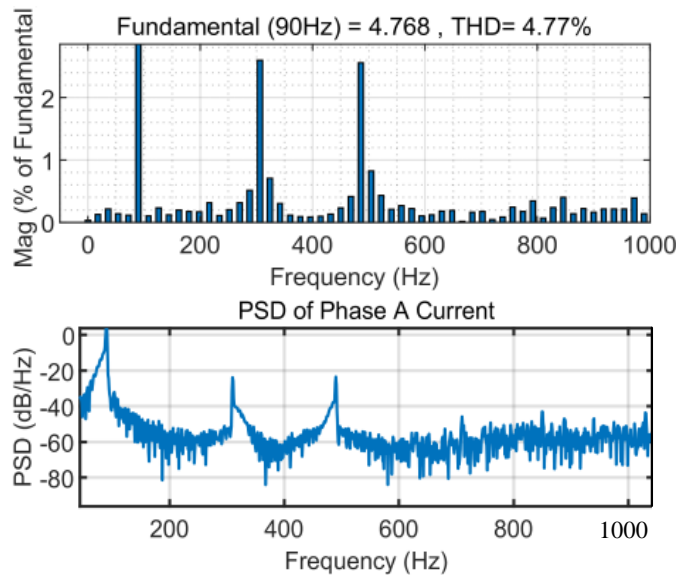
(b)

Fig. 4.1-7 Phase current and its harmonic distribution without signal injection (a) phase current

and its partial enlargement; (b) harmonic distribution using FFT and PSD analysis.



(a)



(b)

Fig. 4.1-8 Phase current and its harmonic distribution with CFSI (a) phase current and its partial enlargement; (b) harmonic distribution using FFT and PSD analysis.

To research the influence caused by the signal injection method including the CFSI and PRFSI, the phase current and the harmonic disturbance using FFT and PSD were demonstrated. Fig. 4.1-7(a) shows the phase current and its partial enlargement, in which the current is a sine wave. From its partial enlargement figure, the current is approximately a straight line, in which the disturbance was

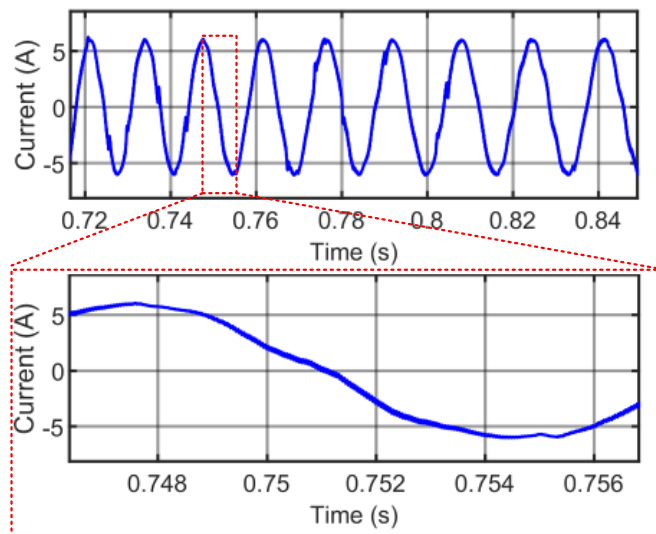
caused by the switching frequency of the IGBT.

From Fig. 4.1-7(b), the Total Harmonic Distribution (THD) was 2.3%, which was mainly caused by the switching of the IGBT. Meanwhile, the distribution of harmonics is approximately uniform, in which it can be get by both FFT analysis and PSD analysis. With the same configurations of speed loop and current loop, the comparison simulation between the CFSI and PRFSI was further carried out compared to the no signal injection situation.

Fig. 4.1-8(a) shows the phase current under the rated load working conditions, in which the current distortion could be detected.

In the partial enlargement figure, a sine wave in the base frequency could be observed, but the distortion ratio is very small. This is because the injected current occupied only 5% percent of the current and a high frequency loop has existed to reduce the influence of the injected current.

From the simulation results, the current distortion ratio is under the acceptable range. Compared to the simulation with signal injection, the current distortion ratio is increased.



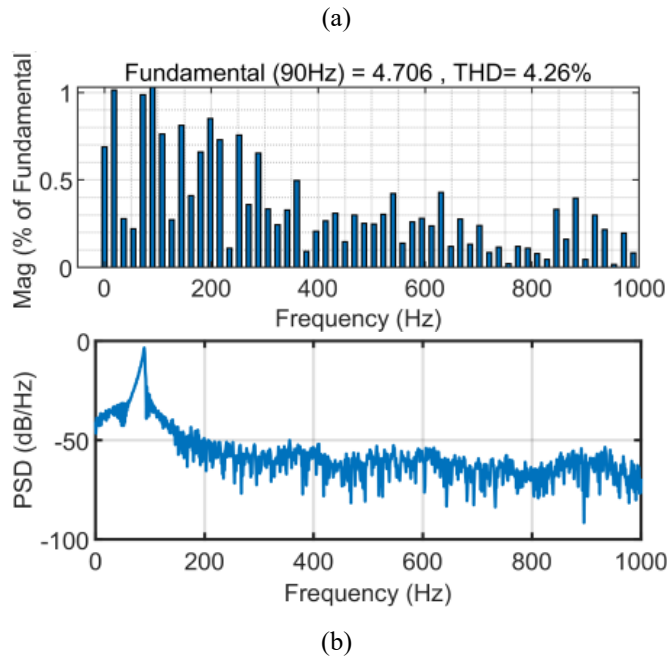


Fig. 4.1-9 Phase current and its harmonic distribution with PRFSI (a) phase current and its partial enlargement; (b) harmonic distribution using FFT and PSD analysis.

Fig. 4.1-8 (b) shows the FFT and PSD analysis results of the phase current with CFSI method. From the results, a peak existed around 400 Hz because of the signal injection, which conforms to the results of Eq.n 4.1-45. Compared to Fig. 4.1-5, a fixed frequency distortion around the injected signal existed, and the THD increased.

Fig. 4.1-9 shows the simulation results of the PRFSI, in which (a) shows the current distortion and (b) shows the harmonic analysis based on the FFT and PSD analysis. From (a), it could be found that the phase current was distortion because of the PRFSI, and the injected signal is hard to differentiate because of the two kinds of the signal is very close, which is 280 Hz and 350 Hz according to the selection method discussed in Chapter 4.1.5.

From Fig. 4.1-9 (b), it is obvious that the CFSI method features a discrete harmonic distribution, where the peak happens around 400 Hz. For the PRFSI, the peak disappears and features a continuous harmonic distribution, which is

consistent with the theoretical analysis. Furthermore, the THD of the two methods are almost same compared to the no signal injection simulations. The PRFSI method could eliminate the peak of the frequency distortion and transmit it to a continuous distribution, in which decrease the THD ratio simultaneously.

C. Selection of Signal Injection Frequency

In the following part, the frequency selection of the two injected frequency considering sampling effect and the possibility of the two frequencies will be analyzed. In the simulations, the sampling frequency of the current is 20 kHz.

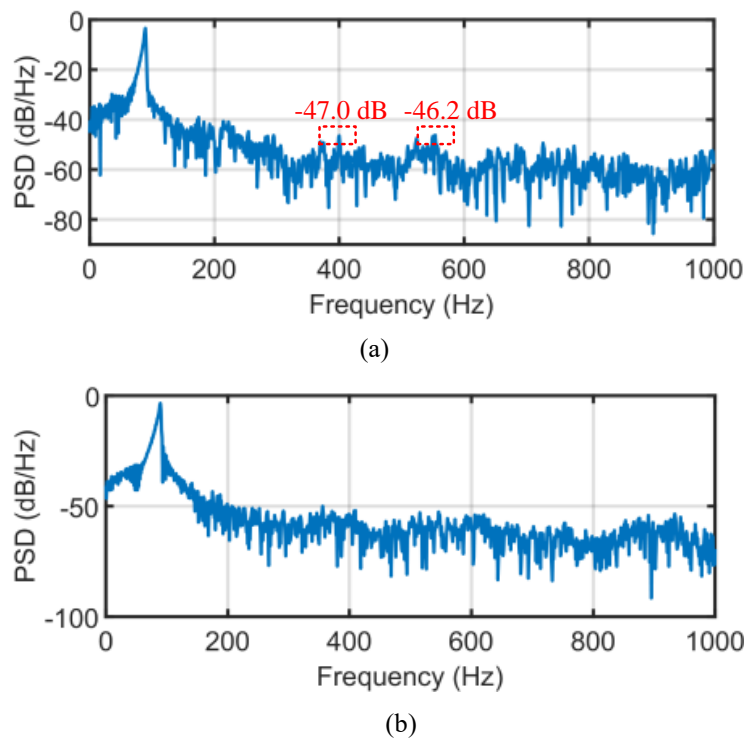


Fig. 4.1-10 PSD of different pair of frequencies selection (a) PRFSI method with frequency of multiplier; (b) PRFSI method with frequency of non-multiplier.

Fig. 4.1-10(a) shows the PRFSI method with frequency of multiplier and non-multiplier. In (a), the frequency was selected as 280 Hz and 350 Hz, which the frequency of the injected signal is non-multiplier of sampling frequency 20 kHz. In (b), the pair of frequency are selected as 250 Hz and 400 Hz, which is a multiplier of the sampling frequency. In (a), several peaks occur and were

labeled in the figure. This is because the frequency selection of the injected signal is a multiplier of the sampling frequency causing discrete harmonic distribution and harmonic peak as discussed in Chapter 4.1.5 and Chapter 4.1.6.

D. Possibilities Selection

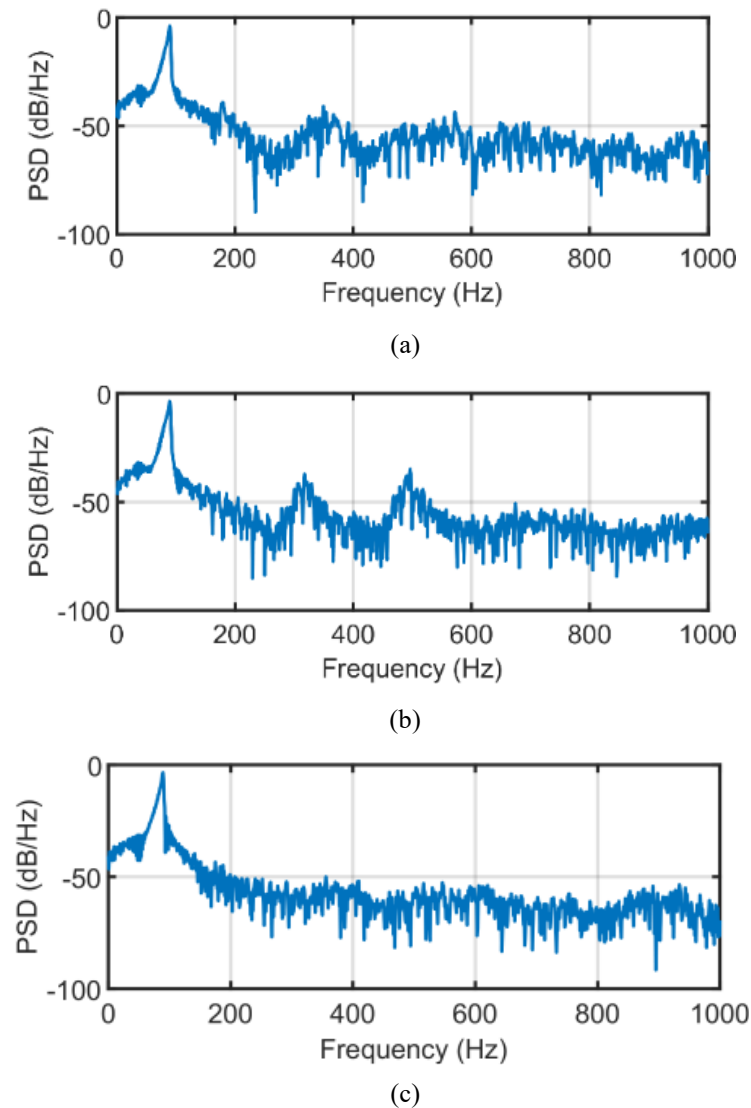
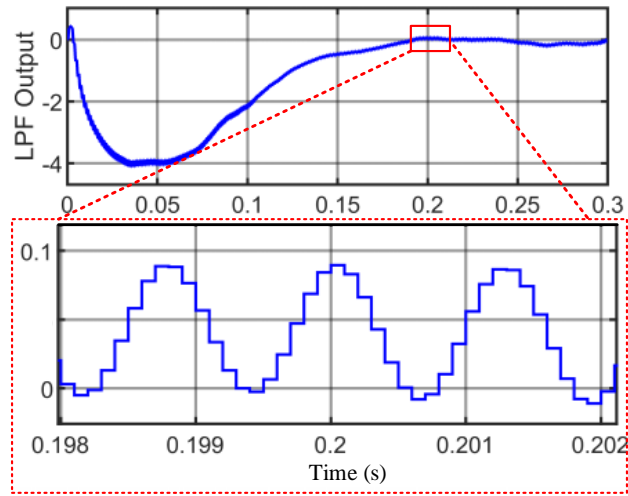


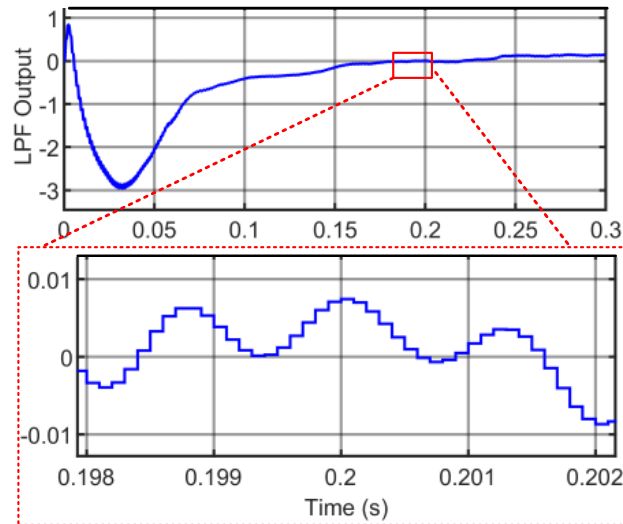
Fig. 4.1-11 Possibility selection of frequency for PRFSI (a) possibility of 0.1 for 350 Hz; (b) possibility of 0.1 for 280 Hz; (c) possibility of 0.5 for 350 Hz and 280Hz

The possibility of the signal selection will be discussed in this part. From the analysis in Chapter 4.1.5, the signal selection needs to be the non-multiplier of the sampling frequency. However, the possibility selection is equally important to have a better harmonic distribution and further improve the dynamic

response of the PMa-SynRMs.



(a)



(b)

Fig. 4.1-12 Output of the LPF under the rated load (a) output based on the CFSI method; (b) output based on the PRFSI.

Fig. 4.1-11 shows the PSD distribution in different possibility selection. For the possibility selection of 0.1 and 0.9 for 280 Hz injected signal, the peak existed. However, for the possibility of 0.5, the peak of the harmonic distribution disappears. To be more specific, the possibility of 0.5 means that the frequency of occurrence for 280 Hz and 350 Hz signal are equally same. In the following experiments, the frequency of PRFSI is selected as non-multiplier and 50% possibility.

4.1.8. Experiments Verification

A. Noise Suppression Ability Experiments

As discussed in Chapter 4.1.5, the PRFSI method features a continuous harmonic distribution compared to the CFSI method, this means that harmonic caused by the PRFSI method is easier to filter out compared to CFSI under the same cut frequency of the low pass filter described in Fig. 4.1-8 for the PMA-SynRMs control system. Under the same low pass filter, comparison experiments were performed under based on the CFSI method and PRFSI method. Fig. 4.1-12 shows the output of the LPF (Low-pass filter) under the rated load, where the MTPA angle is given as a constant to test the performance of the LPF.

Fig. 4.1-12 shows the output of the LPF under the rated load, from the comparison of (a) and (b), it could be found that the output of the LPF based on the PRFSI method contains less high frequency noise because of the continuous harmonic distribution and it is easier to filter out the high frequency noise. However, for the CFSI method, the harmonic noise suppression capability around 400 Hz is weakened than the high frequency noise for a LPF because of the LPF is generally selected around 50 Hz or even smaller to balance the dynamic response and noise immunity. And the noise suppression ability for high frequency noise is better than the noise around a relatively low frequency, which is around 400 Hz. In this way, the LPF with the PRFSI features a better performance compared to the CFSI method under the same cut-off frequency.

B. Experiments of Bandpass Filter Verification

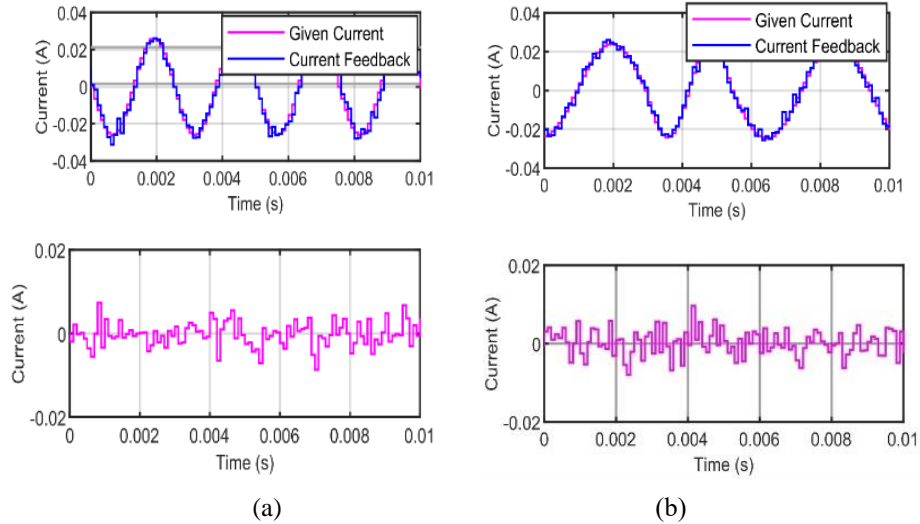


Fig. 4.1-13 High frequency current loop and tracking error of CFSI and PRFSI (a) tracking performance of CFSI; (b) tracking performance of PRFSI.

In the PRFSI, a specially designed bandpass filter was used to extract the output power for further MTPA angle control and high frequency current control. In this way, the performance of the bandpass filter directly decides the performance of the whole control system.

Fig. 4.1-13 shows the tracking performance of the BPF (Band-pass Filter) in the CFSI and adaptive BPF in the PRFSI method. Meanwhile, the error of the given current and the current feedback was given to do further explanation. From the error of the high frequency loop by using CFSI and PRFSI method, it could be learned that the error of the high frequency loop is in the same level. By using the adaptive BPF, the high frequency injected current could be tracked in a time manner.

C. Dynamic Response of CFSI and PRFSI

Rated Load Test:

To test the performance of the CFSI and PRFSI, the same cut-frequency of the LPF was adopted to further verify the anti-disturbance ability, dynamic

response, and steady-state error of the control system.

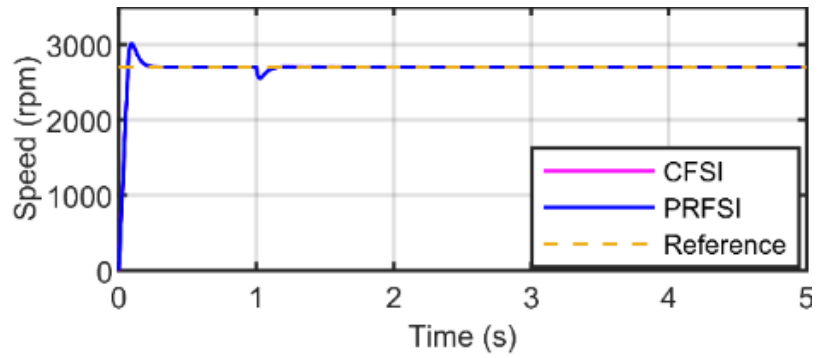


Fig. 4.1-14 Speed response of CFSI and PRFSI

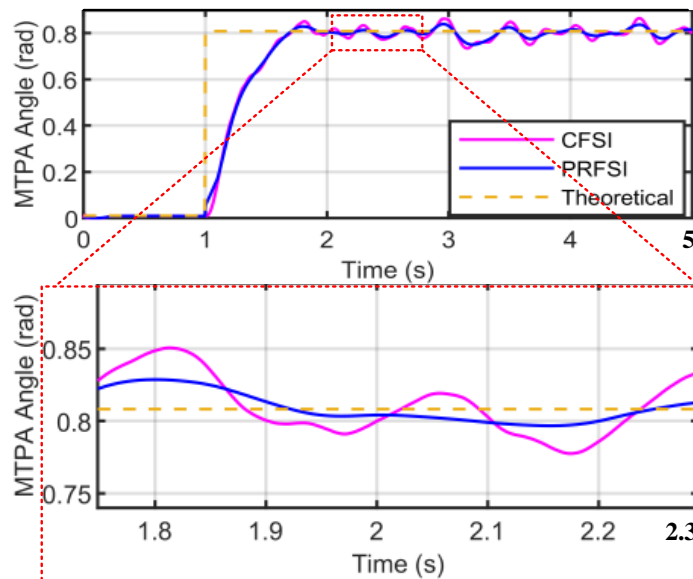


Fig. 4.1-15 Rated load current angle detection with CFSI and PRFSI

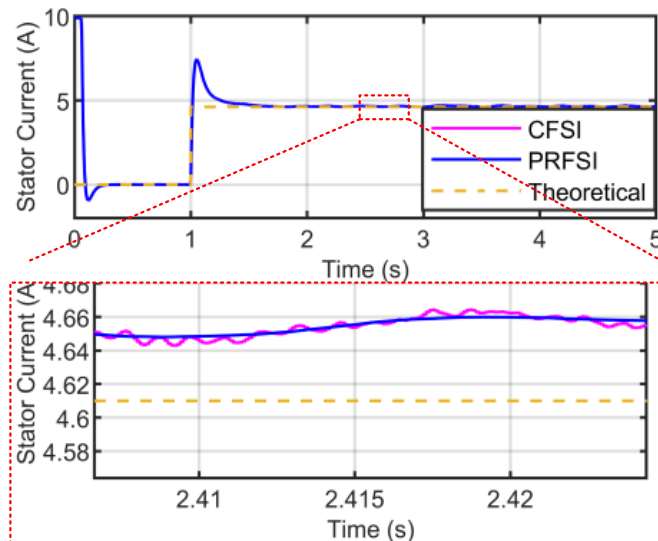


Fig. 4.1-16 Stator current with CFSI and PRFSI

Fig. 4.1-14 shows the response for the speed loop, which shows that almost

the same response could be obtained by adopting the two methods. Fig. 4.1-15 shows the detected current angle with CFSI and PRFSI. From the comparison simulations, the PRFSI part features a higher accurate detection angle results and a better dynamic response. Fig. 4.1-16. shows the theory current and detected current in the two methods, the PRFSI features a smaller stator current, which is more consistent with the theory value. From the experiments, PRFSI features a better dynamic response with higher accuracy.

4.2 Improved Precision Online MTPA Considering Magnet Flux Mismatch for Reduced Control Error

4.2.1. Error Analysis on the traditional method

According to Eq.n 4.1-1, Eq.n 4.2-1 and Eq.n 4.2-2 could be obtained:

$$\psi_{pm} - L_{qd}i_d = L_q i_q - \psi_q = L_q i_q + \frac{u_d - R_s i_d}{\omega_e} \quad \text{Eq.n 4.2-1}$$

$$(L_d - L_q)i_d + L_{dq}i_q = \frac{u_q - R_s i_q}{\omega_e} - L_q i_d \quad \text{Eq.n 4.2-2}$$

Substituting Eq.n 4.1-1, Eq.n 4.1-2 and Eq.n 1.3-5 into Eq.n 4.1-9 leads to Eq.n 4.2-3

$$T_{e1} = \frac{3}{2}p \left[\left(\frac{u_q - R_s i_q}{\omega_e i_d} - L_q \right) i_d i_q + \left(L_q i_q - \frac{u_d - R_s i_d}{\omega_e} \right) i_d \right] \quad \text{Eq.n 4.2-3}$$

The significance of Eq.n 4.2-3 is that only L_q is required for the output torque evaluation and calculation, which less parameters are needed compared to Eq.n 1.3-5.

The Eq.n 4.2-3 analyzes the situation where small angle signals were not injected. However, the injected signals expressed in Eq.n 4.1-12 and Eq.n 4.1-13 must be evaluated, in which Eq.n 4.2-4 could be obtained.

$$T_{eh} = \frac{3}{2}p \left[\left(\frac{u_q - R_s i_q}{\omega_e i_d} - L_q \right) i_{dh} i_{qh} + \left(L_q i_q + \frac{u_d - R_s i_d}{\omega_e} \right) i_{dh} \right] \quad \text{Eq.n 4.2-4}$$

To simplify the calculation process, Eq.n 4.2-3 could be simplified as Eq.n 4.2-5.

$$T_{e1} = \frac{3}{2}p \left[(a_1 + a_2 i_d) i_d + (b_1 + b_2 \frac{i_q}{i_d}) i_d i_q \right] \quad \text{Eq.n 4.2-5}$$

where, $a_1 = \psi_{pm}$; $a_2 = -L_{qd}$; $b_1 = L_d - L_q$; $b_2 = L_{dq}$.

According to Eq.n 4.2-4, Eq.n 4.2-6 could be obtained.

$$T_{eh} = \frac{3}{2}p \left[\frac{u_d - R_s i_d}{\omega_e} + L_q (i_q - i_{qh}) + \frac{u_q - R_s i_q}{\omega_e i_d} i_{qh} \right] i_{dh} \quad \text{Eq.n 4.2-6}$$

Assuming that $i_q \approx i_{qh}$, $L_q (i_q - i_{qh})$ could be ignored and Eq.n 4.2-7

could be get:

$$T_{eh} \approx \frac{3}{2}p \left[\frac{u_d - R_s i_d}{\omega_e} + \frac{u_q - R_s i_q}{\omega_e i_d} i_{qh} \right] i_{dh} \quad \text{Eq.n 4.2-7}$$

Simplify Eq.n 4.2-7, we get:

$$T_{eh} \approx \frac{3}{2}p \left[-c i_{dh} + (d_1 + d_2 \frac{i_q}{i_d}) i_{dh} i_{qh} \right] \quad \text{Eq.n 4.2-8}$$

where, $c = -(L_q i_q - a_2 i_d (i_{qh}/i_q) - a_1)$, and $d_1 = L_d$; $d_2 = b_2 = L_{dq}$

In Eq.n 4.1-11, the deviation of the torque to angle is considered, while this part was not considered in the MTPA online detection part.

According to Eq.n 4.2-3 and Eq.n 4.2-5, Eq.n 4.2-9 and Eq.n 4.2-10 could be obtained:

$$\frac{\partial T_{e1}}{\partial \theta} = \frac{3}{2}p [-a i_s \sin \theta + b i_s^2 \cos 2\theta] \quad \text{Eq.n 4.2-9}$$

$$\frac{\partial T_{eh}}{\partial \theta} = \frac{3}{2}p [-\psi_{pm} i_s \sin \theta + (L_d - L_q) i_s^2 \cos 2\theta + (L_{dq} + L_{dq}) i_s^2 \sin 2\theta] \quad \text{Eq.n 4.2-10}$$

Eq.n 4.2-9 and Eq.n 4.2-10 describes the situation that the online MTPA control strategy where the injected signals were not considered. However, the influence of the injected signal needs to be considered. Eq.n 4.2-11 and Eq.n 4.2-12 describe the derivation of torque with respect to angle where the injected

angle was considered.

$$\frac{\partial T_{eh}}{\partial \theta} = \frac{3}{2} p [-a_1 i_s \sin \theta + b_1 i_s^2 \cos 2\theta + (b_2 - a_2) i_s^2 \sin 2\theta - L_{qd} i_d^2 - L_{qd} i_d^3 / i_q] \quad \text{Eq.n 4.2-11}$$

$$\frac{\partial T_{eh}}{\partial \theta} = \frac{3}{2} p [-\psi_{pm} i_s \sin \theta + (L_d - L_q) i_s^2 \cos 2\theta + (L_{dq} + L_{dq}) i_s^2 \sin 2\theta + (L_{dq} + L_{dq}) i_s^2 \sin 2\theta - L_{qd} i_d^2 - L_{qd} i_d^3 / i_q] \quad \text{Eq.n 4.2-12}$$

It is obvious that an error existed in the proposed online signal injection based MTPA control strategy. In the following part, this error will be analyzed and compensated. Eq.n 4.2-13 describes the error where the injected signal was not considered while Eq.n 4.2-14 depicts the situation in the real signal injection process.

$$\begin{aligned} error_L &= \frac{\partial T_e}{\partial \theta} - \frac{\partial T_{e1}}{\partial \theta} \\ &= \frac{3}{2} p i_s \left(\left(\frac{\partial L_d}{\partial \theta} - \frac{\partial L_q}{\partial \theta} \right) i_s \frac{1}{2} \sin 2\theta - \frac{\partial \psi_{pm}}{\partial \theta} \cos \theta - \frac{\partial L_{dq}}{2 \partial \theta} i_s \cos 2\theta - \frac{\partial L_{qd}}{2 \partial \theta} i_s \cos 2\theta \right) \quad \text{Eq.n 4.2-13} \end{aligned}$$

$$\begin{aligned} error_h &= \frac{\partial T_e}{\partial \theta} - \frac{\partial T_{eh}}{\partial \theta} \\ &= \frac{3}{2} p i_s \left(\left(\frac{\partial L_d}{\partial \theta} - \frac{\partial L_q}{\partial \theta} \right) i_s \frac{1}{2} \sin 2\theta - \frac{\partial \psi_{pm}}{\partial \theta} \cos \theta - \frac{\partial L_{dq}}{2 \partial \theta} i_s \cos 2\theta - \frac{\partial L_{qd}}{2 \partial \theta} i_s \cos 2\theta - L_q i_d^2 - \frac{L_{qd} i_d^3}{i_q} \right) \quad \text{Eq.n 4.2-14} \end{aligned}$$

4.2.2. Error Compensation Method

From Eq.n 4.2-13 and Eq.n 4.2-14, an error existed with the proposed signal injection method. It is hard to calculate the error directly because it is not easy

to calculate the differential part and the parameters are unknown. Since $\partial T_{eh}/\partial\theta$ comes from T_{eh} , it can be observed that the mechanism of the signal processing from T_{eh} to T_o is a derivative operation, where T_{eh} to T_o could be calculated in Fig. 4.2.1 using the relationship between power and torque. Likewise, the error present in equation Eq.n 4.2-14 can be derived by computing the derivative of an additional function relative to the electrical phase angle. Consequently, this thesis introduces a novel error formulation predicated on the construction of an underlying function associated with the error inherent in equation Eq.n 4.2-14. The resultant mathematical expression is presented as Eq.n 4.2-15:

$$T_{error} = \frac{3}{2}p[-\psi_{pm}i_d - L_q i_d i_{qh} - L_{qd}i_d^2 + L_d i_d i_q + L_{dq}i_q^2] \quad \text{Eq.n 4.2-15}$$

where

$$-\frac{\partial\psi_{pm}}{\partial\theta}i_d = -(\partial\psi_{pm}i_d)'|_{\theta} \quad \text{Eq.n 4.2-16}$$

$$-\frac{\partial L_q}{\partial\theta}i_d i_q - L_q i_d^2 - \frac{\partial L_{qd}}{2}i_s^2 - \frac{\partial L_{qd}}{2\partial\theta}i_s^2 \cos 2\theta - \frac{L_{qd}i_d^3}{i_q} \quad \text{Eq.n 4.2-17}$$

$$= (-L_q i_d i_{qh} - L_{qd}i_d^2)'|_{\theta}$$

$$\frac{\partial L_d}{\partial\theta}i_d i_q + \frac{\partial L_{dq}}{2}i_s^2 - \frac{\partial L_{dq}}{2\partial\theta}i_s^2 \cos 2\theta = (L_d i_d i_q + L_{dq}i_q^2)'|_{\theta} \quad \text{Eq.n 4.2-18}$$

In Eq.n 4.2-15, a new compensation equation was proposed and used to compensate the error caused by the MTPA signal injection method. However, the information of the machine including d - and q -axis inductance and magnet flux need to be known to calculate this part. To solve the problem, Eq.n 4.2-19 could be obtained according to Eq.n 4.1-1 and Eq.n 4.2-15.

$$T_{error} = \frac{3}{2}p[-\psi_{pm}i_q + \frac{u_q - R_s i_q}{\omega_e}i_q - \frac{u_d - R_s i_d}{\omega_e i_q} - \frac{\psi_{pm}i_d i_{qh}}{i_q}] \quad \text{Eq.n 4.2-19}$$

In Eq.n 4.2-19, only resistor of the machine and magnet flux are needed to

get the torque error, in which resistor is easily obtained and considered to be temperature independent in the controlling process. As for the magnet flux, the variation could be observed from Fig. 1.3-4. The variation of the flux varies about 10% because of the cross saturation of the PMA-SynRM and it cannot be neglected. From Eq.n 4.2-19, the error could be compensated if the magnet flux is obtained. To solve the problem, the magnet of flux will be analyzed and fitted in Chapter 4.2.3.

4.2.3. Magnet Flux Modelling and Overall Control

Fig. 4.2-1 shows the overall control diagram of the system. In the first step, the magnet flux of the machine was obtained from the fitted polynomial. Next, the error of the torque was obtained from Eq.n 4.2-19. After that, the torque was translated in the form of the power and this part was compensated to the MTPA detection part. The error was calculated and compensated to the control system compared to the convention control. Meanwhile, the variation of the magnet flux is considered and fitted to get a better control performance.

As shown in Fig. 1.3-3, three sets of 31×31 flux linkage data are obtained from the FEA software. To solve the mentioned problem, the magnet flux needs to be further learned and modelled. As shown in Fig. 1.3-3(c), the magnet flux will be influenced by the d -axis current because of the cross saturation of the magnet. Meanwhile, the q -axis current has little influence on the magnet flux. So, the magnet flux linkage could be fitted as a polynomial and the accuracy will be more accurate with the increasing of the order. However, the calculation will be more complicated. To balance the calculation time and accuracy, the magnet

flux could be expressed as Eq.n 4.2-20.

$$\hat{\psi}_{pm} = p_0 + p_1 i_d + p_2 i_d^2 + p_3 i_d^3 + p_4 i_d^4 \quad \text{Eq.n 4.2-20}$$

In real applications, 31×31 flux linkage data is not always acceptable. To address this issue, only two sets of data are needed to get a satisfactory polynomial function for the proposed fitting method. This data could be obtained from the experiments using the method from Chapter 2. To get the parameters of the polynomial, the LSM is used Chapter 2. Meanwhile, two sets of data are used to get the polynomial and error analysis is carried out as shown in Fig. 4.2-2.

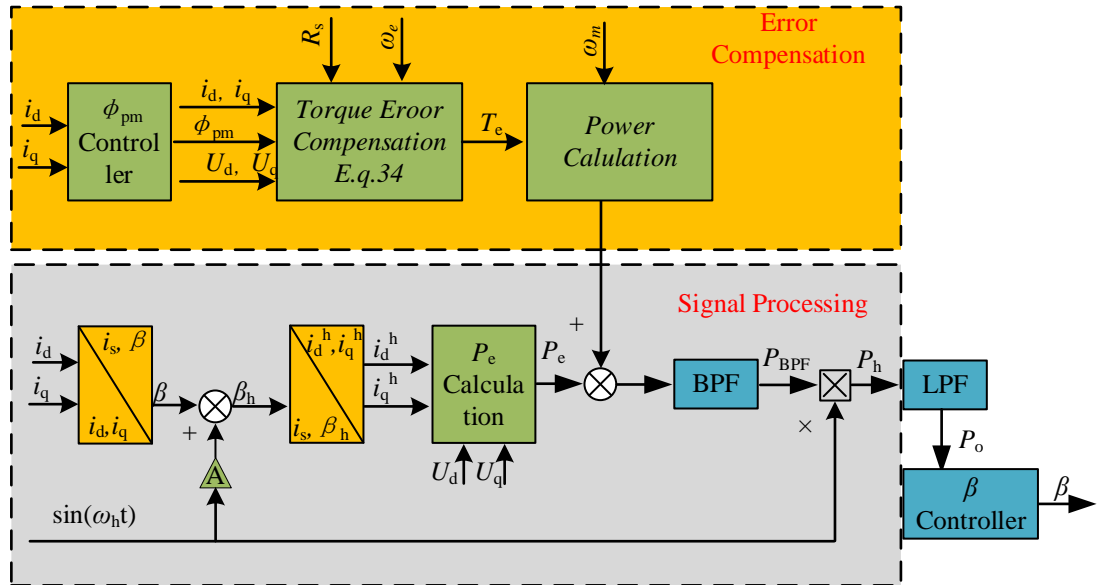


Fig. 4.2-1 Overall control diagram of error compensation method

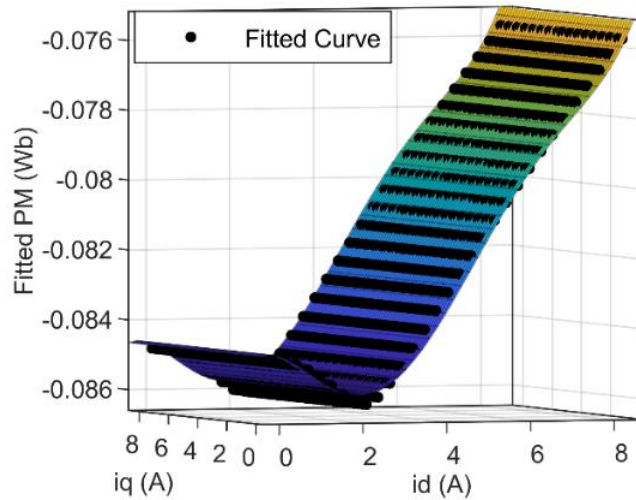


Fig. 4.2-2 Error analysis of the proposed polynomial function

From analysis, the average errors are 1.2% for the magnate flux which is smaller than the variation of the magnate flux and is satisfied to describe the variation of magnate flux in the changing of working condition.

4.2.4. Experiments Verification

Table 4.2-1 PMA-SynRM Signal Injection Parameters

Specification	Value
Injection Signal Frequency	400 Hz
Amplitude of Injected Current	0.05 Times Current
Sampling Frequency	4 kHz
LPF Cutoff Frequency	50 Hz
BPF Cutoff Frequency	400 Hz

The reason for selecting the BPF cutoff frequency in 400Hz is that the frequency should be higher than the LPF filter and the calculation ability of the controller should be taken into account. In this experimental part, the objective is to monitor the MTPA characteristics as the speed of the PMA-SynRM is maintained at 2700 rpm, while the command torque is incrementally adjusted from 0 to 1.9 Nm steps of 0.2 Nm. Fig. 4.2-3 delineates the MTPA locus obtained experimentally. This figure juxtaposes the tracking outcomes of the original signal injection method and the proposed error compensation method.

For the generation of these curves, the data acquisition protocol stipulates that the PMA-SynRM, subjected to two distinct tracking methodologies, operates at steady-state conditions. The MTPA locus points are derived from the mean values of the measured currents at these operating points. A notable observation is the significant variance in the magnitude of currents required by the standard signal injection method and its compensated counterpart. A comparative analysis of these two tracking methodologies is presented in Table 4.2-2. The

optimization rate is defined as Eq.n 4.2-21 to evaluate the improvements performance of the proposed control strategy.

$$r_{-} = \frac{i_s(\text{ original}) - i_s(\text{ proposed method})}{I_s(\text{ original})} 100\%. \quad \text{Eq.n 4.2-21}$$

Table 4.2-2 Comparison between original signal injection method and the proposed compensation method

Torque (Nm)	Original Current (A)	Compensation Optimization Current (A)	Rate
0.2	0.7457	0.7438	0.25%
0.4	1.3593	1.3559	0.01%
0.6	1.8791	1.8744	0.13%
0.8	2.3138	2.3080	0.43%
1.0	2.7706	2.7637	0.62%
1.2	3.1845	3.1765	0.81%
1.4	3.5931	3.5841	1.06%
1.6	4.0026	3.9926	1.22%
1.8	4.4131	4.4021	1.42%
1.9	4.6133	4.6018	1.53%

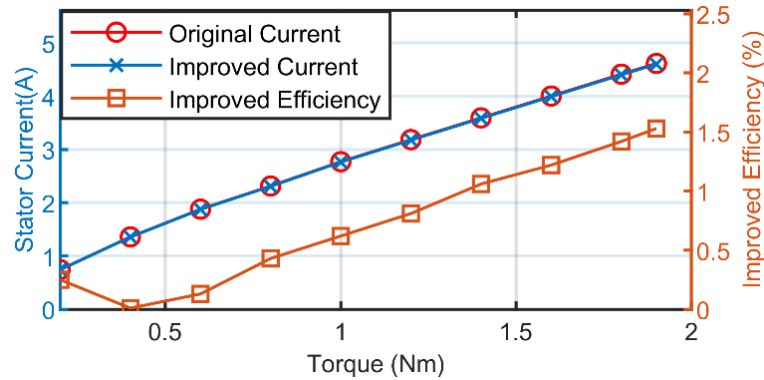
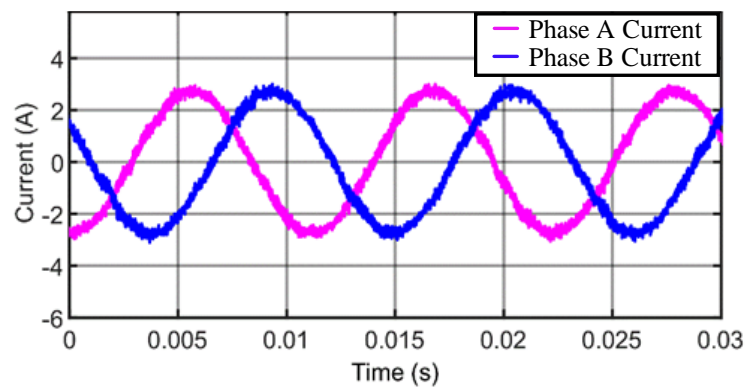


Fig. 4.2-3 Performance of the proposed supplementation control strategy

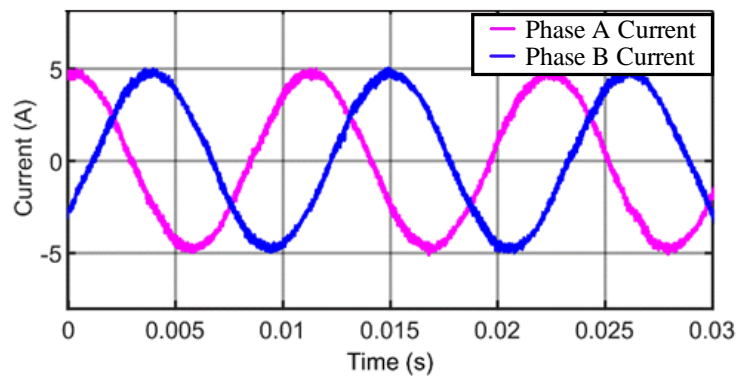
Table 4.2-2 and Fig. 4.2-3 shows the experiments results of the proposed supplementation control strategy compared to the original one. The improved efficiency in the resultant current amplitude between the original model and the new proposed supplementary method, as defined in Eq.n 4.2-21, is clear. The proposed method features a smaller current amplitude in the same working condition, thereby the efficacy was improved. Notably, the improvement is most

significant when the torques are elevated, achieving an optimization rate as high as 1.53%.

In the test experiments process, the three-phase current is measured from both the oscilloscope and the power analyzer. Fig. 4.2-4 shows the phase current of the rated working condition and half-rated working condition, in which it could be observed that it reaches the steady state working condition and the magnitude of the current remains unchanged in a limited time.



(a)



(b)

Fig. 4.2-4 Phase current with the proposed MTPA detection method (a) half-rated load working condition; (b) rated load working condition.

The experiments show that the half-rated current and the rated current is around 2.3 A and 4.9A, respectively, which is consistent with theoretical analysis. Meanwhile, the phase angle between phase A and phase B is around 120 degrees, which verified the feasibility of the control strategy.

A. Analysis on the Influence of the temperature

To ascertain the impact of resistance fluctuations attributable to thermal variations, experimental investigations were conducted under two distinct thermal regimes: a 'cold' temperature setting, typically operational for durations less than one minute, and a 'hot' temperature condition, with operational spans exceeding fifteen minutes. The 'cold' temperature scenario typically denotes a lower winding temperature, approximately 25°C, representing the initial or ambient state of the windings. Conversely, the 'hot' temperature scenario corresponds to an elevated winding temperature, contingent upon the design parameters of the machinery. This higher temperature, usually in the vicinity of 85°C, is observed under conditions of thermal equilibrium [127].

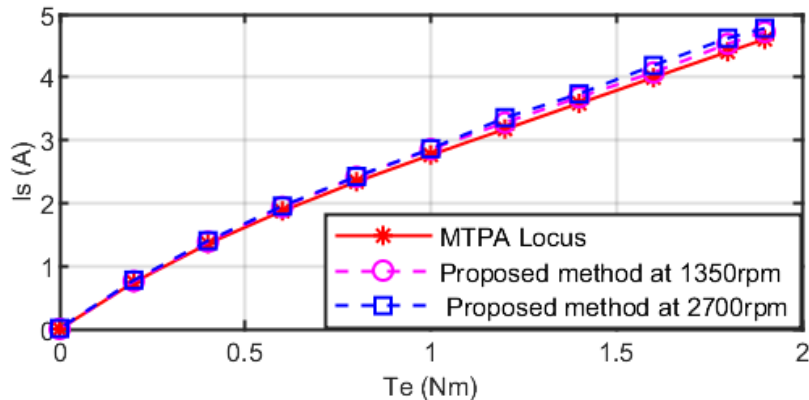


Fig. 4.2-5 Proposed MTPA method in cold machine condition

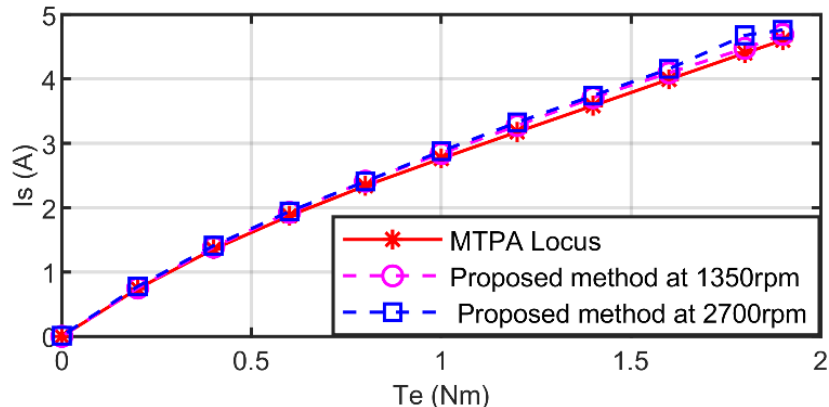


Fig. 4.2-6 Proposed MTPA method in hot machine condition

Fig. 4.2-5 shows the theoretical value of the MTPA and the MTPA locus

determined by the proposed control method in 1350 rpm and 2700rpm under the cold machine conditions and Fig. 4.2-6 shows the MTPA locus in hot machine conditions.

In the comparative analyses presented in Fig. 4.2-5 and Fig. 4.2-6, which assess different operational scenarios, it is observed that the MTPA operating point ascertained through the proposed methodology exhibits negligible deviation. This minimal variation is attributed to the gradual nature of resistance change, allowing for its consideration as a quasi-constant within a confined temporal scope.

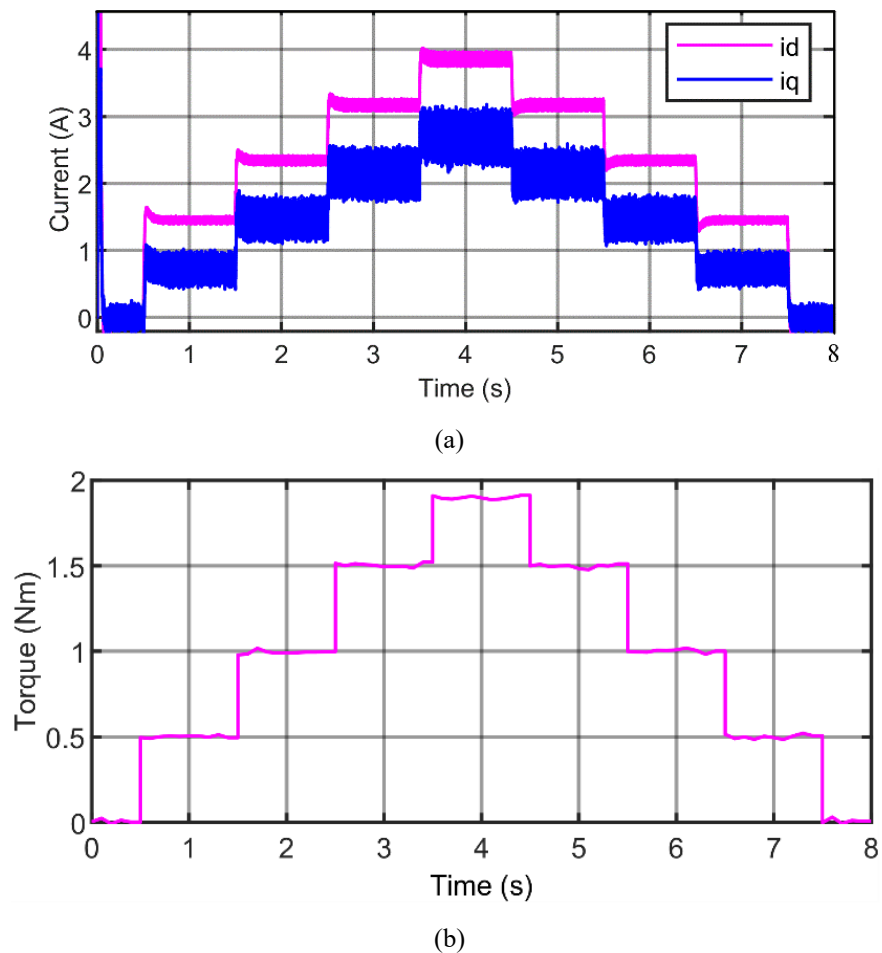


Fig. 4.2-7 d - and q -axis current under the whole working condition (a) d - and q -axis feedback current; (b) given torque.

These experimental outcomes substantiate the resilience of the proposed

method to fluctuations in resistance, underscoring its robustness in varying operational conditions. Meanwhile, it could be observed that the stator current in 1350 rpm and 2700 rpm is not perfect match in the experiments. This is mainly due to the following reasons: a) the designed low pass filter features different performance in different frequencies for the current, which leads to a different control sensibility for different speed; b) the iron loss is not the same in different speed, which was not considered in this thesis [128]. The reason for the large q-axis ripple is due to the large variation in the inductance.

B. Performance of the MTPA tracking

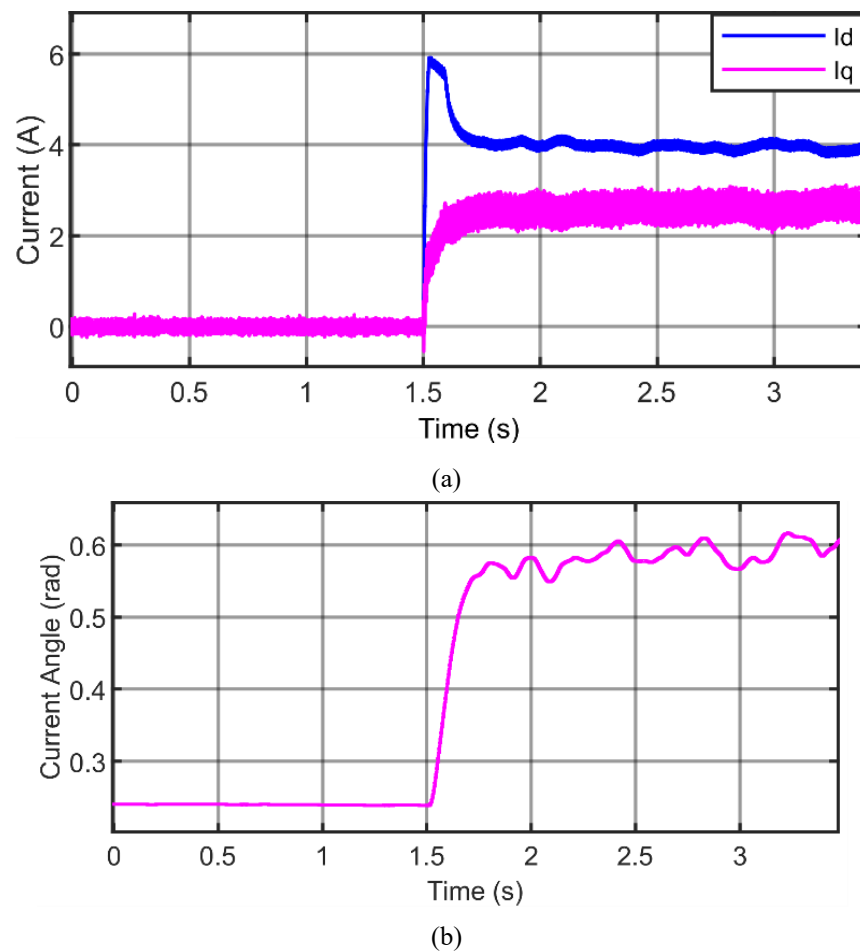
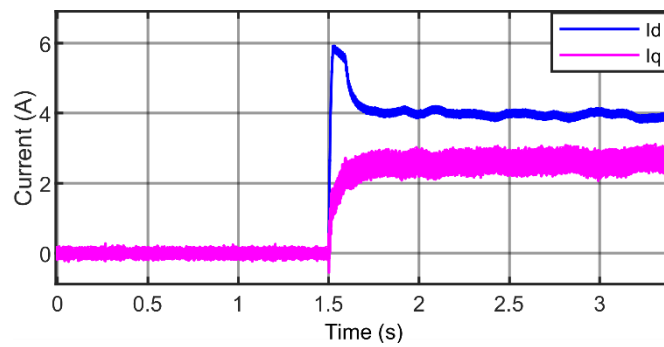


Fig. 4.2-8 Step load from 0 Nm– 1.9 Nm. (a) d- and q-axis current response; (b) current control angle response

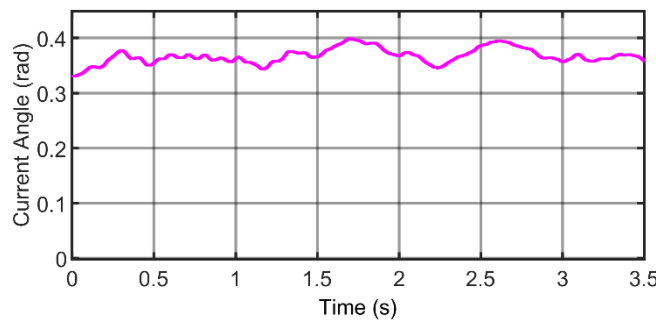
Fig. 4.2-7 shows the load disturbance from 0 Nm to 1.9 Nm and 1.9 Nm to

0 Nm with a step load every second at 2700 rpm. Fig. 4.2-7 (a) shows the feedback of the d - and q -axis current while Fig. 4.2-7 (b) shows the given torque. The proposed control strategy could be converged in a limited time. Generally, it depends on the speed loop and current loop, the PI controller was specially designed, and 0.5 s convergence time could be achieved [129].

In Fig. 4.2-8, the MTPA angle reaches stability within 0.5 seconds, and it fluctuates around 0.58 rads because the functions of the low pass filter. It should be noticed that the convergence process only influences the efficiency of the machine but not influence the stability of the machine.



(a)



(b)

Fig. 4.2-9 Step speed reference variation from 1350 rpm to 2700 rpm. (a) d - and q -axis current feedback; (b) current angle variation

Fig. 4.2-7 shows that the proposed MTPA tracking method tracks the MTPA working points well. Fig. 4.2-8 (a) shows the step load from 0 Nm to 1.9 Nm at 2700 rpm and the feedback of the d - and q -axis current with the current control

angle. It could be observed that the current control angle gets to a steady state in a limited time. This verifies the feasibility of the proposed control strategy. Fig. 4.2-8 (b) shows the current control angle in the step load process. With the increasing of the torque, the current control angle increases to meet MTPA requirements.

In Fig. 4.2-8, the control system's stability is marginally affected[72], as the current angle predominantly impacts the steady-state d - and q -axis currents. This observation underscores the robustness of the proposed control strategy, capable of achieving stability within half a second in response to step torque variations.

In Fig. 4.2-9, it could be found that the control angle for the no load condition is around 0.3 rads. This is because the current amplitude in no load condition is very small, which is 0 A considering no damping situation. In this way, the current angle has no and little influence on the theoretical analysis and experiments, which is consistent with theoretical analysis.

Fig. 4.2-9(a) illustrates the transition of the speed reference from 1350 rpm to 2700 rpm under a half-rated load, alongside the corresponding feedback of the d - and q -axis. Concurrently, Fig. 4.2-9(b) depicts the evolution of the current control angle during this process. It is evident that the d - and q -axis current loops stabilize within 0.05 seconds, even though the current angle requires more than 1 second to reach a stable condition. This implies that the currents exhibit minimal variation despite the fluctuating current angle throughout the process. Empirical evidence from these experiments confirms that both the current control loop and the current angle control loop achieve stability within a

predetermined timeframe, thereby validating the effectiveness of the proposed control strategy.

The experimental setup under investigation utilizes a small power PMSynRM as its controlled object. It is important to note that the applicability of the proposed control methodology remains consistent irrespective of the motor's power rating, whether high or low. In the context of larger motors, a notable characteristic is the increased magnitude of the stator current. The absence of real signal injection into the stator currents allows the proposed approach to precisely track the MTPA points, concurrently facilitating a reduction in the stator current's amplitude.

Furthermore, the proposed method's efficacy and robustness are unaffected by the motor's power rating, whether low or high, particularly in the signal injection and error compensation stages. These stages maintain their processing efficiency regardless of the motor's power. Consequently, the proposed strategy demonstrates commendable robustness and effectiveness. Future research endeavors will focus on reducing the reliability of the magnet flux information and extending this methodology to high power motors, exploring its applicability and potential refinements in such contexts.

4.3 SLC Based MTPA Online Control for Better Dynamic Performance

4.3.1. Methodology of Proposed Online Detection

The objective of MTPA control is to maximize T_e with the current limit. When the inductance variation, magnetic saturation, cross-saturation effect is considered, additional terms will be introduced into Eq.n 4.1-1 and the steady-

state model considering this effect can be denoted as Eq.n 4.3-1 and Eq.n 4.3-2.

$$\begin{aligned} u_d &= Ri_d - \omega_e(L_q i_q - \psi_{pm} + L_{qd} i_d + \Delta L_q i_q) \\ u_q &= Ri_q + \omega_e(L_d i_d + L_{dq} i_q + \Delta L_d i_d) \end{aligned} \quad \text{Eq.n 4.3-1}$$

$$\begin{aligned} T_e &= \frac{3p}{2} [\psi_{pm} i_d + (L_d - L_q) i_d i_q + L_{dq} i_q i_q - L_{qd} i_d i_d \\ &\quad + (\Delta L_d - \Delta L_q) i_d i_q] \end{aligned} \quad \text{Eq.n 4.3-2}$$

where L_{dq} and L_{qd} represent the cross-saturation inductances between the d -axis and the q -axis; ΔL_d and ΔL_q represent the inductance variation caused by the d - and q -axis flux saturation.

The first equation in Eq.n 4.3-1 multiplied by i_d is Eq.n 4.3-3 and the second one multiplied by i_q is Eq.n 4.3-4.

$$u_d i_d = Ri_d^2 - \omega_e i_d (L_q i_q - \varphi_{PM} + L_{qd} i_d + \Delta L_q i_q) \quad \text{Eq.n 4.3-3}$$

$$u_q i_q = Ri_q^2 + \omega_e i_q (L_d i_d + L_{dq} i_q + \Delta L_d i_d) \quad \text{Eq.n 4.3-4}$$

The sum of Eq.n 4.3-3 and Eq.n 4.3-4 is:

$$\begin{aligned} u_d i_d + u_q i_q - R(i_d^2 + i_q^2) &= \omega_e (i_q (L_d i_d + L_{dq} i_q + \Delta L_d i_d) \\ &\quad - i_d (L_q i_q - \varphi_{PM} + L_{qd} i_d + \Delta L_q i_q)) \end{aligned} \quad \text{Eq.n 4.3-5}$$

Substituting Eq.n 4.3-2 into Eq.n 4.3-5 , the result is

$$\frac{2}{3} \omega_m T_e = u_d i_s \cos\theta + u_q i_s \sin\theta - Ri_s^2 \quad \text{Eq.n 4.3-6}$$

where ω_m is the mechanical speed and $\omega_e = p\omega_m$.

Based on Eq.n 4.3-6 $g(\theta)$ can be denoted as

$$g(\theta) = \frac{3 u_d i_s \cos\theta + u_q i_s \sin\theta}{\omega_m i_s} - \frac{3R}{2\omega_m} \quad \text{Eq.n 4.3-7}$$

In Eq.n 4.3-7, $1.5R/\omega_m$ is independent of θ . MTPA control is performed in a short period, during which the change of R is negligible. Also, motor speed is independent of θ . Hence, maximizing $g(\theta)$ is equivalent to maximizing the first term on the right-hand side of Eq.n 4.3-8. Hence, MTPA is obtained by solving

$$\max_{\theta} \frac{u_d \cos\theta + u_q \sin\theta}{\omega_m i_s} \quad \text{Eq.n 4.3-8}$$

In this part, capital letters U , I , and Ω are used to denote the DC values of the voltage, current, and speed, respectively. Eq.n 4.3-8 can be rewritten by using the DC values as

$$\max_{\theta} \frac{U_d \cos\theta + U_q \sin\theta}{\Omega_m I_s} \quad \text{Eq.n 4.3-9}$$

In a PMA-SynRM drive, the voltage, current, and speed are available, and thus, θ_{MTPA} can be detected from Eq.n 4.3-9 by using an optimization algorithm, such as gradient descent algorithm.

The reference voltages from the outputs of the PI controllers are often employed for machine parameter estimation. Due to inverter nonlinearity, the reference voltages are unequal to the actual one, but their relation can be modeled as:

$$U_d^* = U_d + V_d, U_q^* = U_q + V_q \quad \text{Eq.n 4.3-10}$$

where U_d^* and U_q^* are the reference d - and q -axis voltages from the PI controllers and V_d and V_q are the voltages imposed on d - and q -axis due to deadtime, which are obtained by applying the Park transformation to the distorted voltages in the abc -frame. V_d and V_q are functions of V dead defined as Eq.n 4.3-11:

$$\begin{aligned} V_d &= \frac{V_{\text{dead}}}{N} \sum_{k=1}^N 2\cos \left[\theta_b - \text{int} \left\{ 3 \left(\theta_b + \theta + \frac{\pi}{6} \right) / \pi \right\} \times \frac{\pi}{3} \right] \\ V_q &= \frac{V_{\text{dead}}}{N} \sum_{k=1}^N 2\sin \left[\theta_b - \text{int} \left\{ 3 \left(\theta_b + \theta + \frac{\pi}{6} \right) / \pi \right\} \times \frac{\pi}{3} \right] \end{aligned} \quad \text{Eq.n 4.3-11}$$

where V_{dead} is the distorted voltage term that is dependent on the deadtime. Once the deadtime is set, V_{dead} will be constant. V_d increases with the increase of θ , while V_q decreases with the increase of θ .

Substituting Eq.n 4.3-11 into Eq.n 4.3-10 θ_{MTPA} is obtained by solving

$$\max_{\theta} \frac{(U_d^* - V_d) \cos \theta + (U_q^* - V_q) \sin \theta}{\Omega_m I_s} \quad \text{Eq.n 4.3-12}$$

Hence, θ_{MTPA} can be obtained by maximizing

$$g_{\text{MTPSA}}(\theta) = \frac{(U_d^* - V_d) \cos \theta + (U_q^* - V_q) \sin \theta}{\Omega_m I_s} \quad \text{Eq.n 4.3-13}$$

In Eq.n 4.3-13, $g_{\text{MTPA}}(\theta)$ can be calculated from the measurements. A gradient descent algorithm will be employed to find θ_{MTPA} to maximize $g_{\text{MTPA}}(\theta)$ in Chapter 4.3.2

4.3.2. Analysis of the Proposed Method

The overall control scheme was shown in Fig. 4.3-1.

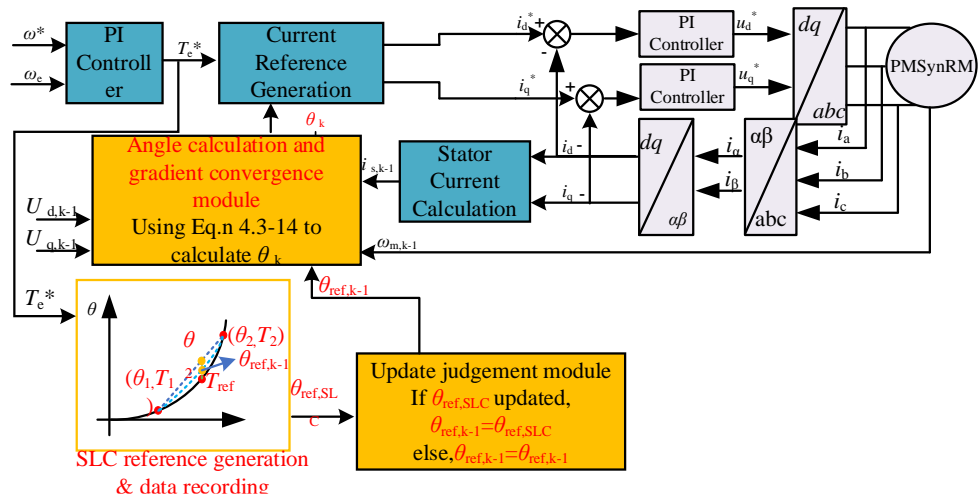


Fig. 4.3-1 Overall control diagram of Online Tracking method

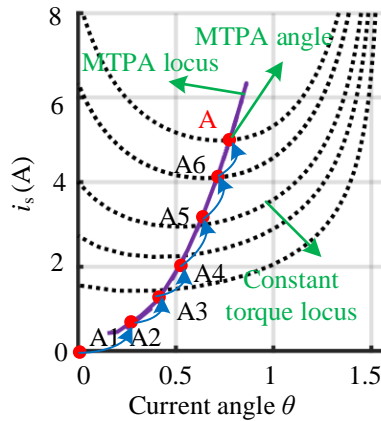


Fig. 4.3-2 Principal diagram of gradient descent algorithm

$g_{\text{MTPA}}(\theta)$ in Eq.n 4.3-14 increases at first and then decreases as θ increases from 0° to 90° . Hence, the gradient descent algorithm is employed to maximize

$g_{\text{MTPA}}(\theta)$ and then to find θ_{MTPA} . Specifically, θ_{MTPA} is detected iteratively until θ converges to θ_{MTPA} . At time $k+1$, the current angle is updated based on the current angle at time k and the gradient of $g_{\text{MTPA}}(\theta)$. Let θ_{k-1} , θ_k , and θ_{k+1} be the current angle at time $k-1$, k , and $k+1$ during detection of θ_{MTPA} , respectively. At time $k + 1$, θ_{k+1} is updated by using Eq.n 4.3-14.

$$\begin{aligned} \theta_{k+1} &= \theta_k + \alpha \frac{\partial g_{\text{MTPA}}(\theta)}{\partial \theta} \\ &= \theta_k + \alpha \frac{(U_{d,k}^* - V_{d,k}) \cos \theta_k + (U_{q,k}^* - V_{q,k}) \sin \theta_k}{I_{s,k} \Omega_{m,k}} \\ &= \theta_k + \alpha \frac{(U_{d,k-1}^* - V_{d,k-1}) \cos \theta_{k-1} + (U_{q,k-1}^* - V_{q,k-1}) \sin \theta_{k-1}}{I_{s,k-1} \Omega_{m,k-1}} \frac{\theta_k - \theta_{k-1}}{\theta_k - \theta_{k-1}} \end{aligned} \quad \text{Eq.n 4.3-14}$$

where the subscript k denotes time instance and α is the weight of the gradient descent algorithm controlling the convergence speed. The gradient descent algorithm keeps updating θ using Eq.n 4.3-14 until θ_{MTPA} is detected. The rule to determine whether θ_{MTPA} is detected or not is defined as

$$|\theta_{k+1} - \theta_k| < \varepsilon \quad \text{Eq.n 4.3-15}$$

that is, the update of θ from time k to $k + 1$ is smaller than the predefined small value ε . In the Eq.n 4.3-14, the convergence rate will be analyzed.

The gradient descent method calculates the process of the control algorithm in the direction of the steepest descent, enabling the control system to meet the control requirements within a short period. The principle of the gradient descent algorithm is illustrated in Fig. 4.3-2. Within the gradient descent algorithm, the minimal value point of the given objective function $g(\theta)$ is attained by moving in the direction opposite to the gradient, relative to the magnitude of the gradient, as indicated by Eq.n 4.3-16. For the iterative starting point, 0° is selected. This choice is made because, at this starting point, the PMA-SynRM can start

smoothly, and 0° can provide sufficient electromagnetic torque regardless of the MTPA angle. This ensures convergence even under extreme operating conditions.

$$\theta_{k+1} = \theta_k - \nabla f(\theta) = \theta_k - \frac{\partial f(\theta)}{\partial \theta} \quad \text{Eq.n 4.3-16}$$

If θ simply moves a constant distance while tracking the minimum value point of $g(\theta)$, the tracking time proportionally increases with the distance to the minimum value point. However, in the gradient descent algorithm, since the movement is proportional to the size of the gradient, it can reduce the tracking time. Given that θ varies with the current vector angle θ within the range (0° , 90°) in a manner that inversely mirrors the convex function depicted for $g(\theta)$, which possesses a unique extremal point, the search process avoids the pitfall of local optima. Consequently, the gradient descent algorithm can be effectively employed as an optimization method with $g(\theta)$ as the objective function, as described in Eq.n 4.3-16.

In Eq.n 4.3-14, α is the search step size of gradient descent, which determines the size of the current vector angle command change. $\frac{\partial g_{MTPA}(\theta)}{\partial \theta}$ is the gradient direction of descent $\partial g_{MTPA}(\theta)$. The gradient of it is a continuous function, so its derivation can be calculated using the discrete differential. It is represented in a separate form, and a digital controller is used to implement the gradient descent algorithm.

$$F_{MTPA}(\theta) = i_s \times F_{MTPSA}(\theta) - \frac{R i_s}{\omega_m} \quad \text{Eq.n 4.3-17}$$

Compared to Eq.n 4.3-17, the stator resistance R is not required in Eq.n 4.3-16, so the proposed method does not require the stator resistance information.

When utilizing Eq.n 4.3-16 to determine $g_{MTPA}(\theta)$, the tracking performance depends on the step size α . Improper selection of α can lead to the following issues: if α is chosen too small, the magnitude of $\theta_k - \theta_{k-1}$ becomes too small, leading to a longer time required for the current vector angle θ to

converge to $g_{MTPA}(\theta)$. Similarly, within a small gradient range, before θ converges to $g_{MTPA}(\theta)$, $\theta_k - \theta_{k-1}$ can approach a value near zero, hence tracking may stop. Conversely, when α is chosen too large, tracking becomes oscillatory or divergent. When α is appropriately selected, $g_{MTPA}(\theta)$ can be accurately tracked in a short amount of time. The examination for choosing the suitable α can be performed as follows: initially set α to a smaller value and gradually increase α until the convergence speed is satisfactory. This method allows for the selection of an appropriate θ , facilitating accurate and rapid search for $g_{MTPA}(\theta)$. However, since $g_{MTPA}(\theta)$ is derived from electromagnetic torque and power formulas, it depends on the load, and the magnitude of the gradient of $g_{MTPA}(\theta)$ is contingent upon load conditions. This implies that tracking performance, such as tracking time and accuracy, is dependent on load conditions. When the PMa-SynRM reaches a new load state, this method will be activated to search for a new $g_{MTPA}(\theta)$ from the current state. To solve the problem, a new convergence function will be introduced in the next part.

4.3.3. Improved Gradient Descent

To address the dependency of the optimal current vector angle tracking performance of the gradient descent algorithm on the load, the adjustment of the current vector angle is facilitated by employing a new gradient Q that is unaffected by load conditions. This new gradient Q reflects the rate of change of the objective function $g_{MTPA}(\theta)$, and is defined by Eq.n 4.3-18:

$$Q = \frac{[F_{MTPA,k}(\theta)/F_{MTPA,k-1}(\theta)] - 1}{\theta_k - \theta_{k-1}} \quad \text{Eq.n 4.3-18}$$

In Eq.n 4.3-18, a significant rate of change in the objective function $g_{MTPA,k}(\theta)$ implies a notable variation in $g_{MTPA,k}(\theta)$ due to changes in the current vector angle. This also indicates that the current electric vector angle is

far from the optimal electric vector angle θ_{MTPA} , and vice versa. The magnitude of Q is not directly proportional to the difference in the objective function values $g_{MTPA,k}(\theta) - g_{MTPA,k-1}(\theta)$, but rather proportional to the rate of change of the objective function $[g_{MTPA,k}(\theta)/g_{MTPA,k-1}(\theta)] - 1$. Therefore, the magnitude of Q does not depend on the load but on the distance from the current electric vector angle to the optimal electric vector angle.

The rate of change of the objective function $g_{MTPA,k}(\theta)$ is greater than 1 when $g_{MTPA,k}(\theta)$ decreases, and less than 1 when $g_{MTPA,k}(\theta)$ increases. Thus, with an increase in the current vector angle, Q is positive when $g_{MTPA,k}(\theta)$ decreases and negative when $g_{MTPA,k}(\theta)$ increases. Conversely, with a decrease in the current vector angle, Q is negative when $g_{MTPA,k}(\theta)$ decreases and positive when $g_{MTPA,k}(\theta)$ increases. Therefore, Q provides directional information towards the optimal current vector angle $g_{MTPA,k}(\theta)$ in all scenarios and can serve as a new gradient for tracking the optimal current vector angle θ_{MTPA} . The improved optimal current vector angle tracking algorithm using the newly defined gradient Q is presented in Eq.n 4.3-19.

$$\begin{aligned}
\theta_{k+1} &= \theta_k + \alpha Q \\
&= \theta_k + \alpha \frac{[F_{MTPSA,k}(\theta)/F_{MTPSA,k-1}(\theta)] - 1}{\theta_k - \theta_{k-1}} = \theta_k + \\
&\quad \frac{u_{d,k} \cos \theta_k + u_{q,k} \sin \theta_k}{(i_{s,k} \omega_{m,k})(\theta_k - \theta_{k-1})} \\
&\quad \alpha \frac{1}{\left(\frac{u_{d,k-1} \cos \theta_{k-1} + u_{q,k-1} \sin \theta_{k-1} - 1}{i_{s,k-1} \omega_{m,k-1}} \right)}
\end{aligned} \tag{Eq.n 4.3-19}$$

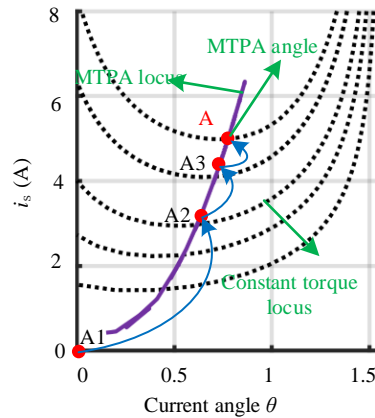


Fig. 4.3-3 Principal diagram of improved descent algorithm

Fig. 4.3-3 shows the convergence situation based on the improved function. As the objective function value ceases to change near the optimal point, Q converges to zero, and the current vector angle command produced by the modified gradient descent algorithm also converges to the optimal current vector angle θ_{MTPA} . Furthermore, the larger the difference between the current vector angle and the optimal current vector angle, the greater the rate of change of the objective function caused by changes in the current vector angle, and thus, the larger the value of Q . Therefore, if the current vector angle is far from the optimal current vector angle, it may be possible to increase the tracking speed.

4.3.4. Self-Learning-Based Control

Fig. 4.3-4 shows the overall setting up of the control system. This control system is designed for regulating the PMA-SynRM. The system uses PI controllers to adjust speed and current, generating reference currents based on the desired torque and reference current angle θ . For the SLC current angle reference and recording model, the model collects the working status of the machine in real time and determines whether to output a new angle reference signal or record a new working point. By designing this module, the response time could be reduced, especially for the large step load working condition

because the working condition could be determined and an optimal calculated current angle, which is near the real working condition could be provided and regard as the new initial condition for the angle calculation and gradient convergence module in Fig. 4.3-4 if an updated value from the SLC module generated. It then controls the d - and q - axis currents through coordinate transformations and current calculations. The system dynamically updates the SLC table to find the optimal operating point, thereby optimizing motor performance and efficiency. From adopting the proposed topology, the response performance could be improved.

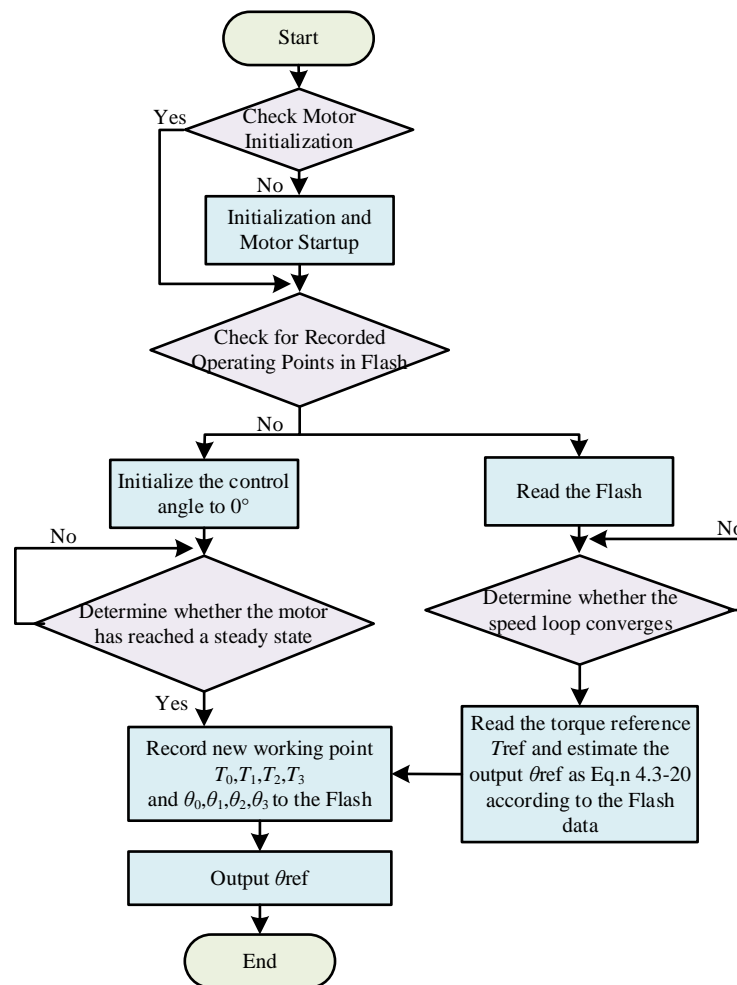


Fig. 4.3-4 Diagram of current angle reference calculation scheme for SLC reference generation and data recording module

The flowchart expressed in Fig. 4.3-6 delineates the control process of a SLC system, commencing with an assessment of the motor's initialization status.

In instances where initialization has not been completed, the motor undergoes an initialization and startup procedure. Subsequently, the system interrogates the Flash memory for any previously recorded operating points. If such data is available, it is retrieved, enabling the system to adjust control parameters accordingly. In the absence of pre-recorded data, the control angle is initialized to 0° , and the system monitors the motor's transition to a steady-state condition. Depending on the achievement of steady-state operation or the convergence of the speed loop, new operating points are either recorded or utilized to estimate and output the reference signal θ_{ref} .

4.3.5. Improved Current Angle Estimation Method for SLC

Fig. 4.3-5 illustrates the relationship between the reference stator current and the corresponding optimal current angle for MTPA operation. For a given reference torque, the MTPA operation determines a unique optimal current angle. If a sufficient number of MTPA working points are known as described on the curve, the remaining points can be approximated through interpolation between these known points. The proposed SLC scheme is based on this principle. If a new MTPA point is tracked during the m -th step, the m -th element of the MTPA and MTPA angle arrays will be updated with the values corresponding to the new MTPA point. This process is repeated iteratively during SLC operation.

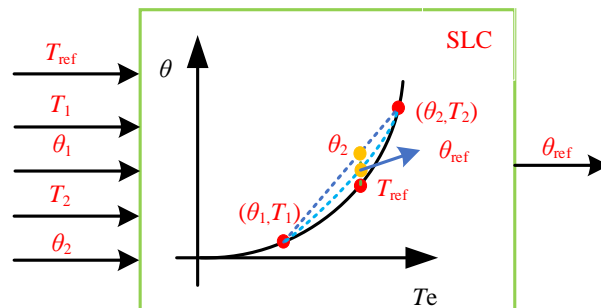


Fig. 4.3-5 Schematic of the proposed SLC scheme

Furthermore, Fig. 4.3-5 provides a detailed explanation of the current angle difference calculation process as outlined in the proposed six-step flowchart. In

conventional SLC, the angle is typically considered to have a linear relationship with torque output, as illustrated by θ_3 , which is the result of linear interpolation. However, by examining the MTPA curve of the PMA-SynRM motor, it becomes evident that the accuracy of the linear interpolation method is limited. This limitation arises due to the significant curvature present in the MTPA curve. Consequently, this thesis proposes a novel interpolation method for calculating the MTPA current angle. A comparison reveals that this method achieves higher computational accuracy, as demonstrated by the calculation formula in Eq.n 4.3-20. This interpolation method fully accounts for the non-linearity of the machine's magnetic flux linkage. It is important to note that this method can be applied to other types of motors, as they primarily differ in power, while the general trend of the MTPA angle remains consistent.

Considering the magnetic saturation and the cross saturation of the PMA-SynRM, the quadratic polynomial function was adopted to replace the linear interpolation to obtain an accurate evaluation of the current angle. It shows that the SLC obtains additional operating points to fit the MTPA working curve by learning new operating points. This means that the more operating points are learned, the higher the accuracy of the output angle. During the fitting process, the least squares method was adopted for online fitting [130]. The curve obtained through training is expressed in the form shown in equation Eq.n 4.3-20.

$$f(\theta) = aT_e^4 + bT_e^3 + cT_e^2 + dT_e \quad \text{Eq.n 4.3-20}$$

It is worth noting that the relationship between the torque and the current angle is generally described for PMA-SynRM and IPMSMs. The difference for different machines is that the rated current and torque are not the same and need to be normalized to make the SLC feasible. In this way, the proposed SLC is a general method for PMA-SynRM and could be further used in other machines.

4.3.6. Simulation Verification

A. Resistance Variation Robustness Verification

In this study, simulation was done on the modified MTPA tracking method to verify its effect and accuracy as shown in Fig. 4.3-6. In the simulation environment settings, two different resistance values, namely 0.8Ω and 1Ω , were selected to test the adaptability and stability of the algorithm under different conditions. By performing an 11-step iteration process on the algorithm, the results show that the proposed algorithm can effectively converge regardless of whether the resistance value is 0.8Ω or 1Ω .

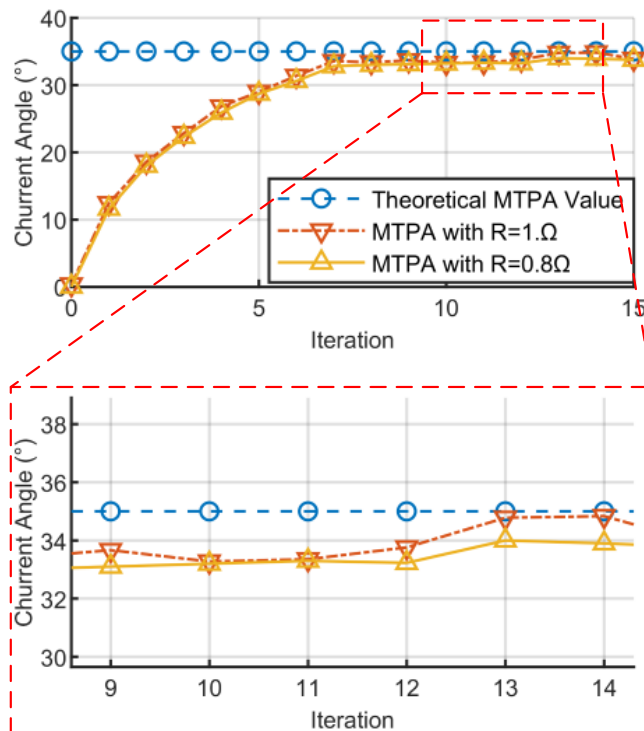


Fig. 4.3-6 Simulation results under different resistance setting

After convergence, the steady state error of the algorithm was further analyzed. The results show that under the two resistance settings, the steady state accuracy of the algorithm is basically the same. This finding not only demonstrates the robustness of the algorithm, but also verifies the feasibility of its application in the field of electrical engineering. These results confirm the

correctness of the proposed algorithm and provide an experimental basis for subsequent related research.

4.3.7. Experiments Verification

A. Verification of Proposed Convergence Function

In this experiment, the different loading was set up to verify the feasibility of the proposed MTPA control, the MTPA accuracy compared to the theoretical value was shown in Table 4.3-1.

Table 4.3-1 PMa-SynRM test angles in different working conditions

Load Torque (Nm)	0.6	1.2	1.9
Theoretical Angle	13.4	26.1	35.6
Detected Angle	12.8	25.8	34.7
Detected Error	0.6	0.3	0.9
Error Percentage	4.48%	1.15%	2.53%

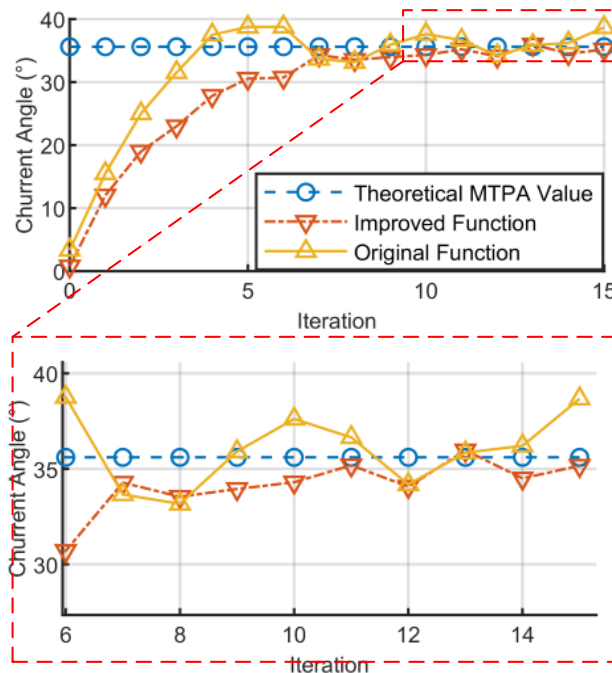


Fig. 4.3-7 MTPA detection in different convergence function

In the control loop, the function for MTPA angle convergence is placed within the speed loop. In this control system, the execution time for the speed loop is set to 100ms. The convergence time and execution time can be

determined by the number of iterations. This study verified the performance of the improved convergence function and the original convergence function in terms of stability through experiments. The experimental design aims to compare the convergence performance and system stability of the two functions when reaching the same number of steps.

Experimental results show that compared with the original convergence function, the improved convergence function shows no overshoot when reaching the same number of iterations steps and has higher accuracy and better stability after convergence. This difference is mainly attributed to the adjustment of the convergence gain in the improvement function. In the original function which denoted as 4.3-14, a higher convergence gain may lead to unstable system performance, but the improved function effectively avoids this problem by optimizing the gain parameters, thus improving the stability and reliability of the overall system.

B Verification of Different Working Speed

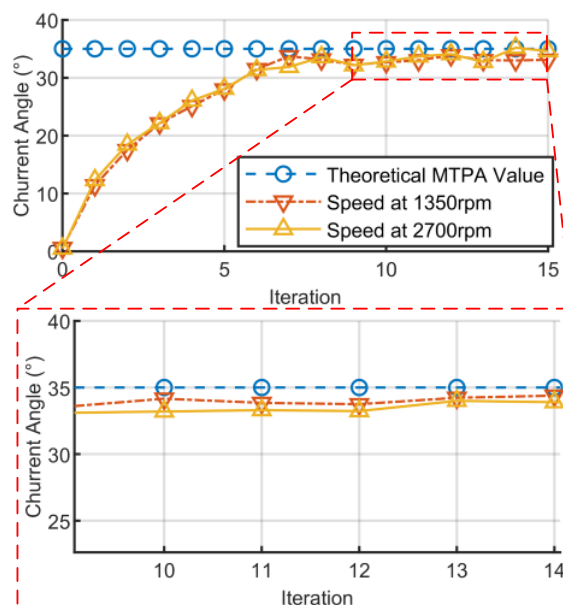


Fig. 4.3-8 MTPA detection performance at different speed

This part describes experiments to verify the angular convergence of the MTPA at different rotational speeds, namely 1350 rpm and 2700 rpm. The purpose of the experiment is to observe and analyze the response characteristics and accuracy performance of MTPA under different dynamic conditions.

Experimental results show that the MTPA algorithm exhibits good convergence performance at both test speeds. Specifically, no matter under the conditions of 1350 rpm or 2700 rpm, the algorithm can quickly and accurately converge to the predetermined angle value without obvious overshoot or oscillation. This finding shows that the MTPA algorithm has good adaptability and stability and can maintain efficient performance under different operating speeds.

C. Verification of SLC and current angle estimation link

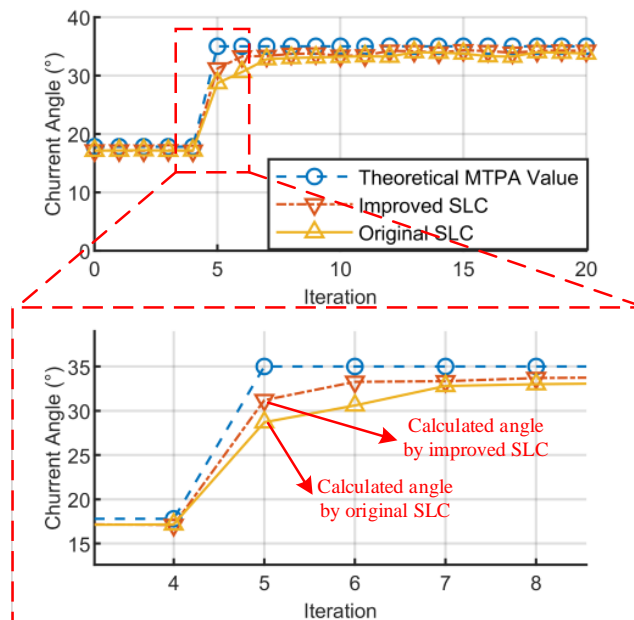


Fig. 4.3-9 MTPA detection with original SLC and improved SLC estimation function

From Fig. 4.3-9, experimental results show that when encountering a load jump, the improved SLC only needs 2 steps to achieve convergence, while the

original SLC requires 3 steps. This result not only shows the advantage of the improved SLC in convergence speed but also indicates its higher accuracy in calculating the true angle. This enhanced performance can be attributed to the more efficient control algorithm and parameter optimization adopted in the improved SLC. These adjustments allow the SLC to adapt to load changes faster, thereby reducing the number of iteration steps required for convergence.

4.4 Chapter Summary

This study presents a series of advancements in MTPA control strategies for PMA-SynRMs, addressing key limitations in conventional methods. The work focuses on enhancing the dynamic response, reducing current noise, and improving control accuracy by developing novel detection and control schemes.

Firstly, a PRFSI MTPA detection scheme is proposed, overcoming the shortcomings of the CFSI method, which generated three-phase current noise and restricted the machine's performance. The PRFSI method effectively disperses and continuously distributes the PSD of the excited high-frequency current, minimizing additional acoustic noise and improving dynamic response. Simulations and experiments demonstrated that the PRFSI method significantly reduced steady-state current angle error, resulting in better performance and applicability.

Additionally, an online MTPA control strategy was introduced to address the magnet flux mismatch and improve the accuracy of the MTPA control angle. This approach includes a supplementary control strategy that corrects for the omission of inductance differentiation concerning the current angle, yielding a

control method with low computational complexity, high precision, and minimal dependence on motor parameters. Experimental results indicated an improvement of up to 1.52% in control accuracy.

Finally, the study proposed an online tracking MTPA control method that incorporates a SLC and an enhanced convergence function to address flux non-linearity in PMA-SynRMs. This method eliminates the need for LUTs and prevents additional current harmonics, achieving faster dynamic response and shorter steady-state convergence time. Experimental validations confirmed that the proposed method offers a significant improvement in MTPA control angle and reliability, making a substantial contribution to the field of electric machine control.

Chapter 5 High Dynamic Performance Control of PMA-SynRM

5.1 A-DESO Based Control for Noise Suppression and Fast Dynamic Response

5.1.1. Problem Statement and Parameter Calculation of ESO

This part provides a concise and precise description of the experimental results, their interpretation, and the experimental conclusions that can be drawn.

According to Eq.n 5.1-4, the error dynamics of ESO can be obtained as Eq.n 5.1-1:

$$\ddot{e} = -\beta_1 \dot{e} - \beta_2 e - (B\dot{\omega}_m + \dot{T}_L) \quad \text{Eq.n 5.1-1}$$

where \dot{e} and \ddot{e} are the first differential of error and second differential error of ω_m , respectively. Then, the estimated speed error and the estimated mechanical speed can be derived in the frequency domain as Eq.n 5.1-2.

$$\begin{cases} \frac{e(s)}{\omega_m(s)} = \frac{-s}{s^2 + 2\omega_0 s + \omega_0^2} \\ \frac{\hat{\omega}_m(s)}{\omega_m(s)} = \frac{\beta_2}{s^2 + 2\omega_0 s + \omega_0^2} \end{cases} \quad \text{Eq.n 5.1-2}$$

By increasing ω_0 , the response performance can be improved, but the observer will be more sensitive to noise [131]. In this way, A tradeoff should be reached between rapidity of estimation and noise immunity in practical applications. When ESO becomes stable, the estimation of load disturbance can be obtained as Eq.n 5.1-3:

$$d(t) = T_L + T_F \quad \text{Eq.n 5.1-3}$$

where T_F represents the viscous friction of the system.

Since $\dot{d}(t)$ is bounded by h_0 , the following inequality holds in the time

domain [131] expressed as Eq.n 5.1-4,

$$|e| \leq \frac{h_0}{\omega_0^2} \quad \text{Eq.n 5.1-4}$$

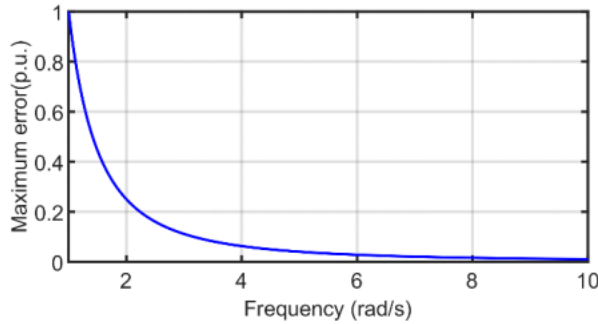


Fig. 5.1-1 Relationship between maximum error and frequency

According to Eq.n 5.1-8, the maximum estimation error of ESO is proportional to h_0 if the bandwidth ω_0 is fixed. Therefore, ESO is highly dependent on h_0 for its estimation accuracy. A higher cut-off frequency can reduce the observation error, but it also amplifies noise and is more sensitive to high-frequency noise. Due to this, in practice, it is necessary to adjust the cut-off frequency ω_0 to maintain an acceptable level of error, noise and response time.

Fig. 5.1-1 shows the relationship between maximum error and frequency. To be more specific, large observed speed errors may result in control switching repeatedly between the area of FW and the area of MTPA and reducing the control efficiency. However, to obtain a better noise suppression ability, the reduction of the cut-off frequency ω_0 will increase the observation error. As a result, in the control system, noise, observation error, and response time are effectively traded off.

The purpose of this part is to design an A-DESO observer to effectively balance observation error, noise sensitivity, and response time, which features a better response performance in low frequency and a better noise suppression ability in high frequency within the same error range simultaneously.

5.1.2. Research Aims and Content Arrangements

To further enhance the dynamic response of the system in constant torque and the FW control for the PMA-SynRM, a novel A-DESO control method based on a LUT is proposed to solve these problems. The main contributions are as follows:

(a) A new constant torque and FW (Flux Weakening) control strategy based on an A-DESO and a LUT is proposed, which features a small steady-state error, quick response, high anti-load-disturbance, and other lumped disturbance resistant abilities.

(b) Compared with the traditional ESO, the proposed A-DESO features a higher low-frequency amplification gain and a high-frequency noise suppression ability for the disturbance in torque and speed observation under the same error acceptance range.

(c) The oscillation problem caused by speed observation error and amplified noise could be alleviated by adopting the proposed A-DESO.

(d) The A-DESO parameters calculation method was given for PMA-SynRMs, considering stability requirements and parameter mismatch analysis.

5.1.3. Design of the Extended State Observer

According to Equations Eq.n 1.3-4 and Eq.n 1.3-6, the speed and electrical angle can be obtained as shown in Eq.n 5.1-5 and Eq.n 5.1-6,

$$\dot{\omega}_m = \frac{1}{J} (T_e - B\omega_m - T_L) \quad \text{Eq.n 5.1-5}$$

$$\dot{\theta}_m = \omega_m \quad \text{Eq.n 5.1-6}$$

where, θ_m is the mechanical angle of the machine.

According to Eq.n 1.3-6 and Eq.n 5.1-5, Eq.n 5.1-7 could be obtained.

$$\dot{\omega}_m = \frac{1}{J} \left(\frac{3}{2} p (\psi_d i_q - \psi_q i_d) - B \omega_m - T_L \right) \quad \text{Eq.n 5.1-7}$$

Regard $B\omega_m$ and T_L as lumped disturbance in torque. The ESO is designed as

Eq.n 5.1-8:

$$\begin{aligned} \hat{\omega}_m &= \frac{1}{J} \left(\frac{3}{2} p (\psi_d i_q - \psi_q i_d) - d(t) - \beta_1 (\hat{\omega}_m - \omega_m) \right) \\ \dot{\hat{T}}_L(t) &= -\beta_2 (\hat{\omega}_m - \omega_m) \\ \beta_1 &= 2\omega_0 \\ \beta_2 &= \omega_0^2 \end{aligned} \quad \text{Eq.n 5.1-8}$$

where, $\hat{\cdot}$ represent the observed variables; $d(t)$ represents the observed load torque; ω_0 is the cut-off frequency of the ESO observer. The bandwidth parameterization method is also used to select the parameter of β_1 and β_2 [131].

5.1.4. Performance Analysis of the Conventional ESO

Define the estimation speed error of the ESO as:

$$\Delta\omega_m(t) = \omega_m(t) - \hat{\omega}_m(t) \quad \text{Eq.n 5.1-9}$$

According to Eq.n 5.1-9, the error dynamic can be obtained as shown in

Fig. 5.1-2. The transfer function from $\dot{\hat{T}}_L(t)$ to $T_L(t)$ is shown in Equation Eq.n 5.1-10.

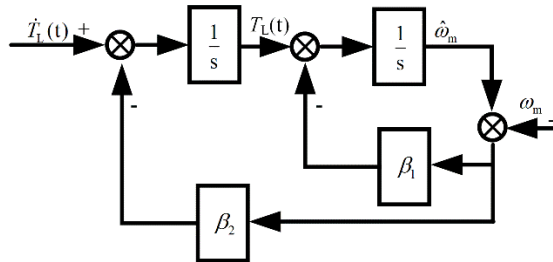


Fig. 5.1-2 Error dynamics diagram of the ESO

$$G_d(s) = \frac{s + 2\omega_0}{s^2 + 2\omega_0 s + \omega_0^2} \quad \text{Eq.n 5.1-10}$$

The ESO has the following properties.

(1) If the total disturbance is a constant one, that is, $\dot{T}_L(t) = 0$, then the steady error is zero. This means that the ESO could obtain the real value for a constant torque load.

(2) If the load is a ramp one, as in, $\dot{T}_L(t) = C$, the error will converge to $2/\omega_0$. This means that the error existed for a ramp torque load and this error will be decreased with the increase of the cut-off frequency.

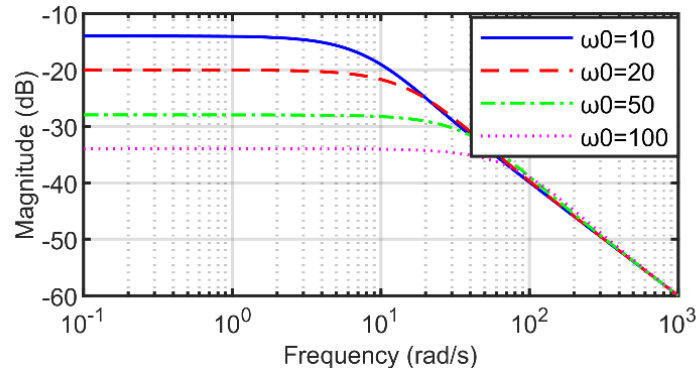


Fig. 5.1-3 Frequency responses of disturbance estimation for the ESO

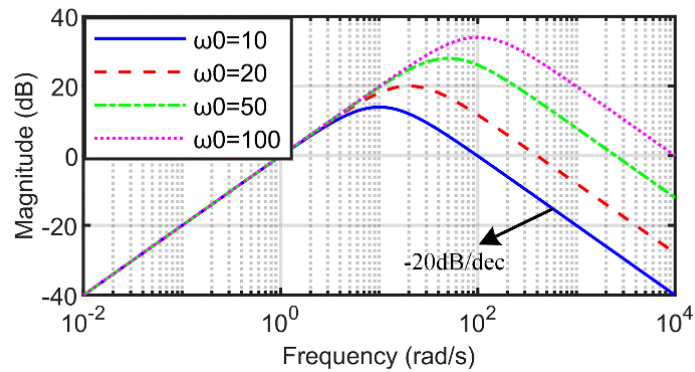


Fig. 5.1-4 Frequency responses of noise suppression for the ESO

Fig. 5.1-3 shows the frequency responses of disturbance estimation for the ESO. It is shown that the load torque estimation performance improves as ω_0 increases at low frequencies. Therefore, the ESO is effective for slow time-varying disturbances.

In Fig. 5.1-4, the transfer function from $\omega_m(t)$ to $T_L(t)$ is:

$$G_{\xi}(s) = \frac{-\omega_0^2 s}{s^2 + 2\omega_0 s + \omega_0^2} \quad \text{Eq.n 5.1-11}$$

The noise suppression ability and error of the observer need to be balanced. So, the ESO needs to be improved to have a better high-frequency noise suppression capability. In Chapter 5.1.5, an A-DESO is devised to improve the overall performance and solve the tradeoff.

5.1.5. Design and Analysis of A-DESO

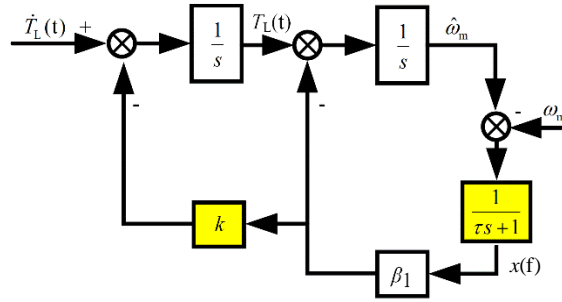


Fig. 5.1-5 Error dynamics diagram of A-DESO

Since the noise existed in the feedback current, calculated speed and the nonlinearity of the system are considered as a total disturbance, A-DESO is proposed to separate disturbance estimation from state reconstruction and uses a LPF to suppress the unmeasurable noise. The A-DESO is.

$$\begin{cases} \dot{\hat{\omega}}_m(t) = \frac{3}{2}p(\psi_d i_q - \psi_q i_d) + \beta_1 x_f(t) \\ \dot{\hat{T}}_L(t) = k\beta_1 x_f(t) \\ \dot{x}_f(t) = -\frac{1}{\tau}x_f(t) + \frac{1}{\tau}[\hat{\omega}_m(t) - \omega_m(t)] \\ \hat{y}(t) = \hat{T}_L(t) \end{cases} \quad \text{Eq.n 5.1-12}$$

where $x_f(t)$ and τ are the state and the time constant of the filter, respectively, and k is a parameter to adjust the disturbance estimation.

The error dynamics of the A-DESO is:

$$\begin{cases} \hat{\omega}_m(t) = T_L(t) - \beta_1 x_f(t) \\ \hat{T}_L(t) = \dot{T}_L(t) - k\beta_1 x_f(t) \\ \dot{x}_f(t) = -\frac{1}{\tau} x_f(t) + \frac{1}{\tau} [\hat{\omega}_m(t) - \omega_m(t)] \end{cases} \quad \text{Eq.n 5.1-13}$$

Fig. 5.1-5 shows the block diagram of the error dynamics. The control input of the A-DESO is not the same as that of the ESO. The state observation is independent of the disturbance estimation. If $\beta_2 = k\beta_1$ for the ESO and $\tau = 0$ are chosen, then the A-DESO becomes

$$\begin{cases} \hat{\omega}_m(t) = u_0(t) + \beta_1 [\hat{\omega}_m(t) - \omega_m(t)] \\ \hat{T}_L(t) = k\beta_1 [\hat{\omega}_m(t) - \omega_m(t)] \\ \hat{y}(t) = \hat{\omega}_m(t) \end{cases} \quad \text{Eq.n 5.1-14}$$

According to Fig. 5.1-2 and Fig. 5.1-5, Eq.n 5.1-14 yields the traditional ESO. The parameter k is introduced to adjust the disturbance-rejection performance independently and the filter is added to achieve the noise-suppression performance, and the selection of the parameter will be discussed in a detailed way in the following part. The bandwidth parameterization method is also used to select the gains β_1 that same to the conventional ESO, which gives:

$$\beta_1 = 2\omega_0 \quad \text{Eq.n 5.1-15}$$

A. Anti-disturbance ability for torque estimation

The transfer function from $\hat{T}_L(t)$ to $T_L(t)$ is

$$G_d(s) = \frac{\tau s^2 + s + 2\omega_0}{\tau s^3 + s^2 + 2\omega_0 s + 2k\omega_0} \quad \text{Eq.n 5.1-16}$$

The magnitude of error at low frequencies can be decreased by increasing k . The A-DESO provides a new parameter k to tune the disturbance estimation performance, while the conventional ESO uses the bandwidth parameter ω_0 to do that. For comparison with the ESO, $k = 0.75\omega_0$ and $\tau = 0.01$ are set to investigate the disturbance-estimation performance of the A-DESO.

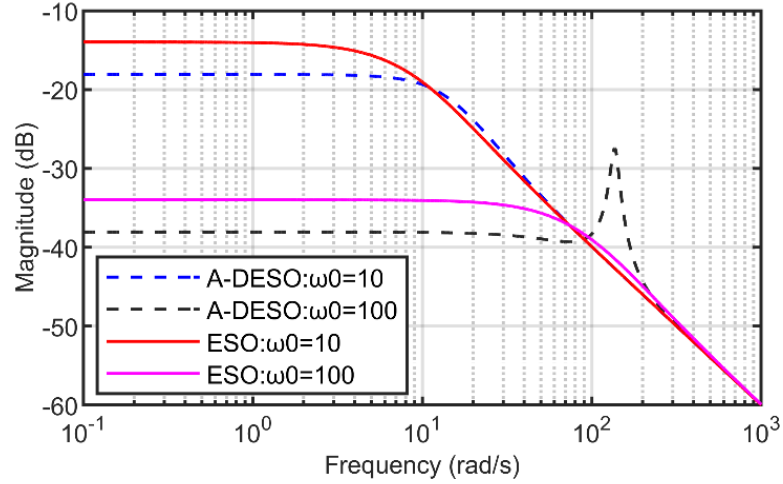


Fig. 5.1-6 Frequency responses of disturbance estimation error for the A-DESO and ESO

Fig. 5.1-6 shows that the A-DESO achieves a better performance than the ESO does at low frequencies for the same ω_0 . For example, when $\omega_0 = 100$, the magnitude of $G_d(s)$ approximates -38 dB for the A-DESO and -34 dB for the ESO at low frequencies. This indicates that the A-DESO obtains a smaller disturbance-estimation error than the ESO. In other words, the gain β_1 could be smaller for the A-DESO than for the ESO to achieve the same torque observation error range, which means a better noise suppression ability.

The transfer function from ω_m to $T_L(t)$ in Fig. 5.1-5 is:

$$G_\xi(s) = \frac{-2k\omega_0 s^2}{\tau s^3 + s^2 + 2\omega_0 s + 2k\omega_0} \quad \text{Eq.n 5.1-17}$$

Fig. 5.1-7 shows the frequency responses of noise suppression ability for the disturbance caused by the speed calculation under the same ω_0 . The noise-suppression performance is better for the A-DESO than for the ESO at high frequencies when using the same ω_0 . On the other hand, to approach the same disturbance-estimation performance, ω_0 should be smaller for the ESO than for the A-DESO. In many practical systems, torque inputs are often low frequency

and unmeasurable noise signals are often high frequency. The A-DESO provides a way to achieve disturbance rejection and noise attenuation simultaneously.

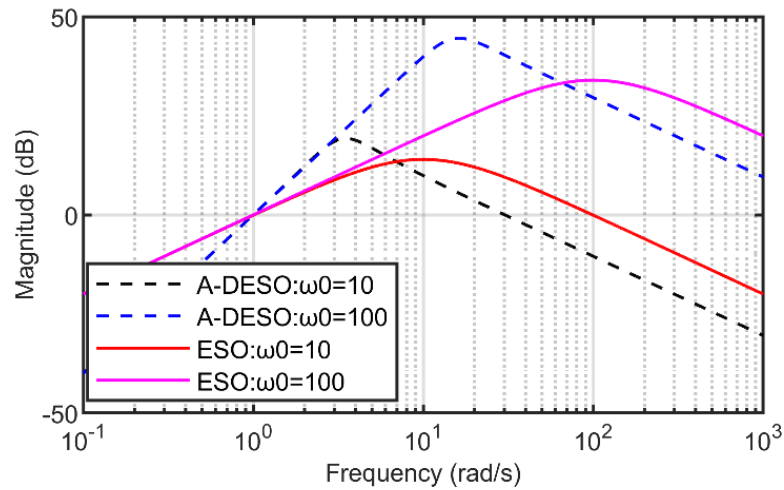


Fig. 5.1-7 Frequency responses of noise suppression for the A-DESO and ESO

Compared to the ESO, the A-DESO has three distinguishing features. First, it integrates a disturbance-estimation module into an existing observer without changing its parameters. This helps the observer avoid the high-gain form and makes the method easy to implement. Second, it employs a new parameter to adjust the disturbance-estimation performance. This increases the flexibility of the design of the A-DESO. Third, it uses a low-pass filter to filter out the high-frequency components in the unmeasurable input. This leads to a smaller amplitude compared to the ESO at high frequencies, which improves the noise-suppression performance. For the PMA-SynRMs control system, it achieves a smaller estimate error, a better observer dynamic response, and better noise suppression ability simultaneously using the same ω_0 compared to the conventional ESO.

B. Anti-disturbance ability for speed estimation

As discussed in Chapter 5.1.5A, the speed observation performance will influence the dynamic response of the control system. In this part, the

performance of the proposed A-DESO will be analyzed compared to the conventional ESO. The transfer function from $\dot{T}_L(t)$ to $\hat{\omega}_{mest}(t)$ for the conventional ESO can be obtained as Eq.n 5.1-18.

$$G_{L\omega m}(s) = \frac{1}{s^2 + 2\omega_0 s + \omega_0^2} \quad \text{Eq.n 5.1-18}$$

As for the A-DESO, $\dot{T}_L(t)$ to $\hat{\omega}_{mest}(t)$ can be obtained as Eq.n 5.1-19.

$$G_{ADL\omega m}(s) = \frac{\tau s + 1}{\tau s^3 + s^2 + 2\omega_0 s + 2k\omega_0} \quad \text{Eq.n 5.1-19}$$

For comparison with the conventional ESO, $k = 0.75 \omega_0$ and $\tau = 0.01$ are set to investigate the disturbance-estimation performance of the A-DESO. As can be seen in Fig. 5.1-8, the error decreases with the increasing of ω_0 .

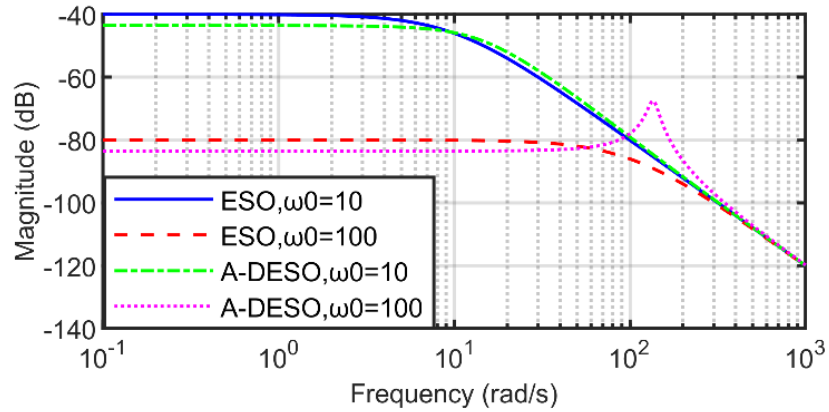


Fig. 5.1-8 Error dynamic response for speed of ESO and A-DESO

Fig. 5.1-8 shows that the A-DESO features better error suppression performance than ESO does. It means that the speed observation error of the A-DESO is smaller than the conventional ESO when a load disturbance is added. As for the high frequency observation ability, the performance is the same. However, torque disturbance is generally in low frequency. In this way, A-DESO features a better speed observation ability in the same ω_0 . In other words, the A-DESO features a better noise suppression ability in the same error performance.

Then, the noise suppression ability will be analyzed for speed observation.

The transfer function from $\omega_m(t)$ to $\hat{\omega}_{mest}(t)$ for the conventional ESO can be obtained as Eq.n 5.1-20.

$$G_{H\theta}(s) = \frac{-2\omega_0 s - \omega_0^2}{s^2 + 2\omega_0 s + \omega_0^2} \quad \text{Eq.n 5.1-20}$$

As for the A-DESO, the transfer function from $\omega_m(t)$ to $\hat{\omega}_{mest}(t)$ can be obtained as Equation Eq.n 5.1-21.

$$G_{ADH\theta}(s) = \frac{-2\omega_0 s - 2k\omega_0}{\tau s^3 + s^2 + 2\omega_0 s + 2k\omega_0} \quad \text{Eq.n 5.1-21}$$

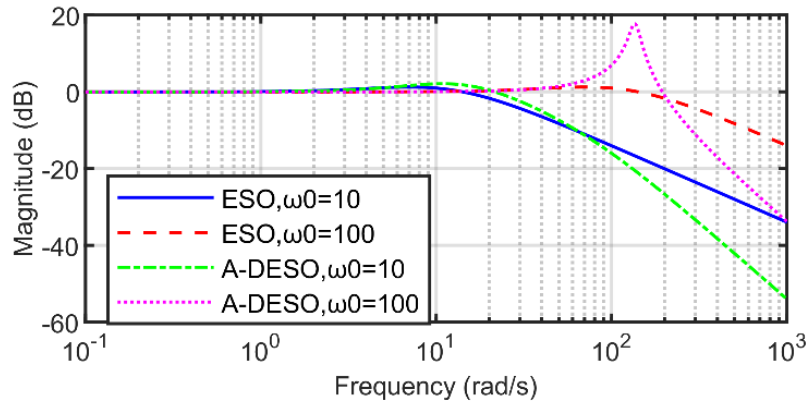


Fig. 5.1-9 Error suppression response for position observation of ESO and A-DESO

Fig. 5.1-9 shows frequency responses of noise suppression for $k=0.75\omega_0$ and $\tau=0.01$. The noise-suppression performance is better for the A-DESO than for the ESO at high frequencies when using the same ω_0 . In other words, to approach the same disturbance estimation performance, ω_0 should be smaller for the ESO than for the A-DESO. For instance, when $\omega_0 = 100$, the magnitude approximates -54 dB for the A-DESO and -36 dB for the ESO at high frequencies. This indicates that the A-DESO obtains a better noise suppression ability than the ESO. Furthermore, the slope of the A-DESO is -40dB/dec, while -20dB/dec for ESO, which indicates that the A-DESO features a better noise suppression ability in high frequency.

5.1.6. Stability of A-DESO and Parameter Design

As described in Chapter 1.4.2, regarding the PMA-SynRM system as a linear one, in which nonlinearity was not discussed in this thesis. To ensure the stability of the system, we need to ensure both the stability of the control system and the stability of the observer. This part discusses the stability of A-DESO observations under the PMA-SynRM control system.

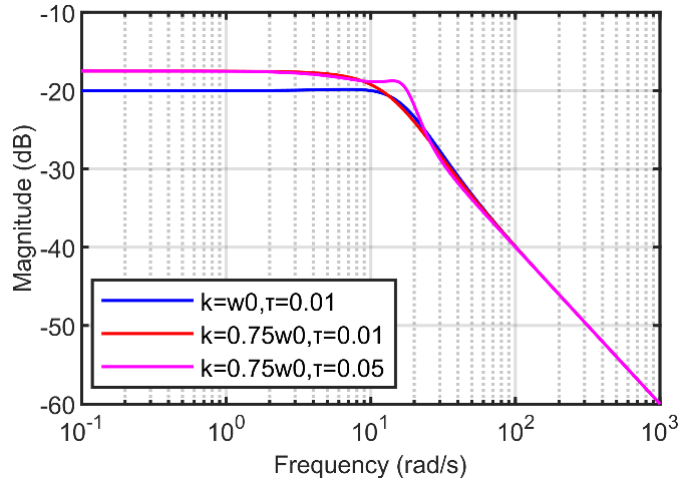


Fig. 5.1-10 Frequency responses of load torque estimation with different k and τ

Fig. 5.1-10 shows the parameters relationship between the response ability in the low frequency domain. It can be seen that τ has little influence on the low frequency response while k directly determines the response ability of low frequency. In summary, k needs to be adjusted to determine the low frequency response for the PMA-SynRM.

There is an equivalent stability of the A-DESO system as well as the stability of the system. The characteristic equation of the system is shown in Eq.n 5.1-22.

$$\tau s^3 + s^2 + \beta_1 s + \beta_1 k_1 = 0 \quad \text{Eq.n 5.1-22}$$

From Eq.n 5.1-22, the stability criterion could be obtained according to the Routh–Hurwitz stability criterion.

$$\tau k < 1$$

$$\text{Eq.n 5.1-23}$$

where, $\tau > 0$ and $k > 0$ should be satisfied.

As for the parameter design of the A-DESO, the bandwidth of the A-DESO should be larger than the bandwidth of the control system, so that the rapidity and stability could be guaranteed. According to Eq.n 5.1-23, the stability of the A-DESO deteriorates with the increase of τ , where τ represent the anti-disturbance ability of the control system. In other words, the anti-disturbance ability and the stability of the system should be balanced.

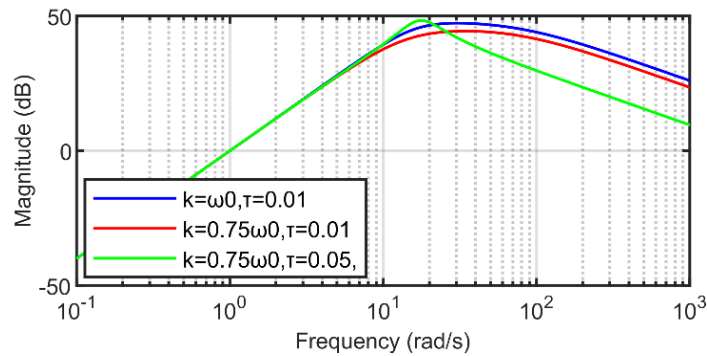


Fig. 5.1-11 Frequency responses of noise suppression with different k and τ

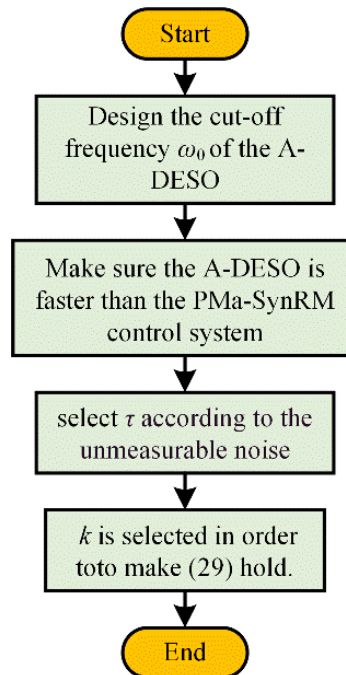


Fig. 5.1-12 Parameter calculation process of A-DESO based on the PMA-SynRM.

Fig. 5.1-11 shows the parameters relationship between the noise suppression ability in the high frequency domain. It can be seen that k has little influence on the noise suppression ability while τ directly determines the response of high frequency domain. In summary, τ need to be adjusted to determine the high frequency response for the PMA-SynRM.

In general, the signal to noise ratio of the measurement sensor should be considered, thus τ could be decided. Then, k could be decided to meet Eq.n 5.1-23. To sum up, the parameter design process of the whole control system could be described as Fig. 5.1-12.

5.1.7. Parameter Mismatch Analysis

The proposed adaptive ESO requires a knowledge of stator resistance and inductance. As a result of magnetic saturation, the inductance will vary under different load conditions. It is possible to describe the influence of parameter mismatch on the estimated disturbance in the following manner:

$$d(t) = \frac{3}{2J} p((L_d + \Delta L_d)i_d i_q - (L_q + \Delta L_q)i_q i_d) + T_L + T_F \quad \text{Eq.n 5.1-24}$$

Fig. 5.1-13(a) shows the observation error with d - and q -axis inductance mismatch in rated load condition. From the calculated data, its observation error of torque is not linear with the inductance mismatch error absolutely. Meanwhile, the observation error of torque is bounded, which is the most fundamental condition to ensure that the observer can converge in the finite time. (b) shows the observation error with d - and q -axis inductance mismatch in half load condition. The same results could be obtained compared to (a).

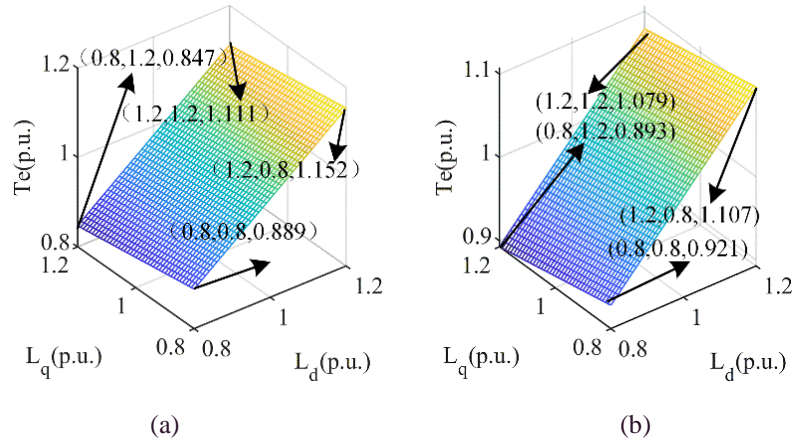


Fig. 5.1-13 Observation error with d - and q -axis inductance mismatch. (a) observation error in rated load condition;(b) observation error in half load condition

5.1.8. Overall Control Diagram

The control diagram of the whole control system is shown in Fig. 5.1-14.

Through the first stage PID controller, the given speed is compared with the observed speed feedback from the A-DESO to determine the torque.

Then, the calculated torque is combined with the observed speed and the observed load torque is obtained from the A-DESO to calculate an optimal current. After that, the d - and q -axis current PI controller is used to get the modulated d - and q -axis voltage.

In Fig. 5.1-15, the MTPA LUT was obtained according to Fig. 1.3-3. and the FW LUT was derived from Fig. 1.3-3 and Fig. 1.3-4 with the input of lumped disturbance and observed speed.

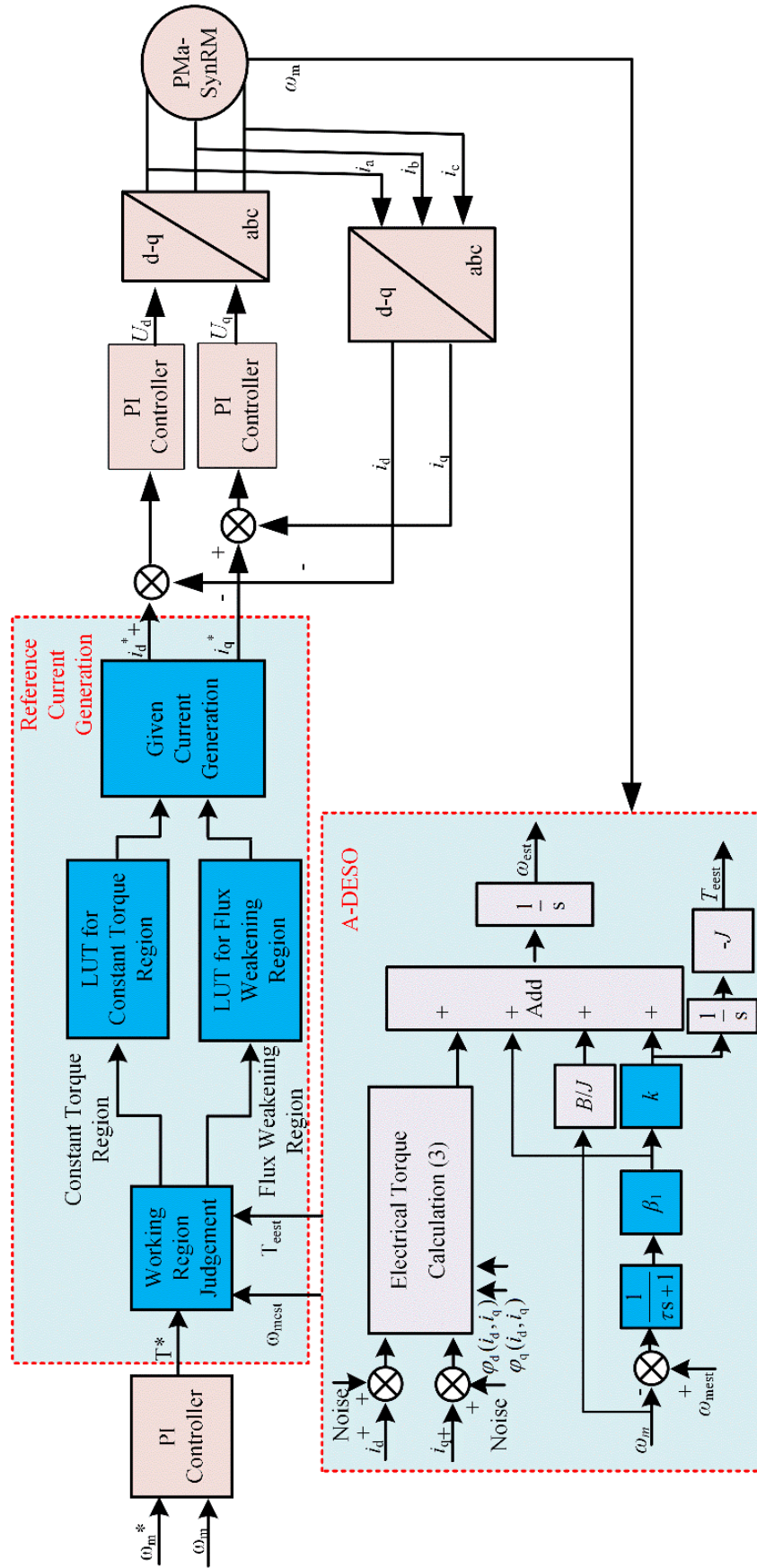


Fig. 5.1-14 Overall control diagram of dynamic improvements based on A-DESO

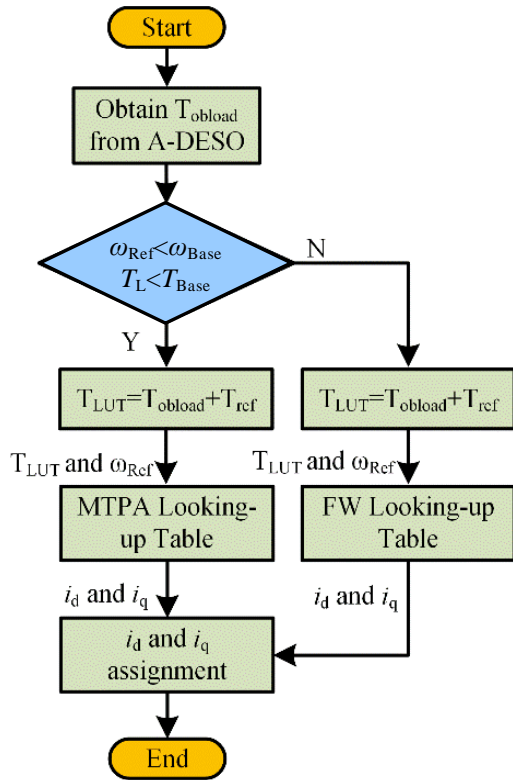
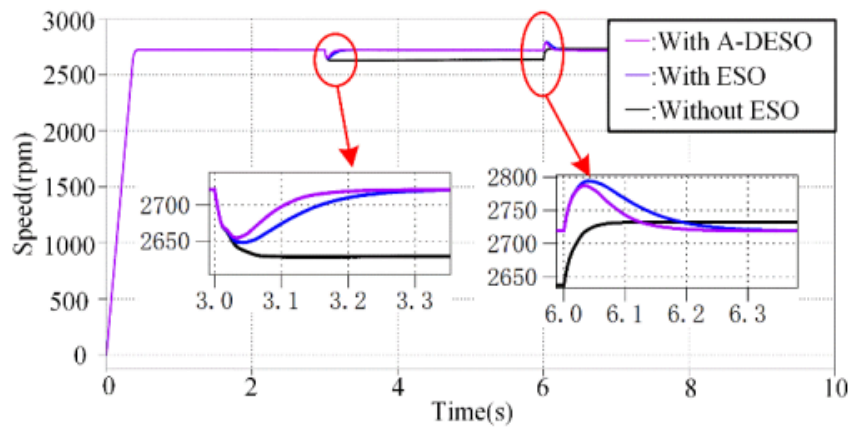


Fig. 5.1-15 Overall control diagram of i_d and i_q generation.

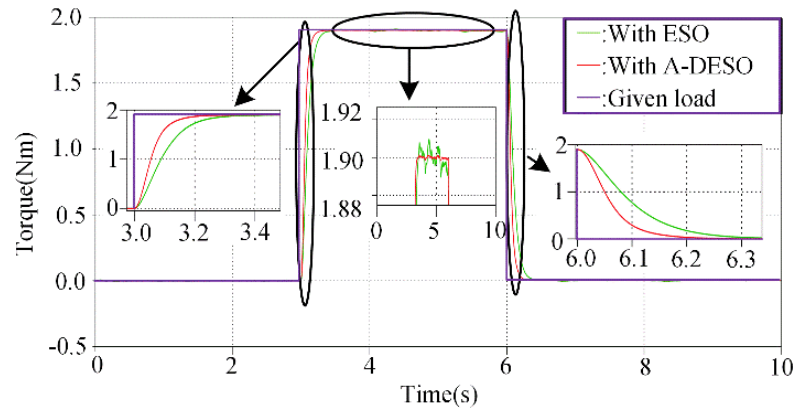
5.1.9. Simulation Results

As a means of verifying the effectiveness of A-DESO, this thesis conducted a comparison experiment between the feedback of A-DESO, traditional ESO and without ESO.

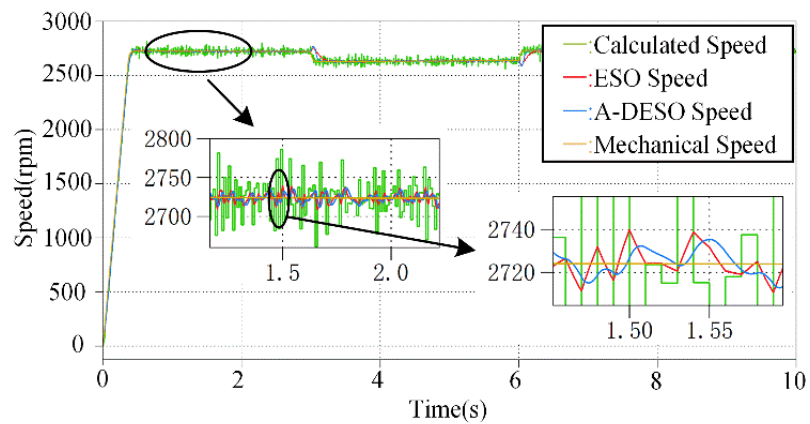
A. Simulation Set 1: Load and unload experiments in MTPA working conditions.



(a)



(b)



(c)

Fig. 5.1-16 Simulation results on step load response in MTPA region: (a) Speed fluctuation when load step; (b) Observed lumped disturbance and given load disturbance; (c) Comparison of the different speed calculation method

From the no-load condition to the rated-load condition and opposite operating mode, this group of simulations verified the speed fluctuation. Fig. 5.1-16 illustrates the change in speed associated with a step load from 0 Nm to 1.9 Nm at $t = 3$ s and a step load from 1.9 Nm to 0 Nm at $t = 6$ s. From the simulation, the machine speed exists a steady-state error for 74 rpm for a long convergence time while the A-DES0 and the ESO exist a 23 rpm steady-state error and the steady-state error is maintained for a considerable period. Meanwhile, the A-DES0 shows a better speed dynamic response compared to the ESO part from (a). The same results could be obtained when a step load

occurs from 1.9 Nm to 0 Nm. It could be summarized that A-DESO has a better speed response performance compared to the ESO and a smaller steady-state error compared to the no ESO simulation part.

Fig. 5.1-16 (b) shows the observed lumped torque disturbance and given load disturbance. It could be obtained that the A-DESO took 0.2 s to stabilize while took 0.3 s for the ESO. Meanwhile, the A-DESO featured a small load torque fluctuation compared to the traditional ESO. In Fig. 5.1-16 (a) and (b), it indicated that the A-DESO features a better dynamic performance at low frequencies and better noise immunity at high frequencies. Fig. 5.1-16(c) shows that the observed speed from the A-DESO features a smaller speed variation compared to the ESO and calculated method in the control system.

B. Simulation Set 2: Load and unload experiments in FW working conditions.

This group of simulations verifies the loading experiments under the working condition of the FW. Fig. 5.1-17(b). shows the observed lumped disturbance and given load disturbance when encountering large current noise. It could be found that the A-DESO took 0.05 s to stabilize while 0.1 s for the ESO in the almost same error tolerance.

From the no-load condition to the half load FW condition and opposite operating condition. Fig. 5.1-17(a). illustrates the change in speed associated with the step load from 0 Nm to 1.0 Nm at $t = 3$ s and a step load from 1.0 Nm to 0 Nm at $t = 6$ s.

From the simulation, the machine speed exists a steady-state error for 100 rpm for a long convergence time while the A-DESO and the ESO features a 2rpm

steady-state error and the steady-state difference is maintained for a considerable period. Meanwhile, the A-DESO shows a better speed dynamic response compared to the ESO in the same torque error acceptance range.

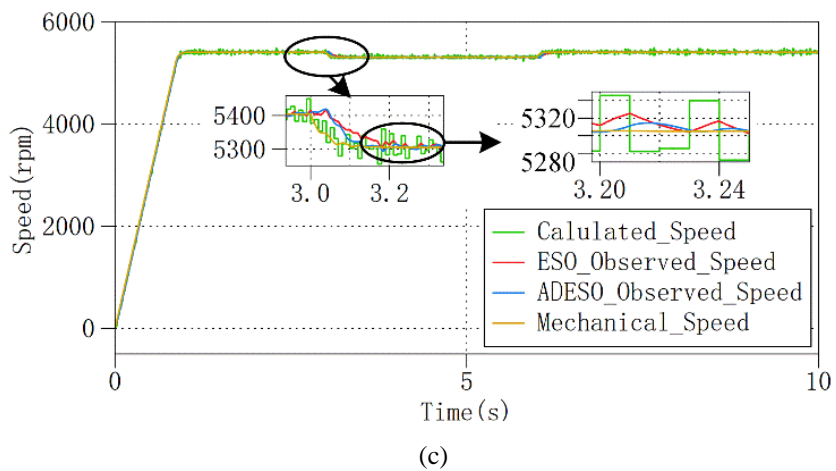
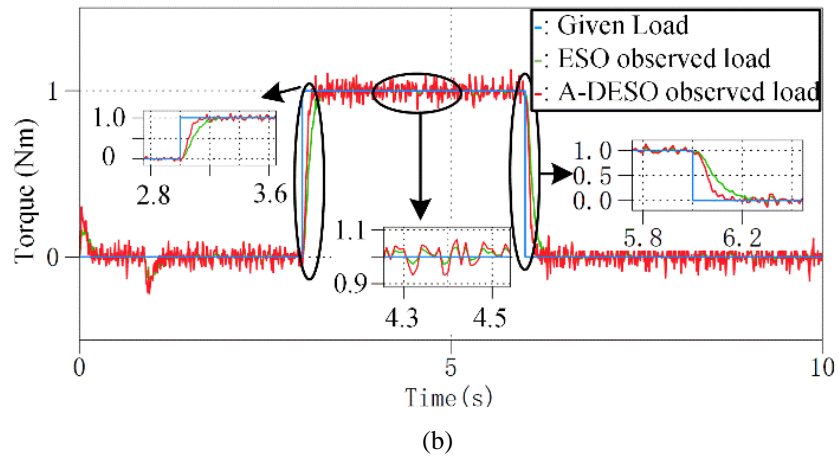
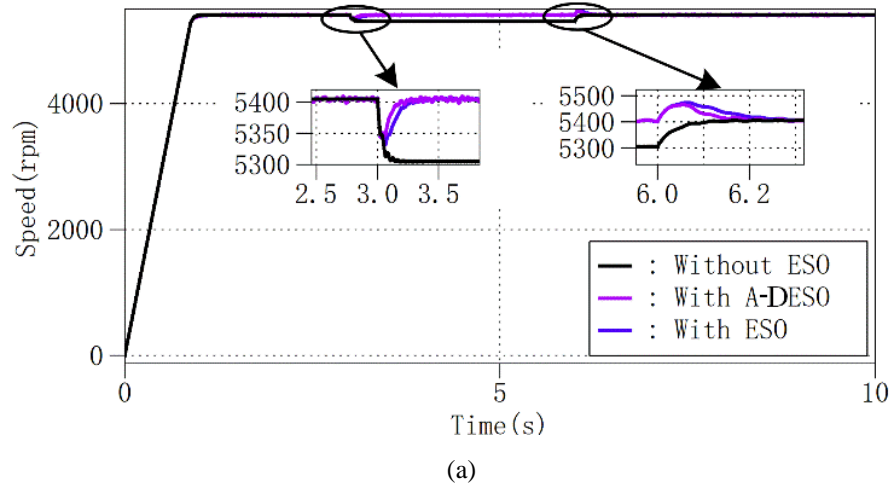


Fig. 5.1-17 Simulation results on step load response in FW region: (a) Observed lumped disturbance and given load disturbance; (b) Speed fluctuation when increasing load under flux weakening control; (c) Comparison of different speed calculation method in FW condition.

The same results could be obtained when a step load occurs from 1.0 Nm to 0 Nm. It could be summarized that A-DESO has a better speed response performance compared to ESO, and a small steady-state error compared to the no ESO part in the FW working condition. Fig. 5.1-17(c). shows that the observed speed from the A-DESO features a smaller speed variation compared to the ESO and calculated method in the control system.

5.1.10. Experiments Results

A. Experiment Set 1: in MTPA region

To verify the base speed and FW region, experiments were conducted. According to Fig. 5.1-18, the step load from 1.5 Nm to 1.9 Nm at 5 s and 1.9 Nm to 1.5 Nm at 25 s.

As can be seen from the experiment, in the presence of A-DESO, the maximum speed fluctuation is reduced by 63 rpm, the stabilization time and the current settling time are reduced by 0.2 s. These experiments demonstrate that A-DESO reduces the speed ripple and shortens stabilization time at rated speed in the const speed region.

B. Experiment Set 2: in FW region

It was found that the A-DESO effect of the FW working condition in this group of experiments. Fig. 5.1-19 shows the torque disturbance, which shows that when the step torque increases, the speed fluctuation of the A-DESO control group is 78 rpm smaller from the top one, and the current stabilization time is shortened by 2 s from the medium one. When the load step decreases, the speed fluctuation with A-DESO is 82 rpm smaller than that of the control group

without ESO, and the current stabilization time is shortened by 2 s. It can be seen from this group of experiments that A-DESO increases the anti-disturbance performance of the system and reduces the speed fluctuation and current adjustment time.

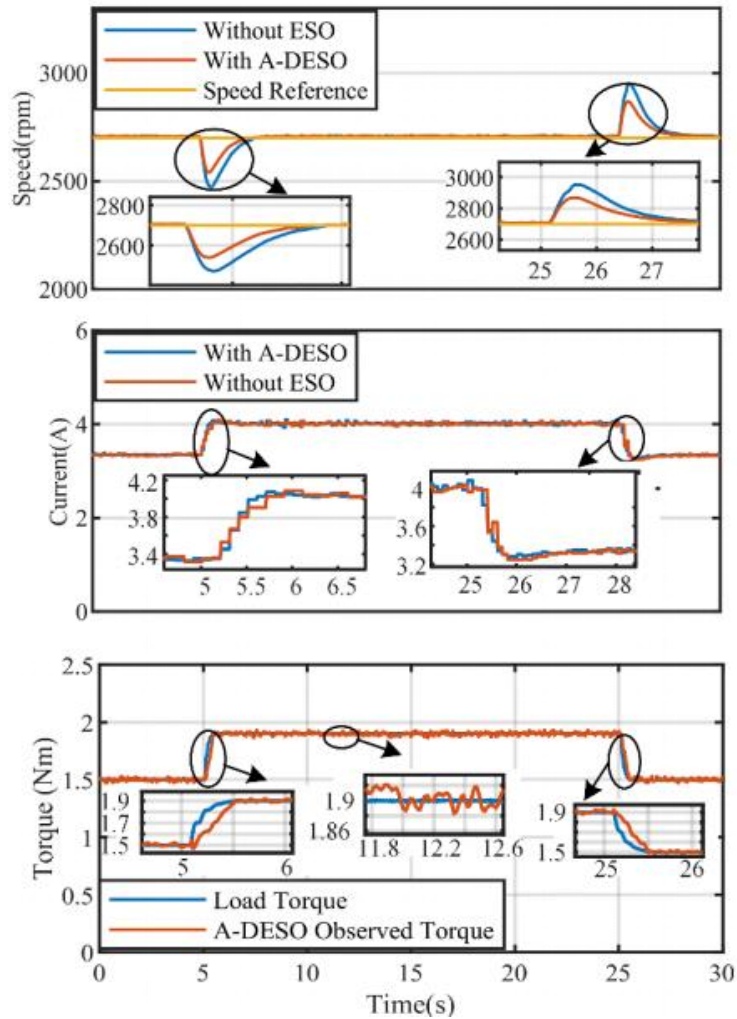


Fig. 5.1-18 Experiments results in MTPA region: Speed fluctuation with A-DESO and without ESO; Current fluctuation with A-DESO and without ESO; Load torque and observed disturbance

C. Experiment Set 3: periodic step load response in MTPA

A set of experiments has been conducted to verify the change in the load cycle. In Fig. 5.1-20 medium one, the load cycle change is shown under the base speed condition, and in the top of Fig. 5.1-20 the speed fluctuation under the load

response was shown. In the experiments, the period of step loads is 3 s as described in the medium one.

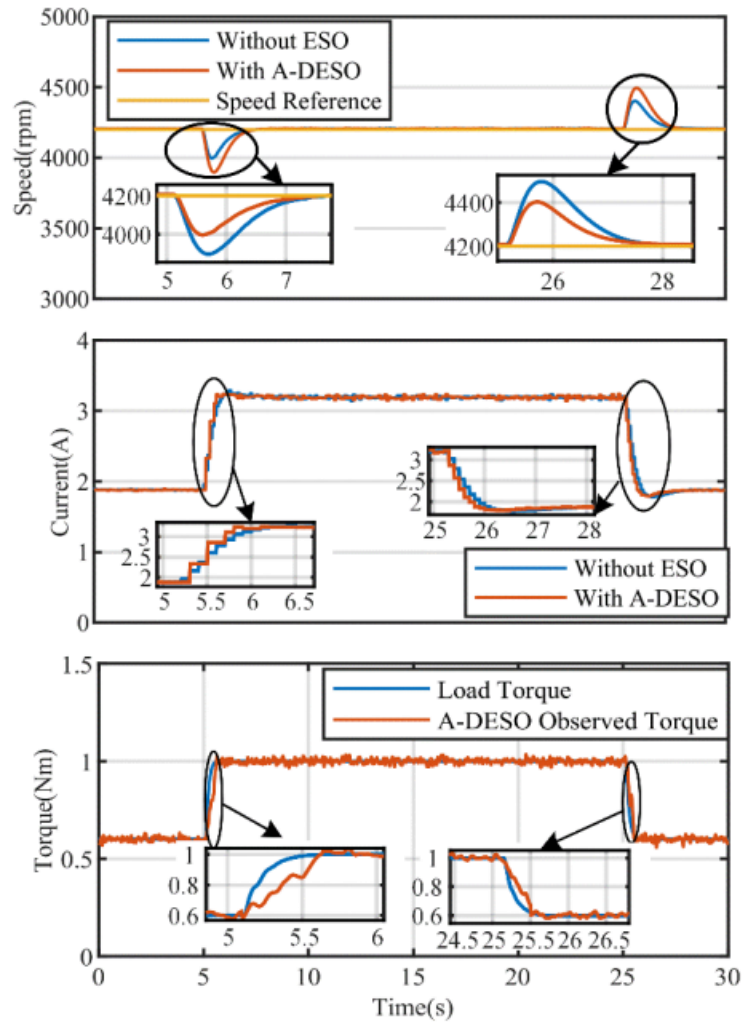


Fig. 5.1-19 Experiments results in FW region: Speed fluctuation with A-DES0 and without ESO; Current fluctuation with A-DES0 and without ESO; Load torque and observed disturbance

A-DES0 has a better control effect when faced with periodic step loads, as shown by this group of experiments. During the load change cycle, the speed of the control group with A-DES0 stabilized rapidly, whereas the speed of the control group without ESO failed to stabilize.

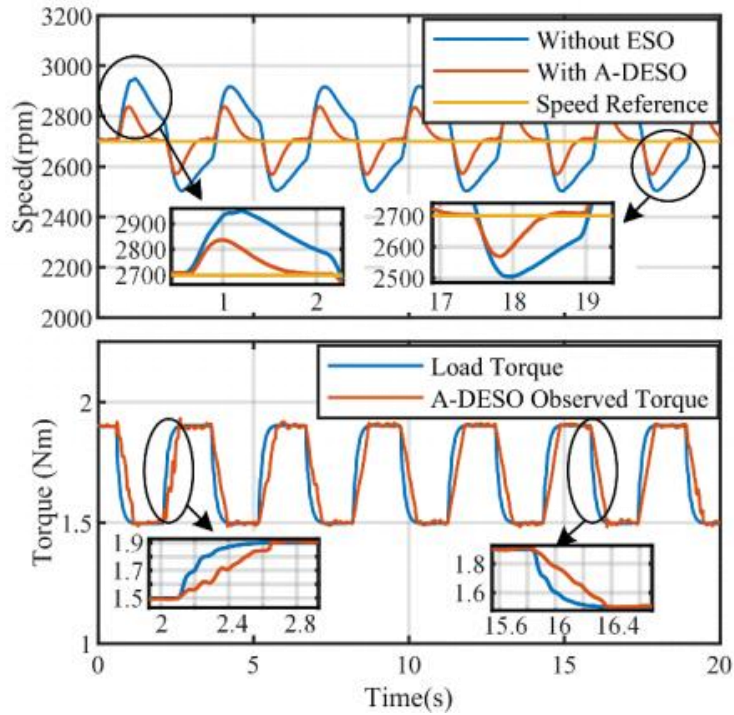


Fig. 5.1-20 Experiments results in repeating step-load response in MTPA working condition: Speed fluctuation with A-DES0 and without ESO; Load torque and observed disturbance

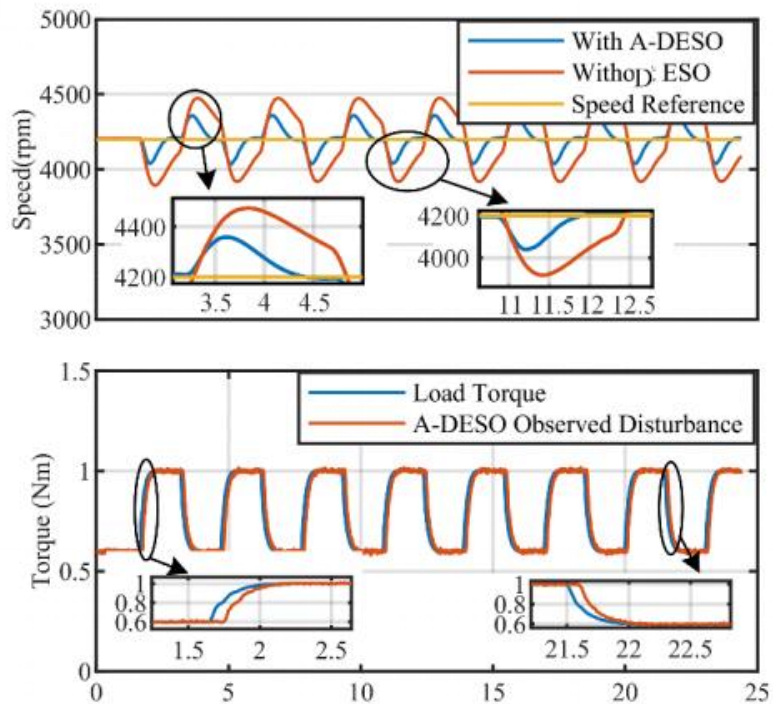


Fig. 5.1-21 Experiments results in repeating step-load response in FW working condition: Speed fluctuation with A-DES0 and without ESO; Load torque and observed disturbance

D. Experiment Set 4: periodic step load response in FW

A set of experiments has been conducted to verify the change in the load cycle in the FW working condition. In the medium one of Fig. 5.1-21 the cycle step load change is shown under the FW condition, and in the top of Fig. 5.1-20 the speed fluctuation under the load response was shown. In the experiments, the period of step loads is 3 s as described in the medium one.

The same results could be got from the previous experiments. A-DESO has a better control effect when faced with periodic step loads in the FW working condition, as shown by this group of experiments. During the cycle load change, the speed of the control group with A-DESO stabilized rapidly, whereas the speed of the control group without ESO failed to stabilize.

E. Experiment Set 5: Ramp load

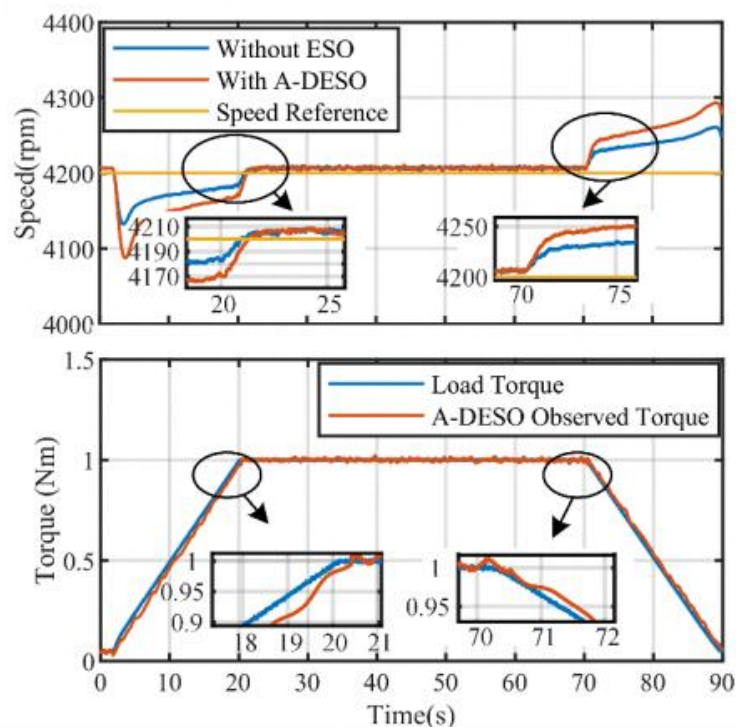


Fig. 5.1-22 Experiments results in ramp load response in the whole working condition: Speed fluctuation with ESO and without ESO; Load torque and observed disturbance

A set of experiments has been conducted to verify the change in the ramp load. Fig. 5.1-22 shows the effect of ramp load tracking in the flux weakening

region.

In Fig. 5.1-22, tracking a ramp load without ESO resulted in an average static difference in speed of 56 rpm, while tracking a ramp load with A-DESO resulted in an average static difference of 36 rpm. Studies have shown that A-DESO can improve the tracking performance of the ramp load and reduce the static error in the tracking state effectively.

5.2 IESO for Reduced Position Noise and Phase-lag and Better Dynamic Response in Sensor-less Control

5.2.1 Proposed Control Structure

This part focuses on the high-speed sensor-less control, and for the low-speed region, it was not considered in this thesis. Based on Eq.n 1.3-1, Eq.n 5.2-1 could be obtained through anti-park transformation to α - β fixed coordinate.

$$\begin{bmatrix} u_\alpha \\ u_\beta \end{bmatrix} = \begin{bmatrix} R_s + L_\alpha \frac{d}{dt} & L_{\alpha\beta} \frac{d}{dt} \\ L_{\alpha\beta} \frac{d}{dt} & R_s + L_\beta \frac{d}{dt} \end{bmatrix} \begin{bmatrix} i_\alpha \\ i_\beta \end{bmatrix} + \omega_e \psi_{pm} \begin{bmatrix} \cos\theta \\ \sin\theta \end{bmatrix} \quad \text{Eq.n 5.2-1}$$

where $L_\alpha = L_0 + L_1 \cos 2\theta$; $L_\beta = L_0 - L_1 \cos 2\theta$; $L_{\alpha\beta} = L_1 \sin 2\theta$; $L_0 = (L_d + L_q)/2$; $L_1 = (L_d - L_q)/2$

From Eq.n 5.2-1, it is worth to notice that it contains 2θ in the α - β frame voltage calculation, which increases the calculation burden to the sensor-less control. By adopting the method proposed in [132], Eq.n 5.2-1 could be reconstructed and rewritten as Eq.n 5.2-2.

$$\begin{bmatrix} u_\alpha \\ u_\beta \end{bmatrix} = \begin{bmatrix} R_s + pL_d & \omega_e(L_d - L_q) \\ -\omega_e(L_d - L_q) & R_s + pL_d \end{bmatrix} \begin{bmatrix} i_\alpha \\ i_\beta \end{bmatrix} + \{(L_d - L_q)(\omega_e i_q + i_d) + \omega_e \psi_{pm}\} \begin{bmatrix} \cos\theta \\ \sin\theta \end{bmatrix} \quad \text{Eq.n 5.2-2}$$

The second term on the right side of Eq.n 5.2-2 is defined as the EEMF as

Eq.n 5.2-3. In this term, besides the conventionally defined EMF generated by the permanent magnet, there is a kind of voltage related to the saliency of the PMa-SynRM. It includes the position information from both the EMF and the stator inductance. If the EEMF can be estimated, then the position of the magnet can be obtained from its phase.

$$e = \begin{bmatrix} e_\alpha \\ e_\beta \end{bmatrix} = \{(L_d - L_q)(\omega_e i_q + \dot{i}_d) + \omega_e \psi_{pm}\} \begin{bmatrix} \cos\theta \\ \sin\theta \end{bmatrix} \quad \text{Eq.n 5.2-3}$$

There is a differential term of i_d in the EEMF. This means that even when the motor's velocity is near zero, the EEMF is not zero if the d -axis current i_d is changing. This property will be useful for standstill and low-speed drives. In this way, a current observer to obtain the position of the machine could be reconstructed as Eq.n 5.2-4 according to Eq.n 5.2-1 assuming the speed ω_e could be regarded as the input of the observer.

$$\begin{bmatrix} \hat{i}_\alpha \\ \hat{i}_\beta \end{bmatrix} = \frac{1}{L_d} \begin{bmatrix} u_\alpha^* \\ u_\beta^* \end{bmatrix} - \frac{R_s}{L_d} \begin{bmatrix} \hat{i}_\alpha \\ \hat{i}_\beta \end{bmatrix} - \begin{bmatrix} 0 & \frac{\omega_e(L_d - L_q)}{L_d} \\ \frac{-\omega_e(L_d - L_q)}{L_d} & 0 \end{bmatrix} \begin{bmatrix} \hat{i}_\alpha \\ \hat{i}_\beta \end{bmatrix} - \frac{1}{L_d} \begin{bmatrix} \hat{E}_{ext,\alpha} \\ \hat{E}_{ext,\beta} \end{bmatrix} \quad \text{Eq.n 5.2-4}$$

As shown in Eq.n 5.2-4, u_α^* and u_β^* represent the given voltage in the α - β frame. \hat{i}_α and \hat{i}_β represent the estimated current in the α - β frame. In this way, the EEMF could be observed from the constructed equation. Meanwhile, the current error is only depending on the error of EEMF. So, A PI regulator could function as an error compensator, thereby constituting the complete EEMF

observer as Eq.n 5.2-5.

$$\begin{bmatrix} \hat{E}_{\text{ext},\alpha} \\ \hat{E}_{\text{ext},\beta} \end{bmatrix} = \left(K_p + \frac{K_i}{s} \right) \begin{bmatrix} \hat{i}_\alpha - i_\alpha \\ \hat{i}_\beta - i_\beta \end{bmatrix} \quad \text{Eq.n 5.2-5}$$

The stability of the observer is highly dependent on the value of the K_p and K_i . So, this value needs to be specially designed to make it convergent as discussed in [132].

Although the error caused by the error compensation link from adding a PI controller could be reduced in some way, the parameter precision considering parameter variation, self- saturation and cross-saturation still plays an important role in the accurate of the position observation. In this part, a LUT considering d - and q -axis currents was established to get a precise inductance and flux value. And the data was got from the FEA software. In this way, the observed position error could be reduced.

Assuming the current observer converges stably, $E_{\text{ext},\alpha}$ and $E_{\text{ext},\beta}$ can be acquired as Eq.n 5.2-6, allowing for the direct calculation of the estimated rotor position using the arctan function.

$$\hat{\theta}_{\text{arc}} = \arctan \left(\frac{\hat{E}_{\text{ext},\beta}}{\hat{E}_{\text{ext},\alpha}} \right) \quad \text{Eq.n 5.2-6}$$

Due to the substantial bandwidth of the current observer, the EEMF inevitably incorporates numerous noisy signals, resulting in significant fluctuations in the estimated rotor position when calculated using the arctan function. To address this issue, it is common to employ a PLL observer with an appropriately chosen bandwidth to simultaneously obtain more precise motor rotor position and speed estimation information. Furthermore, LPFs are

generally added to eliminate HF components and reduce position estimation noise, thereby ensuring transient-state performance [133,134].

However, the approach introduces phase lag into the observed output signal and degrades the steady-state performance of the PLL as discussed in Chapter 2.3.3. Both the PLL and LPF methods are inadequate for accurately tracking rapidly changing speeds, especially when power steering motors encounter abrupt load disturbance during operation, leading to inevitable transient-state errors in position and speed estimation. Consequently, the processing of the preliminary estimated rotor position obtained from EEMF observation fails to simultaneously consider both steady-state and transient-state performance aspects.

To further address this issue, an IESO will be proposed to calculate the position signal which comes from the EEMF of the observer. The position signal could be effectively extracted, and the torque disturbance could be detected and compensated to the speed controller from the proposed control. So, the position error could be reduced, and the dynamic response could be improved from the proposed control.

5.2.2 Speed Controller Design

For the sake of improving the dynamic response of the system and improving the efficacy of the machine, a LUT based on the detected torque disturbance and the machine speed from the IESO is proposed. The diagram of the speed controller is shown in Fig. 5.2-1.

As shown in Fig. 5.2-1, the given torque T_e^* was obtained through a PI

controller with the speed reference and feedback speed. After that, the controller will decide which working region it would be according to the given torque T_e^* , speed reference and observed torque disturbance T_L . Then, the controller will generate the given d - and q -axis current according to the working region using a separate LUT table.

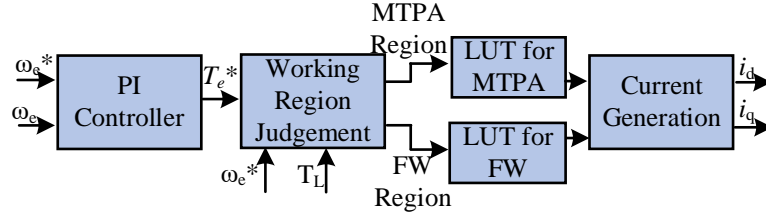


Fig. 5.2-1 Structure of speed controller

5.2.3 Design of the IESO

To further address the issue mentioned in Chapter 2, an IESO was proposed to reduce the noise and estimation error in the position observer caused by the arctan function. Furthermore, the load disturbance could be detected and feedback to the speed controller by the IESO. The motion equation of the PMSynRM can be expressed as Eq.n 5.2-7:

$$T_e - T_L - T_F = \frac{J}{n_p} \frac{d\omega_e}{dt} \quad \text{Eq.n 5.2-7}$$

where T_e represents the electrical torque, T_L represents the load disturbance, T_F represents the friction torque caused by air friction, J represents the inertia of the machine, n_p represents the pole pairs of the machine.

In this part, the proposed IESO will be compared with the traditional ESO and the influence on the system will also be analyzed. A three order ESO was established to observe the position and the load disturbance. Specially, select $x_1 = \theta_{\text{earc}}$, $x_2 = \omega_e$, $d(t) = \hat{T}_L$. Then, the observed angle $\hat{\theta}_{\text{eeso}}$ and lumped torque

disturbance \hat{T}_L from the ESO will be feedback to the speed controller. In this way, the position error and noise from the original position signal θ_{earc} could be reduced and the detected lumped torque disturbance \hat{T}_L could help to improve the dynamic response in a time manner.

The traditional ESO could be constructed as Eq.n 5.2-8.

$$\begin{cases} e = \hat{\theta}_{\text{eeso}} - \hat{\theta}_{\text{earc}} \\ \dot{\hat{\theta}} = \hat{\omega}_m - \beta_1 e \\ \dot{\hat{\omega}}_m = \frac{1}{J} \left[\frac{3}{2} n_p (\psi_d i_q - \psi_q i_d) - \hat{T}_L - \beta_2 e \right] \\ \dot{\hat{T}}_L = -\beta_3 e \end{cases} \quad \text{Eq.n 5.2-8}$$

where $\beta_1, \beta_2, \beta_3$ are the gains of the ESO; T_L is the lumped torque disturbance.

The error dynamic of the conventional ESO was shown in Fig. 5.2-2.

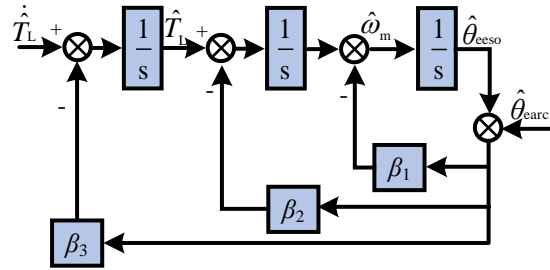


Fig. 5.2-2 Error dynamics of conventional ESO

To ensure the convergence of the traditional ESO, the parameter of the ESO is selected as Eq.n 5.2-9.

$$[\beta_1 \ \beta_2 \ \beta_3]^T = [3\omega_0 \ 3\omega_0^2 \ \omega_0^3]^T \quad \text{Eq.n 5.2-9}$$

where ω_0 is the bandwidth of the observer, and $\omega_0 > 0$ should be satisfied to guarantee the convergence of the controller. For the parameter selection of the IESO, the details will be discussed in Chapter 5.2.5 and Chapter 5.2.6 according to its characteristics.

Given the recognition of disturbances and nonlinearity as a collective disturbance, this study introduces an IESO characterized by a novel architecture

aimed at segregating the estimation of disturbances from state reconstruction. Furthermore, a high frequency noise suppression link is incorporated within the IESO framework to mitigate the influence on the noise. The proposed IESO thus constitutes a comprehensive approach to address the issues associated with disturbance estimation and state reconstruction. The structure of the IESO could be expressed as Eq.n 5.2-10.

$$\begin{aligned}
 \dot{\hat{x}}_1 &= \hat{x}_2 + \beta_1 x_{\theta f} \\
 \dot{\hat{x}}_2 &= u + \beta_2 x_{\theta f} \\
 \dot{\hat{x}}_3 &= k_3 \beta_2 x_{\theta f} \\
 \dot{x}_{\theta f} &= -\frac{1}{\tau} x_{\theta f} + \frac{1}{\tau} [y_o - \hat{y}] \\
 \hat{y} &= \hat{x}_1
 \end{aligned}
 \tag{Eq.n 5.2-10}$$

where x_f represents the state variable, τ denotes the filter depth associated with the noise suppression link, and k serves as a tuning factor for adjusting the disturbance estimation. To further understand the proposed IESO, the error dynamic of the proposed IESO is shown in Fig. 5.2-3.

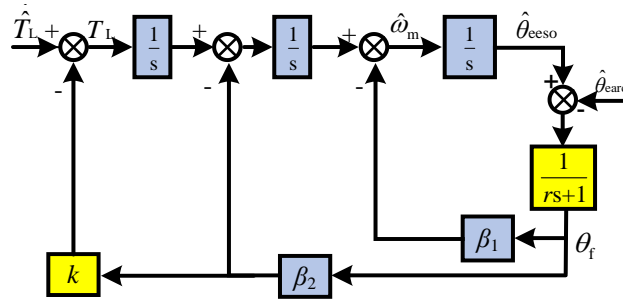


Fig. 5.2-3 Error dynamic of the IESO

As can be seen from Fig. 5.2-3, a LPF was arranged to filter out high-frequency noise from position signals, and the parameter k was used to set the amplifier gain to change the tracking performance of the IESO. In the conventional ESO methods described in [135,136], the calculation of θ_{eeso} relies solely on the integration of e . However, to maintain the system's resistance to

disturbances, this approach necessitates the use of a wide bandwidth, inevitably introducing more noise into the system. Consequently, when the system encounters rapid and unexpected load changes, the observational accuracy significantly diminishes.

In contrast, in the proposed IESO, e is defined as error of the observed angle and the calculated angle after passing through a low-pass filter. In this way, the high frequency noise could be reduced from setting the depth of the filter in an appropriate way. So, the IESO features a better anti-disturbance ability resulting in superior dynamic characteristics and greater observational precision.

From the block diagram shown in Fig. 5.2-3, the transfer function of the IESO could be expressed as Eq.n 5.2-11.

$$\begin{cases} \dot{\hat{\theta}}_{\text{eeso}} = \hat{\omega}_m + \beta_1 \theta_f \\ \dot{\hat{\omega}}_m = \frac{1}{J} \left(\frac{3}{2} n_p (\psi_d i_q - \psi_q i_d) - \hat{T}_L - \beta_2 \theta_f \right) \\ \dot{\hat{T}}_L = k \beta_2 \theta_f \\ \dot{\theta}_f = -\frac{1}{\tau} \theta_f + \frac{1}{\tau} [\hat{\theta}_{\text{earc}} - \hat{\theta}_{\text{eeso}}] \\ \hat{y} = \hat{T}_L \end{cases} \quad \text{Eq.n 5.2-11}$$

5.2.4 Overall control scheme design

To further improve the dynamic response of the control system, the designed IESO will replace the traditional PLL link. In this way, the observed position features a high accurate and smaller phase lag because the LPF is not needed, which may cause large phase delay. Furthermore, the lumped torque disturbance could be observed from the IESO in a time manner so that the transient performance could be guaranteed. The overall control diagram is shown in Fig. 5.2-4.

from the IESO. After that, the given current will be generated, and the inverter part will generate the voltage according to the given current through a current PI controller. Then, the machine will work. The EEMF will calculate the back EEMF of the machine, and the position will be learned from an arctan function. However, this position signal usually contains a lot of noise, the IESO will reduce this noise and feedback the observed signal to the controller. Simultaneously, the IESO will observe the load disturbance and feedback to the speed controller.

In the working process of the controller, the stability of it should be guaranteed, which mainly contains three parts: the speed controller, the EEMF, and the IESO. The stability of these three parts will be analyzed in the next Chapter 5.2.5.

5.2.5 Analysis on Load Disturbance Observation Performance

As discussed in Chapter 1.4.2, the load disturbance observation performance will influence the dynamic response of the control system. In this part, the performance of the proposed IESO will be analyzed compared to the conventional ESO. The transfer function from $\hat{T}_L(t)$ to $\hat{\hat{T}}_L(t)$ for the conventional ESO can be obtained as Eq.n 5.2-12.

$$G_{LT}(s) = \frac{s^2 + 3\omega_0 s + 3\omega_0^2}{s^3 + 3\omega_0 s^2 + 3\omega_0^2 s + \omega_0^3} \quad \text{Eq.n 5.2-12}$$

As for the IESO, the transfer function from $\hat{T}_L(t)$ to $\hat{\hat{T}}_L(t)$ could be obtained as Eq.n 5.2-13.

$$G_{LT}(s) = \frac{\tau s^3 + s^2 + 2\omega_0 s + \omega_0^2}{\tau s^4 + s^3 + 2\omega_0 s^2 + \omega_0^2 s + k\omega_0^2} \quad \text{Eq.n 5.2-13}$$

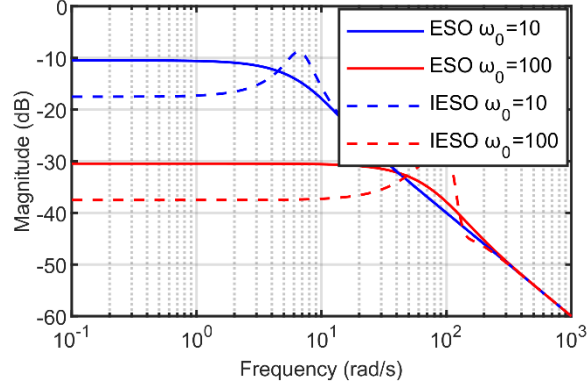


Fig. 5.2-5 Error dynamic response for torque disturbance of ESO and IESO

As can be seen in Eq.n 5.2-13, the IESO introduces two novel coefficients, k and τ , for refining the accuracy of perturbation forecasts, in contrast to the traditional ESO reliance on the frequency domain indicator ω_0 for this purpose. For comparison with the conventional ESO, $k = 0.75\omega_0$ and $\tau = 0.01$ are set to investigate the disturbance-estimation ability of the proposed IESO. As can be seen in Fig. 5.2-5, the observation error was suppressed with the increasing of ω_0 . Fig. 5.2-5 illustrates the superior efficacy of the IESO over the traditional ESO at lower frequency ranges under identical ω_0 conditions. Specifically, at $\omega_0 = 100$, the gain of the loop transfer function $G_{LT}(s)$ is approximately -38 dB for the IESO, compared to -30 dB for the traditional ESO, signifying a more precise estimation of disturbances by the former. In other words, the gain ω_0 is smaller for the IESO than for the ESO to get the same performance in low frequencies.

Then, the noise suppression ability will be analyzed. The transfer function from $\hat{\theta}_{\text{earc}}(t)$ to $\hat{T}_L(t)$ for the conventional ESO can be obtained as Eq.n 5.2-14.

$$G_{HT}(s) = \frac{-\omega_0^3 s^2}{s^3 + 3\omega_0 s^2 + 3\omega_0^2 s + \omega_0^3} \quad \text{Eq.n 5.2-14}$$

As for the IESO, the transfer function from $\hat{\theta}_{\text{earc}}(t)$ to $\hat{T}_L(t)$ could be

obtained as Eq.n 5.2-15.

$$G_{HT}(s) = \frac{-k\omega_0^2 s^2}{\tau s^4 + s^3 + 2\omega_0 s^2 + \omega_0^2 s + k\omega_0^2} \quad \text{Eq.n 5.2-15}$$

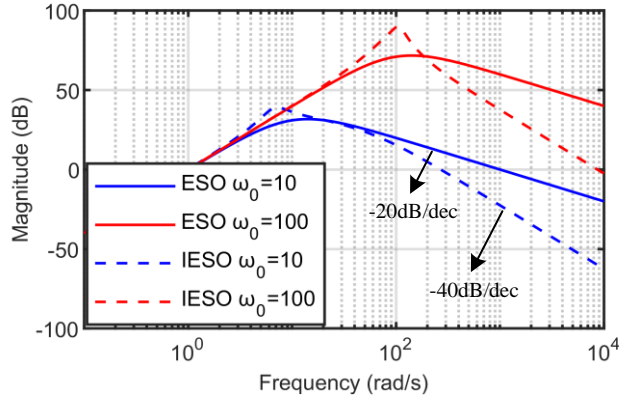


Fig. 5.2-6 Error suppression response of ESO and IESO

Fig. 5.2-6 depicts the frequency response curves for noise attenuation with parameters set at $k=0.75\omega_0$ and $\tau=0.01$. At higher frequency ranges, the IESO outperforms the ESO in terms of noise reduction when both operate under an equivalent ω_0 setting. Consequently, to match the disturbance estimation accuracy of the IESO, the ESO requires a higher value of ω_0 .

For instance, when $\omega_0 = 100$ rad/s, the magnitude of $G_{HT}(s)$ approximates 0 dB for the ESO and 42 dB for the IESO at high frequencies. This indicates that the IESO obtains a better noise suppression ability than the ESO. Furthermore, the slope of the IESO is -40dB/dec, while -20dB/dec for ESO, this suggests that the IESO demonstrates enhanced efficacy in mitigating high frequency noises. In numerous practical scenarios, load disturbances predominantly manifest as low frequency, whereas high frequency pertains to unmeasurable noises. The IESO offers a dual advantage: it enables both disturbance rejection and noise attenuation concurrently.

In comparison to the ESO, the IESO is distinguished by three primary innovations. Firstly, it incorporates a disturbance-estimation module seamlessly into an existing observer framework without necessitating any alterations to its parameters. This integration facilitates avoidance of a high-gain configuration, simplifying implementation. Secondly, the introduction of a novel parameter allows for fine-tuning of the disturbance-estimation accuracy, thereby enhancing the IESO's design flexibility. Thirdly, the adoption of low-pass filters to eliminate high-frequency elements from the measurement output results in a reduced magnitude at elevated frequencies relative to the ESO, consequently elevating the noise suppression capability.

5.2.6 Analysis on Position Observation Performance

As discussed in Chapter 5.2.5, the position observation performance will influence the dynamic response of the control system. In this part, the performance of the proposed IESO will be analyzed compared to the conventional ESO. The transfer function from $\hat{T}_L(t)$ to $\hat{\theta}_{eeso}(t)$ for the conventional ESO can be obtained as Eq.n 5.2-16.

$$G_{L\theta}(s) = \frac{1}{s^3 + 3\omega_0 s^2 + 3\omega_0^2 s + \omega_0^3} \quad \text{Eq.n 5.2-16}$$

As for the IESO, the transfer function from $\hat{T}_L(t)$ to $\hat{\theta}_{eeso}(t)$ could be obtained as Eq.n 5.2-17.

$$G_{L\theta}(s) = \frac{\tau s + 1}{\tau s^4 + s^3 + 2\omega_0 s^2 + \omega_0^2 s + k\omega_0^2} \quad \text{Eq.n 5.2-17}$$

Compared with the conventional ESO, $k = 0.75\omega_0$ and $\tau = 0.01$ are set to research the position estimation ability of the IESO. As can be seen in Fig. 5.2-7, the error decreases with the increasing of ω_0 .

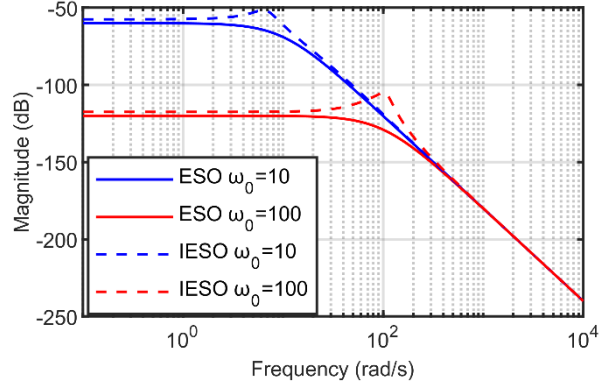


Fig. 5.2-7 Error dynamic response for position of ESO and IESO

Fig. 5.2-7 shows that the position error estimation ability for IESO is almost the same as ESO does. It means that the position observation error is almost the same when a load disturbance is added. As for the high frequency observation ability, the performance is the same.

Then, the noise suppression ability will be analyzed. The transfer function from $\hat{\theta}_{\text{earc}}(t)$ to $\hat{\theta}_{\text{eso}}(t)$ for the conventional ESO can be obtained as .Eq.n 5.2-18.

$$G_{H\theta}(s) = \frac{-3\omega_0 s^2 - 3\omega_0^2 s - \omega_0^3}{s^3 + 3\omega_0 s^2 + 3\omega_0^2 s + \omega_0^3} \quad \text{Eq.n 5.2-18}$$

As for the IESO, the transfer function from $\hat{\theta}_{\text{earc}}(t)$ to $\hat{T}_L(t)$ could be obtained as Eq.n 5.2-19.

$$G_{H\theta}(s) = \frac{-2\omega_0 s^2 - \omega_0^2 s - k\omega_0^2}{\tau s^4 + s^3 + 2\omega_0 s^2 + \omega_0^2 s + k\omega_0^2} \quad \text{Eq.n 5.2-19}$$

Fig. 5.2-8 illustrates the frequency responses related to noise reduction using parameters $k = 0.75\omega_0$ and $\tau = 0.01$. It reveals that the IESO surpasses the ESO in noise-suppression efficiency at higher frequencies under an identical ω_0 setting. Conversely, to achieve comparable levels of disturbance estimation accuracy, the required ω_0 for the ESO must be lower than that for the IESO. For

instance, when $\omega_0 = 100$, the magnitude of $G_{H\theta}(s)$ approximates -72 dB for the IESO and -30 dB for the ESO at high frequencies. This indicates that the IESO obtains a better noise suppression ability than the ESO. Furthermore, the slope of the IESO is -40dB/dec, while -20dB/dec for ESO, which indicates that the IESO features a better noise suppression ability at high frequency.

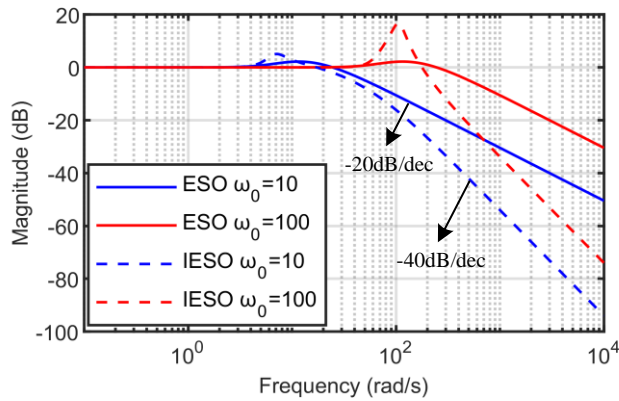


Fig. 5.2-8 Error suppression response for position observation of ESO and IESO

5.2.7 Analysis on System Stability

As described in Chapter 2, regarding the PMA-SynRM system as linear, in which the nonlinearity was not discussed in this part. To ensure the stability of the system, the stability of the control system should be satisfied, as well as the IESO and the EEMF observer. The control system is based on the PI controller and a LUT, where the stability analysis can refer to [137], and the stability of the EEMF can refer to. This part will discuss the stability of IESO under the PMA-SynRM control system in a detail way.

There is an equivalent stability of the IESO system to make the control system stable. The stability constraints could be rewritten as Eq.n 5.2-20.

$$\tau s^4 + s^3 + \beta_1 s^2 + \beta_2 s + k\beta_2 = 0 \quad \text{Eq.n 5.2-20}$$

To make Eq.n 5.2-20 satisfied, Eq.n 5.2-21 could be obtained.

$$\beta_1 > k + \tau\beta_2 \quad \text{Eq.n 5.2-21}$$

According to the Routh–Hurwitz theorem, Eq.n 5.2-22 should be satisfied.

$$\frac{k}{\omega_0} + \tau\omega_0 < 2 \quad \text{Eq.n 5.2-22}$$

where, $\tau > 0$ and $k > 0$ should be satisfied.

Furthermore, the overall stability of the control system must be considered, indicating that the cut-off frequency of the IESO needs to be sufficiently higher than the cut-off frequency of the speed loop. This requirement ensures both the stability, and the dynamic responsiveness of the control system are maintained.

For the step-load torque disturbance, the error dynamics have been discussed in Chapter 5.1-7, the steady-state error is zero for both the ESO and IESO. But for the ramp load disturbance, the error of the ESO could be assumed as $3C/\omega_0$, where C is slope of the ramp. For the IESO, the error of the ESO could be assumed as C/k , which is generally smaller than the ESO does.

5.2.8 Analysis on Parameter Selection

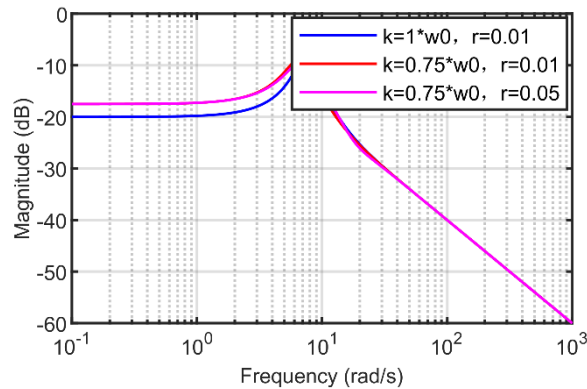


Fig. 5.2-9 Error dynamics with different k and τ

It is important to acknowledge that simultaneously ensuring accuracy in observation, responsiveness, and effective noise suppression is often challenging. Therefore, a thorough analysis of the impact of various parameters on these characteristics is essential to achieve an optimal balance among them. The

primary focus should be on the capability to observe torque disturbances and minimum noise in position effectively. The objective here is to maintain superior noise suppression while simultaneously minimizing observation errors.

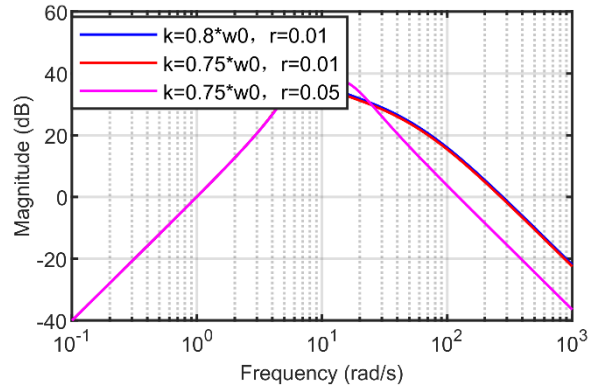


Fig. 5.2-10 Noise suppression with different k and τ

Fig. 5.2-9 and Fig. 5.2-10 show the parameters relationship between the error dynamics and the noise suppression ability in the low frequency and high frequency domain with respect to the torque disturbance estimation performance, respectively. k has little influence on the noise suppression ability while τ directly determines the noise response of high frequency domain. In summary, τ need to be adjusted to determine the high frequency response and k need to be adjusted to determine the low frequency response for the PMA-SynRM.

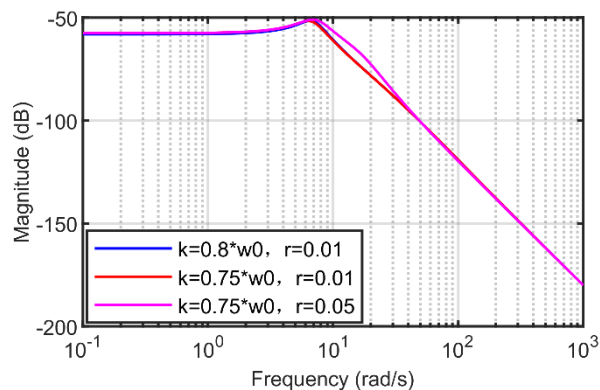


Fig. 5.2-11 Error dynamics for position with different k and τ

On the other hand, the position signal observation ability is another key point that should be considered. Fig. 4.2-11 shows the influence on the position

observation error and Fig. 5.2-12 shows the noise suppression ability with different k and τ .

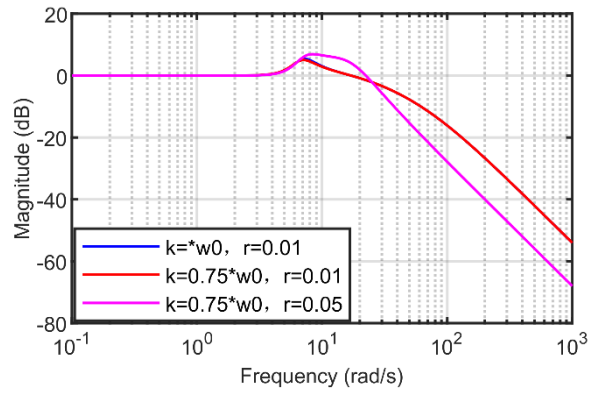


Fig. 5.2-12 Noise suppression for position with different k and τ

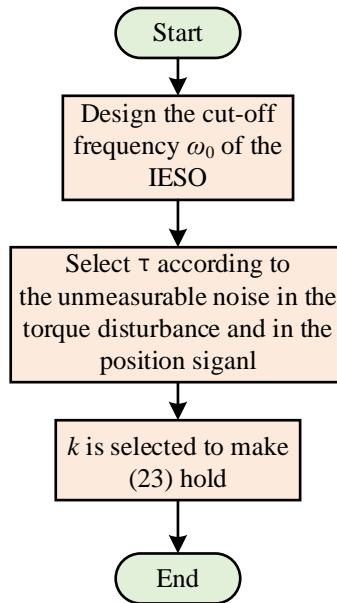
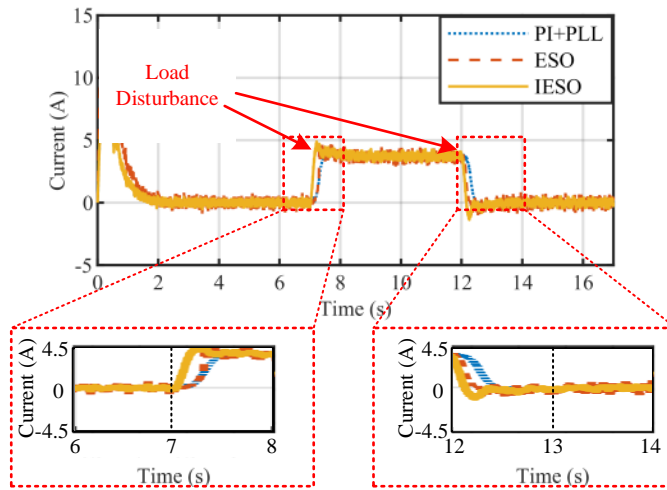
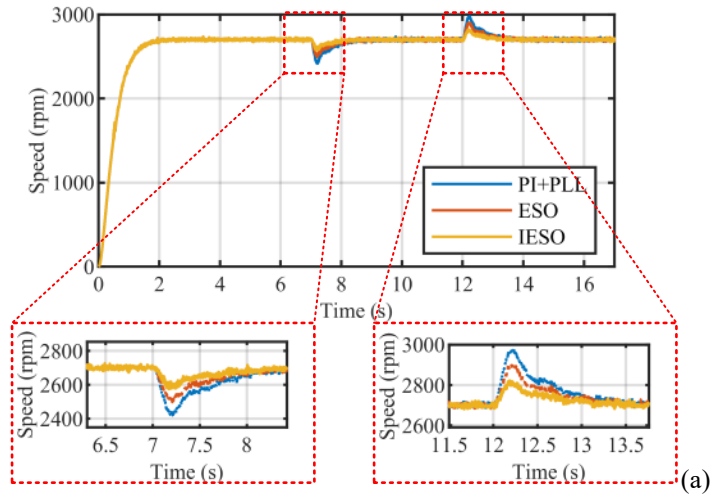


Fig. 5.2-13 Parameter selection procedure

From Fig. 5.2-11 and Fig. 5.2-12, the k and τ have little influence on the position error. But for the noise suppression ability, τ plays a vital role. It could be concluded that parameter τ only need to be considered in the position error selection. In general, the signal to noise ratio of the measurement sensor should be considered, thus τ could be decided. Then, k decided to meet Eq.n 5.2-22. Fig. 5.2-13 shows the steps of the parameter selection process.

5.2.9 Experiments Verification



(b)

Fig. 5.2-14 Speed and current response for the step load

To verify the effectiveness of improving the dynamic response performance of the control system, comparison experiments of PI+PLL, conventional ESO, and IESO control were carried out to research the effectiveness of the proposed control strategies. Fig. 5.2-14 shows the speed and current response for a step load from 0 Nm to 1.9 Nm and reverse load.

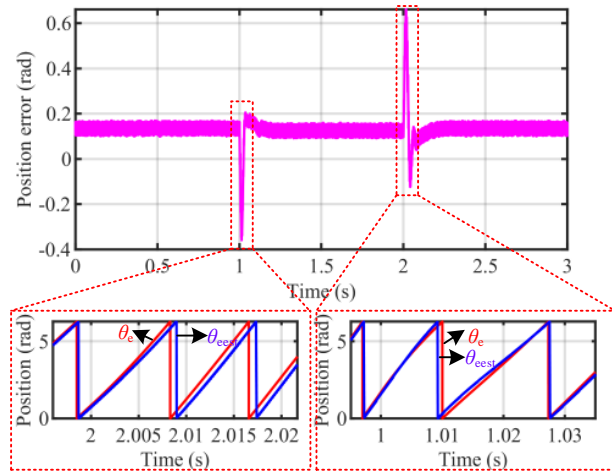
From Fig. 5.2-14, it could be observed that the proposed IESO features a fast dynamic response compared to the ESO and PI+PLL group. For IESO group, it takes 0.2 s to get the steady state in the loading process, while 0.24 s and 0.25 s separately for the ESO and PI+PLL group. Furthermore, it takes 0.21 s to

stabilize, while 0.23 s and 0.26 s separately in the unloading process. This is because that the PI+PLL contains no feedforward loop compared to the ESO and IESO. For the IESO, the improved structure makes it takes less time to converge, so that the fast dynamic response could be obtained. Meanwhile, the current feedback could further verify the method.

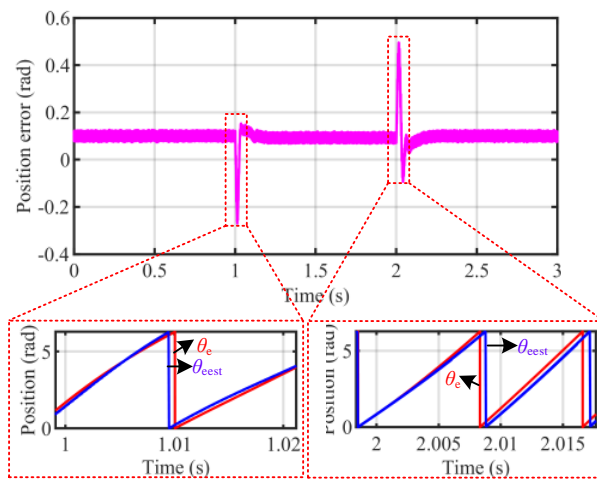
A. Position Estimation Comparison

Fig. 5.2-15 shows the position observation results for different methods including PI+PLL, ESO and IESO group.

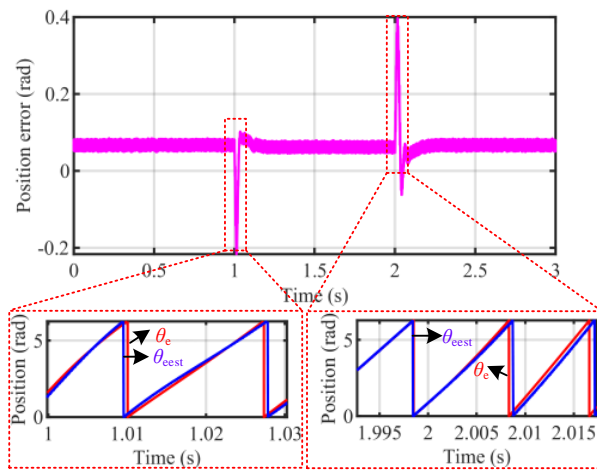
Fig. 5.2-15(a) to (c) present a comparative analysis of position estimation inaccuracies, alongside real and predicted positions during abrupt peak-load torque scenarios, evaluating the performance of the proposed IESO techniques. (a) highlights that the PLL observer integrated with a PI controller exhibits a mean position estimation inaccuracy of roughly 0.136 radians, indicating a high susceptibility to variations in load torque. In a stark contrast, (b) and (c) show that the mean errors in position estimation for the ESO and IESO methodologies are substantially reduced, marked at merely 0.1 radians and 0.067 radians, respectively. Impressively, the accuracy in estimation by the IESO improves by 33% over the ESO. The ESO's peak position estimation discrepancy, which spikes to 0.49 radians amid step peak-load torque conditions, suggests a risk of inadequate estimation precision, potentially impairing stability, and dynamic efficacy. On the other hand, the IESO significantly counters this challenge, limiting its peak error in position estimation to 0.42 rad thanks to the better anti-disturbance ability. According to standard benchmarks, motor control efficacy is



(a)



(b)



(c)

Fig. 5.2-15 Sensor-less performance of a step load (a) PLL+PI group (b) ESO group (c)IESO group

deemed satisfactory when the error in rotor position estimation does not exceed 10° , making the stability of the PLL+PI, ESO, and IESO could be guaranteed.

Summarily, the IESO outshines traditional sensor-less approaches in terms of both steady and transient performance metrics.

B. Noise Suppression Ability Verification

In Chapter 5.2.9A, the position observation ability was verified by the experiments. In this part, the noise suppression ability will be further tested.

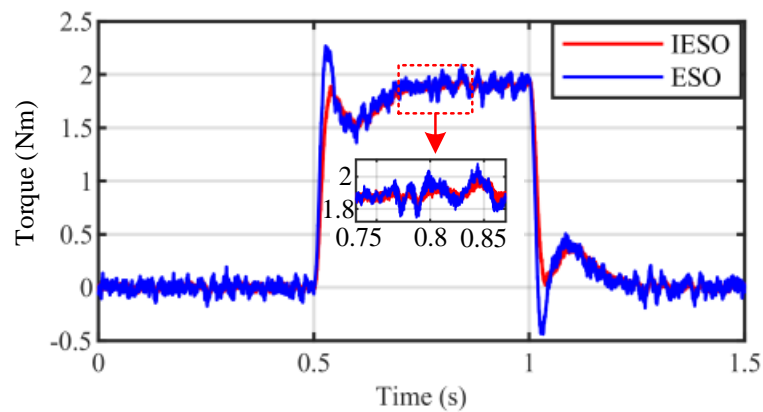


Fig. 5.2-16 Response of ESO and IESO under current noise

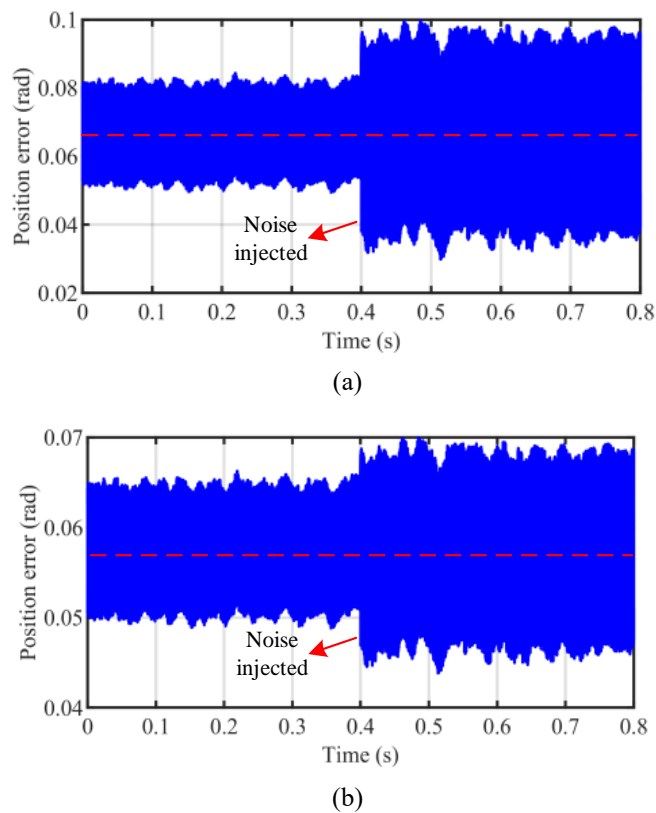


Fig. 5.2-17 Position error under injected noise (a) response for ESO; (b) response for IESO

The influence of the current signal noise was simulated from the MATLAB,

the same level of current noise, which occupies 10% of the rated current, was injected into the ESO and IESO to observe the response of the torque observation. Fig. 5.2-17 shows the result of it. In the simulation, the same response time was adjusted to observe the anti-disturbance ability. It could be got that the IESO features a better anti-disturbance ability under the same dynamic response.

From the analysis in Chapter 5.2.3, the current generally has a big influence on torque observation because the current directly influences the torque calculations. The variation of the torque on the position observation could be regarded as the changing of the torque under the current noise. The influence of it could be referred to the experiments part. And it will not be discussed here.

To verify the influence of the position noise on the position observation ability, the simulation was done. In the simulation, the high frequency white noise of position signal was injected into the input of the ESO and the IESO. The results are shown in Fig. 5.2-17. It could be observed that the position error increases with the noise injection. For the ESO, it is 18.6%. However, for the IESO, it is 6.2% under the same position noise level. It could be concluded that the IESO features a better noise suppression ability from 18.6% to 6.2% under rated speed for position observation.

5.3 Chapter Summary

This chapter presents the development of an advanced MTPA and FW control strategy for PMa-SynRMs, utilizing an A-DESO combined with a LUT. The proposed control strategy demonstrates superior performance, featuring reduced steady-state errors, fast dynamic response, high resilience against load

disturbances, and effective suppression of current and position signal noise. Compared to traditional ESO methods, the A-DESO offers improved low-frequency observation accuracy and stronger high-frequency noise suppression, leading to better stability in both MTPA and FW regions. The strategy also mitigates the issue of rebounding between operational conditions. Rigorous stability proofs and error analyses were conducted, accounting for parameter mismatches, and the parameter calculation method for PMA-SynRM was outlined. Experimental results indicate a significant reduction in overshoot by 63 rpm and a 0.2-second decrease in convergence time within the MTPA region.

Additionally, this study explored a sensor-less control method aimed at improving the dynamic response, reliability, and cost-efficiency of PMA-SynRMs. Traditional sensor-less approaches using EEMF and PLL often result in position observation errors and phase lags. To overcome these limitations, an innovative control topology was proposed, integrating an arctangent function for angle calculation and an IESO to suppress noise in the position signal and accurately monitor torque disturbances. The IESO demonstrated enhanced low-frequency gain and noise suppression capabilities, significantly reducing observation errors and phase lags compared to conventional ESO and PLL techniques.

The proposed A-DESO and IESO control schemes were validated through comprehensive simulations and experiments, confirming substantial improvements in system performance, including better speed regulation, reduced fluctuations, and enhanced noise suppression. This research offers valuable

contributions to sensor-less control strategies for PMA-SynRMs, optimizing their performance and reliability across various industrial applications.

Chapter 6 Conclusions and Further Work

6.1 Summary of this Thesis

This thesis presented a comprehensive study of Permanent Magnet-Assisted Synchronous Reluctance Motors (PMA-SynRMs), focusing on their characteristics and control strategies. PMA-SynRMs have emerged as a promising alternative to conventional motors like IPMSMs and SynRMs, offering a balance between cost and performance due to their reduced reliance on rare-earth materials and improved efficiency.

The introductory chapter provided a detailed background on the motivations for studying PMA-SynRMs, highlighting the technical and economic benefits compared to IPMSMs and SynRMs. It was noted that while IPMSMs offer high efficiency and performance, they are costly due to the use of rare-earth magnets. SynRMs, on the other hand, are cost-effective but lack the same efficiency and power density. PMA-SynRMs were introduced as a hybrid solution that incorporates the reluctance torque of SynRMs and the permanent magnet torque of IPMSMs, using ferrite materials to enhance performance without significantly increasing costs.

Subsequent chapters delved into the technical principles and performance characteristics of these motors. A comparison of IPMSM, SynRM, and PMA-SynRM was carried out to elucidate their respective advantages and application areas. It was found that PMA-SynRMs, with their combined benefits of high power factor, efficiency, and lower cost, are particularly suitable for applications requiring high reliability and moderate cost considerations, such as new energy

vehicles and industrial drive systems.

A significant portion of the thesis focused on addressing the inherent challenges in controlling PMA-SynRMs, such as their high degree of nonlinearity and parameter uncertainties. The proposed advanced control strategies effectively tackled issues like inductance variation, magnetic saturation, and cross-saturation. Through the development of more precise motor models, the research successfully enhanced steady-state performance using optimized MTPA control, with an improvement in MTPA angle ripple reduction by up to 12%. Meanwhile, the stator current reduced 1.52% with the same torque output adopting the proposed MTPA angle error compensation method. Furthermore, the dynamic response was improved by increasing anti-disturbance robustness and minimizing convergence times during large torque fluctuations, with a reduction in response time from 0.6 seconds to 0.4 seconds under specific test conditions.

In conclusion, this thesis successfully demonstrated the potential of PMA-SynRMs as a cost-effective, high-performance alternative to traditional motors. The research provided a solid foundation for their control strategies and practical applications, offering valuable insights that underline the motors' suitability for a wide range of industrial uses. These findings contribute to the growing body of knowledge and lay a robust foundation for further advancements in the field.

6.2 Further Work

Despite the significant advancements presented in this thesis, several areas warrant further exploration to fully harness the potential of PMA-SynRMs.

Future research should focus on the following aspects:

a) Based on the proposed PMA-SynRM model, advanced control including sensor-less control, MTPA control, FW control, sliding mode control could be designed based on the proposed one.

b) For the PRFSI method, the BPF could be improved to get a better high frequency current control performance, because the tracking delay existed for the traditional one.

c) For the online tracking MTPA control, the steady-state error could be further researched and compensated for a smaller steady-state error.

d) the ESO could be designed based on the proposed model, and the non-linear characteristics could be further analyzed.

REFERENCE

- [1] A. H. T. and F. H. M., "Comparative study of pm-assisted synrm and ipmsm on constant power speed range for ev applications," *Ieee Transactions On Magnetics*, vol. 53, no. 11, pp. 1-6, 2017, 10.1109/TMAG.2017.2707125.
- [2] S. S., N. B., T. N., P. S., and M. P. *et al.*, "Model-based control of permanent-magnet assisted synchronous reluctance motors," in *2019 Research, Invention, and Innovation Congress (RI2C)*, 2019, pp. 1-6.
- [3] T. A. Huynh and M. Hsieh, "Comparative study of pm-assisted synrm and ipmsm on constant power speed range for ev applications," *Ieee Transactions On Magnetics*, vol. 53, no. 11, pp. 1-6, 2017, 10.1109/TMAG.2017.2707125.
- [4] G. B. Da Silveira, I. P. Wiltuschnig, R. P. Homrich, A. F. Flores Filho, and A. T. Salton *et al.*, "A comparative performance study of high-speed synrm and pma-synrm rare-earth and rare-earth-less permanent magnets for automotive traction," in *IEEE*, 2024, pp. 1-2.
- [5] L. N., K. T., A. K., and D. L. R., "Design and evaluation of a variable-flux flux-intensifying interior permanent-magnet machine," *Ieee Transactions On Industry Applications*, vol. 50, no. 2, pp. 1015-1024, 2014, 10.1109/TIA.2013.2273482.
- [6] M. T., S. G., and S. B., "Analyzing the magnetic flux linkage characteristics of alternating current rotating machines by experimental method," *Ieee Transactions On Magnetics*, vol. 47, no. 9, pp. 2283-2291, 2011, 10.1109/TMAG.2011.2146266.
- [7] C. H., Y. W., and W. Q., "Electromagnetic analysis of flux characteristics of double-sided switched reluctance linear machine," *Ieee Transactions On Applied Superconductivity*, vol. 26, no. 4, pp. 1-7, 2016, 10.1109/TASC.2016.2539215.
- [8] Y. L. J., W. K. J., R. M. S., H. C. J., and U. C. S. *et al.*, "Dynamic characteristic analysis considering core losses in transverse flux linear machine with solid cores," *Ieee Transactions On Magnetics*, vol. 45, no. 3, pp. 1776-1779, 2009, 10.1109/TMAG.2009.2012819.
- [9] C. Gallardo, J. A. Tapia, M. Degano, and H. Mahmoud, "Accurate analytical model for synchronous reluctance machine with multiple flux barriers considering the slotting effect," *Ieee Transactions On Magnetics*, vol. 58, no. 9, pp. 1-9, 2022, 10.1109/TMAG.2022.3189483.
- [10] W. Liang, W. Fei, and P. C. Luk, "An improved sideband current harmonic model of interior pmsm drive by considering magnetic saturation and cross-coupling effects," *Ieee Transactions On Industrial Electronics*, vol. 63, no. 7, pp. 4097-4104, 2016, 10.1109/TIE.2016.2540585.
- [11] J. H. Seo and H. S. Choi, "Analytical modeling for calculating cogging torque in interior permanent magnet machine with multi flux-barriers," *Ieee Transactions On Applied Superconductivity*, vol. 24, no. 3, pp. 1-4, 2014, 10.1109/TASC.2014.2304835.
- [12] G. Liu, Y. Wang, Q. Chen, G. Xu, and D. Cao, "Design and analysis of a new equivalent magnetic network model for ipm machines," *Ieee Transactions On Magnetics*, vol. 56, no. 6, pp. 1-12, 2020, 10.1109/TMAG.2020.2987546.
- [13] Y. Guo, L. Pan, Y. Yang, Y. Gong, and X. Che *et al.*, "Flux saturation model identification for synrms with deadtime effect compensation and more appropriate

- injection voltage selecting, " *Ieee Transactions On Power Electronics*, vol. 39, no. 1, pp. 309-319, 2024, 10.1109/TPEL.2023.3322107.
- [14] Y. Guo, L. Pan, Y. Yang, Y. Gong, and X. Che *et al.*, "Flux saturation model identification for synrms with deadtime effect compensation and more appropriate injection voltage selecting, " *Ieee Transactions On Power Electronics*, vol. 39, no. 1, pp. 309-319, 2024, 10.1109/TPEL.2023.3322107.
- [15] T. Woo, S. Park, S. Choi, H. Lee, and Y. Yoon, "Flux saturation model including cross saturation for synchronous reluctance machines and its identification method at standstill, " *Ieee Transactions On Industrial Electronics (1982)*, vol. 70, no. 3, pp. 2318-2328, 2023, 10.1109/TIE.2022.3174233.
- [16] D. Hu, Y. M. Alsmadi, and L. Xu, "High-fidelity nonlinear ipm modeling based on measured stator winding flux linkage, " *Ieee Transactions On Industry Applications*, vol. 51, no. 4, pp. 3012-3019, 2015, 10.1109/TIA.2015.2407864.
- [17] E. Levi, "Impact of cross-saturation on accuracy of saturated induction machine models, " *Ieee Transactions On Energy Conversion*, vol. 12, no. 3, pp. 211-216, 1997, 10.1109/60.629705.
- [18] E. Levi and V. A. Levi, "Impact of dynamic cross-saturation on accuracy of saturated synchronous machine models, " *Ieee Transactions On Energy Conversion*, vol. 15, no. 2, pp. 224-230, 2000, 10.1109/60.867004.
- [19] M. Fasil, C. Antaloae, N. Mijatovic, B. B. Jensen, and J. Holboll, "Improved dq-axes model of pmsm considering airgap flux harmonics and saturation, " *Ieee Transactions On Applied Superconductivity*, vol. 26, no. 4, pp. 1-5, 2016, 10.1109/TASC.2016.2524021.
- [20] Z. Liu, X. Fan, W. Kong, L. Cao, and R. Qu, "Improved small-signal injection-based online multiparameter identification method for ipm machines considering cross-coupling magnetic saturation, " *Ieee Transactions On Power Electronics*, vol. 37, no. 12, pp. 14362-14374, 2022, 10.1109/TPEL.2022.3192692.
- [21] S. Park, T. Woo, S. Choi, H. Lee, and Y. Yoon, "Mitigating rotor movement during estimation of flux saturation model at standstill for ipmsms and synrms, " *Ieee Transactions On Industrial Electronics*, vol. 70, no. 2, pp. 1171-1181, 2023, 10.1109/TIE.2022.3159918.
- [22] S. Li, D. Han, and B. Sarlioglu, "Modeling of interior permanent magnet machine considering saturation, cross coupling, spatial harmonics, and temperature effects, " *Ieee Transactions On Transportation Electrification*, vol. 3, no. 3, pp. 682-693, 2017, 10.1109/TTE.2017.2679212.
- [23] M. Petrun, S. Steentjes, K. Hameyer, and D. Dolinar, "Modeling of magnetization dynamics using saturation wavefronts, " *Ieee Transactions On Magnetics*, vol. 53, no. 4, pp. 1-4, 2017, 10.1109/TMAG.2016.2618947.
- [24] A. Accetta, M. Cirrincione, M. Pucci, and A. Sferlazza, "Space-vector state dynamic model of the synrm considering self, cross-saturation and iron losses and related identification technique, " *Ieee Transactions On Industry Applications*, vol. 59, no. 3, pp. 3320-3331, 2023, 10.1109/TIA.2023.3252528.
- [25] L. Zhu, J. Park, and C. Koh, "A dynamic hysteresis model based on vector-play model for iron loss calculation taking the rotating magnetic fields into account, " *Ieee Transactions On Magnetics*, vol. 54, no. 3, pp. 1-4, 2018,

- 10.1109/TMAG.2017.2748961.
- [26] Y. Liu and A. M. Bazzi, "A general analytical three-phase induction machine core loss model in the arbitrary reference frame," *Ieee Transactions On Industry Applications*, vol. 53, no. 5, pp. 4210-4220, 2017, 10.1109/TIA.2017.2695442.
- [27] Q. Zhu, Q. Wu, W. Li, M. Pham, and L. Zhu, "A general and accurate iron loss calculation method considering harmonics based on loss surface hysteresis model and finite-element method," *Ieee Transactions On Industry Applications*, vol. 57, no. 1, pp. 374-381, 2021, 10.1109/TIA.2020.3036017.
- [28] W. Yu, W. Hua, Z. Zhang, Z. Wu, and P. Wang *et al.*, "Comparative analysis of ac copper loss with round copper wire and flat copper wire of high-speed stator-pm flux-switching machine," *Ieee Transactions On Industry Applications*, vol. 58, no. 6, pp. 7131-7142, 2022, 10.1109/TIA.2022.3194042.
- [29] D. Kowal, P. Sergeant, L. Dupre, and L. Vandenbossche, "Comparison of iron loss models for electrical machines with different frequency domain and time domain methods for excess loss prediction," *Ieee Transactions On Magnetics*, vol. 51, no. 1, pp. 1-10, 2015, 10.1109/TMAG.2014.2338836.
- [30] C. Patsios, E. Tsampouris, M. Beniakar, P. Rovolis, and A. G. Kladas, "Dynamic finite element hysteresis model for iron loss calculation in non-oriented grain iron laminations under pwm excitation," *Ieee Transactions On Magnetics*, vol. 47, no. 5, pp. 1130-1133, 2011, 10.1109/TMAG.2010.2073690.
- [31] F. Birnkammer, J. Chen, D. Bachinski Pinhal, and D. Gerling, "Influence of the modeling depth and voltage level on the ac losses in parallel conductors of a permanent magnet synchronous machine," *Ieee Transactions On Applied Superconductivity*, vol. 28, no. 3, pp. 1-5, 2018, 10.1109/TASC.2018.2801292.
- [32] X. Qin, L. Yao, W. Wan, D. Shi, and Y. Wang *et al.*, "Investigation of bessel functions in analytical modeling of rotor eddy current losses in pm machine rotor with copper shield," *Ieee Transactions On Magnetics*, vol. 59, no. 3, pp. 1-9, 2023, 10.1109/TMAG.2023.3239898.
- [33] S. Odawara, S. Yamamoto, K. Sawatari, K. Fujisaki, and Y. Shindo *et al.*, "Iron loss evaluation of reactor core with air gaps by magnetic field analysis under high-frequency excitation," *Ieee Transactions On Magnetics*, vol. 51, no. 11, pp. 1-4, 2015, 10.1109/TMAG.2015.2442984.
- [34] S. Xue, J. Feng, S. Guo, Z. Chen, and J. Peng *et al.*, "Iron loss model for electrical machine fed by low switching frequency inverter," *Ieee Transactions On Magnetics*, vol. 53, no. 11, pp. 1-4, 2017, 10.1109/TMAG.2017.2696360.
- [35] S. Xue, J. Feng, S. Guo, Z. Chen, and J. Peng *et al.*, "Iron loss model under dc bias flux density considering temperature influence," *Ieee Transactions On Magnetics*, vol. 53, no. 11, pp. 1-4, 2017, 10.1109/TMAG.2017.2703587.
- [36] J. Yan, C. Di, X. Bao, and Q. Zhu, "Iron losses model for induction machines considering the influence of rotational iron losses," *Ieee Transactions On Energy Conversion*, vol. 38, no. 2, pp. 971-981, 2023, 10.1109/TEC.2022.3231881.
- [37] S. Steentjes, G. von Pflingsten, M. Hombitzer, and K. Hameyer, "Iron-loss model with consideration of minor loops applied to fe-simulations of electrical machines," *Ieee Transactions On Magnetics*, vol. 49, no. 7, pp. 3945-3948, 2013, 10.1109/TMAG.2013.2244072.

- [38] A. Frias, A. Kedous-Lebouc, C. Chillet, L. Albert, and L. Calegari *et al.*, "Loss minimization of an electrical vehicle machine considering its control and iron losses," *Ieee Transactions On Magnetics*, vol. 52, no. 5, pp. 1-4, 2016, 10.1109/TMAG.2016.2517657.
- [39] H. Zhang, M. Dou, and C. Dang, "Loss-optimization method of permanent-magnet synchronous motor based on precise stator iron loss model," *Ieee Journal of Emerging and Selected Topics in Power Electronics*, vol. 9, no. 5, pp. 5407-5415, 2021, 10.1109/JESTPE.2020.3027864.
- [40] M. Al Eit, P. Dular, F. Bouillault, C. Marchand, and G. Krebs, "Perturbation finite element method for efficient copper losses calculation in switched reluctance machines," *Ieee Transactions On Magnetics*, vol. 53, no. 6, pp. 1-4, 2017, 10.1109/TMAG.2017.2655339.
- [41] S. Hussain and D. A. Lowther, "Prediction of iron losses using jiles – atherton model with interpolated parameters under the conditions of frequency and compressive stress," *Ieee Transactions On Magnetics*, vol. 52, no. 3, pp. 1-4, 2016, 10.1109/TMAG.2015.2487975.
- [42] S. Xue, Z. Q. Zhu, Y. Wang, J. Feng, and S. Guo *et al.*, "Thermal-loss coupling analysis of an electrical machine using the improved temperature-dependent iron loss model," *Ieee Transactions On Magnetics*, vol. 54, no. 11, pp. 1-5, 2018, 10.1109/TMAG.2018.2842708.
- [43] Y. I. S., G. L. S., M. K. D., X. G., and Y. S. S. *et al.*, "Kriging surrogate model-based design of an ultra-high-speed surface-mounted permanent-magnet synchronous motor considering stator iron loss and rotor eddy current loss," *Ieee Transactions On Magnetics*, vol. 58, no. 2, pp. 1-5, 2022, 10.1109/TMAG.2021.3080119.
- [44] Y. Zhou, S. Zhang, C. Zhang, X. Li, and X. Li *et al.*, "Current prediction error based parameter identification method for spmsm with deadbeat predictive current control," *Ieee Transactions On Energy Conversion*, vol. 36, no. 3, pp. 1700-1710, 2021, 10.1109/TEC.2021.3051212.
- [45] S. Wang, X. Shao, L. Yang, and N. Liu, "Deep learning aided dynamic parameter identification of 6-dof robot manipulators," *Ieee Access*, vol. 8, pp. 138102-138116, 2020, 10.1109/ACCESS.2020.3012196.
- [46] G. Gatto, I. Marongiu, and A. Serpi, "Discrete-time parameter identification of a surface-mounted permanent magnet synchronous machine," *Ieee Transactions On Industrial Electronics (1982)*, vol. 60, no. 11, pp. 4869-4880, 2013, 10.1109/TIE.2012.2221113.
- [47] A. S. Babel, J. G. Cintron-Rivera, S. N. Foster, and E. G. Strangas, "Evaluation of a parameter identification method for permanent magnet ac machines through parametric sensitivity analysis," *Ieee Transactions On Energy Conversion*, vol. 29, no. 1, pp. 240-249, 2014, 10.1109/TEC.2013.2288235.
- [48] A. M. A. Oteafy, "Fast and comprehensive online parameter identification of switched reluctance machines," *Ieee Access*, vol. 9, pp. 46985-46996, 2021, 10.1109/ACCESS.2021.3068245.
- [49] M. Micev, M. Calasan, and M. Radulovic, "Full synchronous machine parameters identification based on field and armature current during the short-circuit," *Ieee Transactions On Industry Applications*, vol. 57, no. 6, pp. 5959-5968, 2021,

- 10.1109/TIA.2021.3112141.
- [50] Z. Liu, H. Wei, X. Li, K. Liu, and Q. Zhong, "Global identification of electrical and mechanical parameters in pmsm drive based on dynamic self-learning pso," *Ieee Transactions On Power Electronics*, vol. 33, no. 12, pp. 10858-10871, 2018, 10.1109/TPEL.2018.2801331.
- [51] L. Cao, X. Fan, D. Li, W. Kong, and R. Qu *et al.*, "Improved lptn-based online temperature prediction of permanent magnet machines by global parameter identification," *Ieee Transactions On Industrial Electronics*, vol. 70, no. 9, pp. 8830-8841, 2023, 10.1109/TIE.2022.3208600.
- [52] Z. Liu, X. Fan, W. Kong, L. Cao, and R. Qu, "Improved small-signal injection-based online multiparameter identification method for ipm machines considering cross-coupling magnetic saturation," *Ieee Transactions On Power Electronics*, vol. 37, no. 12, pp. 14362-14374, 2022, 10.1109/TPEL.2022.3192692.
- [53] D. M. Reed, H. F. Hofmann, and J. Sun, "Offline identification of induction machine parameters with core loss estimation using the stator current locus," *Ieee Transactions On Energy Conversion*, vol. 31, no. 4, pp. 1549-1558, 2016, 10.1109/TEC.2016.2601781.
- [54] T. Boileau, N. Leboeuf, B. Nahid-Mobarakeh, and F. Meibody-Tabar, "Online identification of pmsm parameters: parameter identifiability and estimator comparative study," *Ieee Transactions On Industry Applications*, vol. 47, no. 4, pp. 1944-1957, 2011, 10.1109/TIA.2011.2155010.
- [55] G. F. Olson, Y. Wu, and L. Peretti, "Parameter estimation of multiphase machines applicable to variable phase-pole machines," *Ieee Transactions On Energy Conversion*, vol. 38, no. 4, pp. 2822-2831, 2023, 10.1109/TEC.2023.3288368.
- [56] S. A. Odhano, P. Pescetto, H. A. A. Awan, M. Hinkkanen, and G. Pellegrino *et al.*, "Parameter identification and self-commissioning in ac motor drives: a technology status review," *Ieee Transactions On Power Electronics*, vol. 34, no. 4, pp. 3603-3614, 2019, 10.1109/TPEL.2018.2856589.
- [57] M. Nachtsheim, J. Ernst, C. Endisch, and R. Kennel, "Performance of recursive least squares algorithm configurations for online parameter identification of induction machines in an automotive environment," *Ieee Transactions On Transportation Electrification*, vol. 9, no. 3, pp. 4236-4254, 2023, 10.1109/TTE.2023.3244619.
- [58] W. Xu, Y. Tang, D. Dong, X. Xiao, and Y. Liu *et al.*, "Improved deadbeat predictive thrust control for linear induction machine with online parameter identification based on mras and linear extended state observer," *Ieee Transactions On Industry Applications*, vol. 59, no. 3, pp. 3186-3199, 2023, 10.1109/TIA.2023.3235736.
- [59] J. L. F., G. C. S., and W. H. C., "Intelligent backstepping control using recurrent feature selection fuzzy neural network for synchronous reluctance motor position servo drive system," *Ieee Transactions On Fuzzy Systems*, vol. 27, no. 3, pp. 413-427, 2019, 10.1109/TFUZZ.2018.2858749.
- [60] G. Y., Q. R., C. Yu, L. Jian, and X. Wei, "Review of off-line synchronous inductance measurement method for permanent magnet synchronous machines," in *2014 IEEE Conference and Expo Transportation Electrification Asia-Pacific (ITEC Asia-Pacific)*, 2014, pp. 1-6.
- [61] D. R. and F. R. M., "A comparative analysis of two test methods of measuring

- and q -axes inductances of interior permanent-magnet machine, " *Ieee Transactions On Magnetics*, vol. 42, no. 11, pp. 3712-3718, 2006, 10.1109/TMAG.2006.880994.
- [62] O. L., T. F., and Z. M., "Adaptive maximum torque per ampere control of synchronous reluctance motors by radial basis function networks, " *Ieee Journal of Emerging and Selected Topics in Power Electronics*, vol. 7, no. 4, pp. 2531-2539, 2019, 10.1109/JESTPE.2018.2858842.
- [63] D. E., A. Z. H., R. A. M. G., S. J., and B. F., "Online mtpa control approach for synchronous reluctance motor drives based on emotional controller, " *Ieee Transactions On Power Electronics*, vol. 30, no. 4, pp. 2157-2166, 2015, 10.1109/TPEL.2014.2323180.
- [64] P. M. and M. R., "A predictive torque control for the synchronous reluctance machine taking into account the magnetic cross saturation," in *31st Annual Conference of IEEE Industrial Electronics Society, 2005. IECON 2005.*, 2005, p. 6.
- [65] A. E., I. B. R., G. P., P. G., and P. M., "Experimental identification of the magnetic model of synchronous machines, " *Ieee Transactions On Industry Applications*, vol. 49, no. 5, pp. 2116-2125, 2013, 10.1109/TIA.2013.2258876.
- [66] J. Y. and S. S., "Adaptive flux observer with on-line inductance estimation of an ipmsm considering magnetic saturation," in *2005 IEEE 36th Power Electronics Specialists Conference*, 2005, pp. 2467-2473.
- [67] A. C. K., T. K. B., D. S. S., and J. H. H., "An improved method for incorporating magnetic saturation in the q-d synchronous machine model, " *Ieee Transactions On Energy Conversion*, vol. 13, no. 3, pp. 270-275, 1998, 10.1109/60.707607.
- [68] P. C., "Fitting saturation and hysteresis via arctangent functions, " *Ieee Power Engineering Review*, vol. 20, no. 11, pp. 55-57, 2000, 10.1109/39.883282.
- [69] A. A., C. M., P. M., and S. A., "A saturation model of the synchronous reluctance motor and its identification by genetic algorithms," in *2018 IEEE Energy Conversion Congress and Exposition (ECCE)*, 2018, pp. 4460-4465.
- [70] I. Y., N. J., S. T., A. S., and N. H., "Motor drive system using nonlinear mathematical model for permanent magnet synchronous motors," in *2014 International Power Electronics Conference (IPEC-Hiroshima 2014 - ECCE ASIA)*, 2014, pp. 2451-2456.
- [71] Q. Z., T. T., and H. M., "Inclusion of magnetic saturation in dynamic models of synchronous reluctance motors," in *2012 XXth International Conference on Electrical Machines*, 2012, pp. 994-1000.
- [72] S. Kim, Y. Yoon, S. Sul, and K. Ide, "Maximum torque per ampere (mtpa) control of an ipm machine based on signal injection considering inductance saturation, " *Ieee Transactions On Power Electronics*, vol. 28, no. 1, pp. 488-497, 2013, 10.1109/TPEL.2012.2195203.
- [73] L. K. and W. Y., "Maximum torque per ampere (mtpa) control for ipmsm drives using signal injection and an mtpa control law, " *Ieee Transactions On Industrial Informatics*, vol. 15, no. 10, pp. 5588-5598, 2019, 10.1109/TII.2019.2905929.
- [74] S. T. and W. J., "Extension of virtual-signal-injection-based mtpa control for interior permanent-magnet synchronous machine drives into the field-weakening region, " *Ieee Transactions On Industrial Electronics*, vol. 62, no. 11, pp. 6809-6817, 2015, 10.1109/TIE.2015.2438772.
- [75] I. T., I. Y., M. S., and S. M., "Maximum torque per ampere control of a direct torque-

- controlled pmsm in a stator flux linkage synchronous frame, " *Ieee Transactions On Industry Applications*, vol. 52, no. 3, pp. 2360-2367, 2016, 10.1109/TIA.2016.2531618.
- [76] H. Z., L. J., Y. W., B. P. D., and R. N. *et al.*, "Improved online maximum-torque-per-ampere algorithm for speed controlled interior permanent magnet synchronous machine, " *Ieee Transactions On Industrial Electronics*, vol. 67, no. 5, pp. 3398-3408, 2020, 10.1109/TIE.2019.2918471.
- [77] S. T., K. M., and W. J., "Mtpa control of ipmsm drives based on virtual signal injection considering machine parameter variations, " *Ieee Transactions On Industrial Electronics*, vol. 65, no. 8, pp. 6089-6098, 2018, 10.1109/TIE.2017.2784409.
- [78] L. G., W. J., Z. W., and C. Q., "A novel mtpa control strategy for ipmsm drives by space vector signal injection, " *Ieee Transactions On Industrial Electronics*, vol. 64, no. 12, pp. 9243-9252, 2017, 10.1109/TIE.2017.2711507.
- [79] Z. G., W. G., Z. H., W. H., and B. G. *et al.*, "Pseudorandom-frequency sinusoidal injection for position sensorless ipmsm drives considering sample and hold effect, " *Ieee Transactions On Power Electronics*, vol. 34, no. 10, pp. 9929-9941, 2019, 10.1109/TPEL.2019.2893763.
- [80] Z. G., W. G., W. H., X. D., and L. L. *et al.*, "Pseudorandom-frequency sinusoidal injection based sensorless ipmsm drives with tolerance for system delays, " *Ieee Transactions On Power Electronics*, vol. 34, no. 4, pp. 3623-3632, 2019, 10.1109/TPEL.2018.2865802.
- [81] W. G., Y. L., Y. B., W. B., and Z. G. *et al.*, "Pseudo-random high-frequency square-wave voltage injection based sensorless control of ipmsm drives for audible noise reduction, " *Ieee Transactions On Industrial Electronics*, vol. 63, no. 12, pp. 7423-7433, 2016, 10.1109/TIE.2016.2594171.
- [82] W. G., Y. L., Z. G., Z. X., and X. D., "Comparative investigation of pseudorandom high-frequency signal injection schemes for sensorless ipmsm drives, " *Ieee Transactions On Power Electronics*, vol. 32, no. 3, pp. 2123-2132, 2017, 10.1109/TPEL.2016.2569418.
- [83] K. D., C. K. Y., K. S. S., H. K. J., and S. Y. R., "Suppression of injection voltage disturbance for high-frequency square-wave injection sensorless drive with regulation of induced high-frequency current ripple, " *Ieee Transactions On Industry Applications*, vol. 52, no. 1, pp. 302-312, 2016, 10.1109/TIA.2015.2478887.
- [84] C. K. Y. and K. S. S., "Reduction of injection voltage in signal injection sensorless drives using a capacitor-integrated inverter, " *Ieee Transactions On Power Electronics*, vol. 32, no. 8, pp. 6261-6274, 2017, 10.1109/TPEL.2016.2620259.
- [85] L. G., Z. R., C. Z., T. W., and Z. S. *et al.*, "A novel nonlinear modeling method for permanent-magnet synchronous motors, " *Ieee Transactions On Industrial Electronics*, vol. 63, no. 10, pp. 6490-6498, 2016, 10.1109/TIE.2016.2578839.
- [86] L. K., F. J., G. S., X. L., and Q. Z. Z., "Identification of flux linkage map of permanent magnet synchronous machines under uncertain circuit resistance and inverter nonlinearity, " *Ieee Transactions On Industrial Informatics*, vol. 14, no. 2, pp. 556-568, 2018, 10.1109/TII.2017.2722470.
- [87] R. R., S. T., and W. M., "Online stator inductance estimation for permanent magnet

- motors using pwm excitation, " *Ieee Transactions On Transportation Electrification*, vol. 5, no. 1, pp. 107-117, 2019, 10.1109/TTE.2019.2891047.
- [88] G. Feng, C. Lai, X. Tan, and N. C. Kar, "Maximum-torque-per-square-ampere control for interior pmsms considering cross-saturation inductances, " *Ieee Transactions On Transportation Electrification*, vol. 7, no. 3, pp. 1482-1492, 2021, 10.1109/TTE.2021.3059238.
- [89] G. Feng, C. Lai, and N. C. Kar, "Particle-filter-based magnet flux linkage estimation for pmsm magnet condition monitoring using harmonics in machine speed, " *Ieee Transactions On Industrial Informatics*, vol. 13, no. 3, pp. 1280-1290, 2017, 10.1109/TII.2016.2616331.
- [90] J. L. F., S. H. M., G. C. S., W. H. C., and H. L. C., "Adaptive backstepping control for synchronous reluctance motor based on intelligent current angle control, " *Ieee Transactions On Power Electronics*, vol. 35, no. 7, pp. 7465-7479, 2020, 10.1109/TPEL.2019.2954558.
- [91] J. L. F., G. C. S., and W. H. C., "Intelligent backstepping control using recurrent feature selection fuzzy neural network for synchronous reluctance motor position servo drive system, " *Ieee Transactions On Fuzzy Systems*, vol. 27, no. 3, pp. 413-427, 2019, 10.1109/TFUZZ.2018.2858749.
- [92] O. L., T. F., and Z. M., "Adaptive maximum torque per ampere control of synchronous reluctance motors by radial basis function networks, " *Ieee Journal of Emerging and Selected Topics in Power Electronics*, vol. 7, no. 4, pp. 2531-2539, 2019, 10.1109/JESTPE.2018.2858842.
- [93] D. E., A. Z. H., R. A. M. G., S. J., and B. F., "Online mtpa control approach for synchronous reluctance motor drives based on emotional controller, " *Ieee Transactions On Power Electronics*, vol. 30, no. 4, pp. 2157-2166, 2015, 10.1109/TPEL.2014.2323180.
- [94] A. N., M. V., and A. C., "Model predictive control for synchronous reluctance motor drive," in *2017 CHILEAN Conference on Electrical, Electronics Engineering, Information and Communication Technologies (CHILECON)*, 2017, pp. 1-6.
- [95] N. B., D. A., N. P., R. J., and G. C., "Simplified modulated model predictive control of synchronous reluctance motor," in *2020 11th Power Electronics, Drive Systems, and Technologies Conference (PEDSTC)*, 2020, pp. 1-6.
- [96] A. R., C. M., P. L., and Z. M., "Hierarchical scaled-states direct predictive control of synchronous reluctance motor drives, " *Ieee Transactions On Industrial Electronics*, vol. 63, no. 8, pp. 5176-5185, 2016, 10.1109/TIE.2016.2536581.
- [97] L. C., D. F., X. D., and H. Z., "The decoupling control of bearingless synchronous reluctance motor based on differential geometry," in *Proceedings of the 31st Chinese Control Conference*, 2012, pp. 4261-4266.
- [98] D. E., M. A., A. Z. H., and V. S., "Deviation model-based control of synchronous reluctance motor drives with reduced parameter dependency, " *Ieee Transactions On Power Electronics*, vol. 34, no. 7, pp. 6697-6705, 2019, 10.1109/TPEL.2018.2876660.
- [99] C. A., D. L. L., P. C. F., and T. M., "The impact of the control strategy in flux observer based sensorless control of synchronous reluctance motors, " *Ieee Access*, vol. 9, pp. 156380-156391, 2021, 10.1109/ACCESS.2021.3129180.
- [100] S. P., Z. D., B. Z., X. Q., and C. B. *et al.*, "Comparison study of mras and eemf-based

- sensorless control for synchronous reluctance motor," in *2019 22nd International Conference on Electrical Machines and Systems (ICEMS)*, 2019, pp. 1-5.
- [101] R. V. Gandhi and D. M. Adhyaru, "Hybrid extended state observer based control for systems with matched and mismatched disturbances, " *Isa Transactions*, vol. 106, pp. 61-73, 2020, 10.1016/j.isatra.2020.06.019.
- [102] A. Castillo, P. García, R. Sanz, and P. Albertos, "Enhanced extended state observer-based control for systems with mismatched uncertainties and disturbances, " *Isa Transactions*, vol. 73, pp. 1-10, 2018, 10.1016/j.isatra.2017.12.005.
- [103] K. Rsetam, Z. Cao, and Z. Man, "Cascaded-extended-state-observer-based sliding-mode control for underactuated flexible joint robot, " *Ieee Transactions On Industrial Electronics (1982)*, vol. 67, no. 12, pp. 10822-10832, 2020, 10.1109/TIE.2019.2958283.
- [104] J. Liu, S. Vazquez, L. Wu, A. Marquez, and H. Gao *et al.*, "Extended state observer-based sliding-mode control for three-phase power converters, " *Ieee Transactions On Industrial Electronics (1982)*, vol. 64, no. 1, pp. 22-31, 2017, 10.1109/TIE.2016.2610400.
- [105] R. Cui, L. Chen, C. Yang, and M. Chen, "Extended state observer-based integral sliding mode control for an underwater robot with unknown disturbances and uncertain nonlinearities, " *Ieee Transactions On Industrial Electronics (1982)*, vol. 64, no. 8, pp. 6785-6795, 2017, 10.1109/TIE.2017.2694410.
- [106] Y. Long and Y. Peng, "Extended state observer-based nonlinear terminal sliding mode control with feedforward compensation for lower extremity exoskeleton, " *Ieee Access*, vol. 10, pp. 8643-8652, 2022, 10.1109/ACCESS.2021.3049879.
- [107] Z. Zhao and B. Guo, "A nonlinear extended state observer based on fractional power functions, " *Automatica*, vol. 81, pp. 286-296, 2017, 10.1016/j.automatica.2017.03.002.
- [108] J. Yao, Z. Jiao, and D. Ma, "Extended-state-observer-based output feedback nonlinear robust control of hydraulic systems with backstepping, " *Ieee Transactions On Industrial Electronics*, vol. 61, no. 11, pp. 6285-6293, 2014, 10.1109/TIE.2014.2304912.
- [109] C. Liu, G. Liu, and J. Fang, "Feedback linearization and extended state observer-based control for rotor-ambs system with mismatched uncertainties, " *Ieee Transactions On Industrial Electronics*, vol. 64, no. 2, pp. 1313-1322, 2017, 10.1109/TIE.2016.2612622.
- [110] S. Li, J. Yang, W. Chen, and X. Chen, "Generalized extended state observer based control for systems with mismatched uncertainties, " *Ieee Transactions On Industrial Electronics*, vol. 59, no. 12, pp. 4792-4802, 2012, 10.1109/TIE.2011.2182011.
- [111] Comparison study of mras and eemf-based sensorless control for synchronous reluctance motor, ".
- [112] D. Nguyen, L. Loron, and K. Dakhouche, "High-speed sensorless control of a synchronous reluctance motor based on an extended kalman filter," in, Jointly owned by EPE Association and IEEE PELS, 2015, pp. 1-10.
- [113] D. Pasqualotto, S. Rigon, and M. Zigliotto, "Sensorless speed control of synchronous reluctance motor drives based on extended kalman filter and neural magnetic model, " *Ieee Transactions On Industrial Electronics (1982)*, vol. 70, no. 2, pp. 1321-1330,

- 2023, 10.1109/TIE.2022.3159962.
- [114] Signal-injection assisted full-order observer with parameter adaptation for synchronous reluctance motor drives, ".
- [115] P. T. and S. S., "Fictitious flux and a globally stable observer for sensorless control of synchronous reluctance motors," in *2018 International Electrical Engineering Congress (iEECON)*, 2018, pp. 1-4.
- [116] A. Varatharajan, P. Pescetto, and G. Pellegrino, "Sensorless synchronous reluctance motor drives: a full-speed scheme using finite-control-set mpc in a projection vector framework," *Ieee Transactions On Industry Applications*, vol. 56, no. 4, pp. 3809-3818, 2020, 10.1109/TIA.2020.2990834.
- [117] R. Kumar, V. Verma, Y. A. Khan, and B. S. Shiva, "Q-mras based speed sensorless vector controlled synchronous reluctance motor drive," in *IEEE*, 2019, pp. 1-6.
- [118] Z. Mynar, P. Vaclavek, and P. Blaha, "Synchronous reluctance motor parameter and state estimation using extended kalman filter and current derivative measurement," *Ieee Transactions On Industrial Electronics (1982)*, vol. 68, no. 3, pp. 1972-1981, 2021, 10.1109/TIE.2020.2973897.
- [119] A. Varatharajan, P. Pescetto, and G. Pellegrino, "Sensorless synchronous reluctance motor drives: a full-speed scheme using finite-control-set mpc in a projection vector framework," *Ieee Transactions On Industry Applications*, vol. 56, no. 4, pp. 3809-3818, 2020, 10.1109/TIA.2020.2990834.
- [120] G. W. T., W. P. S., C. C. S., J. L. H., and D. Y. Y., "Flux saturation model including cross saturation for synchronous reluctance machines and its identification method at standstill," *Ieee Transactions On Industrial Electronics*, vol. 70, no. 3, pp. 2318-2328, 2023, 10.1109/TIE.2022.3174233.
- [121] L. G., Z. R., C. Z., T. W., and Z. S. *et al.*, "A novel nonlinear modeling method for permanent-magnet synchronous motors," *Ieee Transactions On Industrial Electronics*, vol. 63, no. 10, pp. 6490-6498, 2016, 10.1109/TIE.2016.2578839.
- [122] L. S., H. D., and S. B., "Modeling of interior permanent magnet machine considering saturation, cross coupling, spatial harmonics, and temperature effects," *Ieee Transactions On Transportation Electrification*, vol. 3, no. 3, pp. 682-693, 2017, 10.1109/TTE.2017.2679212.
- [123] S. B., S. G., D. D., H. A., and T. M., "Evaluation of saturation and cross-magnetization effects in interior permanent-magnet synchronous motor," *Ieee Transactions On Industry Applications*, vol. 39, no. 5, pp. 1264-1271, 2003, 10.1109/TIA.2003.816538.
- [124] Z. G., W. G., W. H., X. D., and L. L. *et al.*, "Pseudorandom-frequency sinusoidal injection based sensorless ipmsm drives with tolerance for system delays," *Ieee Transactions On Power Electronics*, vol. 34, no. 4, pp. 3623-3632, 2019, 10.1109/TPEL.2018.2865802.
- [125] L. S., H. D., and S. B., "Modeling of interior permanent magnet machine considering saturation, cross coupling, spatial harmonics, and temperature effects," *Ieee Transactions On Transportation Electrification*, vol. 3, no. 3, pp. 682-693, 2017, 10.1109/TTE.2017.2679212.
- [126] S. B., S. G., D. D., H. A., and T. M., "Evaluation of saturation and cross-magnetization effects in interior permanent-magnet synchronous motor," *Ieee Transactions On Industry Applications*, vol. 39, no. 5, pp. 1264-1271, 2003, 10.1109/TIA.2003.816538.

- [127] F. G., L. C., H. Y., and C. K. N., "Fast maximum torque per ampere (mtpa) angle detection for interior pmsms using online polynomial curve fitting," *Ieee Transactions On Power Electronics*, vol. 37, no. 2, pp. 2045-2056, 2022, 10.1109/TPEL.2021.3109112.
- [128] A. A., C. M., C. D. P. M., L. T. G., and L. M. *et al.*, "Analytical formulation of a maximum torque per ampere (mtpa) technique for synrms considering the magnetic saturation," *Ieee Transactions On Industry Applications*, vol. 56, no. 4, pp. 3846-3854, 2020, 10.1109/TIA.2020.2993525.
- [129] F. G., L. C., H. Y., and C. K. N., "Fast maximum torque per ampere (mtpa) angle detection for interior pmsms using online polynomial curve fitting," *Ieee Transactions On Power Electronics*, vol. 37, no. 2, pp. 2045-2056, 2022, 10.1109/TPEL.2021.3109112.
- [130] K. T., W. Y., S. Z., W. T., and H. S. *et al.*, "A rayleigh quotient-based recursive total-least-squares online maximum capacity estimation for lithium-ion batteries," *Ieee Transactions On Energy Conversion*, vol. 30, no. 3, pp. 842-851, 2015, 10.1109/TEC.2015.2424673.
- [131] L. H., Y. S., and L. Y., "Torque ripple minimization of low-speed gimbal servo system using parameter-optimized eso," *Ieee Journal of Emerging and Selected Topics in Power Electronics*, vol. 11, no. 2, pp. 2094-2103, 2023, 10.1109/JESTPE.2022.3219431.
- [132] Z. Y., Z. Z., Q. W., and W. L., "An extended flux model-based rotor position estimator for sensorless control of salient-pole permanent-magnet synchronous machines," *Ieee Transactions On Power Electronics*, vol. 30, no. 8, pp. 4412-4422, 2015, 10.1109/TPEL.2014.2358621.
- [133] G. C., W. X., S. X., and D. Z., "A pll-based novel commutation correction strategy for a high-speed brushless dc motor sensorless drive system," *Ieee Transactions On Industrial Electronics*, vol. 65, no. 5, pp. 3752-3762, 2018, 10.1109/TIE.2017.2760845.
- [134] L. H., Z. X., X. C., and H. J., "Sensorless control of ipmsm using moving-average-filter based pll on hf pulsating signal injection method," *Ieee Transactions On Energy Conversion*, vol. 35, no. 1, pp. 43-52, 2020, 10.1109/TEC.2019.2946888.
- [135] W. Xue, W. Bai, S. Yang, K. Song, and Y. Huang *et al.*, "Adrc with adaptive extended state observer and its application to air - fuel ratio control in gasoline engines," *Ieee Transactions On Industrial Electronics*, vol. 62, no. 9, pp. 5847-5857, 2015, 10.1109/TIE.2015.2435004.
- [136] S. Shi, J. Li, and Y. Fang, "Extended-state-observer-based chattering free sliding mode control for nonlinear systems with mismatched disturbance," *Ieee Access*, vol. 6, pp. 22952-22957, 2018, 10.1109/ACCESS.2018.2828868.
- [137] Z. Tang and B. Akin, "An improved sliding-mode observer for IPM drives with a new phase delay mitigation algorithm based on extended electromotive force model," 2015 IEEE International Electric Machines & Drives Conference (IEMDC), Coeur d'Alene, ID, USA, 2015, pp. 846-852, doi: 10.1109/IEMDC.2015.7409159.